https://doi.org/10.15388/vu.thesis.263
https://orcid.org/0000-0001-7001-2590

CENTER FOR PHYSICAL SCIENCES AND TECHNOLOGY
VILNIUS UNIVERSITY

Lukas
RAZINKOVAS

Vibrational properties and photoionization of color centers in diamond: theory and *ab initio* calculations

DOCTORAL DISSERTATION

Natural sciences,
Physics (N 002)

VILNIUS 2021

This dissertation was prepared at the Center for Physical Sciences and Technology (FTMC) between 2016 and 2020.

Scientific supervisor:
Prof. Dr. Audrius Alkauskas (Center for Physical Sciences and Technology, Natural sciences, Physics – N 002).

Dissertation Defence Panel:
Prof. Dr. Egidijus Anisimovas – chairman (Vilnius University, Natural sciences, Physics – N 002),
Assist. Prof. Dr. Cyrus E. Dreyer (Stony Brook University, Natural sciences, Physics – N 002),
Assoc. Prof. Dr. Andrius Gelžinis (Vilnius University, Natural sciences, Physics – N 002),
Assoc. Prof. Dr. Vytautas Karpus (Center for Physical Sciences and Technology, Natural sciences, Physics – N 002),
Prof. Dr. Patrick Rinke (Aalto University, Natural sciences, Physics – N 002).

The dissertation will be defended at a public meeting of the Dissertation Defence Panel at 15:00 on December 10, 2021 in Room D401 in the Center for Physical Sciences and Technology.
Address: Saulėtekio av. 3, LT-10257, Vilnius, Lithuania.
Tel. +37052648884; e-mail: office@ftmc.lt.

The text of this dissertation can be accessed at the libraries of Vilnius University and the Center for Physical Sciences and Technology, as well as on the website of Vilnius University: www.vu.lt/lt/naujienos/ivykiu-kalendorius.

https://doi.org/10.15388/vu.thesis.263
https://orcid.org/0000-0001-7001-2590

FIZINIŲ IR TECHNOLOGIJOS MOKSLŲ CENTRAS
VILNIAUS UNIVERSITETAS

Lukas
RAZINKOVAS

Taškinių defektų virpesinės savybės ir fotojonizacija: teorija ir *ab initio* skaičiavimai

DAKTARO DISERTACIJA

Gamtos mokslai,
Fizika (N 002)

VILNIUS 2021

Disertacija rengta 2016–2020 metais Fizinių ir technologijos mokslų centre (FTMC).

Mokslinis vadovas:
prof. dr. Audrius Alkauskas (Fizinių ir technologijos mokslų centras, gamtos mokslai, fizika – N 002).

Gynimo taryba:
prof. dr. Egidijus Anisimovas – pirmininkas (Vilniaus universitetas, gamtos mokslai, fizika – N 002),
prof. dr. Cyrus E. Dreyer (Stony Brook universitetas, gamtos mokslai, fizika – N 002),
doc. dr. Andrius Gelžinis (Vilniaus universitetas, gamtos mokslai, fizika – N 002),
doc. dr. Vytautas Karpus (Fizinių ir technologijos mokslų centras, gamtos mokslai, fizika – N 002),
prof. dr. Patrick Rinke (Aalto universitetas, gamtos mokslai, fizika – N 002).

Disertacija ginama viešame Gynimo tarybos posėdyje 2021 m. gruodžio mėn. 10 d. 15 val. Fizinių ir technologijos mokslų centro D401 auditorijoje.
Adresas: Saulėtekio al. 3, LT-10257, Vilnius, Lietuva.
Tel. +37052648884; el. paštas: office@ftmc.lt.

Disertaciją galima peržiūrėti Vilniaus universiteto bei Fizinių ir technologijos mokslų centro bibliotekose ir Vilniaus universiteto interneto svetainėje adresu: www.vu.lt/lt/naujienos/ivykiu-kalendorius.

CONTENTS

This dissertation is dedicated to Živilė and Ramunė
– the loves of my life

ACKNOWLEDGMENTS

First and foremost, I wish to thank my scientific supervisor, prof. Audrius Alkauskas, who brought me into the field of solid-state physics and shared his knowledge and enthusiasm. He was a caring supervisor and a supportive friend. Thanks to him, I chose the scientific path and had the most exciting and productive doctoral years.

I want to thank the referees of my doctoral dissertation, dr. Vytautas Karpus and dr. Andrius Gelžinis, for their careful review and invaluable feedback in helping me to improve this thesis. I thank prof. Patrick Rinke and prof. Cyrus Dreyer for aggreeing to be in the defense committee, and prof. Egidijus Anisimovas for chairing the defense.

I am grateful for the opportunity to collaborate with prof. Chris G. Van de Walle, dr. Marcus William Doherty and prof. Neil Manson. I am thankful to my dear friends and colleagues with whom I share common interests and had many discussions – dr. Mažena Mackoit–Sinkevičienė, dr. Marek Maciaszek, Rokas Silkinis and Vytautas Žalandauskas.

I thank my dear friends and colleagues who inspired me and contributed to my professional and personal life: prof. Gediminas Juzeliūnas, dr. Thomas Gajdosik, dr. Vytautas Dudėnas and dr. Viktor Novičenko.

My heartfelt gratefulness goes to my deceased mother, Laima Razinkovienė. Mom, I love you, and I will never forget you.

I thank my parents-in-law, Aušra Rimšienė and Saulius Rimša, for invaluable support to my family and me during these intense doctoral years.

Last but not least, I thank my loving wife Živilė, and my beautiful daughter Ramunė. You both are the purpose and joys of my life.

Lukas Razinkovas
Vilnius, 2021

PREFACE

This thesis addresses a few theoretical issues in the physics of deep-level defects in semiconductors. The study of defects in semiconductors has a rich history, dating back more than a half-century. For a long time, deep-level defects have been considered detrimental, as they generally deteriorate the characteristics of the material. Therefore, identifying, understanding, and controlling such defects is crucial in devising better electronic and optoelectronic devices. On the other hand, deep-level defects have highly localized atomic-like electronic states, which are often decoupled from those of the host material. Numerous experiments demonstrated coherent control and readout of such states in the past few decades, sometimes even at room temperature. Therefore, these deep-level defects are interesting quantum systems (called "quantum defects") with many potential and already existing applications.

The theoretical groundwork to study deep-level defects was already established many years ago. However, quantitative description of specific defects turned out to be difficult. Most earlier theoretical models have been used to provide qualitative understanding, as they relied on a simplified picture of the defect's electronic and atomic structure. It was only with the advent of modern electronic structure techniques that a more quantitative description became possible. In the past three decades, the field has experienced rapid development. Many issues that have been hitherto difficult to address were tackled. Still, the development in the field of quantitative electronic structure calculations of defects has been slower than in the case of, e.g., molecules or bulk solids, and many questions remain unsolved.

In this thesis, we focus on two particular aspects of deep-level defects: (i) vibrational and vibronic properties of isolated defects; and (ii) photoionization of deep defects. Our goal is to develop practical methodologies to calculate the relevant quantities completely from the first principles of quantum mechanics. The quantities are vibrational lineshapes of absorption and emission bands, as

well as photoionization thresholds and cross-sections. The knowledge of these quantities is important to understand the physics of known defects, as well as to identify unknown ones.

This thesis is composed of five chapters. Chapter 1 is an introduction with the main focus on preferable properties and novel applications of quantum defects. The nitrogen–vacancy (NV) center in diamond is introduced, as it is a well-understood example of such a defect. The NV center serves as a benchmark system for our theoretical analysis. Chapter 2 presents the theoretical background used to describe the defect's vibrational, vibronic, and spectroscopic properties. Most sections in this chapter contain aggregated theory from classical papers and textbooks. However, Secs. 2.5.3, 2.6.3, and 2.6.4 are original. They present our formulation to describe the multi-mode $E \otimes e$ Jahn–Teller effect at defects with C_{3v} symmetry. Chapter 3 presents the computational methodology to determine and analyze the vibrational structure of defects in the dilute limit. We apply this methodology to explain isotopic shifts of luminescence peaks of the silicon-vacancy center in diamond (Paper [T1]). Chapter 4 presents a theoretical investigation of luminescence and absorption lineshapes in the presence of the Jahn–Teller effect. The methodology is applied to NV centers in diamond (Paper [T2]). In Chapter 5, we address the photoionization of deep defects in solids. We present a new methodology to calculate photoionization cross-sections. This methodology is applied to explain the photoionization mechanisms of the NV center (Paper [T3]).

Chapter 1

INTRODUCTION

Point defects are omnipresent in semiconductor materials. They are imperfections of local lattice sites in the otherwise purely periodic crystal structure. Such defects are classified into two broad categories depending on the ionization energy: shallow- and deep-level defects. Shallow defects can be thermally ionized at an operating temperature of the device (usually room temperature) and make the material n-type or p-type conductive. On the other hand, for deep-level defects, the excitation energy required to release a bound electron (or hole) to the conduction (or valence) band is much larger than the characteristic thermal energy. The typical feature of deep-level defects is strongly localized carrier states, in contrast to more delocalized states of shallow defects.

Historically deep-level defects were considered undesirable as they interfere with the preferable properties of a material. They impede the doping behavior, increase non-radiative recombination, and deteriorate the material's electronic and optoelectronic properties. However, in the past two decades, a new viewpoint emerged towards optically active point defects, also known as *color centers*. Some of them can occur in small concentrations and exhibit strong and photostable optical transitions. This property permits optical detection of individual centers and makes such defects suitable systems for single-photon generation [4]. Furthermore, deep-level defects have electronic states within the host material's band-gap and resemble systems like isolated atoms or molecules. They possess their orbital, spin, and nuclear degrees of freedom which are sufficiently isolated from the host environment. For some defects, such states can be initialized, manipulated, and read out using optical and electrical methods. There has been a lot of progress in the spin control of isolated color centers [5–8]. Due to weak coupling to the environment, spins in solids display low decoherence rates (sometimes even

at room temperature), making it possible to achieve coherent control in the time scales suitable for quantum technology applications [9]. Together with scalable device engineering, they are promising platforms for new kinds of technologies.

A good example of such a "quantum defect" is the negatively charged *nitrogen–vacancy center* (NV^-) in diamond [10]. It is a stable and bright defect with a localized spin that can be prepared and read out using optical excitation and subsequently coherently manipulated using microwave radiation. This unique set of properties made NV center one of the key platforms to test and eventually implement various quantum technologies. A lot of success has already been demonstrated in the field of quantum-enhanced sensing [11], quantum communication [12], and quantum computing [13, 14].

The success of the diamond NV center propelled the research field of deep-level point defects in semiconductors, as there are other systems with similarly useful quantum properties [15]. Indeed, it has been found that other impurity systems can be used for quantum technological applications [6, 8, 16]. However, despite many years of research, the physical understanding of deep-level defects is far from complete. The defect is not an isolated system, as it is embedded in the matrix of the host material. The presence of surfaces and other structural and isotopic impurities introduces non-trivial interactions and makes it hard to disentangle characteristic properties of the defect from those of the surrounding material. From an experimental perspective, not every property can be measured directly. Even the identification of a defect's chemical structure is a non-trivial task. This is where the theoretical analysis can play a strong supportive role.

This thesis is about a theoretical description of such deep-level defects. Here, we focus on the *electronic*, *vibrational*, and *vibronic* structures of defects, as they are essential for the rigorous quantum-mechanical description. Moreover, these structures determine the color center's optical spectra, which have subtle features often unique to the defect. Therefore, the theoretical ability to predict optical lineshapes should help to identify new color centers. Furthermore, in the case of established defects, modeling of optical lineshapes serves as a benchmark for theoretical methods and calculations. In this study, we advance *first-principles* theoretical methods for describing (i) the vibrational and vibronic structure, (ii) electron–phonon interactions, (iii) optical lineshapes, and (iv) photoionization cross-sections of deep-level defects. These methods are then applied to the nitrogen–vacancy center of diamond to explain its optical signatures and the photoionization processes.

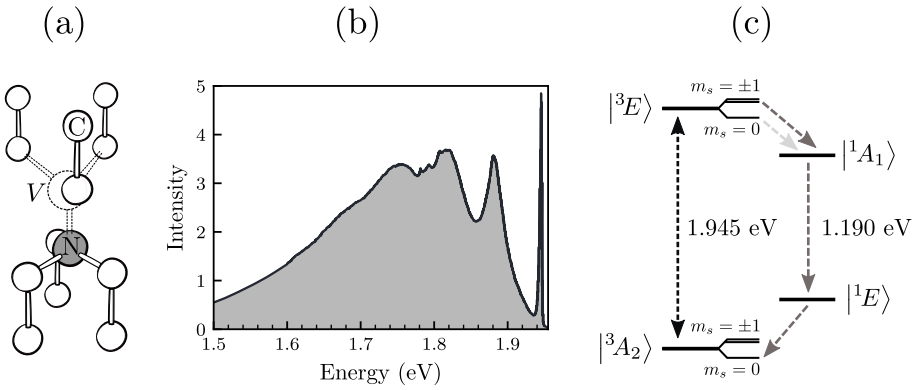

Figure 1.1: (a) Atomic structure of the nitrogen–vacancy (NV) center in diamond. (b) Experimental photoluminescence spectra at 4 K from Ref. [17]. (c) Energy level diagram of the NV center.

1.1 Introduction to the NV center

The nitrogen–vacancy color center in diamond is the central defect system considered in this thesis. It is a well-studied impurity–vacancy complex and has well-characterized optical features, suitable for benchmark calculations. In this dissertation, we perform a rigorous analysis of the NV^- center's vibrational and vibronic structure, and then, using this data, we describe optical processes of emission, absorption, and ionization. This section briefly introduces the electronic structure and the basic physics of the negatively charged NV center.

The NV center is formed when one carbon atom is replaced by a nitrogen, accompanied by the formation of an adjacent vacancy site, shown in Fig. 1.1(a). This geometric structure has C_{3v} point group symmetry. The NV center is known to exist in three charge states: negative (NV^-), neutral (NV^0), and positive (NV^+). The negative charge state is most frequently used in quantum technological applications. The identifying feature of NV^- is its unique spectral signature of the photoluminescence band, shown in Fig. 1.1(b). The sharp peak at 1.945 eV corresponds to a purely electronic transition (with no vibrational excitation) and is known as the *zero phonon line* (ZPL). The broad vibrational sideband extends to the lower energy and reflects electron–lattice interaction. After this band was first reported in 1965 by du Preez [18], the NV center became an active subject of investigation and is now one of the most studied defects in diamond.

The energy-level diagram of NV^- is shown in Fig. 1.1(c). The ground state is of orbital symmetry A_2 and is a spin-triplet with $D_{\rm gs} \approx 2.87$ GHz

zero-field splitting between $m_s = 0$ and $m_s = \pm 1$ spin sub-levels [10]. The optically excited state ^3E is a degenerate orbital-doublet and spin-triplet with the zero-field splitting of $D_{\text{es}} \approx 1.42$ GHz [19]. The spin-conserving transition $^3A_2 \leftrightarrow {}^3E$ is observed to be extremely photostable under off-resonant excitations ($\sim$2.3 eV) [20]. Together with a short decay time ($\sim$12 ns), these properties make the NV^- center an attractive system for single-photon generation.

The optical spin detection and preparation of the NV^- center can be explained as follows. After the optical excitation to the ^3E state, there is a possibility of non-radiative decay to a spin-singlet level $^1A_1$ [Fig. 1.1(c)]. This transition is more probable if the initial spin state is $m_s = \pm 1$ and weaker for $m_s = 0$ [10]. Such spin-selective behavior is reflected in the strength of the photoluminescence signal, as the intensity of optical transition $^3E \rightarrow {}^3A_2$ is stronger for $m_s = 0$. This mechanism enables an *optical readout* of the spin state [21]. After the transition to the $^1A_1$ level, the system non-radiatively decays to the spin-singlet ^1E state and then back to the ground state $^3A_2$. However, this time, the most probable final state is $m_s = 0$. The overall process leads to *optical spin-polarization*, as after a few cycles, the NV^- center has a preferential spin projection $m_s = 0$. An applied magnetic field splits $m_s = \pm 1$ sublevels of the ground state $^3A_2$. Then, the $m_s = 0$ and $m_s = -1$ spin states can be chosen to function as a two-level qubit system, which can be manipulated using microwave radiation adjusted to energy splitting. The coherence times of this spin system can reach milliseconds at room temperature [22] and seconds at cryogenic temperatures [23]. However, in modern practical applications, the qubit is a nuclear spin coupled to the NV center [24].

In summary, the NV^- center is a bright and stable paramagnetic defect, with spin states which can be optically initialized, manipulated, and read out at room temperature.

While the NV^- center is the main focus, we also consider the negatively charged silicon–vacancy center (SiV^-) in diamond [25]. It is another prominent defect system with potential applications in quantum technologies. The short introduction to the SiV^- center is given in Sec. 3.4.1.

1.2 Main goals and tasks of the thesis

The first goal of this research work is to develop a theoretical methodology for describing optical lineshapes and photoionization processes of deep-level defects. The second goal is the application of these methods to explain the

vibrational structure of SiV^- and NV^- centers of diamond and photoionization mechanisms of NV^-. To achieve these goals, we formulated the following tasks:

(1) Improve the computational methodology for the calculation of the defects' vibrational structure in the dilute limit.

(2) Develop practical theoretical methods for the analysis of the dynamical multi-mode Jahn–Teller effect in color centers.

(3) Develop an *ab initio* methodology for the calculation of photoionization cross-sections in the supercell geometry.

(4) Explain the isotopic shift of the phonon side peak in the luminescence spectrum of the negatively charged silicon–vacancy center of diamond.

(5) Model theoretical luminescence and absorption lineshapes of the NV^- center.

(6) Model absolute cross-sections of absorption, emission, and photoionization processes of the NV^- center.

1.3 Statements presented for the defense

(I) We suggest that the experimentally observed sharp vibrational feature in the photoluminescence spectrum of SiV^- is an e_u-symmetry vibrational resonance. The appearance of this feature in the experimental spectrum cannot be explained in the Frank–Condon approximation. We hypothesize that this peak is due to the Herzberg–Teller effect, whereby the vibration modulates the optical transition dipole moment.

(II) We developed a novel computationally tractable methodology for the *ab initio* description of the multi-mode Jahn–Teller effect in point defects. This methodology improves current theoretical techniques that are based on the single-mode approximation.

(III) Our *ab initio* methodology to calculate luminescence and absorption lineshapes accurately reproduces the NV^- center's experimental lineshapes.

(IV) After the photoionization from the ^3E state, NV centers transition into the metastable $^4A_2$ state of NV^0. This explains electron spin resonance experiments and has important consequences for the charge dynamics of the NV center. We determine the threshold for the photoionization to be 1.15 eV.

(V) Our *ab initio* methodology for the photoionization cross-section calculations explains recent photoionization experiments and elucidates the charge-state dynamics of NV centers.

1.4 Authors contribution and presentation of the results

During the doctoral years author contributed to five scientific papers:

(T1) E. Londero, G. Thiering, L. Razinkovas, A. Gali, and A. Alkauskas, *Vibrational modes of negatively charged silicon-vacancy centers in diamond from ab initio calculations*, Phys. Rev. B **98**, 035306 (2018)

(T2) L. Razinkovas, M. W. Doherty, N. B. Manson, C. G. Van de Walle, and A. Alkauskas, *Vibrational and vibronic structure of isolated point defects*: *The nitrogen–vacancy center in diamond*, Phys. Rev. B **104**, 045303 (2021)

(T3) L. Razinkovas, M. Maciaszek, F. Reinhard, M. W. Doherty, and A. Alkauskas, *Photoionization of negatively charged NV centers in diamond*: *theory and ab initio calculations*, Phys. Rev. B, *under review* (2021)

(T4) L. Skuja, K. Smits, A. Trukhin, F. Gahbauer, R. Ferber, M. Auzinsh, L. Busaite, L. Razinkovas, M. Mackoit-Sinkevičienė, and A. Alkauskas, *Dynamics of singlet oxygen molecule trapped in silica glass studied by luminescence polarization anisotropy and density functional theory*, J. Phys. Chem. C **124**, 7244 (2020)

(T5) M. Maciaszek, L. Razinkovas, and A. Alkauskas, *Thermodynamics of carbon defects in hexagonal boron nitride*, *submitted to Phys. Rev. Mater.* (2021)

The author of this thesis is the main contributor in papers (II) and (III).

The results of the thesis were presented at the following conferences:

1. L. Razinkovas, A. Alkauskas, *Virpesinės izoliuotų taškinių defektų savybės*, LNFK42, 2017-10-04, Vilnius, Lithuania.
2. L. Razinkovas, A. Alkauskas, *Defektų liuminescencijos linijos modeliavimas ab initio metodais*, FizTech, 2018-10-17, Vilnius, Lithuania.
3. L. Razinkovas, G. Thiering, A. Gali, A. Alkauskas, *Vibrational modes of negatively charged silicon-vacancy centers in diamond from ab initio calculations*, Diamond Workshop SBDD XXIV, 2019-03-13, Hasselt, Belgium.
4. L. Razinkovas, E. Londero, G. Thiering, A. Gali, A. Alkauskas, *Vibrational modes of negatively charged silicon-vacancy centers in diamond from ab initio calculations*, FizTech, 2019-10-23, Vilnius, Lithuania.
5. L. Razinkovas, M. Maciaszek, F. Reinhard, M.W. Doherty, A. Alkauskas, *Photoionization of negatively charged NV centers in diamond: theory and ab initio calculations*, 31st International Conference on Defects in Semiconductors, 2021-07-25, Oslo, Norway.

Chapter 2

THEORY AND FORMAL DEVELOPMENT

Is this the real life? Is this just fantasy?
Caught in a landslide, no escape from reality
Open your eyes, look up to the skies and see
— Queen, *Bohemian Rhapsody*

This chapter presents a theoretical framework for analyzing electronic, vibrational, and vibronic structures of deep-level defects. In Section 2.1, we formulate the theoretical problem of the defect system in the framework of non-relativistic quantum mechanics. Section 2.2 introduces the crude adiabatic approximation. Section 2.3 discusses the electronic problem and introduces density functional theory (DFT), which is our method of choice for electronic structure calculations. Special attention is given to the excited state calculations and a Kohn–Sham single-particle picture. At the end of Section 2.3, we present a molecular-orbital model that supplements density functional theory calculations and provides an intuitive framework for describing multi-electron states of deep-level defects. Section 2.4 introduces the methods for the analysis of lattice dynamics. In the harmonic approximation, lattice motion corresponds to simple vibrations around the equilibrium configuration. However, when the electronic degeneracy is present, adiabatic approximation fails, and the nuclear dynamics result in a complicated motion, which cannot be reduced to a simple harmonic form. Systems of such behavior are termed as *Jahn–Teller systems*. Therefore, Section 2.5 introduces the theory of the Jahn–Teller effect, which goes beyond the adiabatic approximation. Finally, in Section 2.3, we discuss the interaction with light and the theoretical approach for describing the spectral properties of deep-level defects. The concept of electron–phonon interaction is presented, and general formulae are derived for calculating the optical spectrum.

The content of this chapter mainly aggregates different theoretical ideas from classical papers and textbooks. Our original contribution is presented in Sections 2.5.3, 2.6.3, and 2.6.4. In these sections, we introduce our approach to the multi-mode Jahn–Teller problem and derive formulae for vibronic states, matrix elements, and optical spectrum in the case of $E \otimes (e \oplus e \oplus \cdots)$ vibronic coupling.

2.1 The nature of the problem

From the microscopic point of view, pure crystal is an infinite structure that is periodic with respect to spatial translations. From the theoretical perspective, such a system is effectively modeled by considering only the *unit cell*. The unit cell generates the whole crystal by periodic repetition in space and completely reflects the structural and symmetrical properties of the entire solid. However, the defect breaks this symmetry, and theoretical techniques applicable to periodic structures are partially lost. In some cases, defect-related effects can be treated as small perturbations to the periodic system. This is often done for shallow impurities. However, deep-level defects strongly perturb the surrounding environment and require different theoretical techniques. There are two approaches to model defect systems: (i) a *cluster approach*, where the quasi-infinite system is approximated by a cluster, containing a finite number of atoms; (ii) a *supercell approach*, where periodic modeling is applied for non-periodic systems by selecting the large unit cell with an embedded defect (see Section 2.3.4 for a more detailed discussion).

In the absence of external perturbations, the behavior of a molecular system is described by a time-independent Schrödinger equation:

$$\hat{H}(\mathbf{r}, \mathbf{R})\Psi(\mathbf{r}, \mathbf{R}) = E\Psi(\mathbf{r}, \mathbf{R}). \tag{2.1}$$

Here we use an abstract notation, where index-free bold symbols denote a set of electronic or nuclear degrees of freedom, i.e., $\mathbf{r} = \{\mathbf{r}_1, \ldots, \mathbf{r}_{N_\mathrm{e}}\}$ for electronic coordinates and $\mathbf{R} = \{\mathbf{R}_1, \ldots, \mathbf{R}_{N_\mathrm{n}}\}$ for nuclear coordinates[1] (N_e and N_n label the number of electrons and ions). In this thesis, we ignore all relativistic effects (e.g., spin–orbit interaction). The Hamiltonian $\hat{H}$ contains all information about the system and its particle–particle interactions:

$$\hat{H} = \hat{T}_\mathrm{e}(\mathbf{r}) + \hat{T}_\mathrm{n}(\mathbf{R}) + \hat{U}_\mathrm{ee}(\mathbf{r}) + \hat{U}_\mathrm{en}(\mathbf{r}, \mathbf{R}) + \hat{U}_\mathrm{nn}(\mathbf{R}). \tag{2.2}$$

[1] The electronic spin can be accounted for by replacing $\mathbf{r} \to \mathbf{x} = \{\mathbf{r}, \boldsymbol{\sigma}\}$, where $\boldsymbol{\sigma}$ denotes the spin degrees of freedom.

In this equation, $\hat{T}_{\mathrm{e}}$ and $\hat{T}_{\mathrm{n}}$ are electronic and nuclear kinetic energy operators, respectively:

$$\hat{T}_{\mathrm{e}} = -\frac{1}{2}\sum_{i}^{N_{\mathrm{e}}} \nabla^2_{\mathbf{r}_i}, \quad \hat{T}_{\mathrm{n}} = -\frac{1}{2}\sum_{i}^{N_{\mathrm{n}}} \frac{1}{M_i}\nabla^2_{\mathbf{R}_i}.$$

Here and throughout the thesis, we adopt Hartree atomic units, where $\hbar = m_e = e = 4\pi/\varepsilon_0 = 1$. The potential energy terms $\hat{U}_{\mathrm{ee}}$, $\hat{U}_{\mathrm{en}}$, and $\hat{U}_{\mathrm{nn}}$ individually describe electron–electron, electron–nuclei, and nuclei–nuclei Coulombic interactions:

$$\hat{U}_{\mathrm{ee}} = \sum_{i<j}^{N_{\mathrm{e}}} \frac{1}{|\mathbf{r}_i - \mathbf{r}_j|}, \tag{2.3}$$

$$\hat{U}_{\mathrm{en}} = -\sum_{i}^{N_{\mathrm{e}}}\sum_{j}^{N_{\mathrm{n}}} \frac{Z_j}{|\mathbf{r}_i - \mathbf{R}_j|}, \tag{2.4}$$

$$\hat{U}_{\mathrm{nn}} = \sum_{i<j}^{N_{\mathrm{n}}} \frac{Z_i Z_j}{|\mathbf{R}_i - \mathbf{R}_j|}. \tag{2.5}$$

The direct solution of Eqs. (2.1)–(2.5) is practically impossible due to its complicated many-body nature. Therefore, a sequence of approximations must be adopted to obtain practical results. The correct choice of approximations should lead to a systematic convergence of the theory towards the truthful description of the system. The best example of such approximate treatment is an adiabatic approximation, which effectively separates electronic and nuclear subsystems. In the next section, we present the adiabatic approximation in the form used throughout the whole thesis. This form differs from the original Born–Oppenheimer formulation as it defines the electronic subsystem for fixed nuclear positions $\mathbf{R}_0$ (rather than be dependent on $\mathbf{R}$). Compared to other traditional forms, this is a rougher assumption and is named *crude adiabatic approximation*. However, this simple form is very convenient for a subsequent treatment of non-adiabatic effects, which is the topic of Section 2.5. Once the adiabatic form is reached, we can separate the discussion of electronic and vibrational structures.

2.2 Crude adiabatic approximation

The very notion of the nuclear or electronic configuration of the molecular system essentially relies on the adiabatic approximation. All adiabatic approximations are based on the fact that the nuclear masses are much larger than the

electronic ones. This implies that electron velocity is much larger than that of the nuclei, and we can separate electronic and vibrational degrees of freedom without losing much of the accuracy. From many adiabatic approximations, the crude adiabatic approximation (CAA) [26] is the most straightforwardly applied in electronic structure calculations of solids.[2] Formally, this approximation can be obtained starting from the exact Hamiltonian (2.2) of the system:

$$\hat{H}(\mathbf{r},\mathbf{R}) = \hat{T}_{\mathrm{e}}(\mathbf{r}) + \hat{T}_{\mathrm{n}}(\mathbf{R}) + \hat{U}(\mathbf{r},\mathbf{R}). \tag{2.6}$$

In this equation, $\hat{U} = \hat{U}_{\mathrm{ee}} + \hat{U}_{\mathrm{en}} + \hat{U}_{\mathrm{nn}}$ is the potential energy of all particle–particle interactions [Eqs. (2.3)–(2.5)]. Let us expand $\hat{U}$ around some reference nuclear configuration $\mathbf{R}_0$:

$$\begin{aligned}\hat{U}(\mathbf{r},\mathbf{R}) &= \hat{U}(\mathbf{r},\mathbf{R}_0) + \sum_n \frac{\partial \hat{U}}{\partial \mathbf{u}_n}\Big|_0 \mathbf{u}_n + \frac{1}{2}\sum_{n,m} \frac{\partial \hat{U}}{\partial \mathbf{u}_n \partial \mathbf{u}_m}\Big|_0 \mathbf{u}_n \mathbf{u}_m + O(\mathbf{u}^3) \\ &= \hat{U}(\mathbf{r},\mathbf{R}_0) + \Delta\hat{U}(\mathbf{r},\mathbf{R}).\end{aligned} \tag{2.7}$$

Here, $\mathbf{u}_n = \mathbf{R}_n - \mathbf{R}_{0,n}$ denotes the three-dimensional displacement of nuclei n about the point $\mathbf{R}_{0,n}$. The first term of Eq. (2.7) is a static contribution independent of nuclear motion. In contrast, the second term in the second line of Eq. (2.7) contains all the information about nuclear dynamics. In the CAA, the electronic spectrum $\psi_i(\mathbf{r})$ and energies ε_i are defined as eigenstates and eigenvalues of the electronic Schrödinger equation:

$$\left[\hat{T}_{\mathrm{e}} + \hat{U}(\mathbf{r},\mathbf{R}_0) - \varepsilon_i\right] \psi_i(\mathbf{r},\mathbf{R}_0) = 0. \tag{2.8}$$

The solution of this equation is discussed in the next section. The exact eigenfunction of the Hamiltonian (2.6) can be expressed in the form of the expansion:

$$\Psi(\mathbf{r},\mathbf{u}) = \sum_i \chi_i(\mathbf{u})\psi_i(\mathbf{r},\mathbf{R}_0), \tag{2.9}$$

where $\chi_i(\mathbf{u})$ are functions of nuclear coordinates. Searching for the solution of Eq. (2.6) in the form of Eq. (2.9), one arrives at the equations for $\chi_i(\mathbf{u})$:

$$\hat{T}_{\mathrm{n}}\chi_j(\mathbf{u}) + \sum_i \langle\psi_j|\,\Delta\hat{U}\,|\psi_i\rangle\,\chi_i(\mathbf{u}) = (E-\varepsilon_j)\chi_j(\mathbf{u}). \tag{2.10}$$

Here, $\langle\cdot|\,\cdot\,|\cdot\rangle$ stands for integration over electronic coordinates. The crude adiabatic approximation is obtained by ignoring off-diagonal terms in Eq. (2.10):

$$\langle\psi_j|\,\Delta\hat{U}\,|\psi_i\rangle = 0, \quad \text{for } j \neq i. \tag{2.11}$$

[2] Term "static approximation" is also often used.

In this case, equation (2.10) attains diagonal form (w.r.t. electronic states), and the eigenfunction can be written in the adiabatic form:

$$\Psi_i(\mathbf{r}, \mathbf{u}) = \chi_i(\mathbf{u})\psi_i(\mathbf{r}, \mathbf{R}_0). \tag{2.12}$$

Once the electronic problem of Eq. (2.8) is solved, the coefficients χ_i for selected ψ_i are expressed as the eigenstates of the adiabatic nuclear Schrödinger equation:

$$\left[\hat{T}_\mathrm{n} + \hat{V}_i(\mathbf{u})\right] \chi_i(\mathbf{u}) = E_v \chi_i(\mathbf{u}), \tag{2.13}$$

where $E_v = E - \varepsilon_i$ is the energy contribution due to the motion of nuclei and

$$\hat{V}_i(\mathbf{u}) \equiv \langle \psi_i | \, \Delta\hat{U} \, | \psi_i \rangle \,, \tag{2.14}$$

is the potential energy of nuclei in the presence of electronic state ψ_i. $\hat{V}_i$ holds all the information required to solve the nuclear equation (2.13) and is known as *adiabatic potential energy surface* (APES). Adiabatic approximation significantly simplifies the problem. Instead of solving Eq. (2.1), which treats electronic and nuclear degrees of freedom equally, we first solve the electronic equation (2.8), treating nuclei as an array of fixed point charges. Once the solution is known, we can calculate the adiabatic potential energy surface (2.14) and solve the equation (2.13), which determines the dynamical motion of ions in the selected electronic state ψ_i. Usually, close to the equilibrium configuration, such dynamical motion manifests itself as quantum harmonic oscillations. Thus, one often refers to excitations of the nuclear subsystem as *vibrations* or *phonons*. The formal treatment of the nuclear dynamical problem is presented in Section 2.4.

Approximation (2.11) works well when relatively large energy gaps separate electronic states of interest and fails when this separation is comparable to phonon excitation quanta [27]. Thus, the validity of the adiabatic approximation can be verified by first solving the adiabatic problem and then comparing electronic energies ε_i with vibrational energies E_v. If electronic states are well separated, the expected CAA error for energy is of the order $(m/M)^{1/2} \approx 2.3 \times 10^{-2}$ [28]. The particular case of non-validity of the adiabatic approximation is the presence of electronic degeneracy. For degenerate states, simple separation of electronic and nuclear parts in the form of Eq. (2.12) is not possible. Such states are termed to be Jahn–Teller (JT) systems. The theory of JT effects is the topic of Section 2.5.

2.3 Electronic structure

The topic of this section is the solution of the electronic Schrödinger equation (2.8). Despite the simplification of the adiabatic approximation, it is still a formidable task, especially if one considers large systems where thousands of electrons are present. Thus, the electronic problem requires the use of approximate electronic structure techniques. The method of choice in this thesis is the *density functional theory* (DFT) of Hohenberg and Kohn [29, 30]. It is the leading *ab initio*[3] method for electronic structure analysis of solid-state systems, as it allows to address systems up to several hundred or even thousands of atoms. In Section 2.3.1, a short review of the ground-state density functional theory will be presented. Although DFT is formulated in terms of electron density, a single-particle picture emerges in the Kohn–Sham formulation of the theory [30]. Thereby, in Section 2.3.2, the meaning of single-particle orbitals is discussed, and the methodology for excited-state calculations is presented. Section 2.3.3 reviews different approximate schemes for the exchange–correlation functional, which is the core part of DFT. The practical implementation of Kohn–Sham density functional theory is introduced in Section 2.3.4. Finally, Section 2.3.5 presents the molecular orbital model, which supplements DFT calculations and allows intuitive interpretation of the defect's electronic structure.

2.3.1 Density Functional Theory

The central problem of electronic structure theory is the solution of the eigenvalue problem for electrons [Eq. (2.8)]. The explicit form of the potential $\hat{U}(\mathbf{r}, \mathbf{R}_0)$ involves electron–electron interactions $\hat{U}_{\mathrm{ee}}(\mathbf{r})$ and an external potential $\hat{v}(\mathbf{r}, \mathbf{R}_0)$:

$$\hat{U}(\mathbf{r}, \mathbf{R}_0) = \hat{U}_{\mathrm{ee}}(\mathbf{r}) + \sum_i^{N_\mathrm{e}} \hat{v}(\mathbf{r}_i, \mathbf{R}_0).$$

For isolated molecular systems, the external potential corresponds to electron–nuclei interaction $\hat{v}(\mathbf{r}, \mathbf{R}_0) = -\sum_j Z_j/|\mathbf{r} - \mathbf{R}_{0,j}|$. The exact solution of Eq. (2.8) using traditional wavefunction-based methods is practically impossible for realistic solid-state systems. Contrary to traditional methods, the density functional theory solves the electronic problem in terms of the *electronic density* $\rho(\mathbf{r})$, a function of three spatial variables. The electron density measures

[3] In Latin, *ab initio* means "from the beginning" (or "from first principles"), implying that the only input parameters are physical constants.

the probability of an electron being present at infinitesimal volume element and is defined as an observable of spatial density operator $\hat{\rho}(\mathbf{r}) = \sum_i^{N_\mathrm{e}} \delta(\mathbf{r} - \mathbf{r}_i)$:

$$\begin{aligned} \rho(\mathbf{r}) &\equiv \langle\psi|\hat{\rho}(\mathbf{r})|\psi\rangle \\ &= N_\mathrm{e} \int |\psi(\mathbf{r}, s_1, \mathbf{x}_2, \ldots, \mathbf{x}_{N_\mathrm{e}})|^2 \, \mathrm{d}s_1 \, \mathrm{d}\mathbf{x}_2 \cdots \mathrm{d}\mathbf{x}_{N_\mathrm{e}}. \end{aligned} \quad (2.15)$$

Here $\mathbf{x}_i = (\mathbf{r}_i, s_i)$ denotes the combination of spatial and spin degrees of freedom. The traditional wavefunction based approach relies on the minimization of the energy expectation value with respect to the total wavefunction ψ:

$$E_0 = \min_\psi \left\langle \psi \middle| \hat{T} + \hat{U}_\mathrm{ee} + \sum_i^{N_\mathrm{e}} \hat{v}(\mathbf{r}_i) \middle| \psi \right\rangle. \quad (2.16)$$

However, the wavefunction itself is not directly needed to evaluate the expectation value, as the electron density can be used instead. This statement is formally proven by two Hohenberg–Kohn (HK) theorems [29], laying the groundwork for density functional theory.

Hohenberg–Kohn theorems

The first HK theorem establishes the connection between electron density and the many-electron Schrödinger equation for the wavefunction $\psi(\mathbf{r}_1, \cdots, \mathbf{r}_{N_\mathrm{e}})$. This theorem states:

First Hohenberg–Kohn theorem [29]. *The ground state density $\rho_0(\mathbf{r})$ of a multi-electron system in some external potential $\hat{v}(\mathbf{r})$ determines this potential uniquely.*

In other words, if two electronic systems bound with potentials $\hat{v}_1(\mathbf{r})$ and $\hat{v}_2(\mathbf{r})$ have the same ground-state density, these potentials must be equal up to a constant. This is a significant result as it points out that the ground state density encodes all the electronic properties of the system as well as the ground state wavefunction ψ_0 itself. This fact enables us to write the ground state wavefunction ψ_0 and energy E_0 as functionals of ρ:

$$\begin{aligned} E_0[\rho] &= \left\langle \psi_0[\rho] \middle| \hat{T} + \hat{U}_\mathrm{ee} + \sum_i^{N_\mathrm{e}} \hat{v}(\mathbf{r}_i) \middle| \psi_0[\rho] \right\rangle \\ &= \int \rho(\mathbf{r}) \hat{v}(\mathbf{r}) \, \mathrm{d}\mathbf{r} + \hat{F}_\mathrm{HK}[\rho]. \end{aligned} \quad (2.17)$$

In the last line, the functional is split into two parts: the first term $\int \rho(\mathbf{r})\hat{v}(\mathbf{r})\,\mathrm{d}\mathbf{r}$ describes the interaction with external potential, while the second term:

$$\hat{F}_{\mathrm{HK}}[\rho] = \left\langle \psi_0[\rho] \middle| \hat{T} + \hat{U}_{\mathrm{ee}} \middle| \psi_0[\rho] \right\rangle$$

describes the energy contribution from kinetic energy and mutual electron–electron interactions. $\hat{F}_{\mathrm{HK}}[\rho]$ is defined independently of external potential $\hat{v}(\mathbf{r})$ and is known as the "*universal functional*".

The second HK theorem lays the groundwork for the variational principle:

Second Hohenberg–Kohn theorem [29]. *The functional $E_0[\rho]$ gives the lowest energy of the system if and only if the input density is the actual ground-state density.*

Particularly, if the true functional form of $\hat{F}_{\mathrm{HK}}[\rho]$ is known, the ground-state density and energy can be determined by minimizing the total energy functional:

$$E_0 = \min_{\rho} E[\rho]. \tag{2.18}$$

Once this density is known, all other properties can, in principle, be calculated.

In the original paper, HK theorems were formulated for non-degenerate states and only for particular types of densities. Eq. (2.18) holds only if the given density is associated with the ground state wavefunction of some Hamiltonian $\hat{H} = \hat{T} + \hat{U}_{\mathrm{ee}} + \hat{v}'$, where $\hat{v}'$ is any local potential. Such densities are called v-representable densities. This is a troublesome constrain as it is hard to check whether the given density satisfies the latter condition. Fortunately, Levy [31] and Lieb [32] reformulated density functional theory in a much broader and convenient sense. The requirement of v-representability in HK theorems stems from the fact that only for such densities we can find a one-to-one correspondence between density and the ground-state wavefunction (note that in general, there exists an infinite number of antisymmetric wavefunctions that give the same density $\rho(\mathbf{r})$). Levy [31] noted that from all the antisymmetric wavefunctions that correspond to $\rho_0(\mathbf{r})$, the true ground state wavefunction minimizes the universal functional $\hat{F}_{\mathrm{HK}}[\rho]$, while Lieb [32] proved that such a minimum exists. Following these arguments, the whole theory was augmented using a two-step *constrained-search formulation*, which extends HK theorems to include any densities that can be derived from any N-electron antisymmetric wavefunction (N-representability). Such constraint is very weak since it can be satisfied by any non-negative differentiable function $\rho(\mathbf{r})$ for which $\int \rho(\mathbf{r})\,\mathrm{d}\mathbf{r} = N_{\mathrm{e}}$ [32].

Kohn–Sham formulation

The practical implementation of density functional theory is done via the self-consistent Kohn–Sham formulation [30]. In their work, Kohn and Sham [30] reformulated the variational problem for density in terms of fictitious non-interacting electrons orbitals ϕ_i^{KS}, often termed *Kohn–Sham* (KS) *orbitals*. These orbitals constitute the antisymmetric determinantal wavefunction:

$$\psi_{\mathrm{KS}} = \frac{1}{\sqrt{N_{\mathrm{e}}!}} \left| \phi_1^{\mathrm{KS}} \phi_2^{\mathrm{KS}} \cdots \phi_{N_{\mathrm{e}}}^{\mathrm{KS}} \right|, \tag{2.19}$$

where $|\cdots|$ denotes the determinant made from one-electron wavefunctions:

$$\left| \phi_1^{\mathrm{KS}} \phi_2^{\mathrm{KS}} \cdots \phi_N^{\mathrm{KS}} \right| \equiv \det \begin{pmatrix} \phi_1^{\mathrm{KS}}(\mathbf{r}_1) & \phi_2^{\mathrm{KS}}(\mathbf{r}_1) & \cdots & \phi_{N_{\mathrm{e}}}^{\mathrm{KS}}(\mathbf{r}_1) \\ \phi_1^{\mathrm{KS}}(\mathbf{r}_2) & \phi_2^{\mathrm{KS}}(\mathbf{r}_2) & \cdots & \phi_{N_{\mathrm{e}}}^{\mathrm{KS}}(\mathbf{r}_2) \\ \vdots & \vdots & \ddots & \vdots \\ \phi_1^{\mathrm{KS}}(\mathbf{r}_{N_{\mathrm{e}}}) & \phi_2^{\mathrm{KS}}(\mathbf{r}_{N_{\mathrm{e}}}) & \cdots & \phi_{N_{\mathrm{e}}}^{\mathrm{KS}}(\mathbf{r}_{N_{\mathrm{e}}}) \end{pmatrix}.$$

The wavefunction ψ_{KS} is required to produce the correct electron density:

$$\rho(\mathbf{r}) = \langle \psi_{\mathrm{KS}} | \hat{\rho} | \psi_{\mathrm{KS}} \rangle = \sum_j^{N_{\mathrm{e}}} |\phi_j^{\mathrm{KS}}(\mathbf{r})|^2, \tag{2.20}$$

where $\hat{\rho} = \sum_i \delta(\mathbf{r} - \mathbf{r}_i)$ is the density operator. The wavefunction (2.19) is not required to correspond to the true wavefunction of an interacting electron system.

The derivation of single particle Kohn–Sham equations is illustrated as follows. Let us consider the system of non-interacting electrons, with the Hamiltonian:

$$\hat{H}_s = \sum_i^{N_{\mathrm{e}}} \hat{T}_i + \sum_i^{N_{\mathrm{e}}} \hat{v}_s(\mathbf{r}_i). \tag{2.21}$$

Its ground state is a single-determinant wavefunction:

$$\psi_s = \frac{1}{\sqrt{N_{\mathrm{e}}!}} \left| \phi_1 \phi_2 \cdots \phi_{N_{\mathrm{e}}} \right|.$$

Here ϕ_i's are N lowest eigenstates of the one-particle Hamiltonian:

$$\hat{h}_s = \hat{T}_i + \hat{v}_s(\mathbf{r}_i).$$

The HK theorems still hold for such system, and the ground state density can be determined via the minimization of:

$$E_s[\rho] = \hat{T}_s[\rho] + \int \rho(\mathbf{r}) \hat{v}_s(\mathbf{r}) \, \mathrm{d}\mathbf{r}, \tag{2.22}$$

where

$$\hat{T}_s[\rho] = \sum_i^{N_\mathrm{e}} \left\langle \phi_i \middle| \hat{T} \middle| \phi_i \right\rangle, \tag{2.23}$$

is the *kinetic energy of non-interacting electrons*. The minimization of Eq. (2.22) with respect to the total density, under constraint $\int \rho \, \mathrm{d}\mathbf{r} = N$, yields the following Euler–Lagrange equation:

$$\mu = \hat{v}_s(\mathbf{r}) + \frac{\delta \hat{T}_s[\rho]}{\delta \rho}, \tag{2.24}$$

where μ is a Lagrange multiplier.

For the interacting system, Kohn and Sham suggested rewriting the universal functional in the form:

$$\hat{F}_\mathrm{HK}[\rho] = \hat{T}_S^\mathrm{KS}[\rho] + J[\rho] + \hat{E}_\mathrm{xc}[\rho]. \tag{2.25}$$

where $\hat{T}_S^\mathrm{KS}[\rho]$ is the kinetic energy of non-interacting KS orbitals [defined as in Eq. (2.23)]. $J[\rho]$ is the classical Coulomb interaction of the density with itself:

$$\hat{J}[\rho] = \iint \frac{\rho(\mathbf{r}_1)\rho(\mathbf{r}_2)}{|\mathbf{r}_2 - \mathbf{r}_1|} \, \mathrm{d}\mathbf{r}_1 \, \mathrm{d}\mathbf{r}_2. \tag{2.26}$$

The final term of Eq. (2.25) is the *exchange-correlation energy functional*. $\hat{E}_\mathrm{xc}[\rho]$ is defined to account for the remaining energy contributions:

$$\hat{E}_\mathrm{xc}[\rho] = \underbrace{\hat{T}[\rho] - \hat{T}_s^\mathrm{KS}[\rho]}_{\text{(i)}} + \underbrace{\hat{U}_\mathrm{ee}[\rho] - \hat{J}[\rho]}_{\text{(ii)}}. \tag{2.27}$$

Here (i) is the difference between the true kinetic energy $\hat{T}$ and the artificial kinetic energy of non-interacting electrons $\hat{T}_s^\mathrm{KS}$, and (ii) is a non-classical part of electron–electron interaction. The Euler–Lagrange equation for the functional (2.17) of the interacting system now becomes:

$$\mu = \left[\hat{v}(\mathbf{r}) + \frac{\delta \hat{J}[\rho]}{\delta \rho} + \frac{\delta \hat{E}_\mathrm{xc}[\rho]}{\delta \rho} \right] + \frac{\delta \hat{T}_s[\rho]}{\delta \rho}.$$

This equation is precisely the same as one obtained for non-interacting electrons [Eq. (2.24)], except $\hat{v}_s(\mathbf{r})$ is replaced with:

$$\begin{aligned} \hat{v}_\mathrm{KS}(\mathbf{r}) &= \hat{v}(\mathbf{r}) + \frac{\delta \hat{J}[\rho]}{\delta \rho} + \frac{\delta \hat{E}_\mathrm{xc}[\rho]}{\delta \rho} \\ &= \hat{v}(\mathbf{r}) + \int \frac{\rho(\mathbf{r})}{|\mathbf{r} - \mathbf{r}'|} \, \mathrm{d}\mathbf{r}' + \hat{v}_\mathrm{xc}(\mathbf{r}). \end{aligned}$$

The *exchange–correlation potential* $\hat{v}_{\mathrm{xc}} = \delta \hat{E}_{\mathrm{xc}}[\rho]/\delta\rho$ is the only formally unknown term, which contains all non-classical contributions. Therefore, for given $\hat{v}_{\mathrm{KS}}(\mathbf{r})$, the variational problem is mapped to the solution of one-electron Schrödinger-like equations:

$$\left[\hat{T}_i + \hat{v}_{\mathrm{KS}}(\mathbf{r})\right] \phi_i^{\mathrm{KS}} = \varepsilon_i \phi_i^{\mathrm{KS}}. \tag{2.28}$$

Here, the potential $\hat{v}_{\mathrm{KS}}$ is a functional of ρ, while ρ is constructed from single-particle KS orbitals through Eq. (2.20). Hence, the whole problem must be solved self-consistently as it is done in the Hartree–Fock method. In principle, one begins with a guessed ρ (or equivalently, a set of ϕ_i^{KS}'s), constructs $\hat{v}_{\mathrm{KS}}$, and then finds a new ρ. The process is repeated until the required convergence is reached. The Kohn–Sham formulation of DFT is formally rigorous. That is, if $\hat{v}_{\mathrm{xc}}$ were the exact exchange–change correlation potential, the solution of Eq. (2.28) would yield the exact ground-state energy and charge density.[4] The main practical complication is the form of $\hat{E}_{\mathrm{xc}}$ (and thus $\hat{v}_{\mathrm{xc}}$), which is only approximately known. However, the search for proper exchange–correlation functionals is a very active field of research, and increasingly accurate functionals are being developed (see Section 2.3.3 for review on approximate functionals).

Spin

Another important property for electronic structure analysis is *spin*. The wavefunctions of the electronic Hamiltonian must be eigenfunctions of spin operators $\mathbf{S}^2$ and $\mathbf{S}_z$. In the formulation above, Kohn–Sham density (2.20) was required to be identical to the total density of the interacting system. There is no distinction between spin-up and spin-down states of Eq. (2.28) with this constraint only. This formulation leads to *spin-restricted DFT*, where the spatial parts for both spin counterparts are identical, i.e.:

$$\psi_{\mathrm{KS}} = \left|\phi_1^{\mathrm{KS}}\left|\uparrow\right\rangle, \phi_1^{\mathrm{KS}}\left|\downarrow\right\rangle, \phi_2^{\mathrm{KS}}\left|\uparrow\right\rangle, \phi_2^{\mathrm{KS}}\left|\downarrow\right\rangle, \cdots\right|.$$

This formulation is suitable for *closed-shell* systems, where all spins are paired. However, this approach could lead to undesirable results for *open-shell* systems, where there are unpaired electrons. Most importantly, in spin-restricted DFT,

[4] However, there is an open question of the v-representability of ρ in terms of Kohn–Sham wavefunction. In general, not every ρ can be expressed as a density of a single Slater determinant. Nonetheless, from a practical perspective, this assumption holds in most cases, although some counter-examples can be found.

the spin density $Q_s(\mathbf{r}) = \rho_\uparrow - \rho_\downarrow$ (excess of spin-up electrons at a given point) in principle could be different from the true spin density of the interacting system [33]. Therefore, to overcome this problem, the *spin-unrestricted* formulation of DFT is used [34, 35]. The main idea behind the spin-unrestricted DFT is to introduce different Kohn–Sham potentials $\hat{v}^s_{\text{eff}}$ for spin-up and spin-down electrons to account for contrasting exchange interactions. As a result, two systems of KS equations (2.28) emerge for each spin component. Resultant spin densities $\rho_\uparrow$, $\rho_\downarrow$ are required to be equal to their fully interacting counterparts. In this formulation, the exchange–correlation energy becomes a unique functional of both spin densities. In the case of deep-level defects, paramagnetic states are often encountered. Thus the spin-unrestricted DFT is the usual choice, as it is in this thesis. One drawback of the spin-unrestricted approach is possible artificial mixing of different $\mathbf{S}^2$ eigenstates (spin-contamination). However, such artifacts can be partially avoided if the correct structure of Kohn–Sham wavefunction (2.19) is enforced. This will be the topic of the last Subsection 2.3.5, where the molecular-orbital model is used to determine the appropriate form of ψ_{KS}.

2.3.2 Kohn–Sham orbitals and excited-states

In wavefunction-based methods, like Hartree–Fock, single-particle wavefunctions are rather "physical" constructs. The occupied orbitals constitute the true (approximate) wavefunction, and the energy of the highest orbital is approximately equal to the first ionization energy of the molecular system (as proved by the Koopmans' theorem). These properties strengthen the phenomenological concept of a "chemical orbital", which is extremely useful in explaining the complex reality of molecular structures. In the Hartree–Fock theory, the assumption that a single Slater determinant can describe the electronic wavefunction is equivalent to the notion that each electron can be represented by an effectively independent single-particle function (molecular orbital). The presence of other electrons is felt through averaged Coulomb repulsion and exchange interaction. Although this picture is not very rigorous, it provides a very intuitive interpretation of electronic states. If the ground state is a single-determinant configuration, the excited configuration can be modeled in terms of single-particle excitations, where electron–hole pairs are introduced. Such an orbital picture is also beneficial for the defect system. It provides a simple and intuitive description of electronic states in terms of single-electron localized orbitals (see Section 2.3.5). The main drawback of the traditional Hartree–Fock approach is the assumption of a single configuration, as not all states are described by a single Slater determinant. Thus, improved methods like *configuration-interaction* (CI) or *many-body*

perturbation theory (MBPT) must be used to describe such *correlated systems*.[5] However, in such advanced methods, intuitive orbital interpretation is partially lost. On the other hand, the density functional theory is an exact theory that should account for the electronic correlation to its full extent. However, the role of single-particle orbitals still requires clarification. The main questions of this section are: "what is the meaning of Kohn–Sham single-particle states", and "can they be used to model other electronic states beyond the ground state".

Band-gap problem

From first sight, the single-particle Kohn–Sham orbitals of DFT are just auxiliary constructs without any meaningful "physical" information. In the early days of DFT, the theory was primarily used to determine the ground-state binding energies and related properties, like potential energy surfaces, geometrical structure, and force constants. The explicit use of KS orbitals to rationalize chemical structure was avoided, mostly because it was difficult to extract physical information from these constructs. The picture started to change in the early 1980s after Janak [36] found a rigorous connection between the ground state energies of N_e- and $N_\mathrm{e}+1$-particle systems in terms of KS eigenvalues. In Ref. [36], Janak generalized the KS system to include fractional occupations $0 \leq \alpha_i \leq 1$:

$$\rho = \sum_i \alpha_i |\phi_i^{\mathrm{KS}}|^2.$$

Such a generalization describes the density and energy of a statistical grand canonical ensemble [37]. Janak [36] proved that the variation of the total energy with respect to orbital occupation α_i is equal to the eigenvalue of KS orbital for $N+\alpha_i$ electron system:

$$\frac{\partial E_0}{\partial \alpha_i} = \varepsilon_i(N+\alpha_i). \tag{2.29}$$

Therefore the KS eigenvalue has the meaning of the chemical potential. This result uncovered new possible applications of DFT for a broad class of problems, such as ionization potentials, electron affinities, and work functions of metals. For example, from Eq. (2.29), it follows that the ionization potential I (the energy of removing an electron from the system) and electron affinity A (the energy of adding an electron to the system) for N electron system can be written

[5] The term "electron correlation" in principle describes the deviation from a single-determinant description.

in terms of KS eigenvalues:

$$I = E_0^{N-1} - E_0^N = -\int_0^1 \varepsilon_N(\alpha_N)\,\mathrm{d}\alpha_N,$$
$$A = E_0^N - E_0^{N+1} = -\int_0^1 \varepsilon_{N+1}(\alpha_{N+1})\,\mathrm{d}\alpha_{N+1}, \qquad (2.30)$$

where ε_N and ε_{N+1} are, respectively, the energies of the highest occupied and the lowest unoccupied one-electron levels (these are calculated for different fractional electron numbers). Furthermore, Perdew *et al.* [38] showed that for the exact functional, the energy of the grand canonical ensemble is a piecewise linear function of fractional occupations, connecting energies at integer electron numbers. Thus, the equations (2.30) for the exact functional can be rewritten as:

$$I = -\varepsilon_N(N - \delta),$$
$$A = -\varepsilon_{N+1}(N + \delta), \qquad (2.31)$$

where δ is a very small positive fraction of electrons. One could further argue that adding or removing an infinitesimal number of electrons could only make infinitesimal changes to ensemble density ρ and thus to the effective potential $\hat{v}_{\mathrm{KS}}$. Such change should not alter one-electron energies and Eqs. (2.31) would become $I = -\varepsilon_N(N)$ and $I = -\varepsilon_{N+1}(N)$. This argument leads to extremely simple band-gap expression $E_g = A - I = \varepsilon_{N+1}(N) - \varepsilon_N(N)$ [39]. In the early 1980s, the first DFT band-structure calculations were reported. However, systematic studies showed that with available approximate functionals, fundamental band gaps of semiconductors are typically underestimated by 40%. Perdew and Levy [40] rigorously proved that this inconsistency is not only due to an approximate form of functional but also has more fundamental ground. The Kohn-Sham band-gap $\varepsilon_{\mathrm{gap}}^{\mathrm{KS}} = \varepsilon_{N+1}(N) - \varepsilon_N(N)$ always underestimates the gap width, even with the exact $\hat{E}_{\mathrm{xc}}$ [40, 41]:

$$E_g = \varepsilon_{\mathrm{gap}}^{\mathrm{KS}} + \left\{ \left.\frac{\partial \hat{E}_{\mathrm{xc}}}{\partial N}\right|_{N+\delta} - \left.\frac{\partial \hat{E}_{\mathrm{xc}}}{\partial N}\right|_{N-\delta} \right\}. \qquad (2.32)$$

The second term in Eq. (2.32) comes from the derivative discontinuity of exchange–correlation potential and should always be present in the Kohn–Sham formulation of DFT. This is the well-known *band-gap problem* of DFT [42]. Apart from this band-gap problem, empirical observations show that the Kohn–Sham band-structure calculations typically produce band-shapes and density of states close to the experimental ones. Perdew and Levy [40] noted that band-gap errors could be reduced by improving orbital-dependent one-electron self-energies, which lies beyond the standard Kohn–Sham formulation. During

the past 30 years, many attempts have been made to augment DFT to provide a better description of the band-gap and excited-state properties. The most advanced methods are time-dependent density functional theory (TDDFT) [43], GW-approximation [44–46], and embedding methods [47], which combine DFT with high-accuracy quantum chemistry approaches. Maybe the most popular is the GW-approximation, where a quasi-particle picture is employed to calculate the self-energy of interacting electrons. This approach is remarkably successful in predicting band-gaps (and electronic excitations in general), achieving an error of a few percent with respect to experimental data for "simple" materials [48]. However, the computational cost of GW and other advanced methods is still very high, especially if one considers an extended defect system.

Generalized Kohn–Sham scheme

The approach for excited states, which is employed in this thesis, is based on *a generalized Kohn–Sham* (GKS) scheme [49]. The idea of GKS is to reformulate the Kohn–Sham variational procedure differently to give more physical meaning to single-particle eigenvalues. In the ideal case, the one-electron band-gap should be equal to the true fundamental gap:

$$E_g = \varepsilon_{\mathrm{gap}}^{\mathrm{GKS}}.$$

In principle, this reformulation could be achieved within the framework of DFT by introducing electron–electron interaction into single-particle equations. In GKS formalism, the density generating wavefunction (2.19) is still a single Slater determinant of one-particle orbitals ϕ_i^{GKS}. Seidl *et al.* [49] showed that ground state energy could be written as a functional of such one-electron orbitals:

$$E_0\left[\rho[\{\phi_i^{\mathrm{GKS}}\}]\right] = \hat{S}[\{\phi_i^{\mathrm{GKS}}\}] + \hat{R}^S[\rho] + \int \hat{v}\rho \,\mathrm{d}\mathbf{r}, \tag{2.33}$$

where ρ is a functional of $\{\phi_i^{\mathrm{GKS}}\}$. $\hat{S}$ is an arbitrarily chosen operator, which is explicitly a functional of $\{\phi^{\mathrm{GKS}}\}$, while $\hat{R}^s$ accounts for the difference between $\hat{F}_{\mathrm{HK}}$ and $\hat{S}$. In principle, this is a different partitioning of Eq. (2.25). The minimization of Eq. (2.33) yields the following single-particle equations [49]:

$$\hat{O}^s[\{\phi_i^{\mathrm{GKS}}\}]\phi_j^{\mathrm{GKS}} + \hat{v}_R\phi_j^{\mathrm{GKS}} + \hat{v}\phi_j^{\mathrm{GKS}} = \varepsilon_j^{\mathrm{GKS}}\phi_j^{\mathrm{GKS}}, \tag{2.34}$$

where

$$\hat{v}_R = \frac{\delta R^s}{\delta \rho}.$$

is the remainder single-particle potential. Based on the partitioning of Eq. (2.33), operator $\hat{O}^s$ now may depend on one-electron orbitals. Although this is just a

reformulation of a variational problem, it allows flexibility in choosing single-particle equations. For example, if one chooses $\hat{S}$ to be the kinetic energy of the Slater determinant, $\hat{S} = \sum_i \langle \phi_i^{\mathrm{GKS}} | \hat{T} | \phi_i^{\mathrm{GKS}} \rangle$, the standard Kohn–Sham formulation is recovered. On the other hand, if $\hat{S} = \langle \Phi | \hat{T} + \hat{U}_{\mathrm{ee}} | \Phi \rangle$ (where Φ is a single Slater determinant), $\hat{O}^s$ will have the Fock operator form of Hartree-Fock theory, and $\hat{v}_R$ will contain all correlation effects absent in the HF theory. With the exact functional, the minimization should produce the same ground state energy and density as in the standard Kohn–Sham formulation (though a single-particle description is different). However, the exact form of $\hat{R}^S$ (and thus $\hat{v}_R$) is not known for chosen $\hat{S}$, and appropriate approximations should be used instead. Successful examples of the GKS scheme are meta-GGA [50] and hybrid functionals [51] (see Section 2.3.3 for more detailed discussion). In hybrid functionals, the exact exchange of Hartree–Fock theory is mixed with the exchange-correlation of the approximate DFT functional [52–54]. Such mixture introduces non-local Fock type (integral) operators into the single-particle equations. The partial motivation behind the hybrid functionals is based on the empirical observation that HF single-particle band-gaps are overestimated while KS band-gaps are underestimated. Meta-GGA is another type of functionals, which introduce O^S dependence on the kinetic energy density of the non-interacting system $\tau = \sum_i |\langle \phi_i^{\mathrm{GKS}} | \hat{T} | \phi_i^{\mathrm{GKS}} \rangle|^2$. Modern meta-GGA [55] and hybrid functionals [53] can improve the predictive power of single-particle description. For example, screened hybrid functionals predict band-gaps with 15% accuracy and mean deviations of 0.21 eV for solid-state systems [56].

Excited-state calculations

The discussion above shows that the single-particle orbitals have a physical significance, as they can be used to predict excitation energies (at least as a first estimation). However, for localized systems, like defects, electronic excitation could lead to geometrical rearrangement of atoms and some electronic relaxation in the vicinity of the defect. Ground-state calculations cannot capture such effects. For point defects, geometrical relaxation is a very important property as it leads to electron–phonon coupling, which is one of the central problems of this thesis. To extract information about geometrical rearrangements (or excited-state potential energy surfaces in general), one needs to access excited states in the same manner as the ground states. The practical idea to calculate excited states comes from the fact that Kohn–Sham orbitals generally provide a good qualitative interpretation of the electronic structure and can be used to rationalize chemical description, as is shown by Baerends and Gritsenko [57].

This is even more true for the generalized Kohn–Sham scheme, where the description of single-particle orbitals is improved. Thus, up to some approximation, the excitation of one-particle states should mimic the true excitation of the system. This conception forms the basis of the ΔSCF method [58, 59]. ΔSCF method has formal justification for a subset of excited states. Gunnarsson *et al.* [35] showed that the variational procedure of density functional theory could be formulated for the lowest excited states of each orbital and spin symmetry. In principle, this extended theory should include symmetry restrictions in the exchange–correlation functional $\hat{E}_{\mathrm{xc}}$. However, no general prescription to achieve this is known. A more practical approach is to restrict the variational principle to Kohn–Sham wavefunctions of a specific symmetry. This restriction is achieved by considering different electronic configurations in terms of ground-state KS orbitals (the framework to acquire different symmetry configurations is presented in Section 2.3.5). Suppose the wavefunction of certain symmetry is found to have a single-determinant representation. In that case, the realization is straightforward: on top of ground-state calculations, the electron–hole pairs are introduced by constraining the orbital occupations to form appropriate symmetry wavefunction. Such constraint can be interpreted as single-particle excitation. However, if the state is a multi-determinant wavefunction, direct SCF calculation is impossible. ΔSCF method is widely employed for deep-level defect calculations [60–62], and the results with hybrid functionals produce an excellent agreement with the experiment. In practice, this approach yields satisfactory results even if applied to states which do not have formal justifications.[6]

As a final remark, I think it is essential to emphasize that extracting information from the single-particle picture of density functional theory is far from "ideal". It works in some cases and fails in others. However, more advanced wavefunction-based methods beyond the Hartree–Fock are computationally intractable for large systems, which is the case for defects. Thereby, DFT is the best tool that we have in our hands, and it should be used carefully to predict properties that go beyond the intended use of theory. However, much of the "credibility" can be provided by careful comparison with experimental results. If the theory can predict well-known properties, then it is reasonable to assume that other predictions are also close to the truth.

[6] Some justification of this approach can be given in the context of the extended KS formalism [63]. However, a special exchange–correlation potential should be used for the excited states. As this special component is still unknown, the standard ground-state exchange-correlation potentials are used in practical implementations.

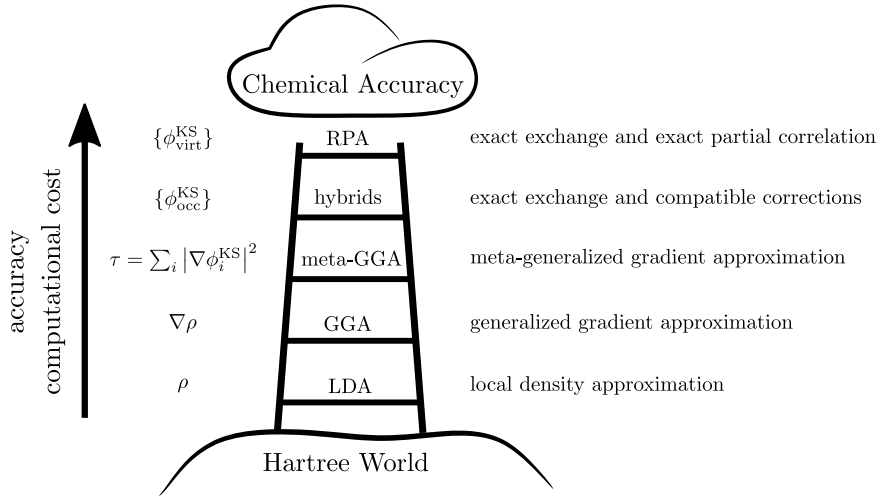

Figure 2.1: Jacob's ladder of density functional approximations [64].

2.3.3 Approximate exchange–correlation potentials

The exact exchange–correlation functional $\hat{E}_{\text{xc}}$ is the "holy grail" of quantum chemistry. However, up to this day, no exact form of this functional is known. Although $\hat{E}_{\text{xc}}$ is fairly small compared to the Coulomb and single-particle kinetic energy terms, it plays an important role in describing chemical phenomena. Luckily, many mathematical features of the exact functional $\hat{E}_{\text{xc}}$ are known. In accord with these mathematical features and predictive power, the whole hierarchy of exchange-functionals can be put in the form of "Jacob's ladder" [64], where functionals of similar capabilities are placed at the same rung (see Fig. 2.1). The ground corresponds to the Hartree theory, where exchange and correlation contributions are completely neglected. Higher rungs employ a more accurate description of exchange and correlation.

Local-density approximation

Originally introduced by Kohn and Sham [30], on the first rung of Jacob's ladder lies the class of functionals which employ the *local-density approximation* (LDA).[7] This approach is based upon the exact exchange energy of the *uniform electron gas*. The uniform electron gas is a well-understood model system, where exchange and correlation are local in character (energy contri-

[7] In the case of unrestricted spin formulation, it is termed *local spin density approximation* (LSDA).

bution from infinitesimal volume element depends only on electron density at that point). Therefore, LDA is a good starting point for the approximate exchange–correlation functional. LDA assumes a small variation of the density and provides the following functional form of the energy:

$$\hat{E}_{\mathrm{xc}}^{\mathrm{LDA}} = \int \varepsilon_{\mathrm{xc}}^{\mathrm{unif}}(\rho_{\uparrow}, \rho_{\downarrow})\rho(\mathbf{r})\,\mathrm{d}\mathbf{r},$$

where $\varepsilon_{\mathrm{xc}}^{\mathrm{unif}} = \varepsilon_{\mathrm{x}}^{\mathrm{unif}} + \varepsilon_{\mathrm{c}}^{\mathrm{unif}}$ is the exchange and correlation energy of the uniform gas. The exchange part is just an analytical result of Dirac [65] for uniform electron gas. However, the correlation part $\varepsilon_{\mathrm{c}}^{\mathrm{unif}}$ is more complicated. Usually, quantum Monte Carlo simulations [66] are performed for multiple intermediate values of density to obtain accurate values of correlation energy. Despite its simplicity, LDA often provides good structural and vibrational properties. It works surprisingly well for extended systems, like solids or solid surfaces. Unfortunately, it performs poorly for binding energies (overbinds) and activation energies of chemical reactions [59]. Thus, in the early 1970s, LDA had become a standard tool for solid-state physicists. However, it never gained much popularity with the majority of quantum chemists.

Generalized gradient approximation

The next step in functional development is the inclusion of density gradient in the formulation of $\hat{E}_{\mathrm{xc}}$. This is the second rung of Jacob's ladder, which introduces the *generalized gradient approximation* (GGA) [67–69]. GGA functionals have the following semi-local generalized form [69]:

$$\hat{E}_{\mathrm{xc}}^{\mathrm{GGA}} = \int \varepsilon_{\mathrm{xc}}^{\mathrm{GGA}}(\rho^{\uparrow}, \rho^{\downarrow}, \nabla\rho^{\uparrow}, \nabla\rho^{\downarrow})\rho(\mathbf{r})\,\mathrm{d}\mathbf{r}.$$

In comparison with LDA, GGA approximations tend to improve many aspects of calculations. They partially repair the overbinding character of the LDA. The functional proposed by Perdew, Burke, and Ernzergof (PBE) [69] is the most used exchange–correlation functional in computational materials science.[8] PBE is a non-empirical functional which satisfies the uniform density limit and several exact properties related to the exchange–correlation hole [69]. It is highly successful in describing ground state structural properties (geometry, bulk-modulus, vibrational frequencies) and is extensively used in this thesis for vibrational structure analysis. However, GGA, as well as LDA, suffers from the already mentioned band-gap problem.

[8] In fact, the PBE paper [69] is among the 100 most cited scholarly articles of all time [70].

Meta-GGA functionals

Meta-GGA functionals [55, 71, 72] occupy the third rung. This class provides fully non-local functionals of density but avoids computationally demanding integral (non-local) formulation on orbital parts. Generally, in addition to ρ and $\nabla\rho$, meta-GGA consider *kinetic energy density* τ_σ of Kohn–Sham orbitals:

$$\tau_\sigma = \sum_i \frac{1}{2} \left|\nabla \phi_{i,\sigma}^{\mathrm{KS}}\right|^2, \quad \text{where } \sigma = \uparrow, \downarrow,$$

as a functional ingredient:

$$\hat{E}_{\mathrm{xc}}^{\mathrm{MGGA}} = \int \varepsilon_{\mathrm{xc}}^{\mathrm{MGGA}}(\rho^\uparrow, \rho^\downarrow, \nabla\rho^\uparrow, \nabla\rho^\downarrow, \tau_\uparrow, \tau_\downarrow)\rho(\mathbf{r})\,\mathrm{d}\mathbf{r}.$$

Such functionals are able to satisfy more exact constraints and achieve higher accuracy in comparison to standard LDA and GGA formulations. Also, meta-GGA falls under the generalized Kohn–Sham scheme as one-particle operators are explicit functionals of orbitals. This formulation improves single-particle description and partially cures band-gap discrepancies by 20%–50%. More recent non-empirical meta-GGA functionals [55, 72] show promising results as their accuracy is consistent for diverse systems and properties.

Hybrid functionals

The next class of density functionals that are most often used nowadays are *hybrid-functionals*, which lie on the fourth rung of Jacob's ladder. The original idea of hybrids stems from the fact that exchange is the most dominant part of the exchange–correlation energy. Thus, coupling the Hartree–Fock theory, which provides an exact treatment of exchange with density-functional approximations, could in principle deliver some improvements over standard LDA and GGA functionals. In the pioneering paper, Becke [52] developed a formally rigorous approach to couple the exact exchange of the Kohn–Sham orbital system with approximate exchange–correlation functional. In his derivation, Becke [52] used the *adiabatic connection formula* for the exact functional [73] and showed that the exchange–correlation functional approximately could be expressed as:

$$\hat{E}_{\mathrm{xc}}^{\mathrm{HH}} \approx \frac{1}{2} E_x^{\mathrm{HF}} + \frac{1}{2} \hat{E}_{\mathrm{xc}}^{\mathrm{DFT}}. \tag{2.35}$$

Here E_x is the exchange energy of Kohn–Sham Slater determinant:

$$E_x^{\mathrm{HF}}[\{\phi_i^{\mathrm{GKS}}\}] \tag{2.36}$$
$$= -\frac{1}{2}\sum_{i,j=1}^{N}\iint \phi_i^{\mathrm{GKS}*}(\mathbf{r}_1)\phi_j^{\mathrm{GKS}}(\mathbf{r}_1)\frac{1}{r_{12}}\phi_i^{\mathrm{GKS}*}(\mathbf{r}_2)\phi_j^{\mathrm{GKS}}(\mathbf{r}_2)\,\mathrm{d}\mathbf{r}_1\,\mathrm{d}\mathbf{r}_2.$$

This scheme is widely known as "half-and-half" functional. Although such simple mixing improved several aspects of standard functionals (especially atomization energies), it had several deficiencies. In a subsequent publication, Becke [74] proposed a *semi-empirical* approach and defined a three-parameter hybrid-functional which mixes LDA, GGA, and exact exchange. Parameter values were determined by an appropriate fit to experimental datasets. This idea opened the door for new semi-empirical hybrids, which became very popular in molecular applications. For example, the B3LYP (Becke, 3-parameter, Lee–Yang–Parr) exchange–correlation functional is one of the most popular functionals for describing molecular properties.

However, initial hybrid functionals were problematic for solids [75]. One problem is computational, as Eq. (2.36) is hard to evaluate numerically for delocalized states. Another, more fundamental problem is connected to the fact that for hybrids, exchange interactions at large spatial separations are approximately canceled by correlation in narrow band-gap semiconductors and metals [75]. To cure these problems, *screened hybrid functional* of Heyd, Scuseria, and Ernzerhof (HSE) [53] was proposed. The main idea was to separate long-range (LR) and short-range (SR) interactions. HSE functional splits the Coulomb operator into two parts:

$$\frac{1}{r_{ij}} = \underbrace{\frac{\mathrm{erfc}(\omega r_{ij})}{r_{ij}}}_{\mathrm{SR}} + \underbrace{\frac{\mathrm{erf}(\omega r_{ij})}{r_{ij}}}_{\mathrm{LR}},$$

where erf and erfc are error and complementary error functions. The parameter ω adjusts the two ranges. Part of HF exchange is only incorporated in the short range, while GGA-PBE exchange is present in both short and long ranges. The mixing takes the following form:

$$E_{xc}(\alpha,\omega) = aE_x^{\mathrm{HF,SR}}(\omega) + (1-a)E_x^{\mathrm{PBE,SR}}(\omega) + E_x^{\mathrm{PBE,LR}}(\omega) + E_x^{\mathrm{PBE}}.$$

The parameter a is a mixing parameter, which determines the part of the exact exchange of HF in the short range. The standard HSE values are $a = 1/4$ and $\omega = 0.2$. The most important aspect of HSE is the ability to rather accurately

predict semiconductor band-gaps. This follows from the fact that hybrids fall under the generalized Kohn Sham scheme and approximately include derivative discontinuity (2.32) [76]. For deep-level defects, HSE functional has become a "gold standard" as it is able to predict accurate thermodynamic properties and excitation energies.

2.3.4 Implementation

In this thesis, all the calculations were carried using the *Vienna ab initio simulation package* (VASP) [77]. VASP uses the plane-wave basis for single-particle wavefunctions and PAW pseudopotentials to effectively separate core and valence electrons. Plane-wave basis implies spatial periodicity of the system, which is natural to solid-state systems but can also be used as an approximation for analysis of point-defects. Here we will briefly discuss these technical topics.

Plane-waves

From a microscopic point of view, extended systems like solids are infinite. However, for pure crystal, translational symmetry simplifies an electronic solution by employing the Bloch theorem [78]. According to the Bloch theorem, single-particle solutions take the form:

$$\phi_{\mathbf{k}}^{\mathrm{KS}}(\mathbf{r}) = e^{i\mathbf{k}\mathbf{r}} u_{\mathbf{k}}(\mathbf{r}),$$

where $\mathbf{k}$ is any vector within the first Brillouin zone of the cell, and $u_{\mathbf{k}}(\mathbf{r})$ has the same translational invariance as potential energy $\hat{v}_{\mathrm{KS}}$. Periodicity of $u_{\mathbf{k}}(\mathbf{r})$ implies that it can be written as a Fourier expansion:

$$u_{\mathbf{k}}(\mathbf{r}) = \sum_{\mathbf{G}} C_{\mathbf{G}}(\mathbf{k}) e^{i\mathbf{G}\mathbf{r}}, \tag{2.37}$$

where summation runs over all reciprocal lattice vectors $\mathbf{G}$. In practice, summation (2.37) is truncated by defining the *kinetic energy cutoff* $|\mathbf{k}+\mathbf{G}|^2/2 \leqslant E_{\mathrm{cut}}$. This cutoff energy is chosen by performing convergence tests for total energy or other sought properties. Thus, effectively the problem reduces to the size of the periodic primitive cell. However, in an infinite system, we must solve for all continuum values of $\mathbf{k}$, as calculations of charge density and other properties involve integration over the whole Brillouin zone. The general form of such an integral is:

$$I(\varepsilon) = \frac{1}{\Omega_{\mathrm{BZ}}} \int_{\mathrm{BZ}} F(\mathbf{k})\, \mathrm{d}\mathbf{k},$$

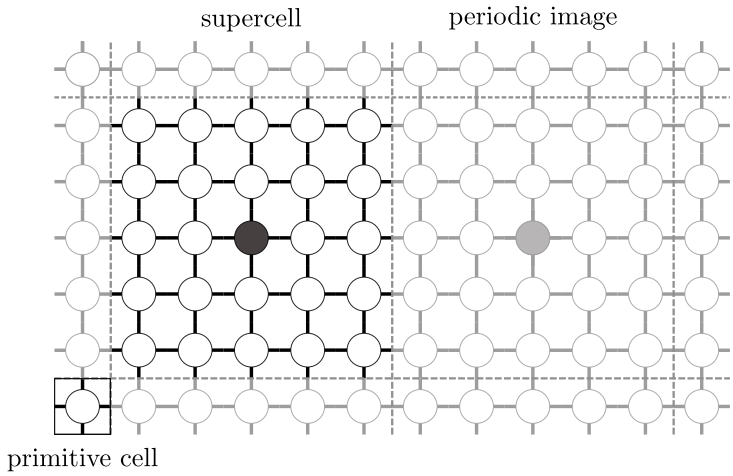

Figure 2.2: A schematic illustration of the supercell method for a point defect in a solid. The supercell is the area enclosed by the dashed lines.

where F is a certain function. In practice, such integration is replaced by approximate summation:

$$\frac{1}{\Omega_{\mathrm{BZ}}} \int_{\mathrm{BZ}} \quad \Rightarrow \quad \sum_{\mathbf{k}} w_{\mathbf{k}},$$

where $w_{\mathbf{k}}$ are weight factors that sum to unity. The most popular method for the Brillouin zone integration is based on Monkhorst–Pack (MK) scheme [79]. MK method generates an evenly spaced k-grid through the whole Brillouin zone with equal weight factors. Three integer numbers $M_1 \times M_2 \times M_3$ define the size of the grid and correspond to partitioning along each reciprocal lattice vector. Convergence tests once again determine the suitable size of the grid.

Supercell approach

When the defect is put into a crystal, all translational symmetry is lost. Yet, electronic and geometrical perturbations are expected to be well localized in a finite neighborhood of impurity for deep-level defects. The *supercell approximation* is based on this assumption. The supercell itself is an effectively large periodic cell with an embedded defect (see Fig. 2.2). The volume of a supercell contains an integral number of primitive (or conventional) unit cells. This approximation has evident drawbacks known as *finite-size effects*, which stem from spurious interactions between defects and their periodic images. The defect wavefunction can overlap with itself and cause wrong localization and dispersive behavior of constituent single-particle orbits. Thus, the validity

of calculated properties must be checked by convergence tests for different-size supercells. Present-day high-performance computers can tackle periodic systems up to a few thousand atoms.[9] Usually, the finite-size effects for neutral defects are eliminated by choosing supercells of several hundred atoms.

On the other hand, for charged defects, long-range electrostatic interactions decay slowly with the cell size, and some additional corrections should be taken into account. The energy correction scheme of Freysoldt *et al.* [80] is a popular and reliable method for charged defects and is also used in this thesis. Another issue is related to geometrical relaxation. The cell size restricts nuclear relaxations to the region contained within a single supercell. Almost no relaxation occurs in the midway between defect and its periodic image. However, the relaxation could have a long-range pattern in the dilute limit, which is not always reflected in finite-sized supercells. We address this problem in Chapter 3 together with additional issues of vibrational structure and electron–phonon interaction.

Pseudopotentials

The plane-wave basis is convenient for the description of periodic systems. However, they introduce some computational problems for the core electrons and regions close to the core. One-electron orbitals have sharp features close to the nuclei as they are required to be orthogonal to core states. This situation is problematic as a huge number of plane waves is required to describe the wave function accurately. The pseudopotential method is based on two observations: (i) Most of the chemical properties only depend on the interaction between some set of valence (outer shell) electrons; (ii) The chemistry is, in a large extent, determined by the character of wavefunctions at a bonding region, which resides at some distance from the core. First, the pseudopotential method effectively removes core orbitals from the simulation as they are almost identical in atomic and bonding environments. Thus, the core degrees of freedom are frozen and taken from atomic calculations (frozen-core approximation). The second simplification is achieved by replacing frozen-core potential with a smooth pseudopotential, for which outer-shell electrons have smooth behavior inside the core region. Pseudo-wavefunctions must be identical to true all-electron wavefunctions outside this core region. In this work, we adopt the projector-augmented-wave (PAW) method [81], which has good transferability

[9] Note that this only applies to semi-local LDA and GGA functionals which have good scalability properties. Hybrid functionals are, by order of magnitude, more expensive.

properties. PAW method maintains the relation between pseudo-wavefunctions and all-electron wavefunctions in the form of the linear transformation:

$$\psi_{\mathrm{PS}} = \hat{\tau}\psi_{\mathrm{AE}}, \tag{2.38}$$

where $\hat{\tau}$ has an identity character outside the core region. Thus, the pseudo-wavefunction only differs from the original one inside the augmentation sphere around the atom. The form of transformation $\hat{\tau}$ is chosen such that the continuation of pseudo-wavefunctions inside the augmentation region is smooth [81]. Once the transformation is known, all operators for single-particle electrons are transformed to the new basis. Relation (2.38) is very important as it allows the recovery of the true all-electron wavefunctions. This property is useful for the evaluation of matrix elements between single-particle Kohn–Sham wavefunctions.

2.3.5 Molecular-orbital model

In Section 2.3.2, when discussing excited-state calculations, we introduced the $\Delta\mathrm{SCF}$ method [58, 59]. This method relies on symmetry restrictions imposed on Kohn–Sham multi-electron wave functions. More precisely, the wave function is chosen to be of well-defined orbital and spin symmetry. This restriction is held during the self-consistent minimization of the total energy. Determining the correct one-electron configuration from which Slater determinants are formed relies on the so-called molecular orbital (MO) model.

Before numerical *ab initio* techniques, the determination of the electronic structure of deep-level defects was a challenging task. Conventional theoretical methods, like effective-mass theory or Greens-function techniques, are inadequate for localized defects, as the variation of the strongly localized wavefunction and perturbing potential is too great [82]. On the other hand, despite interaction with the host material, the deep-level defect resembles localized systems like trapped atoms or molecules. Provided that defect consists only of a small number of active localized "defect electrons" (which only weakly interact with the crystal field), a simplified molecular orbital (MO) picture follows naturally as an intuitive and descriptive model. These assumptions are justified by the observed localized nature of color centers (e.g., by EPR experiments) and the notion that the rest of the crystal is covalently bonded and effectively neutral. Despite its simplicity, the MO model is very illustrative and broadly used to interpret the electronic structure of deep-level impurities.

The MO model was first applied to deep-level defects by Coulson and Kearsley [83]. They used a simplified picture where the defect system (diamond vacancy) was analyzed using several electrons and sp^3-type active bonds. By utilizing spin and spatial symmetry considerations, these orbitals were combined to form different multi-electron states. Although semi-empirical energy calculations could not explain all experimental measurements, this approach became a widely used framework to predict orbital symmetries and spin multiplicities of defects [82]. For example, successive application of this model to the NV^- center by Loubser and Van Wyk [84] provided a coherent explanation of electron spin resonance experiments.

In present-day electronic structure methods, the host states are treated on the same footing as localized defect orbitals. However, the chemistry of a defect mainly depends on localized orbits that are occupied by electrons. Thus, the standard *ab initio* approach to determine excited electronic states is as follows. First, the ground state calculation is performed, and one-electron states of localized character are identified as "defect orbitals". These orbitals are treated as a MO basis to construct excited state wavefunctions of different symmetry. If a sought configuration is a single-determinant wavefunction, electron–hole pairs are introduced by the constrained occupation of Kohn–Sham states. This approach is widely used in modern-day electronic structure calculations of point defects (see, e.g., Refs. [85–88]).

Requirements

Once the localized orbitals are determined, the construction of multi-electron MO states relies on three fundamental requirements:

(i) The total wavefunction must be *antisymmetric* under a binary electron permutation.
(ii) The spin part of the multi-particle wavefunction must be an eigenstate of total spin operators $\mathbf{S}^2$ and $\mathbf{S}_z$.
(iii) The orbital part of the all-electron wavefunction must transform as an irreducible representation of the symmetry point group of the defect [89, 90].

These three principles lay the foundation of the molecular orbital model. The requirement (i) can be satisfied by applying the antisymmetrization procedure. *Antisymmetrizer* $\mathcal{A}$ is a linear operator that makes any N-particle wavefunction antisymmetric [89]:

$$\mathcal{A} = \frac{1}{\sqrt{N!}} \sum_{\mathbf{P}} (-1)^{\Theta(\mathbf{P})} \mathbf{P}. \tag{2.39}$$

Here, the sum runs over all $N!$ permutations, and $\Theta(\mathbf{P})$ is the number of binary transpositions entering the permutation $\mathbf{P}$. If the projection operator of Eq. (2.39) is applied to the Hartree-type product of single-particle states, the result is a well-known Slater determinant:

$$\mathcal{A}\left(\phi_1(1)\phi_2(2)...\phi_N(N)\right) = \frac{1}{\sqrt{N!}} \begin{vmatrix} \phi_1(1) & \phi_2(1) & \cdots & \phi_N(1) \\ \phi_1(2) & \phi_2(2) & \cdots & \phi_N(2) \\ \vdots & \vdots & \ddots & \vdots \\ \phi_1(N) & \phi_2(N) & \cdots & \phi_N(N) \end{vmatrix} \equiv \left|\phi_1\phi_2...\phi_N\right|. \tag{2.40}$$

The permutation operators $\mathbf{P}$ entering Eq. (2.39) commute with spin and orbital symmetry transformations. Therefore, the total wavefunction satisfying requirements (i)–(iii) can be put in the form:

$$|\Psi\rangle = \mathcal{A}\left(\Phi(\mathbf{r})\chi(\boldsymbol{\sigma})\right). \tag{2.41}$$

Here $\chi(\boldsymbol{\sigma})$ and $\phi(\mathbf{r})$ are spin and orbital wavefunctions that fulfill requirements (ii) and (iii). Eq. (2.41) enables a systematic search for well-defined multi-electron states as the spin and orbit counterparts can be analyzed separately. In the following content, we will present construction schemes that we use to obtain correct forms of spin $\chi(\boldsymbol{\sigma})$ and orbital $\Phi(\mathbf{r})$ subsystems.

Spin eigenstates

The spin function $\chi(\boldsymbol{\sigma})$ of Eq. (2.41) must be a simultaneous eigenfunction of multi-particle spin operators [91]:

$$\mathbf{S}^2 = \left(\sum_{i=1}^{N} \mathbf{S}(i)\right)^2, \quad \mathbf{S}_z = \sum_{i=1}^{N} \mathbf{S}_z(i), \tag{2.42}$$

where $\mathbf{S}^2(i) = \mathbf{S}_x^2(i) + \mathbf{S}_y^2(i) + \mathbf{S}_z^2(i)$ is the square of the angular momentum operator, and sums run over all electrons i of the system. The eigenstates of single-electron operators are:

$$\begin{aligned} \mathbf{S}_z(i)\left|S_i = \tfrac{1}{2}, m_i\right\rangle &= m_i \left|S_i = \tfrac{1}{2}, m_i\right\rangle, \\ \mathbf{S}^2(i)\left|S_i = \tfrac{1}{2}, m_i\right\rangle &= S_i(S_i+1)\left|S_i = \tfrac{1}{2}, m_i\right\rangle \\ &= \frac{3}{4}\left|S_i = \tfrac{1}{2}, m_i\right\rangle. \end{aligned} \tag{2.43}$$

The Hilbert space of an N-spin system is a tensor product of spin-$1/2$ particle spaces $\mathcal{H} = \mathcal{H}_1 \otimes \mathcal{H}_2 \otimes \cdots \otimes \mathcal{H}_N$. The trivial basis of such space is a set

of pure (uncoupled) states which are written in the form of direct product: $|\frac{1}{2}, m_1\rangle|\frac{1}{2}, m_2\rangle \cdots |\frac{1}{2}, m_N\rangle$. Such states are eigenstates of $\mathbf{S}_z$, but they are not necessarily eigenstates of $\mathbf{S}^2$. There are many different methods to obtain simultaneous eigenfunctions of $\mathbf{S}^2$ and $\mathbf{S}_z$ (see, e.g., Ref. [91] for a detailed discussion).

For open-shell systems with a small number of electrons, the *genealogical construction scheme* [91] is a relatively straightforward method, which allows obtaining spin states by a successive combination of two spin subsystems. For example, let us consider two spin systems with known eigenfunctions of $\mathbf{S}^2(i)$ and $\mathbf{S}_z(i)$ (i.e., $|S_1, m_1\rangle$ for the first system and $|S_2, m_2\rangle$ for the second one). The theorem of angular momentum addition states that the resultant eigenstate of $\mathbf{S}^2 = (\mathbf{S}(1) + \mathbf{S}(2))^2$ and $\mathbf{S}_z = \mathbf{S}_z(1) + \mathbf{S}_z(2)$ can only attain values between $|S_1 - S_2|$ and $S_1 + S_2$ (differing from each other by 1):

$$S = |S_1 - S_2|, |S_1 - S_2| + 1, \ldots, S_1 + S_2. \tag{2.44}$$

Appropriately, one can construct an N-electron state by combining states of $(N-1)$-electron system with one electron of spin-$1/2$. The resultant angular momentum value can only differ by $\pm 1/2$ from the S value of the $(N-1)$ electron system. In the genealogical construction scheme, we start from a single electron and construct multi-electron states, adding one electron at a time. The "parent" states are tracked and labeled to identify different degenerate spin states. The coupling is done using Clebsch–Gordan (CG) coefficients of the $\mathrm{SO}(3)$ group. CG coefficients $\langle S_1 m_1; S_2 m_2 | S, m\rangle$ connect the states of the uncoupled basis with eigenstates of $\mathbf{S}^2$ and $\mathbf{S}_z$:

$$|Sm\rangle = \sum_{m_1+m_2=m} \langle S_1 m_1 S_2 m_2 | S, m\rangle \, |S_1 m_1\rangle \, |S_2 m_2\rangle \, . \tag{2.45}$$

The tabulated values or analytical expressions for CG coefficients can be found in many books (e.g., [89, 92]) or online references. The procedure is illustrated for up to $N = 4$ electron states in Appendix B.

Symmetry-adapted orbital wavefunctions

The requirement for the orbital part of the wavefunction [Eq. (2.41)] stems from group theory considerations (see Appendix A for a brief review of group theory concepts applied in this thesis). The eigenfunctions must transform as a basis of an irreducible representation of the point group $\mathcal{G}$ of the Hamiltonian [89]:

$$T(G_a) \, |\Gamma\gamma\rangle = \sum_j T^{\Gamma}_{\gamma'\gamma}(G_a) \, \left|\Gamma\gamma'\right\rangle ,$$

where $T(G_a)$ is a functional symmetry transformation of corresponding group element G_a [see Eq. (A.2)], and $T^{\Gamma}_{\gamma'\gamma}(G_a)$ is the matrix of the irreducible representation Γ of a point group $\mathcal{G}$ [89, 90, 92].

In the MO model, single-particle orbitals ϕ_i are chosen to transform as irreducible representations of the group $\mathcal{G}$. In fact, if the mean-field approach (like DFT or Hartree–Fock) is used, the single-particle Hamiltonian has the same symmetry as an all-electron system. Thus, the single-particle wavefunctions automatically satisfy this requirement.[10]

Similarly, as in the case of spin, the basis of the direct product of single-particle eigenstates does not transform as a basis of an irreducible representation of the point group $\mathcal{G}$. The construction of the symmetric multi-particle wavefunctions follows a similar procedure to the genealogical construction scheme. Clebsch–Gordan coefficients of the point group $\mathcal{G}$ combine the basis of the direct product of irreducible representations $\Gamma_i \otimes \Gamma_j$ into the state with well-defined symmetry $\Gamma\gamma$ [89, 90]:

$$|\Gamma\gamma\rangle = \sum_{\gamma_i,\gamma_j} \langle \Gamma_i\gamma_i\Gamma_j\gamma_j|\Gamma\gamma\rangle \, |\Gamma_i\gamma_i\rangle \, |\Gamma_j\gamma_j\rangle \, . \tag{2.46}$$

The values of CG coefficients can be calculated using computer algebra packages (e.g., Ref. [93]) or found from tabular data (e.g., Ref. [94]). Once the CG coefficients are known, the total wavefunction is constructed similarly to the spin states. First, using Eq. (2.46), the two-electron wavefunctions of well-defined orbital symmetry are formed by combining two one-electron orbitals. Then successive states are formed by adding one orbital at a time. The procedure is demonstrated for MO states of NV center in Appendix B.

All electron wavefunctions

Once spin χ and orbital Φ parts are known, the all-electron wavefunction is obtained via Eq. (2.41). Product $\chi(\boldsymbol{\sigma})\Phi(\mathbf{r})$ yields some linear combination of various Hartree-type products (i.e., $\phi_1(\mathbf{r}_1)\bar{\phi}_2(\mathbf{r}_2)\cdots\phi_N(\mathbf{r}_N)$, where "bar" denotes spin-down configuration). Application of antisymmetrizer $\mathcal{A}$ promotes Hartree terms to Slater determinants [Eq. (2.40)]. As a result, the final wave function has a multi-determinant form, which sometimes can be contracted to a single determinant expression. The search for physical states can be exhaustive as one needs to consider all the combinations of possible spin and orbital states. In Appendix B, we show the derivation of NV^0 states, which originally were obtained in the thesis paper [T3].

[10] If atomic orbitals are used as a basis for the MO model, the group theoretical projection operators [90, 92] are employed to find the symmetric basis of one-electron states.

2.4 Vibrational structure

This section focuses on the solution of the nuclear Schrödinger equation (2.13), which follows from the adiabatic treatment of the molecular system. This equation determines the dynamical properties of the lattice. First, in Section 2.4.1, we review the harmonic approximation and introduce the main parameters for the vibrational structure analysis. In the harmonic approximation, the dynamical motion of nuclei is described in terms of normal coordinates and vibrational frequencies. In Section 2.4.2, we briefly review the formal analysis of the periodic systems. The effect of defect perturbation on the vibrational structure of the bulk is discussed in Section 2.4.3. Here we introduce the notion of localized and resonant modes. Finally, at the end of Section 2.4.3, we present the practical supercell approach for first-principle calculations of the vibrational structure of the defect.

2.4.1 Harmonic approximation

The electronic Shrödinger equation (2.8) in principle can be solved for any nuclear configuration $\mathbf{R}_0$. In most practical situations, we are interested in the dynamics of nuclei around the equilibrium geometry. In the classical picture, such equilibrium geometry corresponds to the minimum of the adiabatic potential energy surface (APES) [see Eq. (2.14)]. The procedure of finding this minimum is termed ionic relaxation.

Ionic relaxation relies on the calculation of atomic forces. Once the forces are known, one can apply minimization techniques (like the quasi-Newton or conjugate gradient [95]) to find the local minima. For an atomic system, the nuclear forces on ions are calculated from the Hellman–Feynman theorem [95]:

$$\mathbf{F}_{\mathbf{R}_{0,n}} = -\frac{\partial \varepsilon_i}{\partial \mathbf{R}_{0,n}} = \left\langle \psi_i \middle| \frac{\partial \hat{U}(\mathbf{r}, \mathbf{R}_0)}{\partial \mathbf{R}_{0,n}} \middle| \psi_i \right\rangle, \tag{2.47}$$

where $\mathbf{R}_{0,n}$ is the coordinate of the n-th ion, ε_i is the electronic energy of state ψ_i, and $\hat{U}(\mathbf{r}, \mathbf{R}_0)$ is the potential energy of the electronic Shrödinger equation (2.8). The potential energy has two $\mathbf{R}_0$-dependant terms: the potential energy of electron–nuclear interaction, $\hat{U}_{\mathrm{en}}(\mathbf{r}, \mathbf{R}_0)$, and the potential energy of nuclear–nuclear interaction, $\hat{U}_{\mathrm{nn}}(\mathbf{R}_0)$ [see Eqs. (2.4) and (2.5)]. From Eq. (2.47), it follows that the force explicitly depends on the electron density:

$$\mathbf{F}_{\mathbf{R}_{0,n}} = \int \rho(\mathbf{r}) \frac{\partial \hat{U}_{\mathrm{en}}(\mathbf{r}, \mathbf{R}_0)}{\partial \mathbf{R}_{0,n}} \, \mathrm{d}\mathbf{r} + \frac{\partial \hat{U}_{\mathrm{nn}}(\mathbf{R}_0)}{\partial \mathbf{R}_{0,n}},$$

and can be calculated using density functional theory. Hence, in the following analysis, we will assume that the system is in its equilibrium geometry.

From Eqs. (2.7) and (2.14), it follows that the adiabatic potential energy surface of the nuclear Shrödinger equation (2.13) can be written as:

$$\begin{aligned}\hat{V}_i &= \langle\psi_i|\Delta\hat{U}(\mathbf{r},\mathbf{R})|\psi_i\rangle \\ &= \sum_n \left\langle\psi_i\right|\frac{\partial\hat{U}}{\partial\mathbf{u}_n}\left|\psi_i\right\rangle_{\mathbf{u}=0}\mathbf{u}_n + \frac{1}{2}\sum_{n,m}\left\langle\psi_i\right|\frac{\partial\hat{U}}{\partial\mathbf{u}_n\partial\mathbf{u}_m}\left|\psi_i\right\rangle_{\mathbf{u}=0}\mathbf{u}_n\mathbf{u}_m + O(\mathbf{u}^3),\end{aligned}$$

where $\mathbf{u}$ are displacements from the reference configuration $\mathbf{R}_0$, $\hat{U}$ is the potential energy of all particle–particle interactions, and $\Delta\hat{U}$ is defined as $\Delta\hat{U}(\mathbf{r},\mathbf{R}_0) = \hat{U}(\mathbf{r},\mathbf{R}) - \hat{U}(\mathbf{r},\mathbf{R}_0)$. If $\mathbf{R}_0$ corresponds to the equilibrium geometry, the first term of the expansion vanishes. The harmonic approximation is obtained when only the second-order terms are considered:

$$\hat{V}_i^{\mathrm{har}}(\mathbf{u}) = \frac{1}{2}\sum_{n,m}\mathbf{\Phi}_{nm}\mathbf{u}_n\mathbf{u}_m. \tag{2.48}$$

In the crude adiabatic approximation, the quadratic coefficients:

$$\mathbf{\Phi}_{nm} = \left\langle\psi_i\right|\frac{\partial^2\hat{U}}{\partial\mathbf{u}_n\partial\mathbf{u}_m}\left|\psi_i\right\rangle_{\mathbf{u}=0} = \frac{\partial^2 V_i}{\partial\mathbf{u}_n\partial\mathbf{u}_m}, \tag{2.49}$$

are second-order derivatives of the APES.[11] The matrix $\mathbf{\Phi}$ is known as the *force constant matrix* (or *Hessian matrix*). The corresponding harmonic Hamiltonian of the nuclear system is given by:

$$\hat{H}_v = \sum_n \frac{\mathbf{p}_n^2}{2M_n} + \frac{1}{2}\sum_{nm}\mathbf{\Phi}_{nm}\mathbf{u}_n\mathbf{u}_m. \tag{2.50}$$

The direct solution of $\hat{H}_v\chi = E_v\chi$ is still a challenging task since nuclear degrees of freedom are coupled through $\mathbf{\Phi}_{nm}$. The canonical transformation of coordinates to the basis where potential and kinetic energy terms have diagonal forms could simplify the problem. Such transformation is obtained by solving the classical problem of a harmonic motion, as described below.

Classical solution

The classical equations of motion for Hamiltonian (2.50) are:

$$M_n\ddot{\mathbf{u}}_n = -\sum_m \mathbf{\Phi}_{nm}\mathbf{u}_m. \tag{2.51}$$

This is the coupled system of second-order differential equations. The standard ansatz for the stationary solution has the harmonic form:

$$\mathbf{u}_n(t) = \mathbf{w}_n\exp(-i\omega t). \tag{2.52}$$

[11] These coefficients are multi-dimensional analogs of Hooke's constant.

Here, $\mathbf{w}_n$ is a three-dimensional *amplitude vector* that describes the shape of the vibration. Substituting Eq. (2.52) into Eq. (2.51) yields a generalized eigenvalue equation:

$$\mathbf{\Phi w} = \omega^2 \hat{\mathbf{M}} \mathbf{w}, \tag{2.53}$$

where the *mass matrix* is defined by $\|\hat{\mathbf{M}}\|_{mn} = M_n \delta_{mn}$.[12] This equation can be easily transformed to the standard eigenvalue problem by the introduction of *mass-weighted coordinates/displacements* $\boldsymbol{\eta}$:

$$\boldsymbol{\eta}_n = \sqrt{M_n}\mathbf{w}_n.$$

In this coordinate system, the equation (2.53) becomes:

$$\hat{\mathbf{D}}\boldsymbol{\eta} = \omega^2 \boldsymbol{\eta}. \tag{2.54}$$

The matrix $\hat{\mathbf{D}}$ is just a mass-weighted force constant matrix:

$$\hat{\mathbf{D}} = \hat{\mathbf{M}}^{-1/2} \mathbf{\Phi} \hat{\mathbf{M}}^{-1/2} \quad \left(\text{or } \hat{\mathbf{D}}_{nm} = \frac{\mathbf{\Phi}_{nm}}{\sqrt{M_n M_m}} \right), \tag{2.55}$$

which is often termed the *dynamical matrix* [96]. The solution of Eq. (2.54) yields a set of $3N_\mathrm{n}$ orthonormal vectors $\boldsymbol{\eta}_k$ and corresponding frequencies ω_k. These are the stationary vibrations of the classical system.

Quantum-mechanical description

Once the classical solution is found, we can define so-called *normal coordinates* Q_k [96]:

$$\begin{aligned} Q_k &= \sum_n \boldsymbol{\eta}_n \boldsymbol{\eta}_{k;n} = \sum_n \sqrt{M_n}\left(\mathbf{R}_n - \mathbf{R}_{0,n}\right)\boldsymbol{\eta}_{k;n}, \\ \boldsymbol{\eta}_n &= \sum_k Q_k \boldsymbol{\eta}_{k;n}, \end{aligned} \tag{2.56}$$

where $\mathbf{R}_n$ is the position of atom n, $\mathbf{R}_{0,n}$ is its equilibrium position, and $\boldsymbol{\eta}_{k;n}$ is an eigenvector of dynamical matrix $\hat{\mathbf{D}}$, that describes the three components of the mode k of atom n. The normal coordinates are scalars that represent the collective motion/displacement of the nuclear system. The second relation of Eq. (2.56) follows from the ortho-normality condition $\sum_n \boldsymbol{\eta}_{k;n}\boldsymbol{\eta}_{k';n} = \delta_{kk'}$, which implies that $\boldsymbol{\eta}^{-1}_{k;n} = \boldsymbol{\eta}_{n;k}$ (note index transposition). Canonical

[12] The notation $\|\mathbf{A}\|_{mn}$ denotes the matrix element of operator $\mathbf{A}$.

transformation to normal coordinates transforms the kinetic and potential energy term into the diagonal form:

$$\sum_n \frac{\mathbf{p}_n^2}{2M_n} = \frac{1}{2}\sum_k \frac{\partial^2}{\partial Q_k^2}, \quad \frac{1}{2}\sum_{nm} \hat{\mathbf{D}}_{nm}\boldsymbol{\eta}_n\boldsymbol{\eta}_m = \frac{1}{2}\sum_k \omega_k^2 Q_k^2.$$

In the basis of normal coordinates, the harmonic Hamiltonian becomes the sum of one-dimensional harmonic oscillator equations:

$$\hat{H}_v = \sum_k \hat{H}_v^k, \quad \text{where } \hat{H}_v^k = \frac{1}{2}\frac{\partial^2}{\partial Q_k^2} + \frac{1}{2}\omega_k^2 Q_k^2. \tag{2.57}$$

Since $[\hat{H}_v^k, \hat{H}_v^{k'}] = 0$ for every k, the eigensolution of $\hat{H}_v$ can be written in the multiplicative form:

$$\chi(\mathbf{Q}) = \chi_i(Q_1)\chi_2(Q_2)\cdots\chi_{3N_\mathrm{n}}(Q_{3N_\mathrm{n}}),$$

where each $\chi_k(Q_k)$ is found by solving a one-dimensional Schrodinger equation:

$$\hat{H}_v^k \chi_k(Q_k) = \epsilon_k \chi_k(Q_k). \tag{2.58}$$

Therefore, each one-dimensional oscillator is described by a quantum number $n_k = 0, 1, \ldots$, and the corresponding energy is $\epsilon_k = \omega_k(n_k + 1/2)$. The vibrational state of the whole system is characterized by Fock state vector $|n_1 n_2 \cdots n_{3N_\mathrm{n}}\rangle$, and related energy is the sum of harmonic oscillator energies:

$$E_v = \sum_k \epsilon_{n_k}.$$

The discussion above shows that the vibrational problem can be solved by diagonalizing the dynamical matrix [Eq. (2.55)]. Once the solutions are found, the quantum-mechanical vibrational states are described by a set of one-dimensional harmonic oscillators. However, direct diagonalization is impossible for extended systems like solids, as we have an effectively infinite number of degrees of freedom. In the next section, we will shortly revision the solution of the vibrational problem in the systems with translational symmetry.

2.4.2 Crystal vibrations

For periodic crystals, the translational symmetry is utilized to simplify the analysis and reduce the computational cost. Crystal is divided into an array of unit cells. A unit cell is the volume element that generates the whole structure by periodic repetition in space. Therefore, each atomic position can be described by two vectors:

$$\mathbf{R}_n^\alpha = \mathbf{R}^\alpha + \mathbf{R}_n,$$

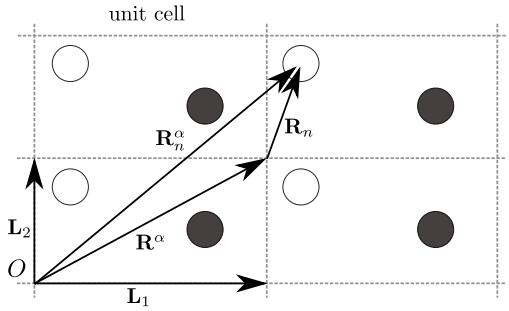

Figure 2.3: Principle scheme of crystal structure.

where $\mathbf{R}^\alpha$ defines the position of unit cell α, and $\mathbf{R}_n$ labels the relative position within the unit cell (see Fig. 2.3). Accordingly, we label the dynamical matrix (2.55) of the periodic system by four indices:

$$\hat{\mathbf{D}}_{\alpha m,\beta n} \equiv \hat{\mathbf{D}}_{m,n}(\mathbf{R}^\alpha, \mathbf{R}^\beta).$$

The translational invariance of Hamiltonian implies translational invariance of the dynamical matrix:

$$\hat{\mathbf{D}}_{mn}(\mathbf{R}^\alpha + \mathbf{L}, \mathbf{R}^\beta + \mathbf{L}) = \hat{\mathbf{D}}_{mn}(\mathbf{R}^\alpha, \mathbf{R}^\beta),$$

where $\mathbf{L}$ is a crystal lattice vector. Such symmetry allows to employ the Bloch theorem, which states that any eigenvector of a periodic operator has the following mathematical form:

$$\boldsymbol{\eta}_n(\mathbf{R}^\alpha) = \exp(i\mathbf{q}\mathbf{R}^\alpha)\tilde{\boldsymbol{\eta}}_{\mathbf{q}n}. \tag{2.59}$$

Here, $\mathbf{q}$ is any vector, and $\tilde{\boldsymbol{\eta}}_{\mathbf{q},n}$ is a lattice-periodic part. Plugging Eq. (2.59) into Eq. (2.54) yields:

$$\sum_n \sum_\beta \hat{\mathbf{D}}_{mn}(\mathbf{R}^\alpha, \mathbf{R}^\beta) e^{i\mathbf{q}\mathbf{R}^\beta} \tilde{\boldsymbol{\eta}}_{\mathbf{q}n} = \omega^2 e^{i\mathbf{q}\mathbf{R}^\alpha} \tilde{\boldsymbol{\eta}}_{\mathbf{q}m}.$$

Finally, the translational symmetry of $\hat{\mathbf{D}}$ allows us to set the coordinate system to $\mathbf{R}^\alpha = 0$, and the dynamical equation becomes:

$$\hat{\mathcal{D}}(\mathbf{q})\tilde{\boldsymbol{\eta}}(\mathbf{q}) = \omega(\mathbf{q})^2 \tilde{\boldsymbol{\eta}}(\mathbf{q}). \tag{2.60}$$

Here, $\hat{\mathcal{D}}(\mathbf{q})$ is the *reduced dynamical matrix*:

$$\hat{\mathcal{D}}_{nm}(\mathbf{q}) = \sum_\beta \hat{\mathbf{D}}_{mn}(0, \mathbf{R}^\beta) e^{i\mathbf{q}\mathbf{R}^\beta}. \tag{2.61}$$

Consequently, we must solve Eq. (2.60) for each $\mathbf{q}$ point within the first Brillouin

zone (FBZ) for the periodic crystal. Solutions outside FBZ are equivalent because of the relation:

$$\exp\left(i(\mathbf{q}+\mathbf{G})\mathbf{R}^{\beta}\right) = \exp\left(i\mathbf{q}\mathbf{R}^{\beta}\right),$$

for any reciprocal lattice vector $\mathbf{G}$. In practice, the vibrational structure analysis of the periodic system is performed along some paths inside FBZ. The exemplar calculations of the diamond phonon structure will be presented in Section 3.1.

2.4.3 Defect vibrations

When the point defect is present in an infinite lattice, it spoils the periodic symmetry and, hence, the vibrations of the perfect crystal are modified from their usual form. As a result, the analysis of normal modes cannot be simplified in the same way as for periodic systems. However, the simplifying feature of the point-defect is that the defect is localized in a small region of the volume in the otherwise perfect lattice. The original theoretical method for the defect–lattice vibrational analysis was the *Green's-function* (GF) *approach* [97–99]. This method allows qualitative analysis of general properties of defect-specific vibrational modes. Therefore, in the first part of this section, we will briefly review some findings of the vibrational structure of the point-defect.

However, the practical application of the Green's-function method to real problems is difficult, especially if one needs to obtain accurate geometrical shapes of vibrations. Therefore, in the second part of this section, we will present the computational supercell approach for the quantitative analysis of vibrational modes of the defect.

Localized and quasi-localized modes

Point imperfections may introduce vibrational modes in the frequency region forbidden to the crystal (e.g., phonon bandgap) or modify the bulk vibrations [98, 99]. In the first case, the vibrational modes have large amplitudes and are strongly localized in the vicinity of the defect. Therefore, they are often referred to as "*localized modes*". The formal analysis of Maradudin [98] shows that the amplitude of localized mode is independent of the system size and decays faster than exponentially with increasing distance from the defect. Due to a strong electron–lattice interaction, such modes often leave signatures in the luminescence (or absorption) spectrum. They can also be detected using infrared or Raman spectroscopy [100].

In contrast, if the frequency of defect-specific mode is in the energy band of the perfect crystal, the vibrational mode has a less localized character [99–102].

Such "in-band" modes often appear in collections and are qualitatively characterized by resonance-type amplitude peaks in the frequency spectrum of perturbed lattice (e.g., if the vibrational amplitude of the impurity atom is a function of the frequency, this function has a sharp increase at some resonant value). Such collections of perturbed modes are often referred to as "*resonance modes*" (or "*quasi-local modes*"). The first theoretical prediction of resonant modes was made for pure mass defects [103]. However, they are common features of impurities that cause a decrease of force-constants. The characteristic feature of quasi-local mode is that the amplitude at the defect site is of order $N_{\mathrm{n}}^{-1/2}$, while it is independent of the system size for the localized mode [101]. However, as the size of the system increases, the number of modes that constitute the resonance also grows. Therefore, resonances are significant in describing the electron–phonon interaction, as the collective increase of amplitude in the vicinity of the defect implies a stronger coupling between the lattice and electrons.

Supercell approach

The discussion above indicates that the defect-specific modes are either strongly localized in the defect neighborhood or resemble pure bulk vibrations with usually small perturbations in the vicinity of the defect. Thus, a natural idea for quantitative analysis is to use the sufficiently large defected supercell with periodic boundary conditions. If the supercell is large enough, the local and quasi-local vibrations can be effectively contained in the region of one supercell. This approach is standard for defect vibrational structure analysis (see, e.g., Refs. [104–108]). Although the idea principally is correct, from the practical point of view, we are restricted to somewhat limited size supercells due to computational limitations. In general, localized modes are easily captured in moderate-sized supercells. However, the general features of resonance only slowly converge with the size of the cell (this will be illustrated in Chapters 3 and 4). For small and moderate-sized supercells, the most troublesome region is the low-frequency domain of acoustic modes. In the case of diamond NV center, Alkauskas *et al.* [109] noted that the correct overall shape of electron–phonon interaction could only be obtained if the supercell size reaches tens of thousands of atoms. Correspondingly, Alkauskas *et al.* [109] suggested using the *embedding methodology*, where the dynamical matrix of a very large supercell is constructed from the calculations in computationally feasible moderate-sized supercells. The development and improvement of this embedding methodology were one of the major topics in this thesis. This methodology is presented in Section 3.3.

2.5 Degenerate states and vibronic structure

The adiabatic approximation [Eq. (2.11)] works well if the separation between energies ε_i of electronic states ψ_i is much larger than the characteristic vibrational energy of the nuclear subsystem. However, this approximation fails when ψ_i belongs to the degenerate set of electronic wavefunctions. In such a case, instead of the adiabatic wavefunction (2.12), one needs to consider wavefunctions of the *vibronic* form:[13]

$$\Psi = \sum_i \chi_i(\mathbf{R})\psi_i(\mathbf{r}, \mathbf{R}_0). \tag{2.62}$$

Here, the summation runs over all electronic states of the degenerate subspace. Wavefunction (2.62) is a solution of the vibronic Schrödinger equation [Eq. (2.10)]:

$$\hat{T}_N\chi_j(\mathbf{u}) + \sum_i \langle\psi_j|\,\Delta\hat{U}\,|\psi_i\rangle\,\chi_i(\mathbf{u}) = E_v\chi_j(\mathbf{u}), \tag{2.63}$$

where i runs over all degenerate states, and $E_v = E - \varepsilon_i$ is the energy contribution to the total energy of the molecular system.[14] The non-adiabatic Eq. (2.63) results in complex nuclear dynamics, often titled the *Jahn–Teller* (JT) *effect*.

Degeneracy is a consequence of spatial symmetry and is a common problem for point defects. The Jahn–Teller effect in color centers is responsible for many non-trivial phenomena and impacts optical spectroscopic properties [110]. However, the theoretical treatment of the JT system is difficult, especially if the system has many nuclear degrees of freedom. Therefore, the analysis is often simplified by considering the model of one effective vibrational mode [106, 110, 111]. This reduction is formally justified for strong vibronic coupling [112] but is inadequate for weak and moderate vibronic strengths. One of the important achievements of this thesis is the development of a practical methodology for the multi-mode treatment of the JT problem. This methodology will be presented in Section 4.3.3.

This part is organized as follows. Section 2.5.1 introduces the formal theory of the JT effect.[15] This theory relies on the group theoretical analysis, which is shortly reviewed in Appendix A. In Section 2.5.2, we discuss the practical approach to the solution of the dynamical JT problem. Section 2.5.3 presents

[13] "Vibronic" is often used to refer to a combined electronic and vibrational state. Here, we will use "vibronic" to indicate that the total wavefunction is not simple multiplicative product $\Psi = \chi\psi$.

[14] Note that in the adiabatic approximation, only the diagonal terms $\langle\psi_i|\Delta\hat{U}|\psi_i\rangle$ are kept.

[15] Our presentation loosely follows the theoretical analysis of Bersuker and Polinger [27].

our original treatment of the JT effect in the excited triplet state of the diamond NV^- center. We show that the JT effect has $E \otimes (e \oplus e \oplus \cdots)$ coupling in this system, where e symmetry modes mix two degenerate electronic wavefunctions of E symmetry. Finally, at the end of Section 2.5.3, we derive a practical expression for matrix elements of the $E \otimes (e \oplus e \oplus \cdots)$ Jahn–Teller perturbation. These findings are later used in Chapters 4 and 5, where we analyze the electron–phonon coupling of $A_2 \leftrightarrow E$ electronic transitions.

2.5.1 Vibronic Hamiltonian

Let us first discuss the symmetry properties of the system. As a starting point, we choose the reference nuclear configuration $\mathbf{R}_0$ for which the symmetry is highest and the electronic degeneracy occurs. In practice, $\mathbf{R}_0$ could be selected as an equilibrium geometry of some non-degenerate electronic state. In this configuration, the symmetry of the electronic system is described by the point group $\mathcal{G}$, a set of all spatial symmetry transformations that keep the electronic Hamiltonian [Eq. (2.8)] invariant. The fundamental theorem of group theory [89] states that any eigenstate of the symmetric Hamiltonian must transform as a basis of some *irreducible representation* Γ of the point group $\mathcal{G}$ (see Appendix A for a brief introduction to representation theory). Moreover, degenerate electronic states always transform as different rows γ of same irreducible representation Γ. Therefore, we label degenerate electronic states by $|\Gamma\gamma_i\rangle \equiv |\psi_i\rangle$, where γ_i identifies different degenerate wavefunctions.

For the description of the ionic motion, similarly, as in Eq. (2.56), we define the basis of symmetrized coordinates:

$$Q_{\Gamma_k\gamma_k} = \sum_n \sqrt{M_n}(\mathbf{R}_n - \mathbf{R}_{0,n})\boldsymbol{\eta}_{n;\Gamma_k\gamma_k}.$$

Here, $\boldsymbol{\eta}_{\Gamma_k\gamma_k}$ transforms as row γ_k of some irreducible representation Γ_k and describes the collective displacement from the reference configuration $\mathbf{R}_0$. Index k is used to distinguish different sets of symmetric coordinates. Such symmetrized basis can be directly obtained using group theory projection operators [89, 90]. Alternatively, one can use normal coordinates [Eq. (2.56)] of some non-degenerate electronic state, as they naturally transform as a basis of irreducible representation.

For specific labeling of irreducible representations, we follow the notation suggested by Mulliken [94]: "A" and "E" respectively denote one- and two-dimensional representations (or non-degenerate and doubly degenerate states). The most trivial representation is *totally symmetric representation* A_1.

Mathematical objects of A_1 symmetry are invariant under all symmetry transformations of the point-group (e.g., $T(G_i)Q_{a_1} = Q_{a_1}$).[16]

Using symmetrized basis, we expand the matrix element $\langle \Gamma\gamma_i|\Delta U|\Gamma\gamma_j\rangle$ of Eq. (2.63) around the reference configuration $\mathbf{R}_0$:

$$\begin{aligned}&\langle \Gamma\gamma_i|\Delta U(\mathbf{r},\mathbf{Q})|\Gamma\gamma_j\rangle \\ &\quad=\sum_{\Gamma_k\gamma_k} V^{ij}_{\Gamma_k\gamma_k} Q_{\Gamma_k\gamma_k} + \frac{1}{2}\sum_{\Gamma_k\gamma_k}\sum_{\Gamma_l\gamma_l} W^{ij}_{\Gamma_k\gamma_k,\Gamma_l\gamma_l} Q_{\Gamma_k\gamma_k} Q_{\Gamma_l\gamma_l} + O(Q^3). \quad (2.64)\end{aligned}$$

Here, we have introduced the expansion coefficients:

$$V^{ij}_{\Gamma_k\gamma_k} = \left\langle \Gamma\gamma_i \middle| \frac{\partial \Delta U(\mathbf{r},\mathbf{Q})}{\partial Q_{\Gamma_k\gamma_k}} \middle| \Gamma\gamma_j \right\rangle_{\mathbf{Q}=0}, \quad (2.65)$$

$$W^{ij}_{\Gamma_k\gamma_k,\Gamma_l\gamma_l} = \left\langle \Gamma\gamma_i \middle| \frac{\partial^2 \Delta U(\mathbf{r},\mathbf{Q})}{\partial Q_{\Gamma_k\gamma_k}\partial Q_{\Gamma_l\gamma_l}} \middle| \Gamma\gamma_j \right\rangle_{\mathbf{Q}=0}. \quad (2.66)$$

These matrix elements are called *linear and quadratic constants of vibronic coupling*. The non-diagonal terms of Eqs. (2.65) and (2.66) are essential for the non-adiabatic description, as they characterize the influence of nuclear motion on the electronic distribution and *vice versa*. Following the above notation, the Hamiltonian of Eq. (2.63) up to the second-order expansion can be written as:

$$\begin{aligned}\hat{H}^{\text{vibr}}_{ij} =& \frac{1}{2}\sum_{\Gamma_k\gamma_k} P^2_{\Gamma_k\gamma_k} + \sum_{\Gamma_k\gamma_k} V^{ij}_{\Gamma_k\gamma_k} Q_{\Gamma_k\gamma_k} \\ &+ \frac{1}{2}\sum_{\Gamma_k\gamma_k}\sum_{\Gamma_l\gamma_l} W^{ij}_{\Gamma_k\gamma_k,\Gamma_l\gamma_l} Q_{\Gamma_k\gamma_k} Q_{\Gamma_l\gamma_l}, \quad (2.67)\end{aligned}$$

where $P_{\Gamma_k\gamma_k} = \partial/\partial Q_{\Gamma_k\gamma_k}$ is the conjugate momentum of the coordinate $Q_{\Gamma_k\gamma_k}$.

In the following analysis, we will factor out the non-adiabatic part of Eq. (2.67), $\hat{H}^{\text{JT}}$, that is only present in the case of degeneracy:

$$\hat{H}^{\text{vibr}} = \hat{H}_0 + \hat{H}^{\text{JT}}. \quad (2.68)$$

Here, $\hat{H}_0$ describes the zero-order solution in the absence of vibronic coupling between degenerate electronic states.

Linear vibronic constants

Parameters $V^{ij}_{\Gamma_k\gamma_k}$ are *linear vibronic constant* (LVC) and have a clear meaning when $i = j$: $V^{ii}_{\Gamma_k\gamma_k}$ is the force in the direction of $Q_{\Gamma_k\gamma_k}$ when electrons are in

[16] We will use lower case letters (e.g., a_1, a_2, and e) for irreducible representations of normal coordinates or single-particle states and upper-case letters for multi-electron wave functions.

the state $|\Gamma\gamma_i\rangle$. On the other hand, the off-diagonal LVCs couple degenerate electronic states when the motion of nuclei is turned on.

Let us look at the symmetry properties of LVC. The operator:

$$X_{\Gamma_k\gamma_k} = \frac{\partial \Delta U(\mathbf{r}, \mathbf{Q})}{\partial Q_{\Gamma_k\gamma_k}},$$

has the same symmetry as the ionic displacement $Q_{\Gamma_k\gamma_k}$ [27].[17] When all the terms in the matrix element transform as a basis of the irreducible representation, we can employ the *Wigner–Eckart theorem* [90]. This theorem states that for any symmetric operator $X_{\Gamma_k\gamma_k}$, we have:

$$\langle \Gamma_i\gamma_i | X_{\Gamma_k\gamma_k} | \Gamma_j\gamma_j \rangle = \bar{X}_{\Gamma_k}^{\Gamma_i\Gamma_j} \langle \Gamma_i\gamma_i\Gamma_k\gamma_k | \Gamma_j\gamma_j \rangle ,$$

where $\bar{X}_{\Gamma_k}^{\Gamma_i\Gamma_j}$ is the so-called *reduced matrix element*, and $\langle \Gamma\gamma_i\Gamma_k\gamma_k | \Gamma\gamma_j \rangle$ are the point groups' *Clebsch–Gordan* (CG) *coefficients*. The reduced matrix element does not depend on rows of irreducible representations. Thus, it is the same for all γ_i, γ_j, and γ_k. CG coefficients depend only on the point group and can be found from tabulated data [93] or calculated using computer algebra packages (e.g., Ref. [113]).[18] Therefore, we can write the linear constant of vibronic coupling as:

$$V_{\Gamma_k\gamma_k}^{ij} = V_{\Gamma_k} \langle \Gamma\gamma_i\Gamma_k\gamma_k | \Gamma\gamma_j \rangle . \tag{2.69}$$

If one vibronic constant $V_{\Gamma_k\gamma_k}^{ij}$ is known, all the others belonging to the same symmetric set k can be calculated using the above equation.

Now, let us analyze the matrix element (2.65) in the case of non-degenerate electronic states. Group theory tells us that this matrix element is non-vanishing only if we have a totally symmetric contribution in the direct product of representation $A_1 \in \Gamma \otimes \Gamma_k \otimes \Gamma$. In the case of non-degenerate electronic states, Γ is a one-dimensional representation and $\Gamma \otimes \Gamma = A_1$. In direct product algebra, A_1 has a role of identity, and Γ_k can only be A_1 representation; otherwise, $V_{\Gamma_k\gamma_k}^{ii}$ is zero. Therefore, *for non-degenerate electronic states, the force can only emerge along totally symmetric directions*.

In the case of degeneracy, the matrix element for A_1 symmetry displacement is also diagonal with respect to electronic states $\hat{V}_{A_1}^{ij} = \hat{V}_{A_1}\delta_{ij}$.[19] Therefore, we split the linear term of Eq. (2.64) into the sum that contains A_1 symmetry displacements, and treat the rest as a contribution to Jahn–Teller perturbation $\hat{H}^{\mathrm{JT}}$.

[17] It transforms as the same row of irreducible representation as $Q_{\Gamma_k\gamma_k}$.

[18] Note that CG coefficients are directly related to the matrix form of representation. Thus, for two equivalent representations $T'(G_i) = ST(G_i)S^{-1}$, CG coefficient values generally differ.

[19] This follows from CG coefficient relation $\langle \Gamma\gamma_i A_1 | \Gamma\gamma_j \rangle = \delta_{ij}$ for "simply reducible" groups [92].

Quadratic constants of vibronic coupling

A similar analysis is applied to the second-order coefficients (2.66). This time, the operator:

$$\Omega_{\Gamma_k\gamma_k\Gamma_l\gamma_l} = \frac{\partial^2 \Delta U(\mathbf{r},\mathbf{Q})}{\partial Q_{\Gamma_k\gamma_k}\partial Q_{\Gamma_l\gamma_l}}, \tag{2.70}$$

generally does not transform as an irreducible representation of the point group $\mathcal{G}$. It is a second rank tensor and a direct product of two representations, $\Gamma_k \otimes \Gamma_l$. The same reasoning holds for the product $Q_{\Gamma_k\gamma_k}Q_{\Gamma_l\gamma_l}$. We knwo from the discussion above that only the A_1 part of Eq. (2.70) contributes to the non-degenerate states. To separate this part, we expand operator (2.70) into symmetric components using inverse Clebsch–Gordan coefficients $\langle \Gamma_i\gamma_i|\Gamma_j\gamma_j\Gamma_k\gamma_k\rangle$ [89, 92]:

$$\Omega_{\Gamma_k\gamma_k\Gamma_l\gamma_l} = \sum_{\Gamma'\gamma'} \left\langle \Gamma'\gamma' \middle| \Gamma_k\gamma_k\Gamma_l\gamma_l \right\rangle \Omega_{\Gamma'\gamma'}(\Gamma_k \otimes \Gamma_l), \tag{2.71}$$

$$Q_{\Gamma_k\gamma_k}Q_{\Gamma_l\gamma_l} = \sum_{\Gamma'\gamma'} \left\langle \Gamma'\gamma' \middle| \Gamma_k\gamma_k\Gamma_l\gamma_l \right\rangle \{Q_{\Gamma_k} \otimes Q_{\Gamma_l}\}_{\Gamma'\gamma'}. \tag{2.72}$$

Here, $\Omega_{\Gamma'\gamma'}(\Gamma_k \otimes \Gamma_l)$ and $\{Q_{\Gamma_k} \otimes Q_{\Gamma_l}\}_{\Gamma'\gamma'}$ are projections that transform as rows γ' of the irreducible representation Γ'.

Using the Wigner–Eckart theorem, we define the reduced matrix element $W_{\Gamma'}(\Gamma_k \otimes \Gamma_l)$ of the quadratic vibronic constant as:

$$\left\langle \Gamma\gamma_i \middle| \Omega_{\Gamma'\gamma'}(\Gamma_k \otimes \Gamma_l) \middle| \Gamma\gamma_j \right\rangle = W_{\Gamma'}(\Gamma_k \otimes \Gamma_l) \left\langle \Gamma\gamma_i\Gamma'\gamma' \middle| \Gamma\gamma_j \right\rangle. \tag{2.73}$$

If the representation is unitary and real (and for most groups, it can be chosen to be one by the correct choice of a degenerate basis), the following orthogonality property holds [92]:

$$\sum_{\Gamma_k\gamma_k\Gamma_l\gamma_l} \left\langle \Gamma'\gamma' \middle| \Gamma_k\gamma_k\Gamma_l\gamma_l \right\rangle \left\langle \Gamma''\gamma'' \middle| \Gamma_k\gamma_k\Gamma_l\gamma_l \right\rangle = \delta_{\Gamma'\Gamma''}\delta_{\gamma'\gamma''}. \tag{2.74}$$

Using Eqs. (2.71)–(2.74), we rewrite the second-order term of Hamiltonian (2.67) as:

$$\begin{aligned} &\sum_{\Gamma_k\gamma_k} \sum_{\Gamma_l\gamma_l} W^{ij}_{\Gamma_k\gamma_k,\Gamma_l\gamma_l} Q_{\Gamma_k\gamma_k}Q_{\Gamma_l\gamma_l} \\ &\quad = \sum_{\Gamma_k\Gamma_l} \sum_{\Gamma'\gamma'} W_{\Gamma'}(\Gamma_k \otimes \Gamma_l) \left\langle \Gamma\gamma_i\Gamma'\gamma' \middle| \Gamma\gamma_j \right\rangle \{Q_{\Gamma_k} \otimes Q_{\Gamma_l}\}_{\Gamma'\gamma'}. \end{aligned} \tag{2.75}$$

In the second line of this equation, the first sum is over all pairs of symmetric multiplets of nuclear coordinates, while the second sum runs over all symmetric components of direct product $\Gamma_k \otimes \Gamma_l$. In this form, we can separate $\Gamma'\gamma' \in A_1$

contribution that is also present in the non-degenerate case. To simplify the notation, we define CG coefficient matrices in the basis of electronic states as $\hat{C}_{\Gamma_k}$, such that:

$$\|\hat{C}_{\Gamma_k}\|_{ij} = \langle \Gamma\gamma_i \Gamma_k \gamma_k | \Gamma \gamma_j \rangle \,.$$

and $\|\hat{C}_{A_1}\|_{ij} = \delta_{ij}$ plays the role of the unit matrix.

From the above consideration of linear and quadratic terms, it follows that the zero-order Hamiltonian of Eq. (2.68) contains only A_1 contributions of linear and quadratic vibronic constants:

$$\begin{aligned}\hat{H}^0 = &\Bigg\{ \frac{1}{2} \sum_{\Gamma_k \gamma_k} P^2_{\Gamma_k \gamma_k} + \sum_{\Gamma_k \in A_1} V_{\Gamma_k} Q_{\Gamma_k} \\ &+ \frac{1}{2} \sum_{\Gamma_n \Gamma_m} W_{A_1}(\Gamma_n \otimes \Gamma_m) \left\{ Q_{\Gamma_n} \otimes Q_{\Gamma_m} \right\}_{A_1} \Bigg\} \hat{C}_{A_1}. \end{aligned} \tag{2.76}$$

Since this Hamiltonian is diagonal with respect to electronic states, it does not mix degenerate electronic wavefunctions. Furthermore, we can simplify the last term of Eq. (2.76) by noting that:

$$\begin{aligned} &\sum_{\Gamma_n \Gamma_m} W_{A_1}(\Gamma_n \otimes \Gamma_m) \left\{ Q_{\Gamma_n} \otimes Q_{\Gamma_m} \right\}_{A_1} \\ &\quad = \sum_{\Gamma_n \gamma_n} \sum_{\Gamma_m \gamma_m} W_{A_1}(\Gamma_n \otimes \Gamma_m) \langle \Gamma_n \gamma_n \Gamma_m \gamma_m | A_1 \rangle \, Q_{\Gamma_n \gamma_n} Q_{\Gamma_m \gamma_m} \\ &\quad \equiv \sum_{\Gamma_n \gamma_n} \sum_{\Gamma_m \gamma_m} \mathbf{D}_{\Gamma_n \gamma_n, \Gamma_m \gamma_m} Q_{\Gamma_n \gamma_n} Q_{\Gamma_m \gamma_m} \end{aligned} \tag{2.77}$$

Here, we used the inverse relation of Eq. (2.72) [89, 92]:

$$\{ Q_{\Gamma_k} \otimes Q_{\Gamma_l} \}_{\Gamma' \gamma'} = \sum_{\gamma_k \gamma_l} \left\langle \Gamma_k \gamma_k \Gamma_l \gamma_l \middle| \Gamma' \gamma' \right\rangle Q_{\Gamma_k \gamma_k} Q_{\Gamma_l \gamma_l}.$$

In Eq. (2.77), matrix $\mathbf{D}$ has the same role as the dynamical matrix in the adiabatic problem. Therefore, we will call it the *dynamical matrix of the vibronic system*. The elements of this matrix are called mass-weighted *primary force constants*.

The Jahn–Teller part $\hat{H}^{\text{JT}}$ contains all the terms which are responsible for the non-adiabatic mixing of degenerate states:

$$\begin{aligned} \hat{H}^{\text{JT}} = &\sum_{\Gamma_k \gamma_k \notin A_1} V_{\Gamma_k} Q_{\Gamma_k \gamma_k} \hat{C}_{\Gamma_k} \\ &+ \sum_{\Gamma_n \Gamma_m} \sum_{\Gamma_k \gamma_k \notin A_1} W_{\Gamma_k}(\Gamma_n \otimes \Gamma_m) \{ Q_{\Gamma_n} \otimes Q_{\Gamma_m} \}_{\Gamma_k \gamma_k} \hat{C}_{\Gamma_k}. \end{aligned} \tag{2.78}$$

The mixing of electronic states comes from CG coefficient matrices $\hat{C}_{\Gamma_k}$, which are, in the general case, non-diagonal with respect to electronic states.

The selection of $\hat{H}^0$ could seem a bit arbitrary. However, as pointed out by Bersuker [28], W_{A_1} has a major contribution to the potential energy curvature $\partial^2 E/\partial Q^2_{\Gamma_k\gamma_k}$ (E is the system's total energy). In contrast, the *second-order vibronic terms $W_{\Gamma_k \notin A_1}$ contribute only as a second-order perturbation*. Thus, the majority of electronic coupling comes from linear vibronic constants. The second line of Eq. (2.78) has a small contribution in the case of weak coupling. As the system considered in this thesis (NV center) has a relatively weak coupling, we will omit terms $W_{\Gamma_k \notin A_1}$, which considerably simplifies the analysis. However, in the case of strong coupling, second-order contributions might have a large impact.

A practical approach for calculating primary force constants and linear vibronic constants is presented in Sections 3.2.2 and 4.3.1. In the following analysis, we will assume that these parameters are known.

Zero-order solution

First, let us focus on the zero-order Hamiltonian (2.76) and its eigenfunctions. Later these eigenfunctions will be used as the zero-order basis for the Jahn–Teller problem. Terms $V_{\Gamma_k \in A_1}$ are forces in the direction of A_1 symmetry displacement. Practically, we can get rid of them by a suitable choice of the reference configuration $\mathbf{R}_0$.[20]. Assuming that system has been relaxed along with A_1 symmetry coordinates, and by plugging Eq. (2.77) into Eq. (2.76), we get the Hamiltonian:

$$\hat{H}^0 = \left\{ \frac{1}{2} \sum_{\Gamma_k\gamma_k} \hat{P}^2_{\Gamma_k\gamma_k} + \frac{1}{2} \sum_{\Gamma_k\gamma_k} \sum_{\Gamma_l\gamma_l} \mathbf{D}_{\Gamma_k\gamma_k,\Gamma_l\gamma_l} Q_{\Gamma_k\gamma_k} Q_{\Gamma_l\gamma_l} \right\} \hat{C}_{A_1}. \quad (2.79)$$

This form is equivalent to the harmonic Hamiltonian (2.50). Consequently, we can follow similar steps and perform a canonical transformation to the normal coordinates, diagonalizing the dynamical matrix $\mathbf{D}$. As a result, in this new basis, the Hamiltonian (2.76) takes a simple oscillator form [same as in Eq. (2.57)]:

$$\hat{H}^0 = \sum_{\Gamma_k\gamma_k} \left\{ \frac{1}{2} \hat{P}^2_{\Gamma_k\gamma_k} + \frac{1}{2} \omega^2_{\Gamma_k} Q^2_{\Gamma_k\gamma_k} \right\} \hat{C}_{A_1} \equiv \hat{C}_{A_1} \sum_{\Gamma_k\gamma_k} \hat{H}^0_{\Gamma_k\gamma_k}, \quad (2.80)$$

[20] See Section 3.2 for a practical realization of relaxation along with A_1 symmetry directions.

where the previous notation $Q_{\Gamma_k\gamma_k}$ is used for new normal coordinates. Here, $\omega^2_{\Gamma_k\gamma_k}$ are eigenvalues of $\mathbf{D}$ that describe the frequency of the vibration. Similarly, as in harmonic problem, the solution of the Hamiltonian (2.80) takes the form:

$$\Psi^0 = \chi^{(0)}(\mathbf{Q})\,|\Gamma\gamma_i\rangle\,, \tag{2.81}$$

where nuclear term $\chi^{(0)}(\mathbf{Q}) = \prod_{\Gamma_k\gamma_k}\chi_{\Gamma_k\gamma_k}(Q_{\Gamma_k\gamma_k})$ is a product of one-dimensional harmonic oscillator states. Each one-dimensional phonon state is an eigenstate of $\hat{H}^0_{\Gamma_k\gamma_k} = \{\frac{1}{2}\hat{P}^2_{\Gamma_k\gamma_k} + \frac{1}{2}\omega^2_{\Gamma_k}Q^2_{\Gamma_k\gamma_k}\}$. In conclusion, zero-order solutions of the Jahn–Teller problem take the form where each degenerate state $|\Gamma\gamma_i\rangle$ has the same vibrational manifold $\chi^{(0)}(\mathbf{Q})$ described by $\sum_{\Gamma_k\gamma_k}\hat{H}^0_{\Gamma_k\gamma_k}$.

Jahn–Teller perturbation

As noted above, in this work, we ignore the second-order vibronic coupling and take the linear vibronic constants as the only contribution to the Jahn–Teller effect. In this approximation, the non-adiabatic part of the vibronic Hamiltonian is:

$$\hat{H}^{\text{JT}} = \sum_{\Gamma_k\gamma_k\notin A_1} V_{\Gamma_k\gamma_k}Q_{\Gamma_k\gamma_k}\hat{C}_{\Gamma_k}. \tag{2.82}$$

Here, CG matrices $\hat{C}_{\Gamma_k}$ are responsible for the linear mixing of electronic states. Because of these terms, adiabatic states (2.81) are coupled, and the nuclear motion cannot be reduced to a simple harmonic oscillator form.

Decoupling symmetry-breaking contribution

In the analysis above, we showed that the A_1 symmetry motion of the ionic system does not couple degenerate electronic states.[21] Luckily, we can separate the problem for these vibrations from the symmetry-breaking modes, as shown below. We split the total vibronic Hamiltonian into two parts: $\hat{H}^{\text{vibr}} = \hat{H}^{\text{vibr}}_{a_1} + \hat{H}^{\text{vibr}}_{\text{asym}}$. The first term contains only nuclear coordinates of A_1 symmetry:

$$\hat{H}^{\text{vibr}}_{a_1}(\mathbf{Q}_{a_1}) = \sum_{\Gamma_k\in A_1}\left\{\frac{1}{2}P^2_{\Gamma_k} + \frac{1}{2}\omega^2_{\Gamma_k}Q^2_{\Gamma_k}\right\}\hat{C}_{A_1} \equiv \mathcal{H}^0_{a_1}\hat{C}_{A_1},$$

[21] This is because $\hat{C}_{\Gamma_{A_1}}$ is a unity matrix with respect to degenerate electronic states.

where the summation runs over all A_1 normal coordinates. The motion, along with symmetry-breaking directions, is described by:

$$\begin{aligned}\hat{H}^{\text{vibr}}_{\text{asym}}(\mathbf{Q}_{\text{asym}}) &= \sum_{\Gamma_k\gamma_k \notin A_1} \left\{ \frac{1}{2} P^2_{\Gamma_k\gamma_k} + \frac{1}{2}\omega^2_{\Gamma_k} Q^2_{\Gamma_k\gamma_k} \right\} \hat{C}_{A_1} + \hat{H}^{\text{JT}} \\ &\equiv \mathcal{H}^0_{\text{asym}} \hat{C}_{A_1} + \hat{H}^{\text{JT}}. \end{aligned} \tag{2.83}$$

As these two operators commute and pertain to different sets of coordinates, the general solution can be written as a product:

$$\Psi^{\text{vibr}} = \chi_{a_1}(\mathbf{Q}_{a_1}) \Psi^{\text{vibr}}_{\text{asym}}(\mathbf{r}, \mathbf{Q}_{\text{asym}}), \tag{2.84}$$

where $\chi_{a_1} = \prod_{k \in A_1} \chi_k$ is the nuclear harmonic wavefunction of $\mathcal{H}^0_{a_1}$. The second term:

$$\Psi^{\text{vibr}}_{\text{asym}}(\mathbf{r}, \mathbf{Q}_{\text{asym}}) = \sum_{\gamma_i} \chi_{\gamma_i}(\mathbf{Q}_{\text{asym}}) \left| \Gamma\gamma_i \right\rangle, \tag{2.85}$$

is the solution of symmetry-breaking part $\hat{H}^{\text{vibr}}_{\text{asym}}$. Equations (2.84) and (2.85) describe the general wavefunction of the Jahn–Teller system. If electronic states are non-degenerate, then by symmetry considerations, $\hat{H}^{\text{JT}} = 0$, and Eq. (2.84) reduces to the adiabatic form:

$$\Psi^{\text{adiabatic}} = \chi_{a_1}(\mathbf{Q}_{a_1}) \chi_{\text{asym}}(\mathbf{Q}_{\text{asym}}) \left| \psi_i \right\rangle,$$

where χ_{asym} is the harmonic wavefunction of Hamiltonian $\mathcal{H}^0_{\text{asym}}$. The symmetry-breaking displacements $\mathbf{Q}_{\text{asym}}$ are termed Jahn–Teller active modes (or coordinates). The whole non-adiabaticity is described by Eq. (2.83), and the JT problem reduces explicitly to the eigenvalue problem of $\hat{H}^{\text{vibr}}_{\text{asym}}$. In contrast, a_1 contribution is obtained using standard methods of the adiabatic treatment (see Section 2.4.1).

2.5.2 Solution

In the section above, we presented the formal problem of the Jahn–Teller active system. This part will focus on the practical solution of Eq. (2.83), which explicitly depends on JT active coordinates. To simplify the notation, we will omit script labels and denote the non-adiabatic part of Hamiltonian by $\hat{H} \equiv \hat{H}^{\text{vibr}}_{\text{asym}}$:

$$\hat{H} = \hat{H}^0 + \hat{H}^{\text{JT}} = \mathcal{H}_{\text{ph}} \hat{C}_{A_1} + \hat{H}^{\text{JT}}.$$

Note that this $\hat{H}$ contains all the symmetry-breaking displacements and has no contributions of A_1 coordinates. The zero-order solution (for $\hat{H}^{\mathrm{JT}} = 0$) has an adiabatic form:

$$\Phi^0_{i,n} = \chi_{\mathbf{n}}(\mathbf{Q})\,|\Gamma\gamma_i\rangle\,, \tag{2.86}$$

where $\chi_n(\mathbf{Q})$ are eigenstates of $\mathcal{H}_{\mathrm{ph}}$, and $|\Gamma\gamma_i\rangle$ is one of the degenerate states. In the harmonic approximation, we label phonon states by *Fock-space* vectors $\chi_{\mathbf{n}}(\mathbf{Q}) \Leftrightarrow |n_{\Gamma_1\gamma_1}, \ldots, n_{\Gamma_N\gamma_N}\rangle$. Each state has vibrational energy calculated using standard equation $E^0_v = \sum_{\Gamma_k\gamma_k}(\frac{1}{2} + n_{\Gamma_k\gamma_k})\omega_{\Gamma_k\gamma_k}$. The ground state $|0, 0, \ldots, 0\rangle$ corresponds to a configuration where all harmonic oscillators are in their lowest energy configuration. Using the formalism of the second-quantization, we can define raising and lowering operators by:

$$a^\dagger_{\Gamma_k\gamma_k}\,|\cdots n_{\Gamma_k\gamma_k}\cdots\rangle = \sqrt{n_{\Gamma_k\gamma_k}+1}\,|\cdots n_{\Gamma_k\gamma_k} i + 1\cdots\rangle\,, \tag{2.87}$$

$$a_{\Gamma_k\gamma_k}\,|\cdots n_{\Gamma_k\gamma_k}\cdots\rangle = \sqrt{n_{\Gamma_k\gamma_k}}\,|\cdots n_{\Gamma_k\gamma_k} - 1\cdots\rangle\,, \tag{2.88}$$

where "$\cdots$" represents the same configuration. The phonon number operator is given by:

$$\begin{aligned}\hat{n}_{\Gamma_k\gamma_k}\,|\cdots n_{\Gamma_k\gamma_k}\cdots\rangle &= a^\dagger_{\Gamma_k\gamma_k}a_{\Gamma_k\gamma_k}\,|\cdots n_{\Gamma_k\gamma_k}\cdots\rangle \\ &= n_{\Gamma_k\gamma_k}\,|\cdots n_{\Gamma_k\gamma_k}\cdots\rangle\,.\end{aligned}$$

We can express normal coordinates $Q_{\Gamma_k\gamma_k}$ and their conjugate momentum $\hat{P}_{\Gamma_k\gamma_k}$ in terms of $a^\dagger_{\Gamma_k\gamma_k}$ and $a_{\Gamma_k\gamma_k}$ using standard relations [114]:

$$\begin{aligned}Q_{\Gamma_k\gamma_k} &= \sqrt{\frac{1}{2\omega_{\Gamma_k\gamma_k}}}(a^\dagger_{\Gamma_k\gamma_k} + a_{\Gamma_k\gamma_k}),\\ P_{\Gamma_k\gamma_k} &= \sqrt{\frac{\omega_{\Gamma_k\gamma_k}}{2}}(a^\dagger_{\Gamma_k\gamma_k} - a_{\Gamma_k\gamma_k}).\end{aligned}$$

Finally, in the basis of zero-order wavefunctions (2.81), we can write the matrix element of $\hat{H}^0$ for Jahn–Teller active coordinates as:

$$\begin{aligned}&\left\langle n_{\Gamma_1\gamma_1}\cdots n_{\Gamma_N\gamma_N};\Gamma\gamma_i\middle|\hat{H}^0\middle|n'_{\Gamma_1\gamma_1}\cdots n'_{\Gamma_N\gamma_N};\Gamma\gamma_j\right\rangle \\ &\quad= \delta_{ij}\delta_{\mathbf{nn}'}\sum_{\Gamma_k\gamma_k}\left(\frac{1}{2} + n_{\Gamma_k\gamma_k}\right)\omega_{\Gamma_k}.\end{aligned} \tag{2.89}$$

Here, boldface $\mathbf{n} = \{n_{\Gamma_1\gamma_1}, \cdots, n_{\Gamma_1\gamma_1}\}$ denotes the all-phonon configuration, and $\delta_{\mathbf{nn}'}$ is zero if at least one $n_{\Gamma_k\gamma_k}$ differs for configurations $\mathbf{n}$ and $\mathbf{n}'$.

Similarly, the matrix element of Jahn–Teller perturbation $\hat{H}^{\mathrm{JT}}$ can be evaluated to be:

$$\begin{aligned}
&\left\langle n_{\Gamma_1\gamma_1}\cdots n_{\Gamma_N\gamma_N};\Gamma\gamma_i\middle|\hat{H}^{\mathrm{JT}}\middle|n'_{\Gamma_1\gamma_1}\cdots n'_{\Gamma_N\gamma_N};\Gamma\gamma_j\right\rangle \\
&\quad=\sum_{\Gamma_k}V_{\Gamma_k}\|\hat{C}_{\Gamma_k}\|_{ij}\sqrt{\frac{\omega_{\Gamma_k}}{2}} \\
&\qquad\times\sum_{\gamma_k}\left\langle\cdots n_{\Gamma_k\gamma_k}\cdots\middle|a^\dagger_{\Gamma_k\gamma_k}+a_{\Gamma_k\gamma_k}\middle|\cdots n'_{\Gamma_k\gamma_k}\cdots\right\rangle. \qquad (2.90)
\end{aligned}$$

Using Eqs. (2.87) and (2.88), we can rewrite the matrix element of phonon states as:

$$\begin{aligned}
&\left\langle\cdots,n_{\Gamma_k\gamma_k},\cdots\middle|a^\dagger_{\Gamma_k\gamma_k}+a_{\Gamma_k\gamma_k}\middle|\cdots,n'_{\Gamma_k\gamma_k},\cdots\right\rangle \\
&\quad=\left[\prod_{\Gamma_i\gamma_i\neq\Gamma_k\gamma_k}\delta_{(n_{\Gamma_i\gamma_i},n'_{\Gamma_i\gamma_i})}\right] \\
&\quad\times\left(\sqrt{n_{\Gamma_k\gamma_k}+1}\delta_{(n'_{\Gamma_k\gamma_k},n_{\Gamma_k\gamma_k}+1)}+\sqrt{n_{\Gamma_k\gamma_k}-1}\delta_{(n'_{\Gamma_k\gamma_k},n_{\Gamma_k\gamma_k}-1)}\right). \qquad (2.91)
\end{aligned}$$

Eqs. (2.90) and (2.91) reveal some useful properties of linear vibronic coupling. The mode of symmetry $\Gamma_k\gamma_k$ directly couples two adiabatic wavefunctions if $\|\hat{C}_{\Gamma_k}\|_{ij}\neq 0$ and corresponding phonon states only differ by a single phonon excitation:

$$|\cdots n_{\Gamma_k\gamma_k}\cdots;\Gamma\gamma_i\rangle\overset{V_{\Gamma_k}}{\Longleftrightarrow}|\cdots n_{\Gamma_k\gamma_k}\pm 1\cdots;\Gamma\gamma_i\rangle\,.$$

The coupling strength is of order V_{Γ_k}. Only such states are intermixed in the first order of perturbation theory. Higher-order terms enter as $(V_\Gamma)^{\Delta n}$ corrections, where $\Delta n=\sum_i(n_i-n'_i)$ is the difference in phonon number. Therefore, for a weak coupling ($\hat{V}_\Gamma\ll 1$), we can truncate the basis up to some number of phonon excitations Δn. This makes the problem in principle amenable but still very difficult from a computational perspective, as the basis size is of order $2^{N\Delta n}$. For example, in the system of $N=10$ modes, truncation up to $\Delta n=3$ would yield Hamiltonian matrices of size greater than $10^6\times 10^6$. In the case of a defect, the number of symmetry breaking modes N is huge, and the direct diagonalization is practically impossible due to limited computational resources.

Luckily, in the system studied in this thesis (diamond NV center), the JT problem has some additional symmetries, which can be utilized to reduce the computational cost. Therefore, in the next section, we present our formulation of the JT problem for the diamond NV center.

	e	C_{3z}^{-1}	C_{3z}	σ_1	σ_2	σ_3
A_1	1	1	1	1	1	1
A_2	1	1	1	-1	-1	-1
E	$\begin{pmatrix} 1 & 0 \\ 0 & 1 \end{pmatrix}$	$\begin{pmatrix} -\frac{1}{2} & -\frac{\sqrt{3}}{2} \\ \frac{\sqrt{3}}{2} & -\frac{1}{2} \end{pmatrix}$	$\begin{pmatrix} -\frac{1}{2} & \frac{\sqrt{3}}{2} \\ -\frac{\sqrt{3}}{2} & -\frac{1}{2} \end{pmatrix}$	$\begin{pmatrix} \frac{1}{2} & -\frac{\sqrt{3}}{2} \\ -\frac{\sqrt{3}}{2} & -\frac{1}{2} \end{pmatrix}$	$\begin{pmatrix} \frac{1}{2} & \frac{\sqrt{3}}{2} \\ \frac{\sqrt{3}}{2} & -\frac{1}{2} \end{pmatrix}$	$\begin{pmatrix} -1 & 0 \\ 0 & 1 \end{pmatrix}$

Table 2.1: The irreducible matrix representations of the C_{3v} point group. E matrices are represented in the Cartesian (E_x, E_y) form.

2.5.3 Jahn-Teller effect in the NV$^-$ center

This section analyzes the dynamical JT effect in the electronically excited state ^3E of the diamond NV$^-$ center [see Fig. 1.1(b)]. Here, we present our original analysis of the vibronic coupling and derive practical expressions later used in Chapters 4 and 5.

Symmetry

A short introduction to the diamond NV$^-$ center was given in Section 1.1. The point-group symmetry of the defect is C_{3v} with a threefold rotational axis going through the nitrogen and the vacancy [see Fig. 1.1(a)]. This group has six symmetry elements which fall into three different classes. The first class contains the identity element e, the second class has two C_3 rotations, and the last class contains three vertical reflections σ_i through plains containing the rotational axis. C_{3v} point-group possesses three irreducible representations shown in Table 2.1. Objects of A_1 symmetry are invariant under all symmetry transformations. A_2 symmetry objects transform as pseudo-vectors and correspond to rotational motion around the z-axis in the case of vibrations. E symmetry objects come in pairs and represent doubly-degenerate electronic or vibrational states. For two-dimensional E representation, the choice of representation matrices is not unique. Table 2.1 shows the Cartesian (E_x, E_y) form, which is the conventional selection in many articles and textbooks.[22] However, any other set of matrices T', related by unitary transformation $T' = UTU^{-1}$, is an equivalently good choice.

From Table 2.1, it follows that the degenerate electronic state can only be of E symmetry, as it is the only two-dimensional representation. Accordingly, we label the degenerate subset of electronic states by $\{|E_x\rangle, |E_y\rangle\}$. Jahn–Teller active coordinates (modes) transform as A_2 and E irreducible representations,

[22] This representation reflects how the basis vectors $\hat{e}_x$, $\hat{e}_y$ transform under symmetry operations around rotational axis $\hat{e}_z$.

and the motion along these coordinates mix electronic states $|E_x\rangle \leftrightarrow |E_y\rangle$. We split the JT interaction term (2.82) into two contributions:

$$\hat{H}^{\text{JT}} = \hat{H}^{\text{JT}}_{a_2} + \hat{H}^{\text{JT}}_{e},$$

where parts pertaining to different symmetry coordinates are

$$\hat{H}^{\text{JT}}_{a_2} = \sum_k \hat{C}_{A_2} V_{k;a_2} Q_{k;a_2}, \quad \hat{H}^{\text{JT}}_{e} = \sum_{k,\gamma\in\{x,y\}} \hat{C}_{E_\gamma} V_{k;e} Q_{k;e_\gamma}. \tag{2.92}$$

Here, $\hat{C}_{\Gamma_k}$ are Clebsch–Gordan coefficient matrices for the pair of E electronic states, $\|\hat{C}_{\Gamma_k}\|_{ij} = \langle E_i\, \Gamma_k \gamma_k | E_j\rangle$. In the (E_x, E_y) representation, they are given by [115]:

$$\hat{C}_{A_2} = \begin{pmatrix} 0 & 1 \\ -1 & 0 \end{pmatrix}, \quad \hat{C}_{E_x} = \frac{1}{\sqrt{2}} \begin{pmatrix} 0 & 1 \\ 1 & 0 \end{pmatrix}, \quad \hat{C}_{E_y} = \frac{1}{\sqrt{2}} \begin{pmatrix} 1 & 0 \\ 0 & -1 \end{pmatrix}.$$

Operators (2.92) do not mutually commute, and simple separation of a_2 and e degrees of freedom is impossible. Luckily, for the NV center, vibronic contributions of a_2 symmetry are negligible [116].[23] Therefore, in the following analysis, we omit a_2 symmetry vibronic coupling.

Without a_2 interactions, the Jahn–Teller problem of NV^- center reduces to the $E \otimes (e \oplus e \oplus \cdots)$ problem. This notation means that the degenerate electronic E doublet couples with a large set of e-symmetry modes. In the rest of the analysis, we will omit normal coordinate indices "e" for irreducible representation and write the vibronic problem as:

$$\begin{aligned} \hat{H}^0 &= \hat{C}_{A_1} \sum_{k;\gamma\in x,y} \left(-\frac{1}{2}\frac{\partial^2}{\partial Q^2_{k\gamma}} + \frac{1}{2}\omega_k^2 Q^2_{k\gamma} \right), \\ \hat{H}^{\text{JT}} &= \sum_{k;\gamma\in x,y} \hat{C}_{E_\gamma} V_k Q_{k\gamma}. \end{aligned} \tag{2.93}$$

In Section 2.5.2, we showed that the vibronic problem could be solved by diagonalizing $\hat{H}^{\text{vibr}} = \hat{H}^0 + \hat{H}^{\text{JT}}$ in the basis of eigenvectors of $\hat{H}^0$. The obvious choice is wavefunctions of the type $|n_{1x} n_{1y} \cdots n_{Nx} n_{Ny}; E_i\rangle$. However, we also noted that this choice leads to huge matrices and is not convenient for the computational approach, even for a small number of excitations. For $E \otimes (e \oplus e \oplus \cdots)$ problems, a more suitable choice of the basis could be made by additional symmetry considerations.

[23] In fact, our *ab initio* calculations show that they are zero.

Chiral basis and pseudo-spin

The idea for simplifications stems from the original work of Longuet-Higgins *et al.* [117], where the dynamical $(E \otimes e)$ Jahn–Teller system is analyzed in terms of a complex basis.[24]. The extension to the multi-mode problem can be formulated as follows. The $E \otimes (e \oplus e \oplus \cdots)$ vibronic Hamiltonian has an additional symmetry which can be seen by considering the operator $\hat{J} = \hat{J}_{\text{el}} + \hat{J}_{\text{ph}}$, where [118]:

$$\hat{J}_{\text{el}} = \frac{1}{2}\hat{\sigma}_y, \quad \hat{J}_{\text{ph}} = \hat{C}_{A_1} \sum_k \hat{L}_{z,k}. \tag{2.94}$$

Here, $\hat{J}_{\text{el}}$ operates on the orbital part of the wavefunction, and $\hat{\sigma}_y$ is the Pauli matrix. $\hat{J}_{\text{ph}}$ is the sum of phonon angular momentum operators:

$$\hat{L}_{z,k} = i\left(Q_{kx}\frac{\partial}{\partial Q_{ky}} - Q_{ky}\frac{\partial}{\partial Q_{kx}}\right),$$

which act on a two-dimensional space of degenerate normal modes $\{Q_{kx}, Q_{ky}\}$. It is easy to check that $\hat{J}_{\text{el}}$ and $\hat{J}_{\text{ph}}$ commute with the zero-order Hamiltonian $\hat{H}^0$.[25] Therefore, zero-order wavefunctions can be chosen to be simultaneous eigenstates of $\hat{J}_{\text{el}}$ and $\hat{J}_{\text{ph}}$ separately. The eigenstates of the electronic operator $\hat{J}_{\text{el}}$ are:

$$|E_\pm\rangle = \frac{1}{\sqrt{2}}\left(|E_x\rangle \pm i\,|E_y\rangle\right), \tag{2.95}$$

with corresponding eigenvalues $j_{\text{el}} = \pm\frac{1}{2}$. These eigenvalues are usually called the electronic "*pseudo-spin*". To find common eigenstates of $\hat{H}^0$ and $\hat{J}_{\text{ph}}$, we perform a canonical coordinate transformation to the basis of "*chiral*" (or "circular") phonons. Chiral phonons are described by second-quantization operators [114]:

$$a_{k,+} = \frac{1}{\sqrt{2}}\left(a_{kx} - ia_{ky}\right), \quad a_{k,-} = \frac{1}{\sqrt{2}}\left(a_{kx} + ia_{ky}\right),$$

where a_{kx} and a_{ky} belong to normal modes $Q_{k,x}$ and Q_{ky}. Defining the number of right- and left-hand phonons as $\hat{n}_{k\pm} = a^\dagger_{k,\pm}a_{k,\pm}$, we can rewrite the phonon angular momentum operator as:

$$\hat{J}_{\text{ph}} = \hat{C}_{A_1} \sum_k \left(\hat{n}_{k+} - \hat{n}_{k-}\right). \tag{2.96}$$

[24] By "dynamical", it is meant that the problem considers non-trivial dynamics of nuclei which is intimately correlated with the electronic motion.

[25] $[\hat{J}_{\text{el}}, \hat{H}^0] = 0$ because $\hat{C}_{A_1}$ is the identity matrix, and $[\hat{J}_{\text{ph}}, \hat{H}^0] = 0$ because $\mathcal{H}_{\text{ph}}$ in $\hat{H}^0 = \hat{C}_{A_1}\mathcal{H}_{\text{ph}}$ has rotational SO(2) symmetry for every pair of normal modes $\{Q_{kx}, Q_{ky}\}$.

In this new basis, $\hat{H}_0$ takes the form:

$$\hat{H}^0 = \hat{C}_{A_1} \sum_k \omega_k \left(1 + \hat{n}_{k+} + \hat{n}_{k-}\right). \tag{2.97}$$

By comparing equations (2.96) and (2.97), we see that two quantum numbers can describe mutual eigenfunctions of both operators for each pair of degenerate phonons k:

$$n_k \equiv n_{k+} + n_{k-},$$
$$l_k \equiv n_{k+} - n_{k-}.$$

Here, n_k corresponds to the total number of k-phonons, while l_k is the eigenvalue of operator $\hat{L}_{z,k} = (\hat{n}_{k+} - \hat{n}_{k-})$. Therefore, the common eigenstates of $\hat{H}_0$, $\hat{J}_{\text{el}}$, and $\hat{J}_{\text{ph}}$ can be labeled as $|n_1 l_1 \cdots n_N l_N; E_\pm\rangle$. Finally, we rewrite the JT interaction part in terms of creation and annihilation operators of chiral phonons:

$$\hat{H}^{\text{JT}} = \sum_k K_k \omega_k \begin{pmatrix} 0 & a_{k+} + a_{k-}^\dagger \\ a_{k-} + a_{k+}^\dagger & 0. \end{pmatrix}, \tag{2.98}$$

where, following the notation of O'Brien [119], we define the *dimensionless vibronic constants*:

$$K_k = \frac{V_k}{\sqrt{2\omega_k^3}}. \tag{2.99}$$

Note that Hamiltonian (2.98) is explicitly written in terms of $|E_\pm\rangle$ electronic states.

We can check that $\hat{J} = \hat{J}_{\text{el}} + \hat{J}_{\text{ph}}$ commutes with $\hat{H}^{\text{JT}}$ and thus with the total vibronic Hamiltonian.[26] This implies that vibronic states can be classified by quantum numbers of $\hat{J}$. For eigenstates of $\hat{H}^0$, these numbers are calculated as:

$$j = j_{\text{el}} + \sum_k l_k.$$

Finally, using standard relations for creation and annihilation operators and some algebra, we derive the expression for matrix elements of $\hat{H}^{\text{JT}}$:

$$\begin{aligned} &\left\langle n_1' l_1', \ldots, n_N' l_N'; E_- \middle| \hat{H}^{\text{JT}} \middle| n_1 l_1, \ldots, n_N l_N; E_+ \right\rangle \\ &= \sqrt{2} \sum_k K_k \omega_k \delta_{l_k' l_k + 1} \left[\prod_{j \neq k} \delta_{n_j' n_j} \delta_{l_j' l_j} \right] \\ &\quad \times \left[\sqrt{\tfrac{n_k - l_k}{2}} \delta_{n_k' n_k - 1} + \sqrt{\tfrac{n_k + l_k + 2}{2}} \delta_{n_k' n_k + 1} \right]. \end{aligned} \tag{2.100}$$

[26] Note that separately $\hat{J}_{\text{el}}$ and $\hat{J}_{\text{ph}}$ do not commute with $\hat{H}^{\text{JT}}$.

Such a choice of the basis allows decoupling the problem for different $\hat{J}$ values since matrix elements (2.100) only couple states described by the same quantum number j. Therefore, we can solve the Jahn–Teller problem of diagonalizing $\hat{H}_0 + \hat{H}^{\mathrm{JT}}$ for each value of j separately. This simplification is very useful for numerical analysis of vibronic states, as it reduces computational complexity.

However, for solid-state systems, we still have a large number of vibrational modes, and the diagonalization of $\hat{H}^0 + \hat{H}^{\mathrm{JT}}$ is still a difficult problem. Section 4.3.3 will present our methodology, where a continuum of modes is reduced to a finite set of effective modes. Such simplification makes multi-mode problems in principle tractable.

Perturbative treatment

Equation (2.100) makes the perturbative analysis tractable. In Appendix C, we provide a general solution up to the second-order correction. In the first order of degenerate perturbation theory, energy correction to $\hat{H}^0$ is zero, and the vibronic ground state is given by:

$$\Psi_{0,\pm} = \frac{1}{\sqrt{1+\sum_k K_k}} \left(|\mathbf{00}; E_\pm\rangle - \sqrt{2} \sum_k K_k \, |\mathbf{00}, n_k{=}1, l_k{=}{\pm}1, \mathbf{00}; E_\mp\rangle \right).$$

Second-order perturbation yields energy expression:

$$E^{(2)}_{\mathbf{nl},\pm} = \sum_k \left[\omega_k (n_k + 1) - 2K_k^2 \omega_k (1 \pm l_k) \right]. \tag{2.101}$$

For each value of n_k, phonon angular momentum l_k can take $(n_k + 1)$ values in the range $-n_k, -n_k + 2, \ldots, n_k$. Thus, zero-order adiabatic solutions have degeneracy of order $\mathcal{D}^0 = 2\prod_k (n_k + 1)$ (factor 2 comes from electronic degeneracy). From Eq. (2.101), we see that linear vibronic interaction lifts phonon degeneracy in the second-order of perturbation theory, and each level becomes twofold degenerate for each $j_{\mathrm{el}} = \pm 1$ value. The ground state wavefunction up to second-order correction is:

$$\begin{aligned} \Psi_{0,\pm} = \mathcal{A} \Bigg(& |\mathbf{00}; E_\pm\rangle - \sqrt{2} \sum_k K_k \, |\mathbf{00}, n_k{=}1, l_k{=}{\pm}1, \mathbf{00}; E_\mp\rangle \\ & + \sqrt{2} \sum_k K_k^2 \, |\mathbf{00}, n_k{=}2, l_k{=}0, \mathbf{00}; E_\pm\rangle \\ & + \sqrt{8} \sum_k \sum_{q \neq k} K_k K_q \, |\mathbf{00}, n_k{=}1, l_k{=}1, \mathbf{00}, n_q{=}1, l_q{=}{-}1, \mathbf{00}; E_\pm\rangle \Bigg), \end{aligned} \tag{2.102}$$

where $\mathcal{A} = \left(1 + 2\sum_k K_k^2 + 2\sum_k K_k^4 + 8\sum_k \sum_{q \neq k} K_k^2 K_q^2\right)^{-1/2}$ is the normalization factor.

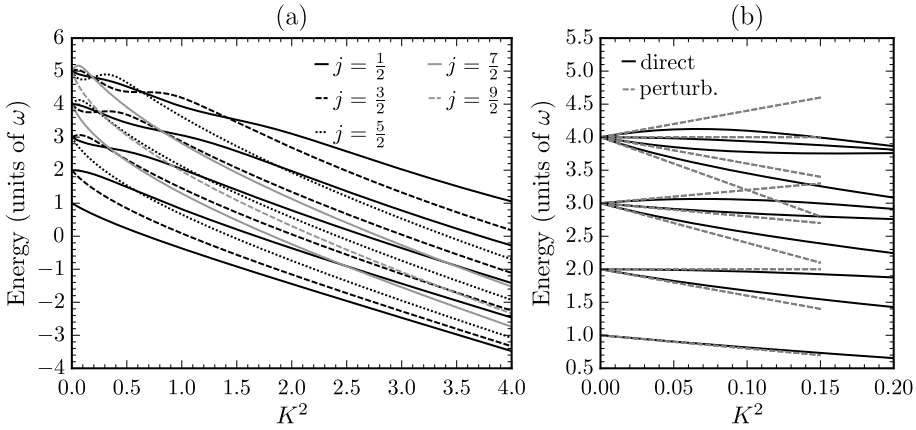

Figure 2.4: The behavior of the vibronic states for $E \otimes e$ coupling. (a) Energy levels in the range $K^2 = 0$–4. (b) Energy levels in the range $K^2 = 0$–0.2 (dashed lines represent perturbative solution). Values for $K^2 = 0$ correspond to the uncoupled states of energy $E = \omega(n + 1)$.

2.5.4 Jahn–Teller effect for $(E \otimes e)$ coupling

In the above sections, we presented the formal development for the analysis of the Jahn–Teller systems. Here we will illustrate the effect of vibronic coupling in the presence of a single degenerate mode. The model of single-mode provides a quantitative understanding of vibronic coupling. Moreover, for strong coupling, the multi-mode problem can be approximately reduced to a single effective mode [112].

Figure 2.4(a) shows the energies for the lowest vibronic states ($n \leqslant 4$) as K^2 value changes from 0 to 4.[27] $K^2 = 0$ corresponds to the uncoupled case, and energies of vibronic states are those of the two-dimensional harmonic oscillator [$\omega(n + 1)$]. The ground state is doubly degenerate for all K values and is always lowered in the presence of vibronic coupling. The first excited state is a fourfold degenerate for $K = 0$ and splits into two doubly degenerate branches for finite values of K. In Figure 2.4(b), we compare energies of the second-order perturbation theory:

$$E_{n,\pm} = \omega(n + 1) - 2K^2(1 \pm l),$$

with the results of the direct diagonalization. The perturbative equation works well for weak coupling strengths ($K^2 \ll 0.05$). However, it is inadequate for larger strengths. Later we will show that the coupling strength is $K^2 \approx 0.5$ for the diamond NV center, and the perturbative treatment does not work.

[27] Diagonalization of vibronic Hamiltonian was performed using a basis limited to a maximal number of excitations $n_{\max} = 15$.

2.6 Spectral properties

In this part, we present the semi-classical theory of optical absorption and emission in semiconductor materials. In Section 2.6.1, we begin by deriving standard equations for transition rates and cross-sections. The main parameters of this theory are position (or momentum) matrix elements calculated between molecular wavefunctions. In Section 2.6.2, we first consider the evaluation of matrix elements for non-degenerate adiabatic states. We show that in this case, the problem decouples into the calculation of overlap integrals between vibrational states and the calculation of electronic matrix elements. At the end of Section 2.6.2, we present the *equal mode approximation*, which significantly simplifies the evaluation of vibrational overlaps and leads to a standard *Huang–Rhys theory* of electron–phonon interaction. Section 2.6.3 presents our original work where we consider $A_2 \leftrightarrow E$ triplet transitions of the diamond NV center. We derive an expression for a matrix element when one of the states is a degenerate $E \otimes (e \oplus e \cdots)$ Jahn-Teller system. Finally, in Section 2.6.4, we derive spectral equations for optical transitions, which are later used in Chapters 4 and 5.

2.6.1 Interaction with light

The rigorous description of light–matter interaction requires theory where the electromagnetic field is treated on the same footing as the quantum system. However, the majority of experiments can be successfully described by a semi-classical picture.[28] In this picture, the light is treated as a classical wave and the system of interest as a quantum object. Here we adopt this formulation.

In the presence of the classical electromagnetic field, the Hamiltonian of the whole system can be split into two parts:

$$\hat{H} = \hat{H}_0 + \hat{H}_{\mathrm{I}},$$

where $\hat{H}_0$ is the Hamiltonian of the molecular system [see Eq. (2.2)], and $\hat{H}_{\mathrm{I}}$ is the interaction term due to the presence of the electromagnetic field. Depending on the gauge fixing formulation, $\hat{H}_{\mathrm{I}}$ can be written in terms of position or momentum operators. In the position formulation, the interaction term is [82]:

$$\hat{H}_{\mathrm{I}} = -\sum_a q_a \mathbf{r}_a \mathbf{E}(\mathbf{r}_a), \tag{2.103}$$

where $\mathbf{E}$ is an electric field, the sum runs over all charged particles a (electrons and nuclei), $\mathbf{r}_a$ is a three-dimensional position vector, and q_a is the particle's

[28] Actually, there is only a handful of experiments where a more sophisticated description is required.

charge. Alternatively, in the momentum formulation, the interaction term can be written as [120]:

$$\hat{H}_{\mathrm{I}} = -\sum_a \frac{q_a}{m_a}\mathbf{A}(\mathbf{r}_a)\mathbf{p}_a,$$

where $\mathbf{A}$ is a vector potential, m_a is the mass of the particle, and $\mathbf{p}_a$ is the momentum operator.

In the semi-classical description, we treat the electromagnetic field as a monochromatic wave of the form:

$$\begin{aligned}\mathbf{A} &= A_0\boldsymbol{\eta}\cos\left(\mathbf{kr}-\omega t\right)\\ &= \frac{1}{2}A_0\boldsymbol{\eta}\left(e^{i(\mathbf{kr}-\omega t)}+e^{-i(\mathbf{kr}-\omega t)}\right)\equiv\mathbf{A}^{+}+\mathbf{A}^{-},\end{aligned} \tag{2.104}$$

where $\boldsymbol{\eta}$ is a unit vector parallel to $\mathbf{A}$, and A_0 is the amplitude. The usual analysis of the time-dependent perturbation theory [121] shows that the first term $\mathbf{A}^{+}$ is responsible only for absorption. On the other hand, the second term $\mathbf{A}^{-}$ induces only stimulated emission.

In the following analysis, we will focus on the position formulation of Eq. (2.103). First, we note that an electric field can be expressed in terms of the vector potential:

$$\mathbf{E}^{\pm} = -\frac{\partial\mathbf{A}^{\pm}}{\partial t} = \pm i\omega\mathbf{A}^{\pm}. \tag{2.105}$$

Combining Eqs. (2.103), (2.104), and (2.105), we write the interaction term as:

$$\hat{H}_{\mathrm{I}}^{\pm} = \pm i\frac{A_0\omega}{2}\sum_a q_a e^{\pm i\mathbf{kr}_a}\boldsymbol{\eta}\mathbf{r}_a e^{\mp i\omega t}.$$

Here, the top sign of "$\pm$" (or "$\mp$") should be taken for the absorption process and the bottom sign for the emission. In the first order of time-dependent perturbation theory, transition rate (average number of events per unit time) for the harmonic perturbation is calculated using Fermi's golden rule [121]:

$$W^{\pm}(\omega) = 2\pi\sum_{m,n} w_m(T)\left|\left\langle\Psi_{f;n}\middle|\hat{H}_{\mathrm{I}}^{\pm}e^{\pm i\omega t}\middle|\Psi_{g;m}\right\rangle\right|^2\delta(E_{e;n}-E_{g;m}\mp\omega), \tag{2.106}$$

where $|\Psi_{g;m}\rangle$ and $|\Psi_{e;n}\rangle$ describe states in the ground (subscript g) and excited (subscript e) electronic manifolds. Quantum numbers n and m label vibrational (or vibronic) excitations, and $\omega_n(T)$ are statistical weights for vibrational/vibronic levels of the initial electronic state. In this thesis, *we always assume a low-temperature limit* and calculate transition rates for $T = 0$ K. In this

limit, statistical weights are non-zero only for the lowest vibrational/vibronic states $w_m(0) = \delta_{m0}$. Therefore, the transition rates for absorption and stimulated emission are:

$$W_{\rm abs}(\omega) = -\frac{\pi A_0^2 \omega^2}{2} \sum_n \left| \boldsymbol{\eta} \cdot \left\langle \Psi_{e;n} \right| \sum_a q_a^2 e^{\pm i\mathbf{k}\mathbf{r}_a} \mathbf{r}_a \left| \Psi_{g;0} \right\rangle \right|^2 \times \delta(E_{e;n} - E_{g;0} - \omega), \tag{2.107}$$

$$W_{\rm st}(\omega) = -\frac{\pi A_0^2 \omega^2}{2} \sum_m \left| \boldsymbol{\eta} \cdot \left\langle \Psi_{e;0} \right| \sum_a q_a^2 e^{\pm i\mathbf{k}\mathbf{r}_a} \mathbf{r}_a \left| \Psi_{g;m} \right\rangle \right|^2 \times \delta(E_{e;0} - E_{g;m} + \omega). \tag{2.108}$$

If electronic states are non-degenerate, wavefunctions are written in the crude adiabatic form of Eq. (2.12). On the other hand, in the presence of electronic degeneracy, the vibronic form of Eq. (2.62) should be used instead. In both forms, electronic wavefunctions $\psi_i(\mathbf{r}, \mathbf{R}_0)$ are independent of nuclear motion, and matrix elements of the nuclear position operator are equal to zero:

$$\left\langle \chi_{e;n}(\mathbf{R}); \psi_e(\mathbf{r}) \right| e^{\pm i\mathbf{k}\mathbf{R}_a} \mathbf{R}_a \left| \chi_{g;m}(\mathbf{R}); \psi_g(\mathbf{r}) \right\rangle \sim \langle \psi_g | \psi_e \rangle = 0.$$

Therefore, the summation over a in Eqs. (2.107) and (2.108) should be carried only over the electronic indices (and $q_a = e = 1$ in the Hartree atomic units).

For the defect system, the wavelength of the electromagnetic field is much larger than the spread of localized charges. This property allows adopting dipole approximation, where $e^{\pm i\mathbf{k}\mathbf{r}_a} \to 1$ in the long-wavelength regime. After this approximation, the matrix element simplifies to *transition dipole moment*:

$$\langle \Psi_{e;n} | \mathbf{r} | \Psi_{g;m} \rangle \equiv \left\langle \Psi_{e;n} \right| \sum_a \mathbf{r}_a \left| \Psi_{g;m} \right\rangle,$$

where $\mathbf{r} \equiv \sum_a \mathbf{r}_a$ denotes the *dipole operator of the electronic system*.

Another simplification is achieved if one considers an ensemble of randomly oriented defects. For a statistical ensemble, instead of calculating $|\boldsymbol{\eta} \cdot \langle \Psi_{e;n} | \mathbf{r} | \Psi_{g;m} \rangle|^2$, one calculates the statistical average over all possible orientations of the interacting system. Let us rewrite the transition dipole moment in the form:

$$\langle \Psi_{e;n} | \mathbf{r} | \Psi_{g;m} \rangle \equiv r_{en;gm}\, \hat{\mathbf{r}},$$

where:

$$|r_{en;gm}|^2 = |\langle \Psi_{e;n} | \mathbf{r} | \Psi_{g;m} \rangle|^2 . \tag{2.109}$$

Here, $r_{en;gm}$ is a complex scalar that determines transition strength, and $\hat{\mathbf{r}}$ is a 3D unit vector parallel to the matrix element. Using this notation, we can

express averaging over all symmetrically equivalent configurations as:

$$\mathrm{Avg}\left(|\boldsymbol{\eta}\cdot\langle\Psi_{e;n}|\mathbf{r}|\Psi_{g;m}\rangle|^2\right)=\beta\,|r_{en;gm}|^2,$$

where averaging factor:

$$\beta=\mathrm{Avg}(|\boldsymbol{\eta}\cdot\hat{\mathbf{r}}|^2),$$

involves only unit vectors.[29]

For an isotropic material, every direction is equally probable and $\beta=1/3$.[30] As for the case of diamond NV center, the N–V complex can be formed along with one of four tetrahedral directions of diamond [see Fig. 1.1(a)]. In a statistical ensemble, each direction has an equal probability. Averaging over four possible directions yields the same value as for isotropic case $\beta=1/3$.

Taking into account all the considerations above, we can write optical transition rates as:

$$W_{\mathrm{abs}}(\omega)=-\beta\frac{\pi A_0^2\omega^2}{2}\sum_n|r_{en;g0}|^2\,\delta(E_{en}-E_{g0}-\omega),\tag{2.110}$$

$$W_{\mathrm{st}}(\omega)=-\beta\frac{\pi A_0^2\omega^2}{2}\sum_m|r_{e0;gm}|^2\,\delta(E_{e0}-E_{gm}+\omega).\tag{2.111}$$

Next, we want to rewrite A_0^2 in terms of experimentally controllable values. For a solid-state system, the amplitude A_0 can be written in terms of energy flux $I(\omega)$ [82]:

$$A_0^2=\frac{8\pi\alpha}{\omega^2 n}I(\omega).\tag{2.112}$$

Here, n is the refractive index of the material, and α is the fine structure constant. Substituting this value into Eqs. (2.110) and (2.111), we get:

$$W_{\mathrm{abs}}(\omega)=-\beta\frac{4\pi^2\alpha}{n}I(\omega)\sum_n|r_{en;g0}|^2\,\delta(E_{en}-E_{g0}-\omega),\tag{2.113}$$

$$W_{\mathrm{st}}(\omega)=-\beta\frac{4\pi^2\alpha}{n}I(\omega)\sum_m|r_{e0;gm}|^2\,\delta(E_{e0}-E_{gm}+\omega).\tag{2.114}$$

[29] Formally, $\mathrm{Avg}f(\mathbf{r})=(1/g)\sum_a f(G_a^{-1}\mathbf{r})$, where G_a is a symmetry transformation, and g is the number of transformations.

[30] This value is obtained by integrating over surface area Ω of unit sphere $\beta=\Omega^{-1}\int|\boldsymbol{\eta}\cdot\hat{\mathbf{r}}|^2\,\mathrm{d}S$.

Alternatively, in the momentum formulation, we can derive similar equations:

$$W_{\mathrm{abs}}(\omega) = -\beta \frac{4\pi^2 \alpha}{n\omega^2} I(\omega) \sum_n |p_{en;g0}|^2 \, \delta(E_{en} - E_{g0} - \omega), \tag{2.115}$$

$$W_{\mathrm{st}}(\omega) = -\beta \frac{4\pi^2 \alpha}{n\omega^2} I(\omega) \sum_m |p_{e0;gm}|^2 \, \delta(E_{e0} - E_{gm} + \omega), \tag{2.116}$$

where

$$|p_{en;gm}|^2 = \left| \left\langle \Psi_{e;n} \right| \sum_\alpha \mathbf{p}_\alpha \left| \Psi_{g;m} \right\rangle \right|^2, \tag{2.117}$$

is the momentum matrix element.

Cross-sections

The transition rate W describes the number of events per unit time for a single defect. It is not easy to measure this value directly. However, in the case of absorption, one can measure the attenuation of light as it passes through the material. The key parameter for this process is the *absorption cross-section* σ. The cross-section σ of a single absorbing unit relates the photon flux Φ and the transition rate W:

$$W(\omega) = \sigma(\omega)\Phi(\omega).$$

The photon flux is related to the energy flux by $\Phi(\omega) = I(\omega)/\omega$, and the equation for absorption cross-section becomes:

$$\sigma_{\mathrm{abs}}(\omega) = \beta \frac{4\pi^2 \alpha \omega}{n} \sum_n |r_{en;g0}|^2 \delta(E_{en} - E_{g0} - \omega). \tag{2.118}$$

The absorption cross-section is related to the Beer–Lambert law of attenuation:

$$I(z) = I(0)e^{-\alpha z},$$

where I is the energy flux of electromagnetic wave in distance z from the surface, and α is an absorption coefficient. If the density of absorbing units is ρ and the light passes in the direction z, then the change in the photon flux (and energy flux) is:

$$\frac{\mathrm{d}\Phi_\omega(z)}{\mathrm{d}z} = -\rho\sigma_{\mathrm{abs}}\Phi_\omega(z) \;\Rightarrow\; \frac{\mathrm{d}I_\omega(z)}{\mathrm{d}z} = -\rho\sigma_{\mathrm{abs}} I_\omega(z).$$

By integrating this equation, we obtain the Beer–Lambert law in terms of cross-section:

$$I_\omega(z) = I_\omega(0)e^{-\rho\sigma_{\mathrm{abs}} z},$$

which relates the absorption coefficient with the cross-section and the density of absorbing units:

$$\alpha = \rho\sigma_{\rm abs}.$$

The cross-section for stimulated emission is equivalent to Eq. (2.118):

$$\sigma_{\rm st}(\omega) = -\beta\frac{4\pi^2\alpha\omega}{n}\sum_m |r_{e0;gm}|^2\delta(E_{e0} - E_{gm} + \omega). \tag{2.119}$$

However, this time the intensity is increased as the light passes through the sample.

Spontaneous emission rate

Spontaneous emission results from the electromagnetic field vacuum fluctuations and cannot be explained using a semi-classical model. In principle, the rate equations should be derived using the theory of quantum electrodynamics. However, one can use the thermodynamic analysis of Einstein to obtain correct formulas by considering conditions of thermodynamic equilibrium [122]. In Einstein's theory, the rates of two-level transitions are written in terms of Einstein coefficients (B_{12}, B_{21}, A_{21}):

$$\begin{aligned} W^{\rm abs}_{1\to 2} &= B_{12}\rho(\omega), \\ W^{\rm st}_{2\to 1} &= B_{21}\rho(\omega), \\ W^{\rm sp}_{2\to 1} &= A_{21}. \end{aligned} \tag{2.120}$$

Here, $\rho(\omega)$ is the energy density, given by Plank's law of black body radiation:

$$\begin{aligned} \rho(\omega) &= F(\omega)\frac{1}{\exp(\omega/k_BT) - 1}, \\ F(\omega) &= \frac{\omega^3 n^3}{\pi^2 c^3}. \end{aligned}$$

The Einstein coefficients for absorption and stimulated emission are related by [122]:

$$B_{21}g_2 = B_{12}g_1, \tag{2.121}$$

where g_1 and g_2 are degeneracy factors, respectively, for the ground and the excited states. The rate of spontaneous emission is related to B coefficients by [122]:

$$W^{\rm sp}_{2\to 1} = A_{21} = \frac{g_1}{g_2}B_{12}F(\omega). \tag{2.122}$$

From Eq. (2.110) it follows, that the transition rate for two-level absorption is:

$$W_{1\to 2}^{\text{abs}} = -\beta \frac{4\pi^2 \alpha}{n} I(\omega) |r_{12}|^2. \tag{2.123}$$

The energy flux is related to the energy density by $I(\omega) = \rho(\omega)c/n$, where c/n is the speed of light in the material. Using equations (2.120), (2.122), and (2.123), we arrive at the expression for the two-level spontaneous emission rate:

$$W_{2\to 1}^{\text{sp}} = \beta \frac{g_1}{g_2} \frac{4\alpha n \omega^3}{c^2} |r_{21}|^2 . \tag{2.124}$$

For a multitude of final states, equation (2.124) transforms to a spectral form:

$$W_{\text{sp}}(\omega) = \beta \frac{g_1}{g_2} \frac{4\alpha n \omega^3}{c^2} \sum_m |r_{e0;gm}|^2 \, \delta(E_{e0} - E_{gm} + \omega). \tag{2.125}$$

From an experimental point of view, $W_{\text{sp}}(\omega)$ describes the number of photons emitted in the solid angle 4π per unit energy per unit time.

2.6.2 Matrix elements: non-degenerate case

The primary parameters for spectral equations (2.118), (2.119), and (2.125) are transition dipole elements $|r_{en;gm}|^2$ (or momentum matrix elements $|p_{en;gm}|^2$). This section focuses on evaluating these parameters when wavefunctions $|\Psi_{g;m}\rangle$ and $|\Psi_{e;n}\rangle$ are non-degenerate. We will drop this restriction in the next section, as the transition to a doubly degenerate electronic state of diamond NV center will be considered.

For non-degenerate electronic states, the adiabatic form of Eq. (2.12) enables to separate vibrational and electronic degrees of freedom:

$$|r_{en;gm}|^2 = |\langle \chi_{e;n} | \chi_{g;m} \rangle|^2 \left| \langle \psi_e | \mathbf{r} | \psi_g \rangle \right|^2 , \tag{2.126}$$

$$|p_{en;gm}|^2 = |\langle \chi_{e;n} | \chi_{g;m} \rangle|^2 \left| \langle \psi_e | \mathbf{p} | \psi_g \rangle \right|^2 . \tag{2.127}$$

In the context of Born–Oppenheimer adiabatic approximation, such separation is known as the *Franck–Condon approximation*. However, for crude adiabatic approximation, this separation is a natural consequence of the selected adiabatic form. Electronic matrix elements $|\langle \psi_e | \mathbf{r} | \psi_g \rangle|^2$ (or $|\langle \psi_e | \mathbf{p} | \psi_g \rangle|^2$) determine the strength of interaction and are required to calculate the absolute values of cross-sections or lifetimes.[31] The overlap integrals between vibrational

[31] The *ab initio* methodology for evaluating these matrix elements will be presented in Chapter 5, where we consider absolute cross-sections of absorption and stimulated emission processes.

wavefunctions $|\langle\chi_{e;n}|\chi_{g;m}\rangle|^2$ are called *Franck–Condon* (FC) *factors*. FC factors determine the lineshape of optical transition and are responsible for a vibrational broadening of emission and absorption spectra. The evaluation of these factors will be the topic of the rest of this section.

Franck–Condon factors

The evaluation of $|\langle\chi_{f;n}|\chi_{i;m}\rangle|^2$ is a computationally challenging task for systems with many degrees of freedom. This complication can be illustrated as follows. In the harmonic approximation, the vibrational wavefunction is a product of one-dimensional harmonic oscillator states $\chi_{i;n_k}$ (see Section 2.4.1):

$$\chi_{i;\mathbf{n}}(\mathbf{Q}_i) = \prod_k \chi_{i;n_k}(Q_{i;k}).$$

Each one-dimensional state $\chi_{i;n_k}$ is described by frequency $\omega_{i;k}$, normal coordinate $Q_{i;k}$, and quantum number n_k. The frequencies and normal coordinates are determined by diagonalizing the dynamical matrix, which encodes the adiabatic potential energy surface (APES) close to the equilibrium (see Section 2.4.1 for more details). However, the electronic transition induces a change in the shape of the APES. This change implies a different vibrational structure. That is, the frequencies $\omega_{f;k}$ and normal coordinates $Q_{f;k}$ are different from those of the initial state. New normal coordinates $\mathbf{Q}_f$ are intermixed with old ones by so-called Duschinsky transformation [123]:

$$\mathbf{Q}_f = \hat{\mathbf{J}}\mathbf{Q}_i + \Delta\mathbf{Q}.$$

Here $\hat{\mathbf{J}}$ is a non-diagonal matrix that mixes normal coordinates of both electronic states. Because of this mixing, Franck–Condon factors are highly multidimensional integrals. Practically, such integrals can only be evaluated for systems that have a small number of nuclear degrees of freedom.

Equal-mode approximation

To overcome the computation problem (presented above), we adopt the *equal-mode approximation* [124].[32] First, we express APES of initial and final electronic states in terms of normal coordinates of initial state $\mathbf{Q} \equiv \mathbf{Q}^i$.[33]

[32] There is no universally accepted notation for this approximation.

[33] In the Appendix of our paper [T2], we show that choosing the normal coordinates and vibrational frequencies of initial states is the best approximation.

Within equal mode approximation, the change of the APES, as a result of the optical transition, is assumed to be linear in normal coordinates:

$$\Delta V(\mathbf{Q}) = V_f(\mathbf{Q}) - V_i(\mathbf{Q}) = \sum_k q_k Q_k, \tag{2.128}$$

where

$$q_k = \left.\frac{\partial V_f(\mathbf{Q})}{\partial Q_k}\right|_{\mathbf{Q}=0} = \left\langle \psi_f \middle| \frac{\partial \Delta\hat{U}(\mathbf{Q})}{\partial Q_k} \middle| \psi_f \right\rangle_{\mathbf{Q}=0} \tag{2.129}$$

are the same *linear vibronic constants* of Eq. (2.65). Here $\Delta\hat{U}$ is the potential energy due to the motion of nuclei [see Eq. (2.7)]. The potential energy surface for the final state can be written as:

$$V_f(\mathbf{Q}) = V_i(\mathbf{Q}) + \sum_k q_k Q_{k;a_1}.$$

The harmonic Hamiltonian (2.57) for the final electronic state becomes:

$$\begin{aligned}\hat{H}_v^f &= \sum_k \left(\frac{1}{2}\frac{\partial^2}{\partial Q_k^2} + \frac{1}{2}\omega_k^2 Q_k^2 + q_k Q_k \right) \\ &= \sum_k \left(\frac{1}{2}\frac{\partial^2}{\partial Q_k^2} + \frac{1}{2}\omega_k^2 \left(Q_k + \frac{q_k}{\omega_k^2} \right)^2 - \frac{q_k^2}{2\omega_k^2} \right),\end{aligned}$$

where ω_k and Q_k are frequencies and normal coordinates of the initial electronic state. We see that in the equal mode approximation, each one-dimensional harmonic potential is displaced by the value:

$$\Delta Q_k = \frac{q_k}{\omega_k^2}.$$

In addition, the energy of each oscillator is lowered by the factor:

$$\Delta\epsilon_k = -q_k^2/(2\omega_k^2) = -\frac{1}{2}\Delta Q_k^2 \omega_k^2. \tag{2.130}$$

This change of potential energy surface for a single Q_k is illustrated in Fig. 2.5. The coefficients ΔQ_k describe the change of the equilibrium defect geometry and can be written in terms of direct nuclear displacements:

$$\Delta Q_k = \sum_n \sqrt{M_n} \Delta\mathbf{R}_n \boldsymbol{\eta}_{k;n}, \tag{2.131}$$

where $\Delta\mathbf{R}_n = \mathbf{R}_{f;n} - \mathbf{R}_{i;n}$ is the change of the equilibrium position of atom n between the initial and the final electronic states.

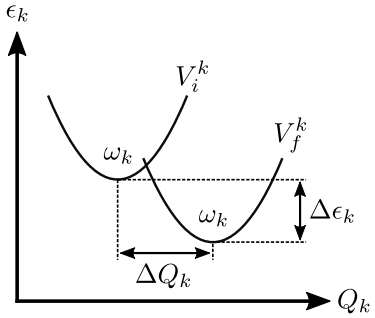

Figure 2.5: Effect of optical transition on one dimensional harmonic potential in the equal mode approximation. Line V_i^k shows the harmonic potential of the initial electronic state, while V_f^k shows potential after the optical transition.

In the equal mode approximation, one-dimensional vibrational states of the final electronic configuration are related to the vibrational states of the initial electronic configuration by:

$$\chi_{f;n_k}(Q_k) = \chi_{i;n_k}(Q_k - \Delta Q_k).$$

For the ground vibrational state, one-dimensional overlap integrals have an elegant analytical expression [110]:

$$|\langle\chi_{0_k}(Q_k)|\chi_{n_k}(Q_k - \Delta Q_k)\rangle|^2 = \frac{S_k^{n_k}}{n_k!}\exp(-S_k), \tag{2.132}$$

where

$$S_k = \frac{\omega_k \Delta Q_k^2}{2\hbar}, \tag{2.133}$$

is the partial Huang–Rhys (HR) factor. The partial HR factor has a statistical interpretation as the average number of k-type phonons created during an optical transition [125]. Finally, the FC factor for all-phonon wavefunction is:

$$|\langle\chi_{f;n}|\chi_{i;0}\rangle|^2 = \prod_k \frac{S_k^{n_k}}{n_k!}\exp(-S_k). \tag{2.134}$$

This form is convenient for the practical calculation of spectral lineshapes, as will be demonstrated in Section 2.6.4.

Symmetry considerations

Now, let us take a look at the electron–phonon coupling from a group theoretical perspective. Expansion coefficients q_k of Eq. (2.128) are the same linear

vibronic constants introduced in the Jahn–Teller problem [see Eq. (2.65)]. In Section 2.5.1, it was shown that for non-degenerate states, LVCs are non-zero only for A_1 symmetry displacements. Therefore, it follows that ΔQ_k is non-zero only if it represents a totally symmetric mode. Following this argument, we can write:

$$\langle \chi^f_{\mathbf{n}} | \chi^i_{\mathbf{m}} \rangle = \prod_{k \in A_1} \langle \chi_{n_k}(Q_k - \Delta Q_k) | \chi_{m_k}(Q_k) \rangle \prod_{q \notin A_1} \delta_{n_q, m_q}. \tag{2.135}$$

The last product of Eq. (2.135) reveals a fundamental fact: *an optical transition between non-degenerate electronic states can only excite vibrational modes of a_1 symmetry*. Otherwise, in the first order of theory, the transition probability is zero.

2.6.3 Matrix elements: degenerate case

In the above section, we saw that for non-degenerate electronic states, only totally symmetric a_1 modes participate in the optical transition. This behavior results from symmetry properties: the nuclear displacements due to electronic transition can only occur along totally symmetric directions if both electronic states are non-degenerate. However, for degenerate states, the vibronic interactions modify nuclear motion along with symmetry-breaking directions, and contributions of other modes become influential.

Here, we illustrate this effect by considering the triplet transition of the diamond NV^- center [see Fig. 1.1(c)]. The ground triplet state of the NV center is an orbital singlet of A_2 symmetry. Since the electronic state is non-degenerate, the wavefunction can be written in the adiabatic form:

$$\left| \Psi_{g;pr} \right\rangle = \chi^{a_1}_{gp}(\mathbf{Q}_{a_1}) \chi^{e}_{gr}(\mathbf{Q}_e) \left| A_2 \right\rangle . \tag{2.136}$$

In this equation, we separated the a_1 and e symmetry components of the vibrational wave function.[34] We need two sets of quantum numbers, p and r, to describe the vibrational states of these components. To avoid confusion, the index "e" for "excited" will be used as a subscript, and the index "e" to label the e irreducible representation will be used as a superscript whenever both indices appear on the same symbol. The excited state is an orbital doublet of E symmetry, and the general expression of its vibronic states is:

$$\left| \Psi_{e;st} \right\rangle = \chi^{a_1}_{es}(\mathbf{Q}_{a_1}) \left| \Phi_{et} \right\rangle . \tag{2.137}$$

[34] For the diamond NV center, a_2 symmetry contribution is omitted because a_2 symmetry modes do not contribute to the vibronic interactions. This is explained in Section 2.5.3.

Here $|\Phi_{et}\rangle$ is the solution of $E \otimes (e \otimes e \cdots)$ vibronic Hamiltonian:[35]

$$|\Phi_{et}\rangle = \chi_{et}^{e+}(\mathbf{Q}_e)\,|E_+\rangle + \chi_{et}^{e-}(\mathbf{Q}_e)\,|E_-\rangle\,.$$

The matrix element between these triplet states can be written as:

$$\left|\left\langle \Psi_{e;st}\middle|\mathbf{r}\middle|\Psi_{g;pr}\right\rangle\right|^2 = \left|\left\langle \chi_{es}^{a_1}\middle|\chi_{gp}^{a_1}\right\rangle\right|^2 \left|\left\langle \Phi_{et}\middle|\mathbf{r}\middle|\chi_{gr}^{e};A_2\right\rangle\right|^2.$$

The first term $|\langle\chi_{es}^{a_1}|\chi_{gp}^{a_1}\rangle|^2$ is a Franck–Condon factor which can be calculated using Eq. (2.134). The second term can be expanded in the following form:

$$\begin{aligned}&\left|\left\langle \Phi_{et}\middle|\mathbf{r}\middle|\chi_{gr}^{e};A_2\right\rangle\right|^2 \\ &\quad= \left|\left\langle \chi_{et}^{e+}\middle|\chi_{gr}^{e}\right\rangle\langle E_+|\mathbf{r}|A_2\rangle + \left\langle \chi_{et}^{e-}\middle|\chi_{gr}^{e}\right\rangle\langle E_-|\mathbf{r}|A_2\rangle\right|^2.\end{aligned} \tag{2.138}$$

Let us rewrite the position operator $\mathbf{r}$ in terms of Cartesian components:

$$\mathbf{r} = r_x\hat{\mathbf{e}}_x + r_y\hat{\mathbf{e}}_y + r_z\hat{\mathbf{e}}_z.$$

If we choose the coordinate system such that $\hat{\mathbf{e}}_z$ corresponds to the rotational axis of the C_{3v} point group (and the symmetry axis of the NV center), then r_x, r_y, and r_z respectively transform as E_x, E_y, and A_1 irreducible representations. Now, let us rewrite electronic matrix elements in the basis of Cartesian representation [see Eq. (2.95)]:

$$\left\langle E_\pm\middle|\mathbf{r}\middle|A_2\right\rangle = \frac{1}{\sqrt{2}}\left\langle E_x\middle|\mathbf{r}\middle|A_2\right\rangle \pm i\frac{1}{\sqrt{2}}\left\langle E_y\middle|\mathbf{r}\middle|A_2\right\rangle. \tag{2.139}$$

From group theory, it follows that:

$$\langle E_i|r_z|A_2\rangle = 0,$$

for $i = \{x, y\}$, because $A_1 \notin (E \otimes A_1 \otimes A_2) = E$. This result implies that *light polarized along the axial direction of NV cannot induce triplet optical transitions*. Furthermore, from the Wigner–Eckart theorem, it follows that:

$$\langle E_i|r_j|A_2\rangle = \mu_0\,\langle E_i; E_j|A_2\rangle\,, \tag{2.140}$$

where μ_0 is the reduced matrix element,[36] and $\langle E_i; E_j|A_2\rangle$ are Clebsch–Gordan coefficients. In the Cartesian representation, CG coefficients are given by:

$$\langle E_i; E_j|A_2\rangle = \frac{1}{\sqrt{2}}\begin{pmatrix}0 & -1\\ 1 & 0\end{pmatrix}. \tag{2.141}$$

[35] See Section 2.5.3 for a more detailed discussion.

[36] Physically, μ_0 is simply the transition dipole moment.

Using Eqs. (2.140) and (2.141), we can rewrite Eq (2.139) as:

$$\langle E_{\pm}|\mathbf{r}|A_2\rangle = \frac{1}{\sqrt{2}}\langle E_x|r_y|A_2\rangle\hat{\mathbf{e}}_y \mp i\frac{1}{\sqrt{2}}\langle E_x|r_y|A_2\rangle\hat{\mathbf{e}}_x. \tag{2.142}$$

Substituting Eq. (2.142) into Eq. (2.138) yields:

$$\left|\langle\Phi_{et}|\mathbf{r}|\chi^e_{gr}(\mathbf{Q}_e); A_2\rangle\right|^2 = \left|\langle E_x|r_y|A_2\rangle\right|^2\left[\left|\langle\chi^+_{et}|\chi^e_{gr}\rangle\right|^2 + \left|\langle\chi^-_{et}|\chi^e_{gr}\rangle\right|^2\right].$$

Finally, we can write the matrix element of triplet transition as:

$$\begin{aligned}&\left|\langle\Psi_{e;st}|\mathbf{r}|\Psi_{g;pr}\rangle\right|^2\\ &\quad= \left|\langle E_x|r_y|A_2\rangle\right|^2\left|\langle\chi^{a_1}_{es}|\chi^{a_1}_{gp}\rangle\right|^2\left[\left|\langle\chi^+_{et}|\chi^e_{gr}\rangle\right|^2 + \left|\langle\chi^-_{et}|\chi^e_{gr}\rangle\right|^2\right].\end{aligned} \tag{2.143}$$

The last term in square brackets comes from vibronic interactions in the degenerate electronic state.

2.6.4 Spectral functions

Calculation of emission and absorption spectra requires evaluating sums over all vibrational/vibronic states of the final electronic manifold [see Eqs. (2.118), (2.119), and (2.125)]. The direct calculation is complicated as there is effectively an infinite number of such states. The exact calculation can be simplified by considering the Fourier transform of the *spectral function of electron–phonon interaction* [109]. We begin this section by defining the spectral function of electron–phonon interaction for transitions involving non-degenerate electronic states. We show how these functions can be directly obtained from the spectrum of Huang–Rhys parameters. In the second part, we present our original analysis, where we extend the definition of the spectral function of electron–phonon interaction when one of the states is a degenerate Jahn–Teller system.

Spectral function for a_1 modes

We define the spectral functions of electron–phonon interaction for a_1 modes for absorption and emission process, respectively, as [109]:

$$A^{a_1}_{\mathrm{abs}}(\omega) = \sum_p \left|\langle\chi^{a_1}_{e0}|\chi^{a_1}_{gp}\rangle\right|^2\delta\big(E_{\mathrm{ZPL}} + \epsilon^{a_1}_{g0} - \epsilon^{a_1}_{gp} - \omega\big), \tag{2.144}$$

$$A^{a_1}_{\mathrm{em}}(\omega) = \sum_s \left|\langle\chi^{a_1}_{es}|\chi^{a_1}_{g0}\rangle\right|^2\delta\big(E_{\mathrm{ZPL}} + \epsilon^{a_1}_{es} - \epsilon^{a_1}_{e0} - \omega\big). \tag{2.145}$$

Here, E_{ZPL} is the *zero-phonon line* (ZPL) of optical transition. This line corresponds to the energy difference between the lowest vibrational/vibronic

level in the excited state and the lowest vibrational/vibronic level in the ground state:

$$E_{\mathrm{ZPL}} = (\varepsilon_e - \varepsilon_g) + (\epsilon^{a_1}_{e0} - \epsilon^{a_1}_{g0}). \tag{2.146}$$

Here, ε_e and ε_g are energies of the electronic Schrödinger equation (2.8), and $\epsilon^{a_1}_{en}$ and $\epsilon^{a_1}_{gm}$ are energies of the vibrational (or vibronic) subsystem.

For the non-degenerate case, vibronic interactions are negligible, and only a_1 modes contribute to the electron–phonon interaction [see Eq. (2.135)]. Therefore, the total spectral function of electron–phonon interaction $A(\omega)$ equals the spectral function of a_1 symmetry modes ($A_{\{\mathrm{em,abs}\}} = A^{a_1}_{\{\mathrm{em,abs}\}}$). In this case, we can write spectral equations (2.118), (2.119), and (2.125) in terms of $A(\omega)$:

$$\sigma_{\mathrm{abs}}(\omega) = -\beta \frac{4\pi^2 \alpha \omega}{n} \left|\langle \psi_e | \mathbf{r} | \psi_g \rangle\right|^2 A_{\mathrm{abs}}(\omega), \tag{2.147}$$

$$\sigma_{\mathrm{st}}(\omega) = -\beta \frac{4\pi^2 \alpha \omega}{n} \left|\langle \psi_e | \mathbf{r} | \psi_g \rangle\right|^2 A_{\mathrm{em}}(\omega), \tag{2.148}$$

$$W_{\mathrm{sp}}(\omega) = \beta \frac{g_1}{g_2} \frac{4\alpha n \omega^3}{c^2} \left|\langle \psi_e | \mathbf{r} | \psi_g \rangle\right|^2 A_{\mathrm{em}}(\omega). \tag{2.149}$$

The evaluation of spectral functions (2.144) and (2.145) is simplified if one considers their Fourier transform to the time domain, commonly denoted as the *generating function* [126]:

$$G_{\{\mathrm{abs,em}\}}(t) = \int A^{a_1}_{\{\mathrm{abs,em}\}}(\omega) e^{i\omega t} \, \mathrm{d}\omega. \tag{2.150}$$

In the equal mode approximation, the FC factor is given by Eq. (2.134), and the spectral function of electron–phonon coupling for emission is:

$$A^{a_1}_{\mathrm{em}}(\omega) = \sum_{\mathbf{n}} \prod_{k \in A_1} \frac{S_k^{n_k}}{n_k} e^{-S_k} \delta\Big(E_{\mathrm{ZPL}} - \sum_i n_i \omega_i - \omega\Big).$$

The sum runs over all possible configurations of $\mathbf{n} = \{n_1, n_2, \ldots, n_N\}$. The Fourier transform of this expression yields generating function:[37]

$$G_{\mathrm{em}}(t) = \exp\left[-iE_{\mathrm{ZPL}}t - S_{a_1} + \int e^{i\omega t} S_{a_1}(\omega) \, \mathrm{d}\omega\right], \tag{2.151}$$

where:

$$S_{a_1}(\omega) = \sum_{k \in A_1} S_k \delta(\omega - \omega_k), \tag{2.152}$$

[37] The trick here is to use the integral form of the delta function.

is the *density of electron-phonon coupling* (also called Huang–Rhys spectrum), and:

$$S_{a_1} = \int_0^\infty S_{a_1}(\omega)\,\mathrm{d}\omega = \sum_{k\in A_1} S_k, \tag{2.153}$$

is the *total Huang–Rhys factor* due to coupling to a_1 modes. Similarly, for the absorption process, the generating function is:

$$G_{\mathrm{abs}}(t) = \exp\left[-iE_{\mathrm{ZPL}}t - S_{a_1} + \int e^{-i\omega t} S_{a_1}(\omega)\,\mathrm{d}\omega\right]. \tag{2.154}$$

Once the generating function is known, the spectral function can be obtained via the inverse Fourier transform:

$$A_{a_1}(\omega) = \frac{1}{2\pi}\int_{-\infty}^{\infty} e^{i\omega t} G(t) e^{-\gamma|t|}\,\mathrm{d}t. \tag{2.155}$$

Here, we include additional Lorentzian broadening term $e^{-\gamma|t|}$. This term accounts for other homogeneous and inhomogeneous effects, which are not treated explicitly in theory. In practice, the value of γ is adjusted to reproduce the experimental broadening of the ZPL line.

Spectral function for e modes

If at least one of the states is degenerate, symmetry breaking modes (other than a_1) start to participate in the electron–phonon interaction. Here, we focus on the $A_2 \leftrightarrow E$ transition of the diamond NV center (however, the analysis can be readily extended to the case of other vibronic systems). To account for vibronic coupling, we extend the definition of the spectral function of electron–phonon interaction by:

$$A_{\{\mathrm{em,abs}\}}(\omega) = \int A^{a_1}_{\{\mathrm{em,abs}\}}(\omega-\omega') A^{e}_{\{\mathrm{em,abs}\}}(\omega')\,\mathrm{d}\omega'. \tag{2.156}$$

The contribution of a_1 modes is given by equations (2.144) and (2.145). The spectral functions pertaining to e symmetry modes are chosen to recover the form of Eqs. (2.147)–(2.149):

$$A^{e}_{\mathrm{em}}(\omega) = \sum_r \left[\left|\left\langle \chi^{e+}_{e0}\middle|\chi^{e}_{gr}\right\rangle\right|^2 + \left|\left\langle \chi^{e-}_{e0}\middle|\chi^{e}_{gr}\right\rangle\right|^2\right]\delta(\epsilon^{e}_{g0} - \epsilon^{e}_{gr} - \omega), \tag{2.157}$$

$$A^{e}_{\mathrm{abs}}(\omega) = \sum_t \left[\left|\left\langle \chi^{e+}_{et}\middle|\chi^{e}_{g0}\right\rangle\right|^2 + \left|\left\langle \chi^{e-}_{et}\middle|\chi^{e}_{g0}\right\rangle\right|^2\right]\delta(\epsilon^{e}_{et} - \epsilon^{e}_{e0} - \omega). \tag{2.158}$$

These spectral functions require the evaluation of $\langle \chi_{et}^{e\pm} | \chi_{g0}^{e} \rangle$. In Section 2.5, we showed that the solution of the vibronic problem produces wavefunctions in the form: $|\Phi_{et}\rangle = |\chi_{et}^{+}\rangle |E_{+}\rangle + |\chi_{et}^{-}\rangle |E_{-}\rangle$ where:

$$\left|\chi_{et}^{\pm}\right\rangle = \sum_{\boldsymbol{nl}} C_{et;n_1 l_1 \ldots n_N l_n}^{\pm} \left| n_1 l_1, \ldots, n_N l_N \right\rangle . \tag{2.159}$$

The coefficients $C_{et;n_1 l_1 \ldots n_N l_n}^{\pm}$ are determined by diagonalization of vibronic Hamiltonian $\hat{H} = \hat{H}^0 + \hat{H}^{\mathrm{JT}}$ [Eqs. (2.97) and (2.100)].

In the zero-temperature limit, overlaps for emission spectrum (2.157) are calculated between the lowest vibronic state of the optically excited electronic state $|^3E\rangle$ and all the vibrational states of the electronic ground state $|^3A_2\rangle$. The lowest vibronic state is always the one with the pseudo-spin[38] $j = \pm\frac{1}{2}$ [27]. Therefore, in the case of luminescence, one has to diagonalize the Hamiltonian for either the $j = \frac{1}{2}$ or the $j = -\frac{1}{2}$ "channel" (the two states are degenerate).

In the case of absorption, overlap integrals in the spectral function (2.158) are calculated between zero-phonon state $|00\ldots0\rangle$ of the electronic ground state $|^3A_2\rangle$ and vibronic states of the electronic excited state $|^3E\rangle$. Overlaps will be non-zero only for vibronic states in the $|^3E\rangle$ manifold that contain the contribution of the zero-phonon state $|00\ldots0\rangle$. This phonon state is only present in vibronic states with $j = \pm\frac{1}{2}$ [117], and therefore in our diagonalization procedure, we again need to consider either only the $j = \frac{1}{2}$ or the $j = -\frac{1}{2}$ "channel".

[38] See Eq. (2.94) for the definition of the "pseudo-spin".

Chapter 3

VIBRATIONAL STRUCTURE OF DEFECT: *ab initio* APPROACH

Good, good, good, good vibrations (oom bop bop)
She's giving me the excitations (excitations, oom bop bop)
I'm pickin' up good vibrations
— The Beach Boys, *Good Vibrations*

The vibrational structure is an essential component for the complete description of quantum mechanical states of deep-level defects. It is revealed in the optical spectrum of color centers and plays an important role in other physical processes of the defect (e.g., non-radiative transition, spin–phonon coupling, vibrational averaging of the fine structure, etc.). This chapter focuses on the *ab initio* theoretical description of the vibrational structure of defects in lattices. For adiabatic states, the vibrational structure completely determines the nuclear dynamics. In contrast, for non-adiabatic degenerate states, it serves as a zero-order solution for the more complicated Jahn–Teller problem.

The content of this chapter is organized as follows. Section 3.1 starts with the analysis of the pure bulk vibrational structure. There, we discuss the calculation of interatomic force constants and show the performance of density functional theory in the case of diamond. In Section 3.2, we review the standard supercell approach for the defect vibrational structure calculations. We illustrate this approach for the diamond NV center and show that in computationally accessible supercell sizes, the vibrational structure of the defect is not sufficiently converged.

For this reason, in Section 3.3, we present our embedding methodology for the vibrational structure analysis in the effectively dilute limit. Section 3.3.2 illustrates the embedding methodology for the ground state of the diamond NV^- center. Section 3.4 presents our theoretical study of isotopic shifts of negatively charged silicon–vacancy (SiV^-) in the diamond. Finally, in Section 3.5, we conclude our results and present key statements for the defense.

3.1 Lattice vibrations of diamond

Diamond is the host lattice for two defect systems considered in this thesis (NV and SiV centers). Therefore, we begin this chapter by analyzing the vibrational structure of diamond. Here, we introduce a standard methodology for calculating interatomic force constants and test the performance of the density functional theory for the description of the vibrational structure of bulk.

3.1.1 Finite-difference approach

The vibrational structure of the periodic system is found by solving the eigenvalue problem of Eq. (2.60) for different values of $\mathbf{q}$. The central parameter is the *reduced dynamical matrix* (2.61):

$$\hat{\mathcal{D}}_{nm}(\mathbf{q}) = \sum_{\beta} \frac{\Phi_{mn}^{\alpha\beta}}{\sqrt{M_m M_n}} e^{i\mathbf{q}\mathbf{R}^{\beta}}.$$

Here, $\Phi_{mn}^{\alpha\beta}$ are elements of the Hessian matrix (interatomic force constants), which are second-order derivatives of the adiabatic potential energy surface [see Eq. (2.49)]:

$$\Phi_{mi;nj}^{\alpha\beta} = \frac{\partial^2 V(\mathbf{R})}{\partial R_{mi}^{\alpha} \partial R_{nj}^{\beta}} = -\frac{\partial F_{nj}^{\beta}}{\partial R_{mi}^{\alpha}}. \tag{3.1}$$

Indices i and j denote Cartesian directions, and F_{nj}^{β} is the force along direction j exerted on atom n in the primitive cell β.

For a practical calculation of interatomic force constants, we use the *finite-difference approach* [127].[1] This approach relies on the short-ranged character of interatomic interactions in a semiconductor material. Such character implies that if two atoms are sufficiently far apart ($|\mathbf{R}_m^{\alpha} - \mathbf{R}_n^{\beta}| \gg 1$), the corresponding Hessian matrix element vanishes ($\Phi_{mi;nj}^{\alpha\beta} \to 0$). Therefore, in a practical approach, we choose a large supercell where the distance between periodic images is larger than the extent of interatomic interactions. The Hessian matrix is calculated by approximating Eq. (3.1):

$$\Phi_{mi;nj}^{\alpha\beta} = -\frac{\Delta F_{nj}^{\beta}}{\Delta R_{mi}^{\alpha}},$$

where ΔF_{nj}^{β} is the force difference due to atomic displacement ΔR_{mi}^{α}.

[1] This method is also known as the "frozen" phonon approach.

3.1.2 Symmetry considerations

The calculation of the Hessian matrix requires a large number of displacements; however, this number can be reduced by employing symmetry properties. From the second-order derivative form of Eq. (3.1), it follows that the Hessian matrix is symmetric:

$$\Phi^{\alpha\beta}_{mi;nj} = \Phi^{\beta\alpha}_{nj;mi}. \tag{3.2}$$

The crystal lattice has a translational symmetry which also implies:

$$\Phi_{mi;nj}(\mathbf{R}^{\alpha}, \mathbf{R}^{\beta}) = \Phi_{mi;nj}(\mathbf{R}^{\alpha} + \mathbf{L}, \mathbf{R}^{\beta} + \mathbf{L}), \tag{3.3}$$

where $\mathbf{L}$ is a lattice vector. Eq. (3.3) significantly simplifies the evaluation of force constants, as one needs to consider only pairwise interactions where one of the atoms resides in the reference primitive cell. Furthermore, the point group symmetry implies:

$$\Phi_{i'j'}(\mathbf{R}_{n'}, \mathbf{R}_{m'}) = \sum_{ij} S_{ii'} S_{jj'} \Phi_{ij}(\hat{S}\mathbf{R}_n, \hat{S}\mathbf{R}_m), \tag{3.4}$$

where $\hat{S}$ is any 3D transformation of a point group.

According to these symmetry properties, one can choose a reduced set of Hessian matrix elements. Symmetrically equivalent elements are recovered by the application of Eqs. (3.2), (3.3), and (3.4).

3.1.3 Phonon structure of diamond

Here, we present our calculations of the phonon structure of diamond using PBE and HSE exchange–correlation functionals.[2] First principle calculations have been performed with the Vienna ab initio simulation package (VASP) [77].

Lattice relaxation was performed using a conventional cubic cell with eight carbon atoms. We used the projector-augmented wave approach with a plane-wave energy cutoff of 500 eV. The Brillouin zone was sampled using the Monkhorst–Pack [95] $8 \times 8 \times 8$ k-point mesh. Table 3.1 shows the results for PBE and HSE functionals. The electronic bandgap (E_g) is significantly underestimated in PBE (4.12 eV) compared to the experimental value of 5.48 eV [128]. This result illustrates the bandgap problem discussed in Section 2.3.2. The bandgap is much closer to the experiment in the hybrid HSE functional (5.36 eV). However, we observe that PBE provides a better description of the lattice constant and the bulk modulus.

[2] See Section 2.3.3 for introduction to exchange–correlation functionals.

	E_g	a	B	$\omega(\Gamma)$	$\omega(\mathrm{X})$	$\omega(\mathrm{L})$
PBE	4.12	3.574 (+0.20%)	430 (−0.19%)	160.5	147.6	154.2
HSE	5.36	3.548 (−0.53%)	470 (+0.61%)	169.9	155.1	161.1
expt.	5.48[a]	3.567[a]	443[b]	166.7[c]	149.2[b]	153.0[b]

[a] Reference [128]
[b] Reference [129]
[c] Reference [130]

Table 3.1: Calculated Kohn–Sham bandgaps E_g (eV), lattice constants a (Å), bulk moduli B (GPa), and highest phonon frequencies (in meV) at high-symmetry points in the diamond. Experimental values [128–130] are listed for comparison. For the lattice constant and bulk modulus, the deviation from the experimental value is indicated in parentheses.

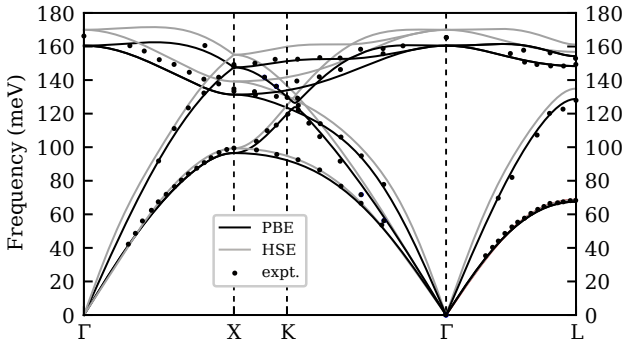

Figure 3.1: Phonon dispersion curves of diamond calculated using PBE (black lines) and HSE (gray lines) functionals. Experimental values are taken from Ref. [130].

Phonon dispersion curves were calculated using the PHONOPY software package [131]. This package generates atomic displacements taking into account symmetry considerations for a given periodic cell. Each displacement requires the separate self-consistent calculation of Hellman–Feynman forces. Once the forces are calculated, PHONOPY builds the Hessian matrix and solves the dynamical equation (2.61) for a selected set of $\mathbf{q}$ points.

We use the conventional unit cell with eight carbon atoms as a building block for supercell construction. For example, the cubic supercell of size $N \times N \times N$ contains $8N^3$ atomic sites. For force constant calculations, we chose the $4 \times 4 \times 4$ supercell (containing 512 atoms) and a single k-point (at Γ) for the Brillouin-zone sampling. The space group of diamond ($Fd\bar{3}m$) permits a reduction in the number of atomic displacements to just two. We have used displacements of amplitude $\Delta R = 0.01$ Å. In Fig. 3.1, the calculated

phonon dispersion curves are compared with inelastic neutron scattering data from Ref. [130]. Our calculations depict phonon dispersion for $T = 0$ K, while experimental data have been obtained at room temperature. However, this comparison is justified due to the very rigid nature of the diamond lattice: The phonon energies in diamond change by less than 0.1 meV from cryogenic to room temperatures [132]. Both functionals describe the phonon dispersion comparatively well. However, the PBE functional provides a slightly more accurate description of the spectrum. The highest phonon frequencies for high-symmetry points are compared with experimental values in Table 3.1.

3.2 Supercell vibrational modes of the diamond NV^- center

The standard *ab initio* calculations of defect properties are usually carried out in a supercell geometry, whereby a single defect is embedded in the periodic cell of the host material (see Section 2.3.4 for a more detailed discussion). In the following calculations, we use supercells that are computationally accessible in the DFT approach.

3.2.1 Electronic structure

We start our analysis by presenting first-principle electronic structure calculations of the ground $^3A_2$ and the excited ^3E triplet states of the diamond NV^- center.[3] Calculations were conducted using PBE and HSE functionals and the same computational parameters as for diamond phonon dispersion curves. The defect supercell is a $4 \times 4 \times 4$ cell with a single diamond NV center.

Ground state

For the ground state, lattice geometry relaxation was carried out, preserving C_{3v} symmetry until Hellman–Feynman forces were less than 0.001 eV/Å. The spatial localization of Kohn–Sham orbitals was determined by calculating the inverse participation ratio (IPR) [133]:

$$\mathrm{IPR} = \left(\int |\phi(\mathbf{r})|^4 \, \mathrm{d}\mathbf{r} \right)^{-1}. \tag{3.5}$$

[3] Density functional theory calculations of the ground and the excited states of the NV center have been reported previously. For a review, see Ref. [86].

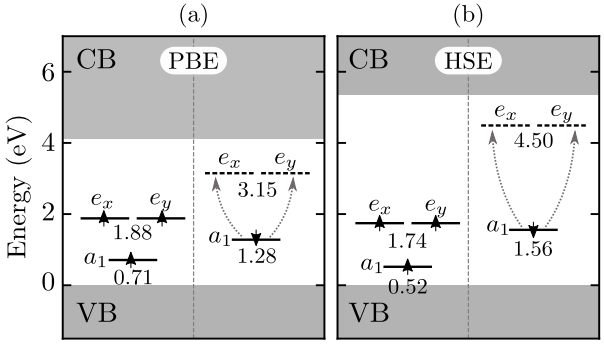

Figure 3.2: Defect-level diagrams of the NV^{-1} center as calculated using (a) PBE and (b) HSE functionals. Diagrams show Kohn–Sham single-particle defect levels for the ground state $^3A_2$. Shaded areas correspond to the valence band (VB) and the conduction band (CB). Dotted arrows show optical excitation.

We define the localization factor $\beta = \Omega/\mathrm{IPR}$ for a supercell of volume Ω, which yields the value of 1 for fully delocalized wavefunction ($\phi = 1/\sqrt{\Omega}$) and higher values for more localized states. The localized "defect orbitals" were identified by selecting Kohn–Sham states with $\beta \gg 1$ (more prominent than the average value of bulk states). Irreducible representations of single-particle orbitals were found by applying group theory projection operators [89]. Calculated Kohn–Sham defect level diagrams are shown in Fig. 3.2(a) for PBE and Figure 3.2(b) for HSE functionals. In both spin channels, there are three localized defect levels in the bandgap: fully symmetric a_1 level and a doubly-degenerate e level. All the orbitals are occupied in the spin-majority channel (left), and only the a_1 orbital is filled in the spin-minority channel (right). Such ground state configuration is A_2 symmetry triplet state:

$$\left|{}^3A_2; m_s = 1\right\rangle = |a_1 \bar{a}_1 e_x e_y|\,, \tag{3.6}$$

where $|\cdots|$ denotes the Slater determinant. This single-particle picture corresponds to the molecular-orbital model of Lenef and Rand [134]. The difference between the highest unoccupied e level and the lowest occupied a_1 level in the spin-minority channel is 1.87 eV for PBE and 2.94 eV for HSE.

Excited state

In the defect-orbital picture, the excited triplet state ^3E is obtained by promoting the electron in the spin-minority channel from the a_1 level to one of the e levels

(as depicted by dotted arrows in Fig. 3.2).[4] Resultant configuration corresponds to the E_x or E_y symmetry wavefunction:

$$|E_x; m_s = 1\rangle = |a_1 e_x e_y \bar{e}_y|\,,$$
$$|E_y; m_s = 1\rangle = |a_1 e_x e_y \bar{e}_x|\,. \tag{3.7}$$

We model this state using the ΔSCF method whereby orbital occupations of localized states are constrained to match the wavefunction form of Eq. (3.7).[5]

The excited ^3E state has an orbital degeneracy of nominal $a_1 e_x^2 e_y$ and $a_1 e_x e_y^2$ configurations. It is a $E \otimes (e \oplus e \cdots)$ Jahn–Teller (JT) system (see Section 2.5.3). Therefore, some additional considerations should be made regarding the lattice geometry relaxation along with the symmetry-breaking directions. DFT calculations directly solve the electronic problem, treating ions as classical motionless point charges. This means that the kinetic energy of nuclei is zero, and the effective Hamiltonian of $E \otimes (e \oplus e \cdots)$ system (2.93) is just a potential energy term:

$$\begin{aligned}\hat{U} &= \sum_{k;\gamma\in\{x,y\}} \left[\frac{1}{2}\omega_k^2 Q_{k\gamma}^2 \hat{C}_{\Gamma_{A_1}} + V_k \hat{C}_{\Gamma_{E_\gamma}} Q_{k\gamma}\right] \\ &= \sum_k \frac{1}{2}\omega_k^2 \left(Q_{kx}^2 + Q_{ky}^2\right) \hat{C}_{\Gamma_{A_1}} + \sum_k V_k \begin{bmatrix} Q_{ky} & Q_{kx} \\ Q_{kx} & -Q_{ky} \end{bmatrix},\end{aligned} \tag{3.8}$$

where k runs over all doublets of e symmetry coordinates. Since both terms in Eq. (3.8) commute, we can diagonalize the vibronic term to find two potential energy surfaces:

$$\hat{U}^{\pm} = \sum_k \frac{1}{2}\omega_k^2 \left(Q_{kx}^2 + Q_{ky}^2\right) \pm \left[\sum_{kk'} V_k V_{k'} \left(Q_{kx} Q_{k'x} + Q_{ky} Q_{k'y}\right)\right]^{1/2}. \tag{3.9}$$

Energy minimization in DFT self-consistent calculation follows the lower-lying branch of Eq. (3.9). It can be determined that the minimum of this potential occurs at coordinates [27]:

$$(Q_{kx}^{\min})^2 + (Q_{ky}^{\min})^2 = \frac{V_k^2}{\omega_k^4} = \frac{2K_k^2}{\omega_k}, \tag{3.10}$$

where V_k is a reduced matrix element of vibronic coupling [see Eq. (2.69)], and K_k is a dimensionless vibronic constant [see Eq. (2.99)]. The corresponding JT

[4] See Appendix B.4 for molecular orbital states of NV^- center.

[5] See Section 2.3.2 for introduction to ΔSCF method.

relaxation energy is [27]:

$$E_{\mathrm{JT}} = \frac{1}{2}\sum_k \frac{V_k^2}{\omega_k^2} = \sum_k K_k^2 \omega_k.$$

From Eq. (3.10) it follows, that the minimum of DFT calculations is not a single configuration but a continuum of configurations (e.g., in polar coordinates $Q_{kx} = \rho_k \sin\phi_k$ and $Q_{kx} = \rho_k \cos\phi_k$, the minima corresponds to $\rho_k = V_k/\omega_k^2$ and any value of ϕ_k). Eq. (3.10) will be important for the analysis of Jahn–Teller coupling (Sec. 4.3.1), as it allows to determine constants of vibronic coupling (V_k or K_k) by measuring lattice relaxation in density functional theory calculations.

3.2.2 Primary force constants for the excited state

The excited state is a JT active system, and the complete analysis requires solving the vibronic problem. This chapter will focus on the zero-order adiabatic solution and leave the treatment of non-adiabatic effects for Chapter 4. For the zero-order description, we need to calculate the dynamical matrix of the vibronic system [see Eq. (2.77)]:

$$\mathbf{D}_{\Gamma_n\gamma_n,\Gamma_m\gamma_m} = W_{A_1}(\Gamma_l \otimes \Gamma_n)\,\langle \Gamma_n\gamma_n\Gamma_m\gamma_m|A_1\rangle\,. \tag{3.11}$$

Here, $W_{A_1}(\Gamma_l \otimes \Gamma_n)$ is the reduced matrix element of $\langle E_i|\Omega_{A_1}(\Gamma_n \otimes \Gamma_m)|E_j\rangle$ [see Eq. (2.73)], and $\Omega_{A_1}(\Gamma_n \otimes \Gamma_m)$ is the A_1 symmetry component of a second-order derivative of potential energy [see Eq.(2.70)]. To separate A_1 contribution from the quadratic vibronic constants $W_{\Gamma'\gamma' \notin A_1}$, we propose the following *ab initio* approach. In DFT calculations, we take the electronic configuration with fractional orbital occupation $a_1 e_x^{1.5} e_y^{1.5}$. Such electronic configuration approximates a mixed state of degenerate configurations $a_1 e_x e_y^2$ and $a_1 e_x^2 e_y$. The density matrix of such an electronic system is given by:

$$\rho = \frac{1}{2}\left(|E_x\rangle\langle E_x| + |E_y\rangle\langle E_y|\right).$$

In this configuration, any calculated value of observable operator $\hat{O}$ corresponds to the ensemble average:

$$\langle\hat{O}\rangle = \mathrm{Tr}(\rho\hat{O}) = \frac{1}{2}\left(\langle E_x|\hat{O}|E_x\rangle + \langle E_y|\hat{O}|E_y\rangle\right).$$

If $\hat{O}$ transforms as a totally symmetric irreducible representation A_1, then:[6]

$$\langle\hat{O}_{A_1}\rangle = \langle E_x|\hat{O}_{A_1}|E_x\rangle = \langle E_y|\hat{O}_{A_1}|E_y\rangle.$$

[6]This follows from CG coefficient relation $\langle\Gamma_n\gamma_n A_1|\Gamma_m\gamma_m\rangle = \delta_{\Gamma_n\Gamma_m}\delta_{\gamma_n\gamma_m}$.

On the other hand, if $\hat{O}$ transforms as non-trivial irreducible representation $\Gamma'\gamma' \notin A_1$, then CG coefficients $\langle \Gamma_n\gamma_n\Gamma'\gamma'|\Gamma_n\gamma_n\rangle = 0$ (in the Cartesian representation of C_{3v} group) and $\langle \hat{O}_{\Gamma'\gamma'\notin A_1}\rangle = 0$.

From consideration above, it follows that for orbital configuration $a_1 e_x^{1.5} e_y^{1.5}$, calculated values of linear and quadratic vibronic constants [see Eqs. (2.69) and (2.73)] are:

$$\bar{V}_{\Gamma_k\gamma_k} = \langle X_{\Gamma_k\gamma_k}\rangle = \begin{cases} \langle E_i|X_{\Gamma_k\gamma_k}|E_i\rangle, & \text{if } \Gamma_k\gamma_k \in A_1 \\ 0, & \text{if } \Gamma_k\gamma_k \notin A_1 \end{cases}, \tag{3.12}$$

and

$$\langle \Omega_{\Gamma'\gamma'}(\Gamma_n \otimes \Gamma_m)\rangle = \begin{cases} \langle E_i|\Omega_{\Gamma'\gamma'}(\Gamma_n \otimes \Gamma_m)|E_i\rangle, & \text{if } \Gamma'\gamma' \in A_1 \\ 0, & \text{if } \Gamma'\gamma' \notin A_1 \end{cases}. \tag{3.13}$$

First, from Eq. (3.12), it follows that the relaxation using electronic occupation $a_1 e_x^{1.5} e_y^{1.5}$ optimizes the geometry only in the direction of A_1 symmetry coordinates.[7] Therefore, after the relaxation, forces along A_1 symmetry directions are zero, and geometry retains the C_{3v} symmetry.

Furthermore, from Eq. (3.13), it follows that the quadratic constants of potential energy expansion are nonzero only for A_1 projection if we use the $a_1 e_x^{1.5} e_y^{1.5}$ orbital configuration. As a result, applying the finite-difference approach (as for the adiabatic case) computes only primary force constants that enter the Eq. (3.11). This consequence is very important for the methodology of vibronic structure analysis, as it provides a practical method to calculate the dynamical matrix of the vibronic system.

3.2.3 Vibrational structure

The vibrational structure of NV^- has been calculated using electronic configurations $a_1^2 e_x e_y$ and $a_1 e_x^{1.5} e_y^{1.5}$, respectively, for the ground and excited state. The interatomic force constants were obtained using the finite-difference approach with displacements of amplitude $\Delta R = 0.01$ Å.[8] All the vibrational modes have been characterized according to the irreducible representations of the C_{3v} point group. This has been done by using character projection operators [90]:

$$P_\Gamma = \frac{s_\Gamma}{g} \sum_a \chi^*_\Gamma(G_a) T(G_a),$$

[7] This is because diagonal terms of linear vibronic constants $V^{ii}_{\Gamma_k\gamma_k}$ are forces in the direction of normal coordinate $Q_{\Gamma_k\gamma_k}$.

[8] This time, the number of symmetry-independent displacements is 574.

where s_{Γ_k} is the dimension of the irreducible representation Γ, $g = 6$ is the order of the group, G_a is the group element, and $T(G_a)$ is the symmetry transformation matrix for vibrational mode. If the vibrational mode is unchanged after the application of P_Γ (i.e., the scalar product $(\boldsymbol{\eta}_k \cdot P_\Gamma \boldsymbol{\eta}_k)$ is unity), then the mode is identified as a basis of irreducible representation Γ.

Modes were also characterized by their spatial localization. A bulk phonon is fully delocalized, and many atoms participate in particular vibration. However, as discussed in Section 2.4.3, point defects usually change the vibrational structure of a solid. Sometimes, the defect gives rise to localized or quasi-localized modes, which often induce observable spectroscopic signatures. To quantify the localization of vibrational mode, we calculate the inverse participation ratio (IPR) similar to electronic wavefunctions Eq. (3.5):

$$\mathrm{IPR}_k = \frac{1}{\sum_n \boldsymbol{\eta}_{k;n}^4},$$

where $\boldsymbol{\eta}_{k;n}$ is the three-dimensional displacement of atom n and $\boldsymbol{\eta}_{k;n}^4 \equiv (\sum_i \eta_{k;ni}^2)^2$. IPR essentially describes onto how many atoms the given mode is localized [109], i.e., if M atoms vibrate with equal amplitudes, $\mathrm{IPR} = M$. We also define a localization ratio β_k [109]:

$$\beta_k = \frac{N_\mathrm{n}}{\mathrm{IPR}_k},$$

where N_n is the number of atoms in the cell. β_k estimates the inverse of a fraction of atoms in the supercell that vibrates for a given vibrational mode. $\beta_k = 1$ when all atoms in the supercell vibrate with the same amplitude and $\beta_k \gg 1$ for localized and resonant modes.

Quasi-localized modes: ground state

Let us first start with the vibrational structure of the ground state. Figure 3.3 shows calculated localization ratios (β_k) using PBE and HSE functionals. The vibrational frequencies in the HSE calculations are slightly shifted to higher energies. This difference stems from the fact that interatomic interactions are stronger in HSE, as reflected in the difference of lattice constants (see Table 3.1). The shaded region shows the region of most probable β values for pure bulk vibrations. These values are within 3σ ($\sigma = 0.22$ for PBE and 0.20 for HSE) deviation from the mean value of bulk IPRs ($\sim$1.56 for both functionals). Both functionals provide clearly pronounced a_1 and e symmetry resonant modes in regions 60–65 meV and 80–85 meV. We also see some small resonances

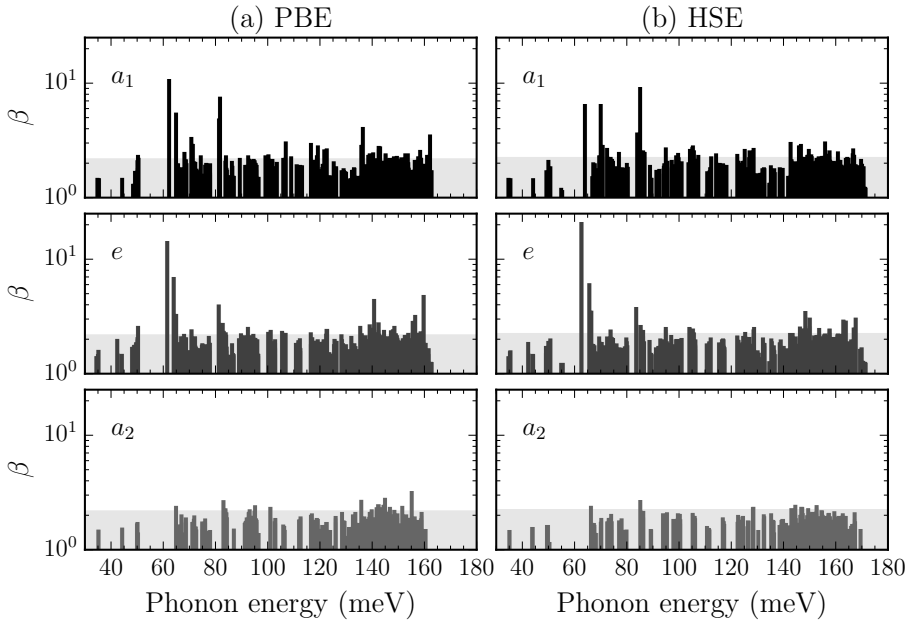

Figure 3.3: Localization ratios of ground state ($^3A_2$) vibrational modes of NV^-, calculated with (a) PBE and (b) HSE functionals. The shaded area shows a region of bulk localization ratios within 3σ deviation from the mean value. Note that the y axis has a logarithmic scale.

forming in the high-energy domain ($\sim$140 and 160 meV in PBE and $\sim$150 and 170 meV in HSE). Larger localization implies possibly stronger electron–phonon interaction as the amplitude of the vibration is localized in the vicinity of the defect. The calculated resonant peaks (for both a_1 and e symmetry modes) can explain many features of the luminescence phonon sideband (see Fig. 3.4). For example, let us take the quasi-local mode of frequency 63 meV (in PBE). This resonance is clearly pronounced in the luminescence spectrum (see Fig. 3.4), as it generates 3 increasingly broad phonon replicas and quantitatively explains overall lineshape. Furthermore, from Fig. 3.4, we see that other PBE resonances at approximately 140 and 155 meV almost perfectly correspond to other small features of the luminescence sideband.

Quasi-localized modes: excited state

Calculated localization ratios for the excited state are shown in Figure 3.5. As for the ground state, PBE and HSE yield quantitatively similar results. In comparison to the vibrational structure of the ground state, the excited state

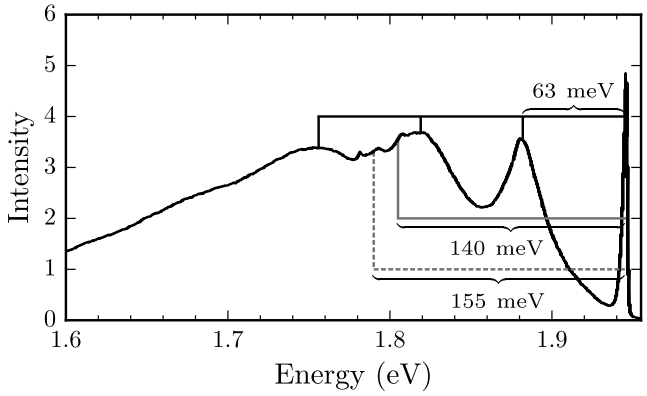

Figure 3.4: Luminescence lineshape of the diamond NV^- center (from Ref. [17]). Phonon replicas of sideband are compared with ground state localized modes of $4 \times 4 \times 4$ supercell calculations (see Fig. 3.3).

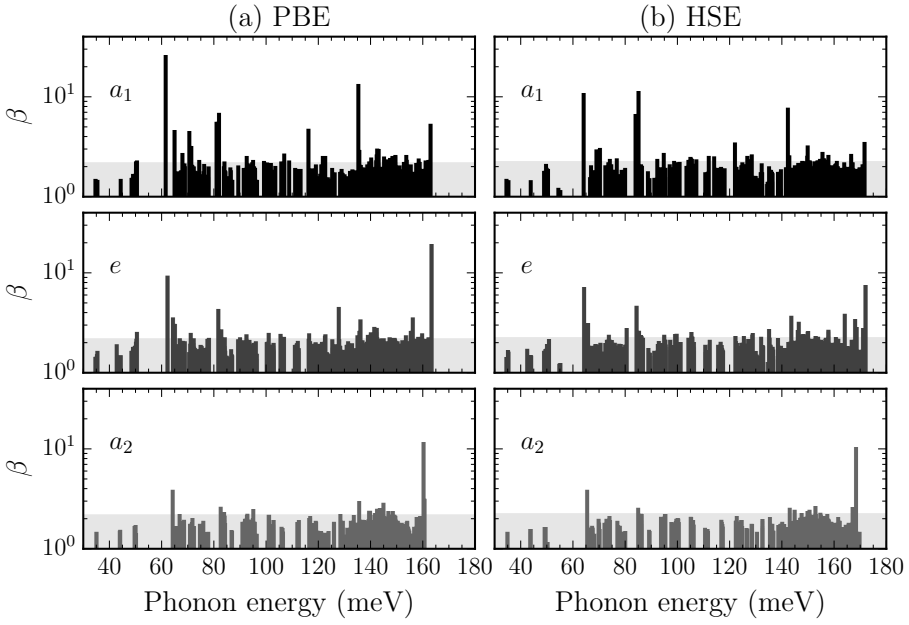

Figure 3.5: Localization ratios of excited state (^3E) vibrational modes of NV^-, calculated with (a) PBE and (b) HSE functionals. The shaded area shows the region of bulk localization ratios within 3σ deviation from the mean value. Note that the y axis has a logarithmic scale.

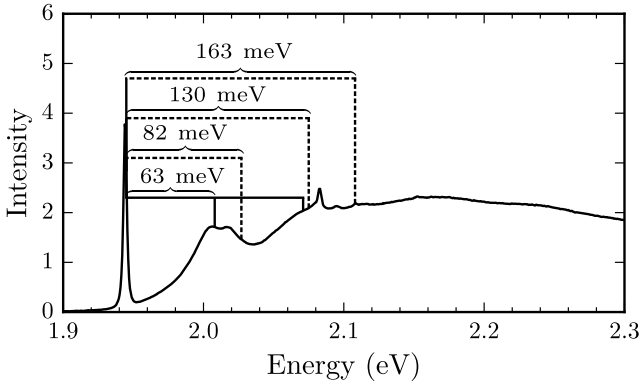

Figure 3.6: Absorption lineshape of the diamond NV^- center (from Ref. [135]). Phonon replicas of sideband are compared with excited state localized modes of $4 \times 4 \times 4$ supercell calculations (see Fig. 3.5).

yields more localized resonances in the high-energy region. One can assume that these modes might be excited in the process of optical excitation. Comparing phonon replicas of the absorption lineshape with PBE result [see Fig. 3.6(a)], one could identify resonant modes at 63, 130, and 163 meV as the possible sources of observed phonon replicas.

However, this time, such quantitative analysis does not completely explain the asymmetry between luminescence and absorption lineshapes. The most prominent difference is $\sim$10 meV splitting of the first phonon replica. This double-peek structure is a famous property of the diamond NV center [136]. The origin of this double-peak is still a subject of some debate. It was often attributed to the Jahn–Teller effect. However, Davies and Hammer [136] obtained the same polarization for the double peak and the ZPL in their uniaxial stress measurements. This implicates that the double-peak is associated with totally symmetric a_1 modes. Davies and Hammer [136] attributed this splitting to tunneling of nitrogen between identical positions of vacancy. However, Gali *et al.* [104], in their *ab initio* study, calculated the potential energy barrier to be greater than 4 eV, which is about two orders of magnitude larger than proposed by Davies and Hammer [136]. Abtew *et al.* [111], in their *ab initio* study, analyzed the dynamic Jahn–Teller effect in a single effective mode approximation. They attributed the splitting of the first phonon replica to the third and the fourth excited vibronic states of symmetry A_2 and E. However, more detailed analysis shows (not presented here) that the transition to E level is forbidden. This can also be deduced from Figure 2.4. The dimensionless

vibronic coupling constant obtained by Abtew *et al.* [111] is $K^2 = 0.35$. The E vibronic level corresponds to the first level of $j = 5/2$. As discussed in Section 2.5.3, in the zero-temperature limit, the excitation can only occur to vibronic $j = 1/2$ states. Therefore, the transition is forbidden and does not explain double peak splitting.

3.2.4 Discussion

The results above demonstrate that the vibrational structure of defects calculated in the supercell geometry can help to explain general features of optical lineshapes. This is particularly true for the luminescence spectrum of the diamond NV^- center. However, localization ratios are not strictly physical quantities, and the direct comparison with an experiment should be taken cautiously. First of all, higher localization does not assuredly lead to a stronger electron–phonon interaction, as this interaction depends on other parameters and symmetry properties (see Section 2.6 and Chapter 4 for more details).

Furthermore, in such moderate-sized supercells, calculated resonant modes are still not sufficiently converged. Let us take the ground state vibrational structure as an example. In Fig. 3.3, each resonance contains only a few strongly localized modes, which are scarcely distributed in a small region of frequency. If the size of the system increases, the number of contributing modes should also increase.[9] In the continuum limit, each resonance should contain an infinite number of modes distributed in some frequency domain. For calculation of optical lineshapes, the continuum limit can be approximated by smoothing spectral densities of a finite system (e.g., by replacing δ-functions of Eq. (2.152) with Gaussian of small width). However, as noted by Alkauskas *et al.* [109], such small supercells are not sufficient for calculations of high accuracy resolution. For example, the lowest frequency mode in $4 \times 4 \times 4$ supercell is $\sim$35 meV (see Figs. 3.3 and 3.5). The resulting calculations of optical lineshapes can therefore not contain any contributions of lower energy modes. In contrast, the optical lineshapes (see Figs.3.4 and 3.6) clearly show contributions of phonons down to zero frequencies.

We postpone the calculation of optical lineshapes to Chapter 4. In the following sections of this chapter, we focus on the vibrational structure of defects.

[9] Note that the amplitude of each mode is of order $N_{\mathrm{n}}^{-1/2}$ and decreases with the system size (see Sec. 2.4.3).

3.3 Embedding methodology

We solve the issue of small supercells by the use of the embedding methodology. This methodology enables to compute defect vibrational modes for supercells $N \times N \times N$ with $N > 5$ for which direct *ab inito* calculations are too expensive. Such methodology was first introduced by Alkauskas *et al.* [109], where the vibrational structure of NV^- ground state was calculated to model the luminescence lineshape. The improvement of this methodology was one of the primary goals of my doctoral years.[10]

3.3.1 Description and justification

The embedding methodology relies on the fact that interatomic interactions in semiconductors are short-ranged. When the atom is displaced from the equilibrium position (as it is done in the finite-difference approach), the induced force on the neighboring atom decays fast as a function of a distance from the displaced atom. This property enables us to construct a Hessian matrix of large supercell as described below.

First, we use the translational symmetry of a pure bulk and construct the bulk Hessian matrix of a large supercell. Let us assume that the cutoff radius, r_{c1}, defines the range after which interatomic interactions in solid become negligible. If the distance between two atoms in a large supercell is smaller than r_{c1}, we take the value of the Hessian matrix element from the matching pair in a small supercell. Otherwise, the Hessian matrix element is set to zero. Once the bulk Hessian is constructed, we embed defect interactions in a finite neighborhood of impurity, as shown in Fig. 3.7. This procedure relies on the assumption that the presence of defect only perturbs interatomic interactions for atoms close to the defect. More precisely, we modify the Hessian matrix elements $\mathbf{\Phi}_{nm}$ only if both atoms, n, and m, are separated from impurity sites by a distance smaller than a cutoff radius r_{c2}.

While the procedure is relatively straightforward, it requires some additional corrections related to the symmetry properties of the Hessian matrix (see Section 3.1.2). Setting matrix elements beyond a certain radius to zero breaks Newton's third law:

$$\Phi_{ni;nj} = -\sum_{m \neq n} \Phi_{mi;nj}. \tag{3.14}$$

[10] We developed a software package for defect vibrational structure calculations in large supercells. This code will be made open-source and available for other researchers who work in the computational field of point defects.

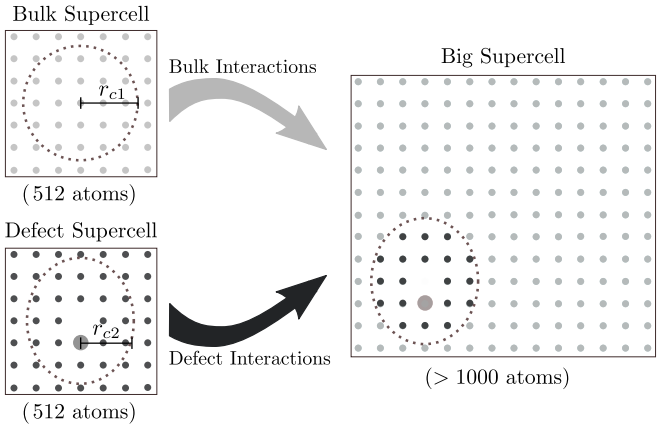

Figure 3.7: Illustration of the embedding methodology for defect vibrational structure calculations.

Breaking this "acoustic sum rule" could introduce a small force on the entire system. This could affect the results for low-frequency acoustic modes. Newton's third law could be enforced by setting each matrix element $\Phi_{ni;nj}$ (diagonal in the atomic index n) to the right-hand side of Eq. (3.14). However, this correction for $i \neq j$ can break the symmetry property (3.2) of the Hessian matrix for $n = m$. To ensure that (i) the symmetry properties of the Hessian matrix are preserved, and (ii) frequency of acoustic modes at the Γ point are equal to 0, we set $\Phi_{ni;nj}$ to the right-hand side of Eq. (3.14) only in the case when Cartesian components are the same, $i = j$.

3.3.2 Vibrations of the diamond NV^- center in the dilute limit

Here we present the vibrational structure calculations of the NV^- center using the embedding methodology.

First, we tested the range of interatomic interactions in diamond by calculating the PBE phonon dispersion lines in the $4 \times 4 \times 4$ supercell. Fig. 3.8 compares dispersion lines of two calculations: black lines ("full") were calculated using the full Hessian matrix from the 512-atom bulk supercell, while for gray lines ("trunc."), Hessian elements were set to 0 for atoms separated by more than 4.2 Å. The maximum difference between the two sets of results is 2.3 meV, which implies that the Hessian matrix is indeed short-ranged, and the accuracy of 2 meV could be achieved by taking the cutoff radius $r_{c1} > 5$ Å. Therefore, for bulk interactions, we chose $r_{c1} = 7$ Å. In the case of r_{c2}, we used a slightly smaller value, $r_{c2} = 5.6$ Å, to reduce the overall computational cost in hybrid HSE calculations.

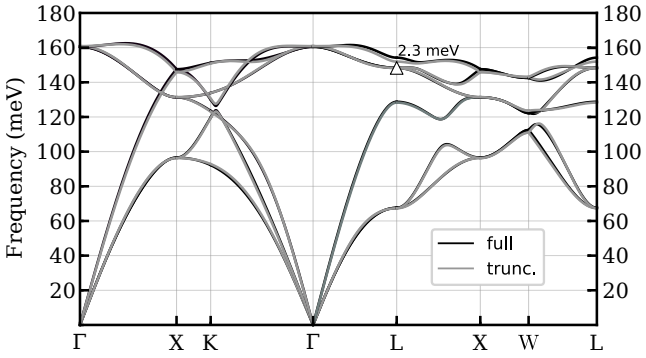

Figure 3.8: Calculated phonon dispersion of bulk diamond. In "full" we have included the full Hessian matrix, while in "trunc." Hessian matrix elements of atoms separated by > 4.2 Å are set to 0.

The embedding procedure was applied to construct defected supercells up to $N = 20$ (64 000 atomic sites). The calculation of vibrational modes in such large supercells requires diagonalization of dynamical matrices as large as $192\,000 \times 192\,000$. Since these matrices are sparse, with only $\sim 0.5\%$ of nonzero elements, for diagonalization we used the spectrum slicing technique [137] based on the shift-and-invert Lanczos method, as implemented in the SLEPc [138] library. Parallelization was done using an interface to the MUMPS [139] parallel sparse direct solver.

Figure 3.9(a) shows PBE localization ratios β_k calculated in the $20 \times 20 \times 20$ supercell for the diamond NV center's ground state (^3E). In contrast to the $4 \times 4 \times 4$ supercell [Fig. 3.3(a)], we can clearly see the emergence of broader resonances. For example, in the $4 \times 4 \times 4$ supercell, we identified ~ 63 meV mode as a possible source for three phonon replicas. However, calculations in a large supercell yield a broad resonance in the range of 60–80 meV, which is shifted towards higher energies. Also, the first e symmetry resonance is shifted towards lower energies and has a peak at 55 meV. We also see highly localized modes of a_1 symmetry at the edge of the diamond phonon structure. Results calculated using the HSE functional are shown in Fig. 3.9(b). In comparison to PBE calculations, HSE yields slightly higher frequencies and stronger localization. However, as in the previous calculations, the general features are qualitatively similar.

Fig. 3.10 shows localization ratios of vibrational modes in the excited state ^3E. In comparison to ground-state calculations, we see a slightly different vibrational structure. For example, the first a_1 resonance is broader for the excited state in comparison to the ground state, which could explain the asymmetry between the first phonon replica in absorption and emission spectra.

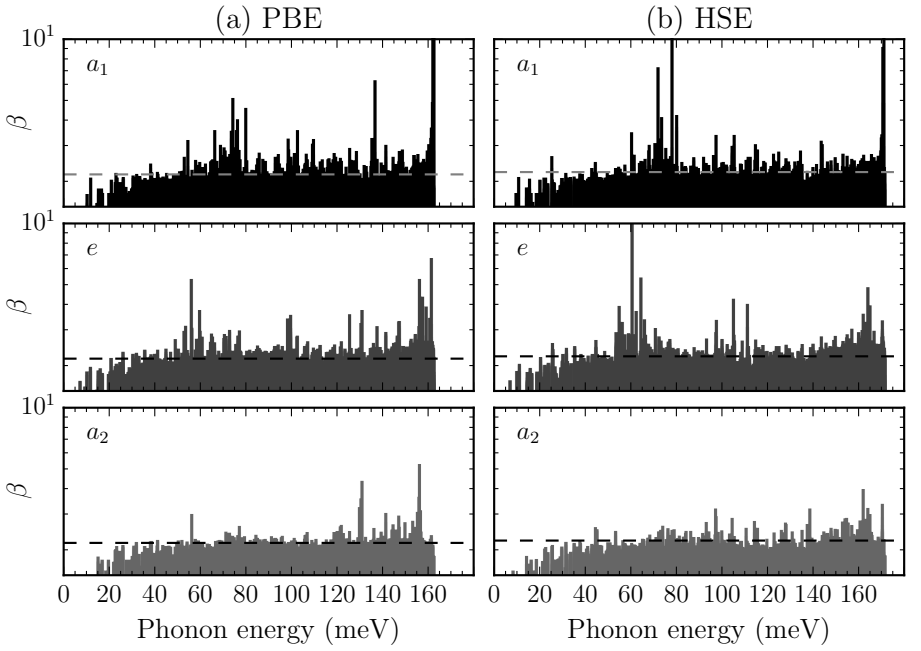

Figure 3.9: Localization ratios of ground state ($^3A_2$) vibrational modes, calculated with (a) PBE and (b) HSE functionals in $20 \times 20 \times 20$ supercell.

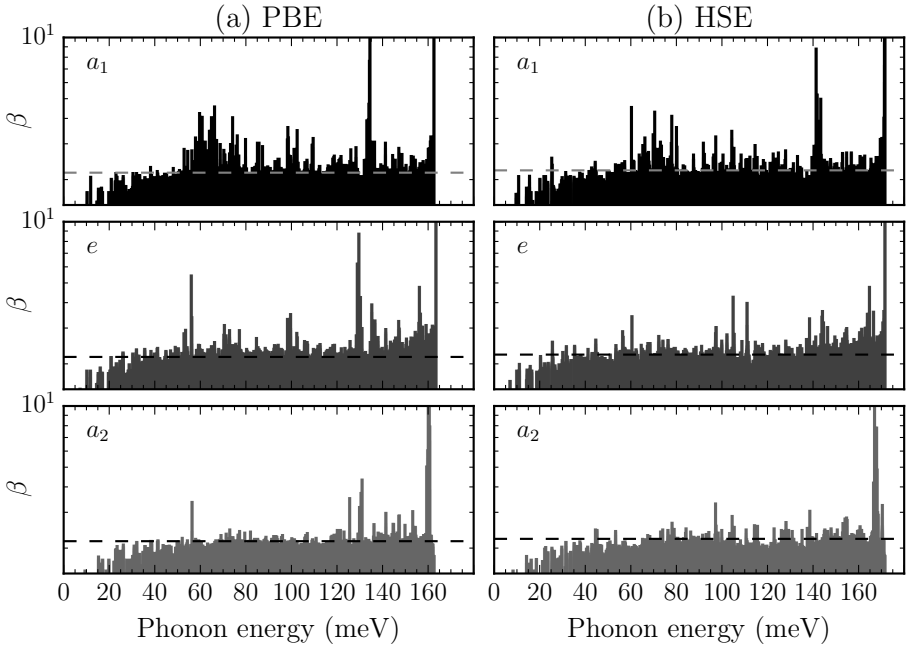

Figure 3.10: Localization ratios of excited state (^3E) vibrational modes, calculated with (a) PBE and (b) HSE functionals in $20 \times 20 \times 20$ supercell.

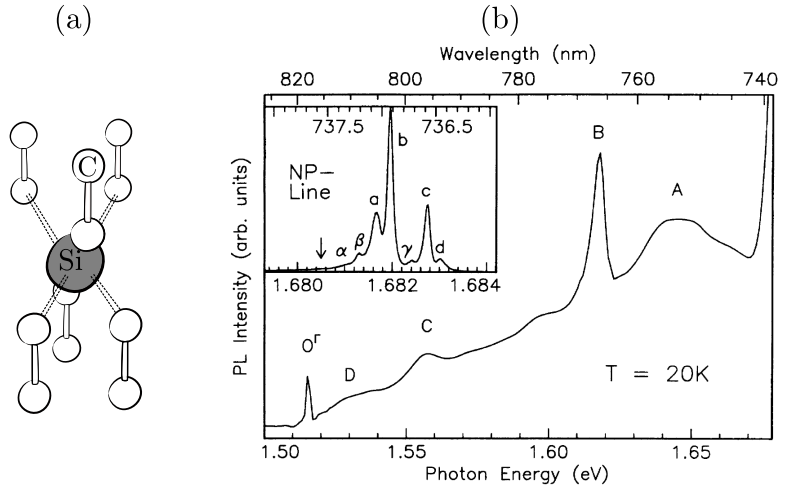

Figure 3.11: (a) Atomic structure of the silicon–vacancy (SiV) center in diamond. (b) Low temperature (20 K) experimental photoluminescence spectra (plot taken from Ref. [142]). Inset shows the fine structure of the ZPL.

3.4 Isotopic shifts of negatively charged silicon-vacancy

This section briefly presents our theoretical study of the vibrational structure of silicon–vacancy (SiV) center in diamond [T1]. Our findings explain several experimental observations and solve the contradiction between previously calculated and measured isotopic shifts in Refs. [140] and [141].

3.4.1 Introduction

The SiV center is formed by removing two neighboring carbon atoms and placing a silicon atom between two vacant sites [see Fig. 3.11(a)]. This configuration is of D_{3d} point group symmetry. SiV center is a bright photoluminescence defect with ZPL energy at 1.681 eV. The luminescence spectrum [see Fig. 3.11(b)] is mainly dominated by the ZPL peak, which contains $\sim 70\%$ of the total emission [142]. It has been established that the luminescence corresponds to a negatively charged defect [60].

A recent experimental study by Dietrich *et al.* [141] showed that phonon replica at 64 meV [peak B in Fig. 3.11(b)] displays an isotope shift that is proportional to the inverse square root of the silicon mass for three different Si isotopes (^{28}Si, ^{29}Si, ^{30}Si). Downward shifts for ^{29}Si and ^{30}Si isotopes were

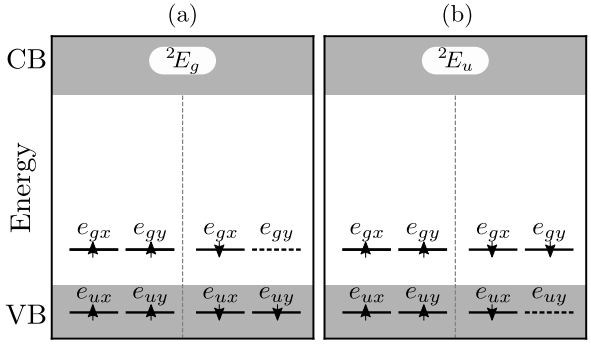

Figure 3.12: Defect-level diagrams of the SiV^- center. Diagrams show Kohn–Sham single-particle configurations for (a) the ground state ^2E_g and (b) the exited state ^2E_u. The spin-majority channel is denoted with upward arrows and the spin-minority channel with downward arrows. Shaded areas correspond to the valence band (VB) and the conduction band (CB).

1.02 meV and 2.21 meV. Earlier first-principles calculations [140] indeed found resonant mode with similar energy (56.5 eV). However, calculated isotope shifts were substantially smaller (0.62 meV for ^{29}Si and 1.24 meV for ^{30}Si). This calls for a deeper analysis of the vibrational structure of SiV. Therefore, here we provide novel *ab initio* calculations of vibrational structure and discuss isotopic shifts of quasi-local modes.

3.4.2 Electronic states

The defect-level diagram of the ground state of SiV^- is shown in Fig. 3.12(a). It is a spin-doublet single determinant configuration ^2E_g. In the molecular orbital picture, the excitation is achieved by promoting an e_u electron from a spin-minority channel to an unoccupied e_g state. The resultant wavefunction has an orbital configuration of ^2E_u symmetry, shown in Fig. 3.12(b). Both electronic states are twofold degenerate and are dynamic Jahn–Teller systems. In this study, we avoid complications associated with the Jahn–Teller effect and use fractional electronic configurations of $e_{ux}^2 e_{uy}^2 e_{gx}^{3/2} e_{gy}^{3/2}$ for the ground state and $e_{ux}^{3/2} e_{uy}^{3/2} e_{gx}^2 e_{gy}^2$ for the excited state. As in the diamond NV center, such fractional configurations avoid vibronic interactions and describe the zero-order Hamiltonian of the vibronic system.

DFT calculations were carried using VASP code [77] and HSE exchange-correlation functional [53]. We used the PAW approach with an energy cutoff

of 400 eV. The Brillouin zone was sampled at the Γ point to ensure that the symmetry of electronic wavefunction is correctly described. The cubic $3 \times 3 \times 3$ supercell (216 sites) was used for actual defect calculations. The calculated ZPL energy for the transition ${}^2E_g \rightarrow {}^2E_u$ is $E_{\mathrm{ZPL}} = 1.72$ eV. This value compares favorably with the experimental value of 1.681 eV.

3.4.3 Vibrational structure

The vibrational structure was calculated using a 216-atom supercell and the same parameters as described above. We used the embedding methodology to model the vibrational structure of supercells $N \times N \times N$ up to $N = 9$ (5832 sites). All the vibrational modes were characterized according to the irreducible representations of the D_{3d} point group ($A_{1g}, A_{1u}, A_{2g}, A_{2u}, E_g$ and E_u).

The localization ratio factors β_k calculated in 5832-atom supercell are shown in Fig. 3.13(a) for the ground (${}^2E_g$) state and in Fig. 3.13(b) for the excited (${}^2E_u$) state. We see that for vibrations of a_{1g}, a_{1u}, a_{2g}, and e_g symmetry, localization ratios are similar to values of bulk modes. Therefore, there are no clearly pronounced quasi-local modes of these symmetries. The situation is entirely different for a_{2u} and e_u modes. For a_{2u} modes, we see clearly pronounced resonances at $\sim$(40–50) meV in the ground state and at $\sim$(50–60) meV in the excited state. As shown in our paper [T1], these resonances are irrespective of the size of the supercell. Analysis of the vibrational shapes shows that in these vibrations, the movement of the Si atom along the symmetry axis is predominant. For e_u symmetry modes, there are pronounced resonances at the $\sim$(50–70) meV in the ground and excited states. The e_u resonance is about two times broader compared to the a_{2u} peak.

To identify the peaks of a_{2u} and e_u resonances, we combine results from different-sized supercells. Figures 3.14(a) and (b) show combined a_{2u} and e_u localization ratios (from $N = 3, 4, 5, 6, 7, 8$ and 9 supercells), respectively, for the ground and excited states. We loosely draw envelope functions to make the interpretation of our results easier.

At the low-temperature limit, the ground state vibrational structure should be reflected in the luminescence spectrum of the defect. However, direct comparison of calculated frequencies with phonon replicas of lineshape should be taken cautiously due to the possible complex nature of electron–phonon interaction.[11] The first resonance in Fig. 3.14(a) is an a_{2u} symmetry peak at $\sim$43 meV. This mode might be the source of the first phonon replica of the

[11] See Section V of our paper [T1] for a more detailed discussion.

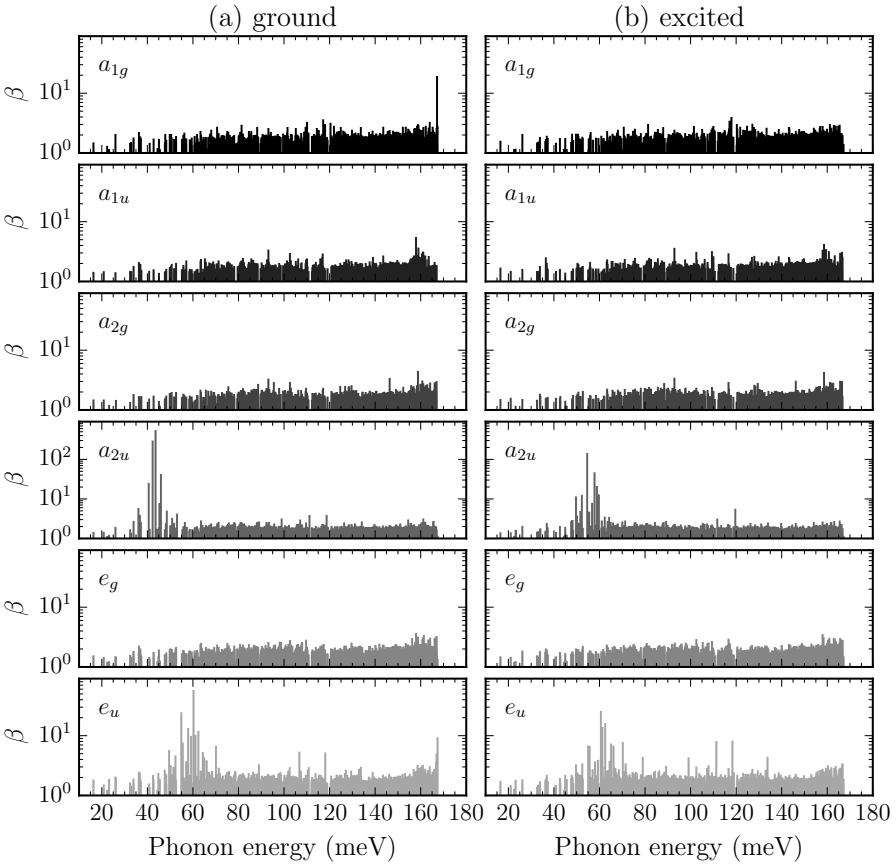

Figure 3.13: Atomic localization ratios of ground (^2E_g) and excited (^2E_u) states of the SiV^- center in $9 \times 9 \times 9$ supercell. The y axis has a logarithmic scale.

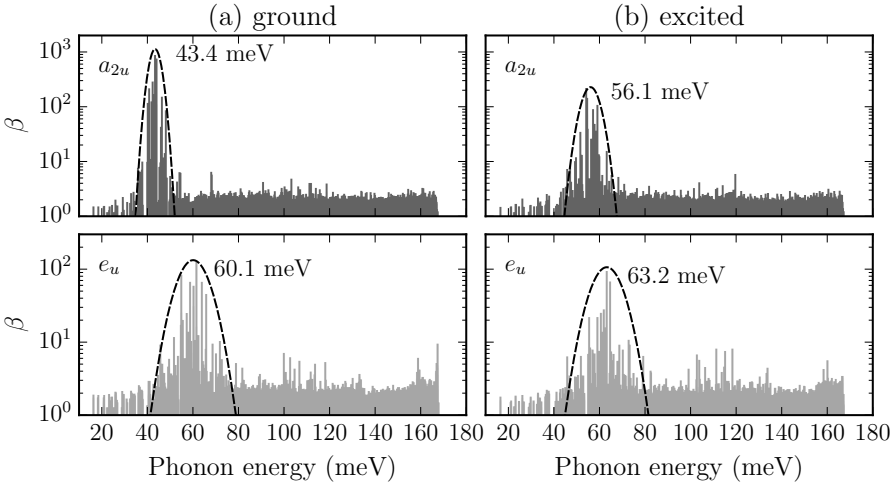

Figure 3.14: Combined localization ratios of ground (^2E_g) and excited (^2E_u) states of the SiV^- center from $N = 3, 4, 5, 6, 7, 8$ and 9 supercells. The y axis has a logarithmic scale.

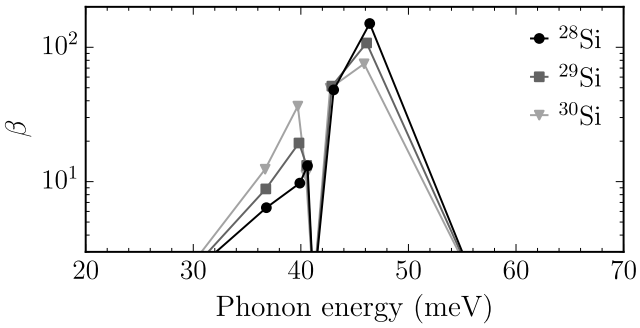

Figure 3.15: Localization ratios for the a_{2u} symmetry quasi-local modes around energy 43 meV for three Si isotopes. Calculations performed for the $5 \times 5 \times 5$ supercell.

luminescence spectrum [see A in Fig. 3.11(b)]. The second e_u peak is located at ∼60 meV. Again, this vibrational mode could be associated with the second phonon replica of the luminescence spectrum [see B in Fig. 3.11(b)].

The energies of corresponding a_{2u} and e_u peaks in the excited state are ∼56 meV and ∼63 meV [see Fig. 3.14(b)]. These peaks are shifted towards the higher energies in comparison to the ground state. The increase of vibrational energies in the excited state can be explained by the electronic structure of the SiV center. The optical excitation corresponds to transferring the electron from a more delocalized orbital e_u to a more localized orbital e_g [85]. This increases the electron density around the Si atom and thus the vibrational energies.

3.4.4 Isotopic shifts

Dietrich *et al.* [141] reported isotopic shifts $\Omega_{28}/\Omega_{29} = 1.016$ and $\Omega_{28}/\Omega_{30} = 1.036$ of sharp phonon replica at 63.8 meV [see B in Fig. 3.11(b)]. These isotope shifts closely correspond to the "ideal" shifts of $\sqrt{29/28} = 1.018$ and $\sqrt{30/28} = 1.036$ (i,e. $\Omega \sim 1/\sqrt{m_{\mathrm{Si}}}$). However, as noted above, in the previous *ab initio* calculations [140], isotopic shifts were substantially smaller.

To explain this discrepancy, we first focus on a_{2u} vibrational resonance of the ground state in the energy range 20–70 meV. Figure 3.15 shows calculated localization ratios for the $5 \times 5 \times 5$ supercell for Si isotopes with $M_{\mathrm{Si}} = 28, 29$, and 30 a.m.u. For each isotope, five vibrations contribute to the quasi-local mode. The vibration with the largest β has energies 46.40, 46.11, and 45.88 meV for ^{28}Si, ^{29}Si, and ^{30}Si isotopes, respectively. The isotope shifts for this most pronounced mode are $\omega_{28}/\omega_{29} = 1.006$ and $\omega_{28}/\omega_{30} = 1.011$.

They are much smaller than the experimental values of 1.018 and 1.036 [141]. However, as can be seen from Fig. 3.15, shifts of a single mode do not explain the behavior of a resonance. As we increase the isotope's mass, we see changes in frequency and localization for individual modes. Most interestingly, the localization of lower-frequency modes tends to increase, while localization of higher frequency modes tends to decrease. We explain the isotope shift of the whole resonance as follows. As the localization ratios redistribute when we change the mass of the Si atom, we associate β with the weight of the contribution of each specific vibration of resonant mode. Then we determine the energy of quasi-local mode Ω as a weighted average of all the modes that contribute to this resonance:

$$\Omega = \frac{\sum_k \beta_k \omega_k}{\sum_k \beta_k}. \tag{3.15}$$

If we now weigh the contribution of localized modes, we get average energies $\Omega_{28} = 44.81$ meV, $\Omega_{29} = 43.90$ meV, and $\Omega_{30} = 42.88$ meV. The isotope shifts are $\Omega_{28}/\Omega_{29} = 1.021$ and $\Omega_{28}/\Omega_{30} = 1.045$.

We performed a similar analysis for all considered supercells and e_u symmetry resonance. We find that the frequency of the most pronounced mode in the resonance has a considerable cell-to-cell variation (qualitative results are presented in our paper [T1]). As we increase the supercell's size, the frequency of the mode oscillates around the average value with amplitude ~ 1.5 meV for small supercells and becomes smaller for larger supercells. However, for the averaged frequency [Eq. (3.15)], the oscillations are smaller, and convergence is much faster. Using this procedure, we determine frequencies of the quasi-local modes as the asymptotic value of Eq. (3.15). In addition, we quantify the width γ of quasi-local mode as:

$$\gamma^2 = \frac{\sum_k \beta_k (\omega_k - \Omega)^2}{\sum_k \beta_k}.$$

Table 3.2 shows our theoretical results for both a_{2u} and e_u resonances. We also include our analysis of the vibrational modes in the excited electronic state (^2E_u). We find that excited-state resonances likewise exhibit nearly "ideal" isotopic shifts.

3.4.5 Discussion

In this section, we briefly discuss how our theoretical calculations compare to experimental measurements. The SiV^- photoluminescence band has two

Theory: vibrational resonances

State	symmetry	Ω_{28} (meV)	γ (meV)	Ω_{28}/Ω_{29}	Ω_{28}/Ω_{30}
^2E_g	a_{2u}	43.4	1.9	1.018	1.035
ground	e_u	60.1	6.1	1.021	1.039
^2E_u	a_{2u}	56.1	3.9	1.016	1.033
excited	e_u	63.2	6.5	1.017	1.036

Experiment: PL phonon sidebands

State	symmetry	Ω_{28} (meV)	γ (meV)	Ω_{28}/Ω_{29}	Ω_{28}/Ω_{30}
^2E_g	a_{2u} (Ref. [143])	63.8	$\sim$5	1.016	1.036
		42	$>$25	ND	ND

Table 3.2: Main results of Ref. [T1] compared with the experiment. Theory: calculated frequencies Ω, widths γ (both for the ^{28}Si isotope), and isotopic shifts of quasi-local A_{2u} and E_u modes in the ground and excited states. Values of frequencies (widths) are given to two (one) significant digits. Experiment: energy Ω, width, and isotopic shifts of vibrational sidebands in the photoluminescence (PL) spectrum. All experimental data from Ref. [141] except where indicated. ND = "not detectable".

prominent phonon side peaks at 63.8 meV and 42 meV (with respective widths $\gamma \approx 5$ meV and $\gamma > 25$ meV [141]) [see Fig. 3.11(b)]. In Ref. [141], a clear isotope shift of 63.8 meV peak with respect to the ZPL line was reported. The 42 meV peak did not show any noticeable changes upon isotope substitution. However, as noted in the same paper [141], the lack of change could have been related to difficulties measuring small differences of broad peaks. Also, it was suggested that the 63.8 meV phonon replica was due to a_{2u} vibration [141, 143].

We focus on the ground state vibrational structure, as it should be revealed in the phonon sideband of the luminescence lineshape. On par with the experiment, our calculations suggest the existence of two resonances, one at 43.4 meV and another one at 60.1 meV. Although these values clearly agree with experimental values of 42 and 63.8 meV, there is a large discrepancy regarding the width of these resonances (see Table 3.2). Also, in our calculations, both resonances undergo isotope shifts $1/\sqrt{m_{\rm Si}}$, while experimental measurement shows only a shift of narrow higher-energy peak. Furthermore, contrary to Refs. [141, 143], our calculations indicated that a narrow peak at 60.1 meV is due to e_u vibrations.

We expect DFT calculations to work well regarding the vibrational structure of the defect. This will be illustrated in Chapter 4, where we present high accuracy optical lineshapes of NV center calculated using the vibrational structure of DFT calculations. Therefore, we tentatively suggest that the experimentally observed 63.8 meV peak is, in fact, of e_u symmetry and not a_{2u}. In this case, our calculations agree with the experiment regarding frequency, width, and isotopic shift of the resonance (see Table 3.2). Furthermore, we hypothetically propose that calculated a_{2u} resonance does not appear in the PL spectrum, and experimental phonon replica at 42 meV is not related to quasi-local modes.

Furthermore, we note that in the adiabatic approximation, only a_{1g} modes are expected to participate in the optical transition. These modes have no pronounced optical signatures in the PL spectrum. In the case of JT coupling, our group-theoretical analysis shows that only e_g modes participate in the vibronic coupling. Therefore, an optical transition between degenerate states should involve such symmetry modes, leaving the appearance of e_u resonance unexplained. This requires alternative coupling mechanisms. We tentatively hypothesize that the appearance of e_u modes could be explained by the Herzberg–Teller effect [144], whereby vibration modulates transition dipole moment. However, quantitative interpretation of the luminescence lineshape of the SiV center requires a more detailed study of optical transitions.

3.5 Summary and conclusions

This chapter presented an *ab initio* methodology to calculate the vibrational spectrum of deep-level defects in the dilute limit. We applied this methodology to the nitrogen–vacancy (NV) and silicon–vacancy (SiV) centers of diamond. The main achievements of the study presented in this chapter are summarized as follows:

1. We presented a practical *ab initio* methodology for calculating primary force constants for the Jahn–Teller active system using fractional occupation of single-particle states (Sec. 3.2.2).
2. We have developed a parallel code (suitable for high-performance calculations) for an embedding procedure, which allows calculations of vibrational modes for deep-level defects in the dilute limit. Using this code, we modeled the vibrational spectrum of defects in supercells as large as 64 000 atoms.

3. We have studied the vibrational spectrum of the negatively charged SiV center in diamond using density functional theory calculations (Sec. 3.4). This work was published in the dissertation paper [T1]. The main findings of this study are:

   a) We have found two pronounced vibrational resonances of a_{2u} and e_u symmetry.
   b) We presented a new methodology to calculate isotope shifts of vibrational resonances.
   c) We assume that the observed experimental feature in the photoluminescence spectrum at 63.8 meV is a quasi-local mode of e_u symmetry.
   d) We hypothesize that the appearance of the e_u mode in the photoluminescence spectrum could be explained by the Herzberg–Teller effect.

Thesis Statement (I)

We suggest that the experimentally observed sharp vibrational feature in the photoluminescence spectrum of SiV^- is an e_u-symmetry vibrational resonance. The appearance of this feature in the experimental spectrum cannot be explained in the Frank–Condon approximation. We hypothesize that this peak is due to the Herzberg–Teller effect, whereby the vibration modulates the optical transition dipole moment.

Chapter 4

LUMINESCENCE AND ABSORPTION LINESHAPES OF DIAMOND NV^- CENTER

Nobody knows where you are
How near or how far
Shine on you crazy diamond
— Pink Floyd,
Shine On You Crazy Diamond

This chapter presents our *first-principle* calculations of optical lineshapes of triplet transition in the diamond NV^- center [T2]. The main goal of this study is a high accuracy description of electron–phonon interaction utilizing density functional theory calculations. The chapter is organized as follows. In Section 4.1, we formulate the general problem of the calculation of optical lineshapes. In Section 4.2, we present our analysis of the electron–phonon coupling to a_1 symmetry vibrational modes. Section 4.3 discusses the vibronic coupling to e symmetry modes and proposes a practical methodology to solve the multi-mode $E \otimes e$ Jahn–Teller problem. The luminescence and absorption lineshapes are presented and compared to the experiment in Section 4.4. Finally, Section 4.5 summarizes our results and discusses possible sources of the remaining discrepancies between experiment and theory.

4.1 General formulation

The general theory of optical lineshapes has been presented in Section 2.6. In the triplet transition of the diamond NV center, only a_1 and e symmetry modes participate in the electron–phonon interaction. Therefore, the main parameters are respective spectral functions of electron-phonon coupling, $A^{a_1}(\omega)$, and $A^{e}(\omega)$. These functions are defined by Eqs. (2.144) and (2.157) for the luminescence process and Eqs. (2.145) and (2.158) for the absorption process. The overall

spectral function $A(\omega)$ is a convolution of both contributions [see Eq. (2.156)]. Once the spectral functions are determined, the emission probability and absorption cross-section are calculated using Eqs. (2.147) and (2.149). In this study, we will not deal with absolute intensities and cross-sections but rather normalized lineshapes. Those are given by:

$$L_{\text{em}}(\omega) = N_1 \omega^3 A_{\text{em}}(\omega), \tag{4.1}$$

for emission and

$$L_{\text{abs}}(\omega) = N_2 \omega A_{\text{abs}}(\omega), \tag{4.2}$$

for absorption. Here, N_1 and N_2 are normalization constants. Therefore, the central task of this chapter is the evaluation of Eqs. (4.1) and (4.2).

4.2 Coupling to a_1 modes

As a first step, let us focus on calculating spectral functions, $A^{a_1}(\omega)$, that describe the coupling to totally symmetric a_1 modes. Since the Jahn–Teller effect in the excited ^3E state of the NV^- center is not strong [111], this spectral function governs the general features of optical lineshapes.

The methodology for the evaluation of $A^{a_1}(\omega)$ has been discussed in Section 2.6.4. In short, we adopt the equal mode approximation, which simplifies the calculation of the Fourier transform of spectral function $G(t) = \int A(\omega) e^{i\omega t} \, \mathrm{d}\omega$ [see Eq. (2.151) for luminescence and Eq. (2.154) for absorption]. Evaluation of $G(t)$ involves the calculation of partial Huang–Rhys factors S_k and resultant densities of electron–phonon coupling $S_{a_1}(\omega)$ [see Eqs. (2.133) and (2.152)]:

$$\begin{aligned} S_k &= \frac{\omega_k \Delta Q_k^2}{2}, \\ S_{a_1}(\omega) &= \sum_{k \in A_1} S_k \delta(\omega - \omega_k). \end{aligned} \tag{4.3}$$

Here, ω_k is the angular frequency of the mode k, and ΔQ_k is given by equation (2.131). Calculation of ΔQ_k requires the knowledge of shapes of vibrational modes, $\boldsymbol{\eta}_k$, as well as the change of equilibrium geometry between the ground and the excited state, $\Delta \mathbf{R} = \mathbf{R}_e^0 - \mathbf{R}_g^0$.

After determining HR factors, we replace delta functions $\delta(\omega - \omega_k)$ in Eq. (4.3) with a small-width Gaussians to obtain smooth density $S_{a_1}(\omega)$ throughout the whole vibrational spectrum.

4.2.1 Vibrational modes and lattice relaxations

Section 3.3.2 of the previous chapter presented the vibrational structure calculations for triplet states of the diamond NV center. We showed that for an accurate description of the phonon structure, one needs to use very large supercells, as the vibrational modes and resonances are poorly described in small-sized supercells, especially in frequency regions where the density of states is low. Therefore, we used the embedding methodology to obtain vibrational modes for supercells up to $64\,000$ atoms.

However, we encounter a similar problem for the lattice geometry relaxation, $\Delta\mathbf{R}$, caused by the optical transition. Relaxations have the lattice's periodicity in supercell geometry, and the cell's size restricts the lowest spatial Fourier component. Therefore, in moderate-sized supercells, the geometric relaxation is smaller than the actual relaxation of an infinite system. We address this problem by noting that within the harmonic approximation, ΔQ_k can be alternatively expressed in terms of atomic forces:

$$\Delta Q_k = \frac{1}{\omega_k^2} \sum_\alpha \frac{\mathbf{F}_\alpha}{\sqrt{M_\alpha}} \boldsymbol{\eta}_{k;\alpha}. \tag{4.4}$$

In this equation, $\mathbf{F}_\alpha$ is the force on atom α induced by the electronic transition. As only atoms in the close neighborhood of defect experience the change in the force, $\mathbf{F}_\alpha$ decays much more rapidly with distance from the defect center than $\Delta\mathbf{R}_\alpha$.[1] Therefore, we calculate ΔQ_k using forces directly calculated in moderate-sized supercell (in this case, $4 \times 4 \times 4$) and vibrational modes of the embedded supercell.[2]

4.2.2 Results: luminescence

We calculate spectral functions for the emission process using vibrational modes of the ground state and forces induced by the transition ${}^3E \to {}^3A_2$.[3] As a first step, we calculate spectral densities of electron–phonon coupling $S_{a_1}(\omega)$ for different-sized supercells and check the convergence of lineshapes. Fig. 4.1

[1] Once atoms start to move under the influence of these short-ranged forces, the resulting displacements $\Delta\mathbf{R}_\alpha$ become long-ranged.

[2] We tested that the contributions to the spectral density of electron–phonon coupling are already converged if we ignore the forces for atoms further than 7 Å from the defect site.

[3] In the equal mode approximation, the state's choice for vibrational structure is ambiguous as both states should have the same structure. However, this is not the case in actual calculations, as the frequencies of both electronic states differ. Our paper [T2] shows that the best approximation for the zero-temperature limit is choosing the final electronic state for vibrational modes and induced forces.

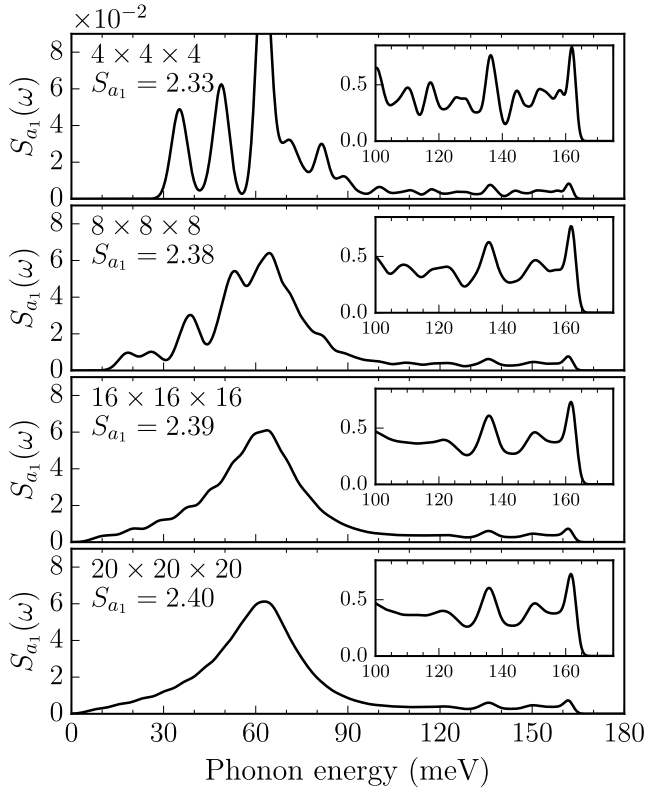

Figure 4.1: Convergence of spectral densities $S_{a_1}(\omega)$ (in units 1/meV) due to coupling to a_1 phonons with respect to the supercell size. Supercells range in size from $4 \times 4 \times 4$ (512 atomic sites) to $20 \times 20 \times 20$ (64 000 sites). Total Huang–Rhys factors for each supercell are also given. The insets enlarge the high-frequency part. Gaussian smearing with varying σ was used, as explained in the text.

shows how the spectral density $S_{a_1}(\omega)$ converges as a function of the supercell size. The results are obtained using PBE functional. The δ-functions in Eq. (4.3) were replaced by Gaussians of variable width. This artificial smoothing was chosen to obtain smooth function in low energy regions (where the density of phonon states is still low) and high resolution in the high-frequency tail (where the density of states is high). Our benchmarks show that choosing σ to vary linearly from $\sigma = 3.5$ meV for $\omega = 0$ to $\sigma = 1.5$ meV for the highest-energy frequency results in a smooth lineshape without introducing any artifacts. This smearing procedure is used for all spectral densities of this chapter.

From Fig. 4.1, we see that for the high-frequency phonons (>120 meV) the spectral densities are already converged for the $8 \times 8 \times 8$ supercell. However, large supercells are needed for a high-resolution description of spectral densities

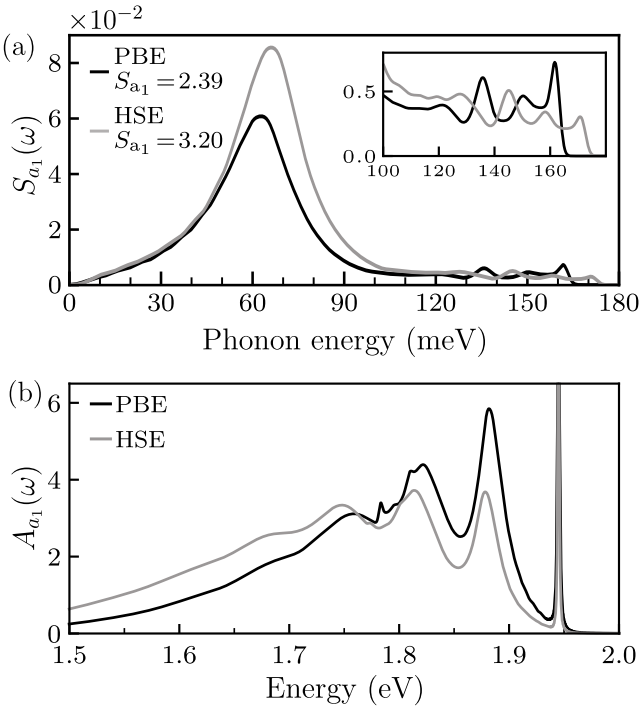

Figure 4.2: (a) Spectral densities $S_{a_1}(\omega)$ (in units 1/meV) due to coupling to a_1 phonons for luminescence, calculated with PBE and HSE functionals. Huang–Rhys factors are also given. The inset enlarges the high-frequency part. (b) Spectral functions $A_{a_1}(\omega)$ [in units 1/eV, Eq. (2.144)] for luminescence calculated using PBE and HSE. The ZPL energy is set to the experimental value.

for coupling with low frequency (<60 meV) phonons. This is the essence of our embedding methodology.

PBE and HSE spectral densities for the $20 \times 20 \times 20$ supercell are shown in Fig. 4.2(a). We see that the functionals provide slightly different results. HSE yields 30% stronger electron–phonon interactions (as can be seen from the total HR factor). In accord with the vibrational structure analysis of Sec. 3.3.2, the most prominent features are shifted towards higher phonon energies.

Corresponding PBE and HSE spectral functions $A_{a_1}(\omega)$ are shown in Fig. 4.2(b). These functions were calculated using Eqs. (2.151) and (2.155). For a better comparison with the experiment, we used the experimental value of the ZPL energy $E_{\mathrm{ZPL}} = 1.945$ eV and $\gamma = 0.3$ meV. Since the actual lineshapes contain additional contributions from e symmetry phonons, we leave the direct comparison with the experiment to Section 4.4.

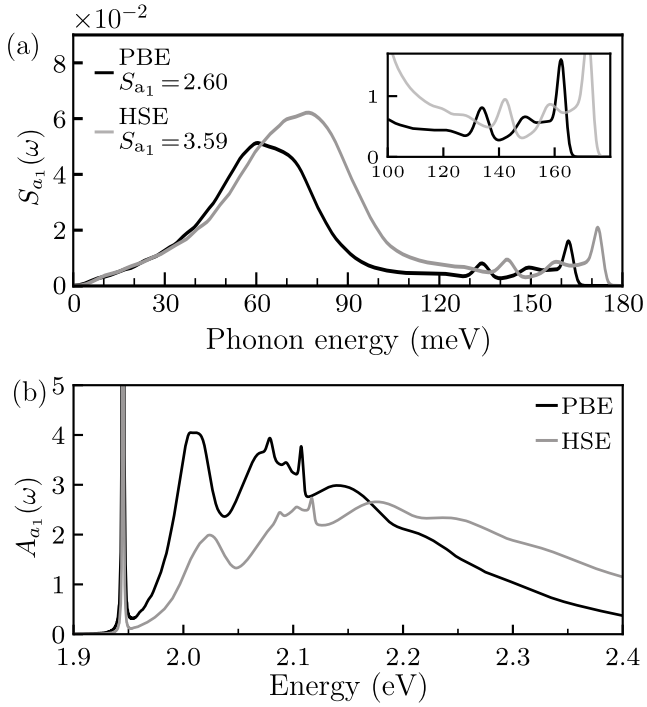

Figure 4.3: (a) Spectral densities $S_{a_1}(\omega)$ (in units 1/meV) due to coupling to a_1 phonons for absorption, calculated with PBE and HSE functionals. Huang–Rhys factors are also given. The inset enlarges the high-frequency part. (b) Spectral functions $A_{a_1}(\omega)$ [in units 1/eV] for absorption calculated using PBE and HSE. The ZPL energy is set to the experimental value.

4.2.3 Results: absorption

The calculations of spectral function $S_{a_1}(\omega)$ for the absorption process require vibrational modes and forces of the excited state. Forces $\mathbf{F}_\alpha$ should be calculated using an orbital configuration of the excited state at the geometry of the ground state. However, in DFT calculations, there are issues related to the convergence of electronic structure calculations for degenerate states. Therefore, to avoid these issues, we calculate these forces indirectly, using Harmonic relation:

$$\mathbf{F}_\alpha = \sqrt{M_\alpha} \sum_k \omega_k^2 \boldsymbol{\eta}_{k;\alpha} \Delta Q_k, \tag{4.5}$$

where ω_k and $\boldsymbol{\eta}_{k;\alpha}$ are calculated in the $4 \times 4 \times 4$ supercell of diamond, and ΔQ_k is given by Eq. (2.131) (see Sec. VI.C of our paper [T2] for a more detailed explanation).

Figure 4.3(a) shows spectral densities $S_{a_1}(\omega)$ for absorption in the case of the $20 \times 20 \times 20$ supercell. There are slightly larger differences between

the shapes of spectral densities calculated in PBE and HSE in this case. PBE calculations produce a broad peak at $\sim$60 meV, which shifts to $\sim$70 meV in HSE calculations. Corresponding spectral functions were calculated using Eq. (2.154) and are shown in Fig. 4.3(b). The comparison with the experimental spectrum is left for Section 4.4.

4.3 Coupling to e modes

In the case of diamond NV center, the coupling to e symmetry modes occurs because of the dynamic Jahn–Teller (JT) effect in the ^3E state.[4] The spectral functions $A^e(\omega)$ of e symmetry modes are given by equations (2.157) and (2.157), respectively, for the emission and absorption process. To find these spectral functions, we must first solve the vibronic problem for the excited state ^3E (see Section 2.5 for a formal introduction to the vibronic problem).

4.3.1 Calculation of coupling parameters

In Sections 3.2 and 3.3.2, we already discussed the zero-order solution of the vibronic Hamiltonian for the diamond NV center. Section 2.5.3 presented our formal analysis of the JT problem in the ^3E state and derived the expression for the matrix element of JT perturbation $\hat{H}^{\text{JT}}$ [Eq. (2.100)]. Calculation of these elements requires the knowledge of linear vibronic constants (2.65). In this section, we present a novel *ab initio* methodology to calculate these vibronic coupling constants.

While discussing actual DFT calculations of the JT system in Section 3.2.1, we showed that the relaxation along symmetry breaking coordinates follows the surface of the potential energy term of the vibronic Hamiltonian [see Eq. (3.8)]. The minimum of this potential is given by equation (3.10). This equation enables the determination of V_k and thus K_k once ΔQ_k is known:

$$K_k^2 = \frac{\omega_k \Delta Q_k^2}{2}, \tag{4.6}$$

where:

$$\Delta Q_k^2 = \Delta Q_{kx}^2 + \Delta Q_{ky}^2.$$

Here, components ΔQ_{kx} and ΔQ_{ky} belong to e symmetry modes and are calculated using Eq. (4.4), as in the case of a_1 relaxation.

[4] The dynamical nature of the JT effect was confirmed by the $\sim T^5$ broadening of the ZPL [145].

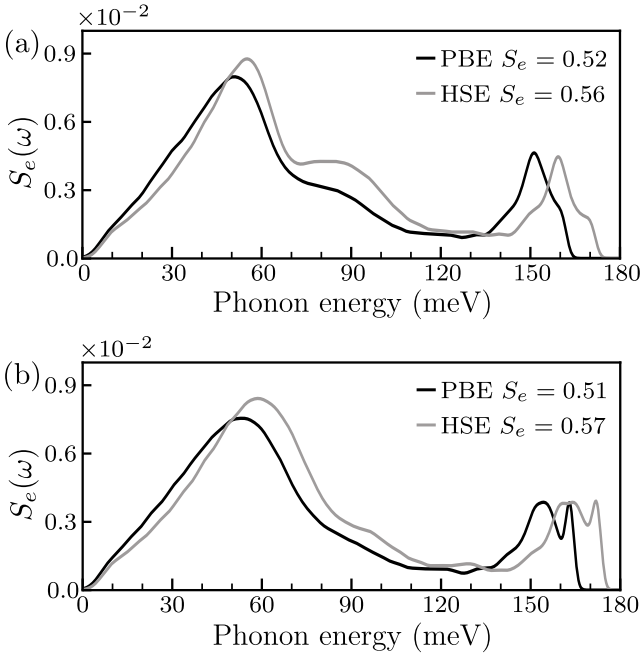

Figure 4.4: Spectral density $S_e(\omega)$ (in units 1/meV) due to coupling to e phonons for (a) luminescence and (b) absorption, calculated with PBE and HSE functionals. Results are for the $20 \times 20 \times 20$ supercell. The total strengths $S_e = \int_0^\infty S_e(\omega)\,\mathrm{d}\omega$ are also given.

Comparing Eq. (4.6) with Eq. (2.133), we see that parameter K_k^2 plays a similar role to the partial HR factor S_k of coupling to a_1 modes. Therefore, in analogy to Eq. (2.152), we define a spectral density of coupling to e symmetry modes:

$$S_e(\omega) = \sum_k K_k^2 \delta(\omega - \omega_k),$$

where the summation runs over all doublets of e symmetry. The integral of $S_e(\omega)$ quantifies the strength of JT coupling in a system:

$$S_e \equiv \int_0^\infty S_e(\omega)\,\mathrm{d}\omega = \sum_k K_k^2.$$

The Jahn–Teller interaction is considered weak for $S_e \ll 1$ and strong in the case of $S_e \gg 1$ [27].

The spectral densities of coupling to e symmetry modes for the $20 \times 20 \times 20$ supercell are shown in Fig. 4.4. Both PBE and HSE functionals yield very similar results for vibronic coupling. Furthermore, lineshapes and total strengths of the vibronic coupling are very alike for the ground and excited states. From S_e values, we see that the JT interaction is of medium strength ($S_e \approx 0.5$).

4.3.2 Luminescence and absorption processes

The solution of the vibronic problem $\hat{H}^{\mathrm{vibr}} = \hat{H}^0 + \hat{H}^{\mathrm{JT}}$ [see Eq. (2.93)] yields the vibronic wavefunctions in the form:

$$|\Phi_{et}\rangle = \left|\chi^+_{et}\right\rangle |E_+\rangle + \left|\chi^-_{et}\right\rangle |E_-\rangle \,,$$

where t labels different vibronic states. Nuclear components $|\chi^{\pm}_{et}\rangle$ are expressed in the basis of vibrational harmonic oscillator states of the zero-order Hamiltonian $\hat{H}^0$:

$$\left|\chi^{\pm}_{et}\right\rangle = \sum_{\boldsymbol{nl}} C^{\pm}_{et;n_1 l_1 \ldots n_N l_n} |n_1 l_1, \ldots, n_N l_N\rangle \,. \tag{4.7}$$

Note that we use a chiral basis for the description of phonon states (see Sec. 2.5.3). The calculation of spectral functions $A^e(\omega)$ in the zero-temperature limit requires the evaluation of $\langle\chi^{\pm}_{et}|\chi_{e0}\rangle$ for the absorption process and $\langle\chi^{\pm}_{e0}|\chi_{er}\rangle$ for the emission process [see Eqs. (2.157) and (2.158)].

In the zero-temperature limit, overlaps for the luminescence spectrum are calculated between the lowest vibronic level of the excited electronic state $|^3E\rangle$ and all the vibrational states of the electronic ground state $|^3A_2\rangle$. On the other hand, for absorption, overlap integrals are calculated between zero-phonon state $|00\ldots00\rangle$ of the $|^3A_2\rangle$ manifold and vibronic states the $|^3E\rangle$ manifold. In Section 2.6.4, we showed that for both processes, the relevant vibronic states are ones with the pseudospin value $j = \pm 1/2$, which significantly simplifies the computational effort.

As for the a_1 coupling, we adopt the equal mode approximation (Sec. 2.6.2) and choose the vibrational modes and frequencies of the ground state for the luminescence and those of excited manifold for the absorption.

4.3.3 Methodology for multi-mode Jahn–Teller coupling

Now, let us summarize the general methodology for treating the JT problem for the diamond NV^- center. First, in Section 2.5.3, we reformulated the JT problem for the ^3E state in terms of chiral phonons and showed that the problem could be decoupled for different pseudo spin values j. While discussing optical matrix elements, we showed that we only need to consider vibronic states of $j = \pm 1/2$ in the zero-temperature limit. Therefore, the matrix of vibronic Hamiltonian involves only the zero-order basis $|n_1 l_1, \ldots, n_N l_N; E_{\pm}\rangle$, where $\sum_k l_k + j_{\mathrm{el}} = \pm 1/2$. In constructing the basis set, we limit the total number of vibrational excitations to specific number $n_{\mathrm{tot}} = \sum_k n_k$. By increasing this number, we can track the convergence of the final result. For a set of lowest

vibronic states, this convergence is easily achieved in the case of diamond NV center, as the vibronic interactions are weak.

However, we are still facing a huge computational problem: in the case of the NV center, we have an extremely large number of e modes that participate in the JT problem. In the actual system, this set is effectively infinite and is described by the spectral density $S_e(\omega)$. For a discrete number of modes, we can calculate smooth spectral functions (2.157) and (2.158) by replacing δ-functions with Gaussians of small width. However, the practical diagonalization of $\hat{H}^0 + \hat{H}^{\text{JT}}$ is impossible for $N > 100$ modes. To address this problem, we propose the following methodology.

We approximate the actual spectral density $S_e(\omega)$ with an effective one:

$$S_e^{(\text{eff})}(\omega) = \sum_{n=1}^{N_{\text{eff}}} \bar{K}_n^2 g_\sigma(\omega_n - \omega). \tag{4.8}$$

Here, the sum runs over N_{eff} "effective" modes with frequencies ω_n and coupling strengths $\bar{K}_n^2$. g_σ is a Gaussian function of width σ. For a selected number of effective modes, N_{eff}, the parameters $\bar{K}_n^2$, ω_n, and σ are obtained by minimizing the integral:

$$I = \int_0^\infty \left| S_e(\omega) - S_e^{(\text{eff})}(\omega) \right| \, \mathrm{d}\omega. \tag{4.9}$$

During the minimization, we constraint the total value of vibronic coupling to the actual one:

$$\sum_{n=1}^{N_{\text{eff}}} \bar{K}_n^2 = \sum_{k=1}^{N} K_k^2 = S_e.$$

For $N_{\text{eff}} = N$, this approach reproduces the result of a full calculation. However, one can expect that the convergence of the final result can be achieved for $N_{\text{eff}} \ll N$, for which the problem is tractable by the diagonalization procedure.

We test the convergence of this approximation by considering NV vibrational modes of the $2 \times 2 \times 2$ supercell (64 sites). Such a system can be solved by direct diagonalization, as it contains only 62 e vibrational doublets. In Fig. 4.5, we show the approximation of $S_e(\omega)$ with $S_e^{(\text{eff})}(\omega)$ for $N_{\text{eff}} = 2, 4, 8$. We see that in the case of $N_{\text{eff}} = 8$, the approximate spectral density $S_e^{(\text{eff})}(\omega)$ is almost identical to the real spectral density $S_e(\omega)$.

For the diagonalization of the Jahn-Teller Hamiltonian, we restrict $n_{\text{tot}} = 3$. Although such a basis is not completely converged with respect to n_{tot}, it is sufficient for testing purposes, as we keep the same n_{tot} for all calculations. Fig. 4.6 shows the resulting spectral functions $A_e(\omega)$ for emission (left) and absorption (right). We used 6 meV Gaussian smoothing. The effective spectral

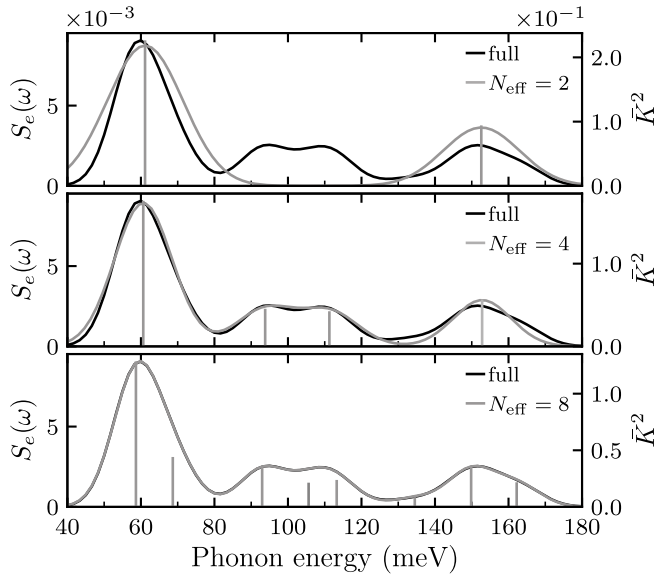

Figure 4.5: Convergence of $S_e^{(\text{eff})}(\omega)$ towards $S_e(\omega)$ when increasing the number of effective modes N_{eff}. The results are for the NV center in the $2 \times 2 \times 2$ supercell. Spectral densities in units 1/meV.

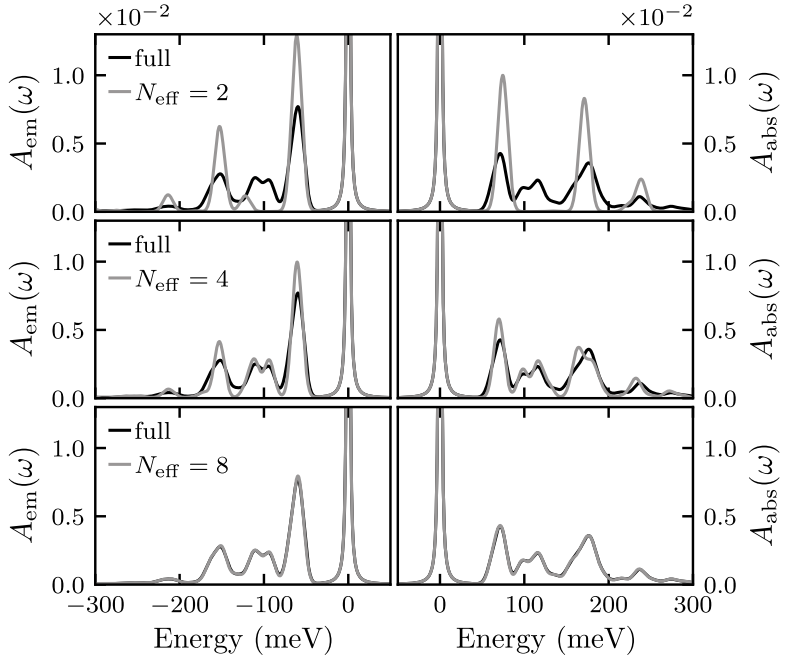

Figure 4.6: Convergence of the spectral function $A_e(\omega)$ [in units 1/meV] for emission (left) and absorption (right) as a function of N_{eff}, the number of effective e modes included in the calculation. The results are for the NV center in the $2 \times 2 \times 2$ fcc supercell.

functions $S_e^{(\mathrm{eff})}(\omega)$ are compared to those calculated from $S_e(\omega)$ that include *all* vibrations for the given supercell. We see that the result with $N_{\mathrm{eff}} = 8$ reproduces the "all-mode" calculations very accurately. This result justifies our methodology for the largest supercell for which the full calculation is still possible. It is reasonable to assume that this methodology applies to a more general case, where we have a quasi-infinite number of vibrational modes.

4.3.4 Spectral functions for absorption and emission

Finally, we discuss the spectral functions $A_e(\omega)$ pertaining to e symmetry modes obtained from $20 \times 20 \times 20$ supercells. We used $N_{\mathrm{eff}} = 22$ to approximate the actual spectral densities of Fig. 4.4. The results for luminescence are shown in Fig. 4.7. In the figure, we compare $A_e(\omega)$ obtained via the solution of the multi-mode JT problem (labeled "JT") with the one obtained via the Huang–Rhys approach (labeled "HR") of the adiabatic problem. Latter spectral functions are obtained in a manner completely identical to those of a_1 modes, as described in Section 4.2.

Somewhat unexpectedly, the HR calculation yields spectral functions almost identical to those of the JT calculation. The agreement between the two calculations is remarkable, and one is tempted to conclude that there is a deep underlying reason for this. However, in the Appendix of our paper [T2], we show that the agreement is to some degree accidental and can only happen in the range $S_e \approx 0.5$–1.0. We conclude that the Huang–Rhys approach applied to symmetry breaking modes can lead to errors in the case of smaller or higher values of S_e and should not be applied in the general case.

The spectral functions $A_e(\omega)$ for the absorption process are shown in Fig. 4.8. In contrast to luminescence, the Jahn–Teller treatment differs substantially from the Huang–Rhys theory. This difference partially stems from the fact that we need to account for multiple vibronic states, and not just the ground state, as for the emission process. Compared to the HR function, the JT spectral function is "stretched" to higher energies.

4.4 Optical lineshapes

This section presents our final calculated luminescence and absorption lineshapes (obtained via Eqs. (2.156), (4.1), and (4.2)). In Table 4.1, we summarize the calculated Huang–Rhys factors and strengths of the vibronic coupling

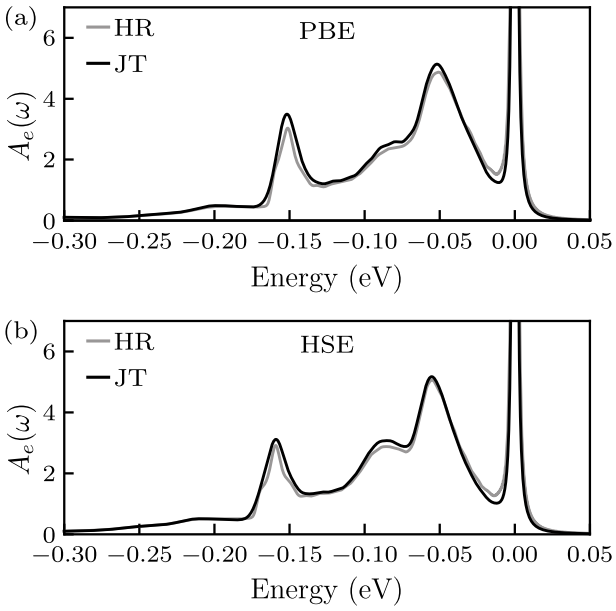

Figure 4.7: The spectral function $A_e(\omega)$ (in units 1/eV) for emission [Eq. (2.157)] obtained with (a) PBE and (b) HSE functionals. We compare spectral functions obtained via the solution of the multi-mode Jahn–Teller problem ("JT") and via the Huang–Rhys treatment ("HR").

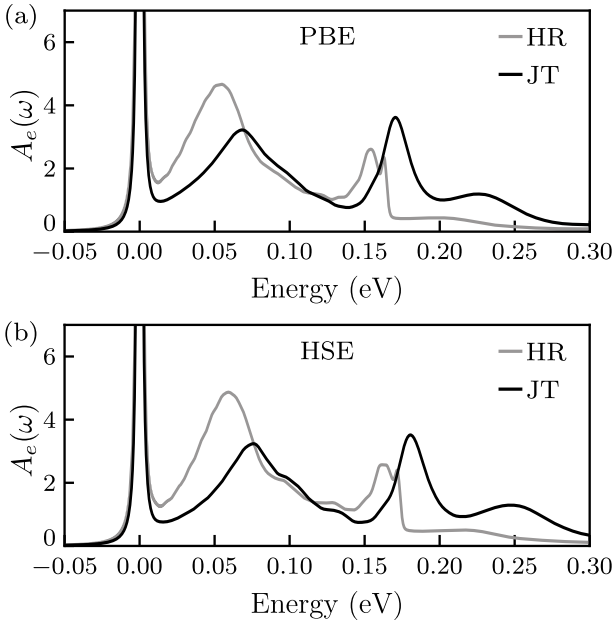

Figure 4.8: The spectral function $A_e(\omega)$ (in units 1/eV) for absorption [Eq. (2.158)] obtained with (a) PBE and (b) HSE functionals. We compare spectral functions obtained via the solution of the multi-mode Jahn–Teller problem ("JT theory") and via the Huang–Rhys treatment ("HR theory").

	Luminescence			Absorption		
	S_{a_1}	S_e	S_{tot}	S_{a_1}	S_e	S_{tot}
PBE	2.39	0.52	2.91	2.60	0.51	3.11
HSE	3.20	0.56	3.76	3.59	0.57	4.16
expt.			3.49[a]			

[a] Reference [17]

Table 4.1: Calculated Huang–Rhys factors for emission and absorption.

($S_e = \sum_k K_k^2$). We define the total Huang–Rhys factor as $S_{\text{tot}} = S_{a_1} + S_e$. The contribution of e symmetry modes to an optical lineshape can be approximately quantified by ratio S_e/S_{tot}, which we find to be 14–18 %. Comparing with the experiment, we see that the total HR factor for emission is overestimated in HSE calculations and underestimated in PBE calculations.

Luminescence

Figure 4.9 shows calculated PBE (a) and HSE (b) luminescence lineshapes. Results are compared to experimental curves from Refs. [17] and [109]. The general agreement between theory and experiment is quite good for both PBE and HSE functionals. However, comparing experimental lineshapes with the PBE result, we see that the intensities of the first two phonon peaks are larger in the calculated spectrum. This is because the total HR factor of PBE calculations is smaller than the experimental one (see Table 4.1). On the other hand, the total HR factor calculated in HSE is larger than the experimental one, rendering smaller intensity of the first three phonon side peeks compared to the experiment.

However, the peak structure agrees remarkably well with the experimental lineshape (especially in PBE calculations). This agreement concerns not only the primary phonon replica at ∼65 meV but even the fine structure of the lineshape (e.g., two small peaks between the second and the third phonon replica of 65 meV). Peak positions are in agreement with the experiment in PBE calculations, while HSE tends to overestimate frequencies. This tendency follows from the fact that PBE provides better values of diamond lattice constant and vibrational frequencies.

Absorption

The calculated absorption lineshapes are compared with an experiment in Fig. 4.10. The experimental absorption lineshape is taken from Ref. [135].

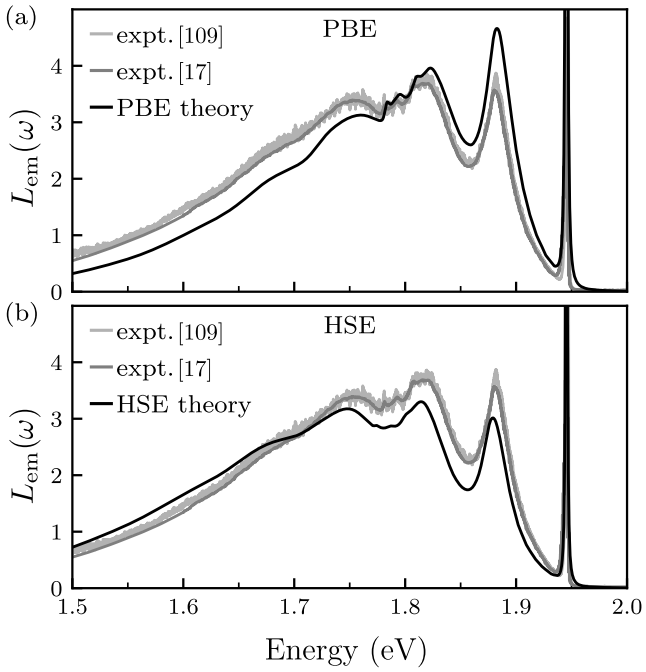

Figure 4.9: Theoretical normalized luminescence lineshapes (in units 1/eV), compared with experimental spectra: (a) PBE functional; (b) HSE functional. Experimental spectra from Refs. [17] (at 4 K) and [109] (at 8 K). The ZPL energy of the theoretical curves is set to the experimental value.

Comparing calculated absorption lineshapes with the experiment in Figure 4.10(a), we see that the intensities of first phonon side-peaks are overestimated in PBE and underestimated in HSE. As in the case of luminescence calculations, we attribute these differences to the general performance of functionals in describing structural lattice properties. The fine structure of the spectra and the positions of side peaks are better described in PBE compared to HSE. The experimental absorption lineshape displays the famous double-peak structure of the first phonon side-peak at $\sim$2.02 eV [136]. While the double peak structure is not clearly revealed in both calculations, the PBE calculations accurately describe the double peak's position and overall shape. This peak is narrower and slightly shifted to higher frequencies in HSE calculations. Our calculations show that this double-peak feature is a consequence of coupling to a_1 vibrational modes, as revealed in a_1 spectral function (Fig. 4.3). We conclude that the asymmetry of this peak between luminescence and absorption lineshapes is a consequence of different vibrational structures in the ground $^3A_2$ and excited ^3E states.

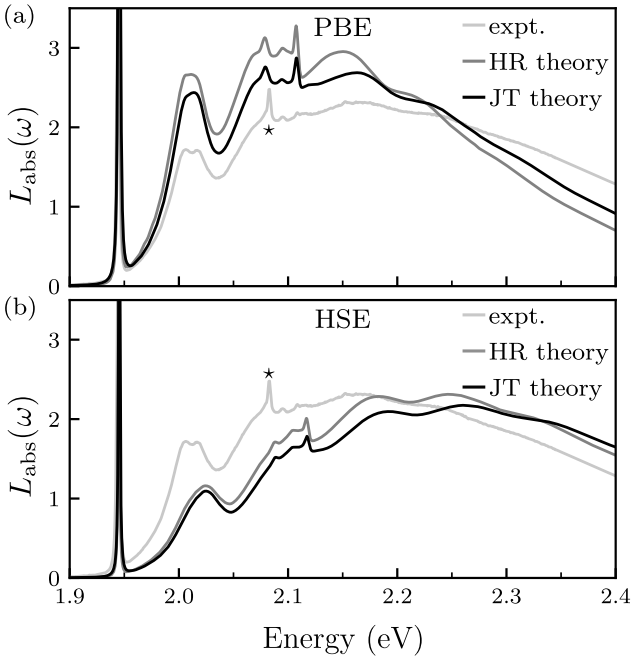

Figure 4.10: Theoretical normalized absorption lineshapes (in units 1/eV) calculated using the Huang–Rhys ('HR theory') and Jahn–Teller treatment ("JT theory"), compared with the experimental spectrum: (a) PBE functional; (b) HSE functional. The experiment is from Ref. [135] at 5 K. The ZPL energy of the theoretical curves is set to the experimental value. The small peak marked with star "$\star$" in the experimental curve is the ZPL of another center and should be disregarded in the comparison.

In Fig. 4.10, we also compare JT treatment with the adiabatic HR theory. Strictly speaking, the HR treatment for the absorption process is not justified in the presence of the dynamical JT effect. However, the positions of peaks in both treatments are reasonably well described, and both lineshapes as qualitatively similar. This could be attributed to a weak coupling strength and broad spectral features of the JT effect (see Fig. 4.4). In the case of more pronounced features of JT coupling, the rigorous treatment could reveal different spectral signatures compared to an approximate HR approach. However, even in the case of NV center, we see some distinct differences. For instance, the JT approach better describes the two features at $\sim$2.15 and 2.24 eV. This improved agreement with an experiment gives support to the validity of our effective multi-mode JT treatment. Nevertheless, this methodology should be tested for other systems with strong JT coupling, where the JT effect has more considerable consequences for optical spectra.

4.5 Discussion

In this section, we critically review our calculations and methodology, focusing on the accuracy of density functionals in a quantitative description of the vibrational and vibronic structure of the NV center. First, let us mention some aspects that *have not* been addressed or have only been partially addressed in this thesis.

Quadratic JT interactions. First of all, our calculations rely only on the linear theory of JT coupling. However, it is estimated that quadratic terms of JT coupling are $\sim 1/3$ of the linear coupling in terms of JT energy lowering E_{JT} [106, 111]. Unfortunately, the inclusion of quadratic terms in the multi-mode treatment increases the complexity of an already complex problem. It would be challenging to account for them with current computational capabilities.

Excited state calculations. The excited ^3E state's electronic structure has been described using the ΔSCF approach (see Section 2.3.2). This approach does not have the same fundamental backing of rigorous theorems as for the ground state.

Hessian matrices for charged defects. For a calculation of Hessian matrix elements, we used moderate-sized supercells ($4 \times 4 \times 4$). For a neutral lattice, such supercells are sufficient for the accurate estimation of force constant. However, for charged defects, long-range Coulombic interactions extend far beyond the cell's dimensions and are not modeled correctly in the supercell approach. Furthermore, a neutralizing background is introduced in supercell calculations to prevent the Coulomb interactions from diverging in a periodic system. These issues may introduce minor errors in the computation of force constants.

Let us assume that the above aspects affect the calculated lineshapes in a minor way. In such conditions, one could attribute the remaining discrepancy between experiment and theory to the accuracy of exchange–correlation functionals of DFT in describing structural and vibrational properties of diamond and the NV center.

To test this assumption, we first assume that the general shapes of PBE spectral densities ($S_{a_1}(\omega)$ and $S_e(\omega)$) are close to the "truth", as PBE functional provides favorable agreement regarding the positions of peaks. However, atomic relaxations are slightly underestimated in PBE, as shown in Table 4.1. Let us assume that atomic relaxations projected on all vibrational modes are underestimated by the same linear factor $\zeta^{1/2}$, and "correct" spectral densities are $S'_{a_1}(\omega) = \zeta S_{a_1}(\omega)$ and $S'_e(\omega) = \zeta S_e(\omega)$.

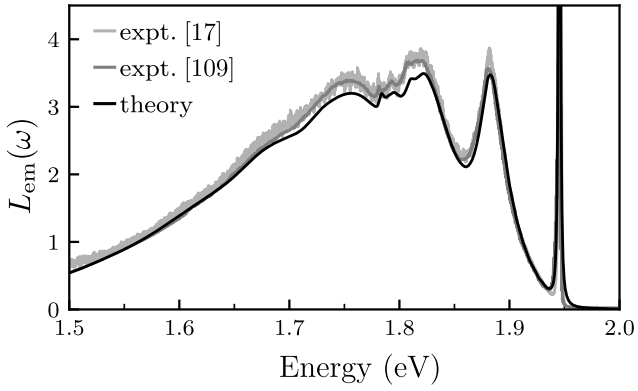

Figure 4.11: Calculated normalized luminescence lineshape compared with the experimental lineshape (both in units 1/eV). In the calculations, we used scaled PBE spectral densities $S'_{a_1} = \zeta S_{a_1}(\omega)$ and $S'_e = \zeta S_e(\omega)$, with $\zeta = 1.2$. Experimental spectra as in Fig. 4.9.

Figure 4.11 shows the calculated luminescence lineshape with $\zeta = 1.2$. This value has been obtained via a least-square fit to the experimental luminescence lineshape and is almost exactly the ratio between the experimental and PBE $S_{\rm tot}$ in Table 4.1 ($3.49/2.91 = 1.199$). Corrected lineshape agrees with the experiment very well, both in terms of general shape and fine features of the spectrum.

Since ζ represents the scaling of the geometry relaxation induced by the electronic transition from the ground to the excited state and vice versa, we fix the value of ζ based on an analysis of the luminescence and use it for absorption spectrum calculations. Like for luminescence calculations, we scale PBE spectral densities with ζ: $S'_{a_1}(\omega) = \zeta S_{a_1}(\omega)$ and $S'_e(\omega) = \zeta S_e(\omega)$. Fig. 4.12 shown shows the "corrected" result for absorption lineshape. Again, the general shape is reproduced very well in the calculation. This favorable agreement supports the hypothesis that PBE calculations produce accurate vibrational frequencies but underestimate geometry relaxation.

Nevertheless, we can identify small discrepancies in the case of the absorption spectrum. The calculation shows a small peak at 2.11 eV, labeled by "#" in Fig. 4.12. This peak originates from a localized vibrational mode just above the diamond phonon spectrum (less than 1 meV). This peak seems absent in the experimental lineshape. This localized mode is present in both PBE and HSE calculations (see Fig. 4.10). The frequency of this localized mode is very sensitive to the parameters of our calculations, and its localized nature might be an artifact. Despite this issue, the calculations clearly agree with the experiment and accurately reproduce the asymmetry between the emission and absorption process.

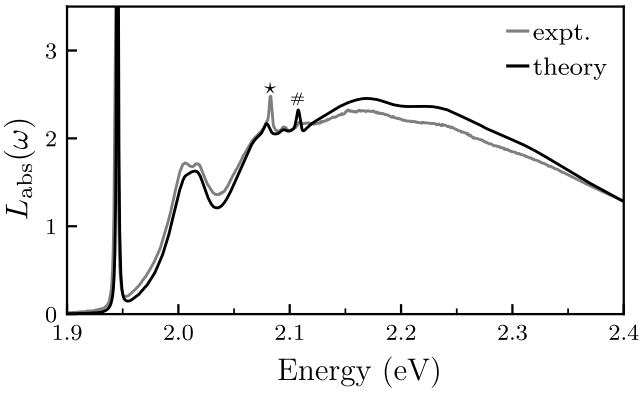

Figure 4.12: Calculated normalized absorption lineshape compared with the experimental lineshape (both in units 1/eV). In the calculations, we used scaled PBE spectral densities $S'_{a_1} = \zeta S_{a_1}(\omega)$ and $S'_e = \zeta S_e(\omega)$, with $\zeta = 1.2$. Experimental spectrum as in Fig. 4.10. The observed peak marked "$\star$" is the ZPL of another defect and should be disregarded in the comparison. The feature marked "#" in the calculated curve is discussed in the text.

4.6 Summary and conclusions

This chapter presented a computational study of electron–phonon coupling of the triplet transition in NV^- centers. The main focus was the calculation of high-resolution luminescence and absorption lineshapes using PBE and HSE functionals. The main achievements of this study are:

1. We have developed a computationally tractable methodology to account for the dynamical multi-mode Jahn–Teller effect in optical lineshapes. We have shown that the Jahn–Teller effect is most important in absorption.

2. Our calculations show that vibrational structure calculated with the PBE exchange–correlation functional agrees slightly better with the experiment than the one computed with the HSE functional.

3. We found that within the ΔSCF approximation, geometry relaxation between the ground state and the excited state was underestimated in PBE and slightly overestimated in HSE. Scaling the PBE relaxation with factor $\zeta = 1.2$, we obtained an excellent agreement with the experiment for both luminescence and absorption lineshapes.

4. We show that the splitting and broadening of the first phonon side-peak in the absorption spectrum is unrelated to the Jahn–Teller effect. The double peak structure comes from the coupling to a_1 phonons.

In conclusion, our study shows that modern density functional theory calculations can predict high-resolution optical lineshapes of deep-level defects with good accuracy. However, certain quantitative discrepancies remain regarding the description of experimental spectra. Therefore, our study shows that the continuing development of more accurate functionals, as well as computational advances for a rigorous treatment of excited states, will be an essential feature of first-principles calculations for point defects.

The methodology presented in this study advances *ab initio* calculations of electron–phonon coupling for defects. It will be useful for the identification and research of other point defects in solids.

Thesis statement (II)

We developed a novel computationally tractable methodology for the *ab initio* description of the multi-mode Jahn–Teller effect in point defects. This methodology improves current theoretical techniques that are based on the single-mode approximation.

Thesis statement (III)

Our *ab initio* methodology to calculate luminescence and absorption lineshapes accurately reproduces the NV^- center's experimental lineshapes.

Chapter 5

PHOTOIONIZATION OF NV^-: THEORY AND *ab initio* CALCULATIONS

To thrill you with delight,
I'll give you diamonds bright.
There'll be things that will excite,
To make you dream of me at night.
— The Yardbirds, *For Your Love*

This chapter presents our theoretical study of photoionization mechanisms of negatively charged nitrogen–vacancy (NV) center in diamond. We show that after the ionization from the ^3E state, the NV center transitions into the metastable $^4A_2$ electronic state of NV^0. This model reveals how the spin polarization of NV^- gives rise to spin polarization of the metastable $^4A_2$ electronic state, explaining recent electron spin resonance (ESR) experiments. We also address the question of the photoionization thresholds and absolute cross-sections using *first-principles* calculations. To obtain smooth absolute cross-sections, we develop a novel computational methodology based on the Brillouin zone integration and band unfolding techniques. The results provided in this chapter are based on our paper [T3].

The content of this chapter is organized as follows. In Section 5.1, we give an introduction to photoionization processes in NV^- centers. Section 5.2 describes the photoionization mechanisms in the framework of the molecular orbital model. Here, we identify the final states of NV^0 and give expressions for photoionization thresholds and cross-sections. Section 5.3 discusses the electronic structure and introduces computational methods for calculating ionization thresholds and absolute cross-sections. Finally, in Section 5.5, we present the results of the calculations and compare them with the experiment.

5.1 Introduction

Most of the practical applications of the NV^- centers rely on triplet optical excitation. However, incident light may induce a photoionization process, whereby an electron from the NV center is excited to the conduction band, and NV^- is converted to NV^0 [146–148]. In many situations, photoionization is a detrimental process for the operation of NV^- and has to be avoided by carefully choosing experimental parameters. However, in some cases, the *deliberate* photoionization of NV^- can also be beneficial. For example, it is used for the photocurrent detection of magnetic resonance (PDMR) [149]. The PDMR can reach spin read-out rates superior to optical protocols, as the radiative lifetime limits the latter. Photoionization of NV^- is also used for the spin read-out via spin-to-charge conversion [150–152].

Figure 1.1(c) shows the energy level diagram of the NV^- center: two spin-triplet states, $^3A_2$ and ^3E, and two metastable spin-singlets, $^1A_1$ and ^1E. Photoionization can occur from any of those levels. The most studied process is the photoionization from the triplet ground state ($^3A_2$). The threshold for this process has been experimentally measured to be $\sim$2.6 eV in Ref. [148] or $\sim$2.7 eV in Ref. [153]. The second process involves two-photon absorption [146–148], whereby first, the NV center is excited to the ^3E state and then, subsequently, is ionized. This process is essential for a majority of practical situations, both when ionization is beneficial or detrimental [149, 150, 154]. Furthermore, the NV center can undergo an inter-system crossing (ISC) to the spin-singlet level $^1A_1$ after the excitation to the ^3E state. $^1A_1$ is a short-lived state (with a lifetime of 0.1 ns [155]), from which there is a nonradiative transition to the ^1E state. The latter is a long-lived metastable state with a lifetime 150–450 ns [156]. Therefore, ionization from the ^1E state is a third mechanism addressed in this study.

For NV^- center, experimental measurements of photoionization cross-sections and thresholds are problematic, especially concerning the photoionization from the excited state ^3E. The first complication is related to the fact that light can induce both the transition $NV^- \rightarrow NV^0$ (ionization) and $NV^0 \rightarrow NV^-$ (recombination), making it hard to separate the two processes [146–148]. Furthermore, if the NV center is in the excited triplet state, photoionization competes with stimulated emission, whereby the center transitions back to the ground state [154, 157]. To the best of our knowledge, neither absolute photoionization cross-sections from $^3A_2$, ^3E and ^1E states nor photoionization thresholds from ^3E and ^1E states have been measured experimentally.

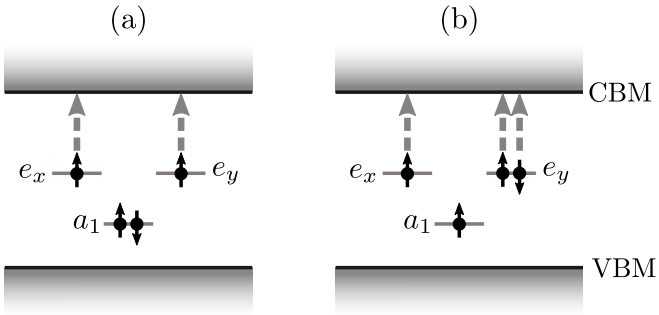

Figure 5.1: Photoionization of NV^- center in the single-electron picture. (a) Electronic configuration of the $m_s = 1$ spin sublevel of the $^3A_2$ state. (b) Electronic configuration of the $m_s = 1$ spin sublevel of the E_x component of the ^3E manifold. Gray arrows show possibilities of photoionization (see text for a more in-depth discussion).

5.2 Photoionization mechanisms

To explain photoionization mechanisms, we use the molecular orbital model (see Sec. 2.3.5), which enables the description of electronic states in terms of localized single-electron orbitals. In this single-particle picture, photoionization corresponds to NV electron being excited to the conduction band state. Accordingly, the photoionization threshold (IP) is the energy of the process, whereby the defect electron ends up in the conduction band minima (CBM).

5.2.1 Photoionization from $^3A_2$ state

The ground triplet state ($^3A_2$) is described by the electronic configuration $a_1^2e^2$. The wavefunctions of spin sublevels $m_s = \pm 1$ are single Slater determinants of localized single-particle orbitals. A single-orbital picture of the $m_s = 1$ state [see Eq. (3.6)] is shown in Fig. 5.1(a). In this picture, the photoionization process corresponds to the excitation of one e electron to the conduction band, as shown by gray arrows in Fig. 5.1(a). The final state of NV^0 is determined from the remaining configuration of electrons ($a_1^2e^1$). The lowest state with this electronic configuration is the ground state ^2E of the neutral center (see Appendix B for a list of single-particle wavefunctions of NV^0). We also depict this process by using the energy-level diagram of the *entire* system in Fig. 5.2.

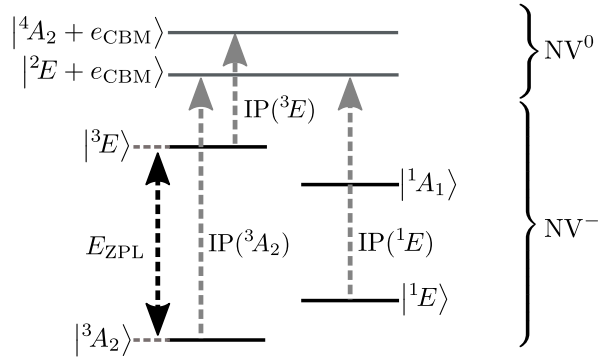

Figure 5.2: Photoionization of NV^- from $^3A_2$, ^3E, and ^1E states. Horizontal lines indicate the energy of the system: black for NV^- and gray for NV^0 plus an electron at the CBM. Gray arrows indicate possible photoionization mechanisms. E_{ZPL} is the ZPL energy of the triplet transition.

5.2.2 Photoionization from ^3E state

The ionization from the excited triplet state (^3E) is presently less understood than the photoionization from the $^3A_2$ state. The initial electronic configuration of the ^3E state is $a_1^1e^3$. The $m_s = 1$ configuration of this state [see Eq. (3.7)] is illustrated in Fig. 5.1(b). Again, in this single-particle picture, the ionization occurs by removing one electron from the e level, as shown by gray arrows in Fig. 5.1(b). The remaining configuration is $a_1^1e^2$, and the lowest-energy state with this configuration is the spin-quartet $^4A_2$ state of NV^0 (see Appendix B). Therefore, the final state of the NV^0 after the photoionization from ^3E is the meta-stable state $^4A_2$ and not the ground state ^2E, as previously assumed [147]. The energy-level diagram for this process is shown in Fig. 5.2: the initial state is the ^3E state of NV^-, while the final state is the $^4A_2$ state of NV^0 plus an electron in the conduction band. From this figure, we can determine the expression for the threshold of photoionization from the ^3E level:

$$\mathrm{IP}(^3E) = \mathrm{IP}(^3A_2) - E_{\mathrm{ZPL}} + \left[E\left(^4A_2\right) - E\left(^2E\right)\right]. \tag{5.1}$$

Eq. (5.1) in principle enables determining the threshold for the photoionization from the ^3E state. Unfortunately, even though the experimental values of $\mathrm{IP}(^3A_2)$ and E_{ZPL} are known, the experimental difference $[E(^4A_2) - E(^2E)]$ is not known. Hence, the experimental value of $\mathrm{IP}(^3E)$ cannot be deduced from this relationship.

5.2.3 Photoionization from ^1E state

The two components of the orbital doubled ^1E are described by multi-determinant wavefunctions (as shown in Appendix B or discussed in Ref. [61]). The electronic configuration of the ^1E manifold is $a_1^2e^2$ (same as for $^3A_2$ state). Again, the photoionization process is described by transferring one e electron is to the conduction band. After this process, the NV center ends up in the ^2E ground state of the neutral defect. Therefore, the photoionization threshold from the ^1E state can be determined using equation (see Fig. 5.2):

$$\mathrm{IP}(^1E) = \mathrm{IP}(^3A_2) - \left[E\left(^1E\right) - E\left(^3A_2\right)\right]. \tag{5.2}$$

The energy difference $\left[E\left(^1E\right) - E\left(^3A_2\right)\right]$ has not been measured directly. However, the analysis of the intersystem crossing between the ^3E and the $^1A_1$ levels, as well as the knowledge of the ZPL energy between the two singlets, allows determining this energy difference to be about 0.38 eV [158]. As a result, IP(^1E) is estimated to be 2.2 ± 0.1 eV.

5.3 Theory and computational methodology

5.3.1 Photoionization cross-section

The general theory of optical absorption and emission has been given in Section 2.6. The absorption cross-section of a single transition is given by Eq. (2.147). The photoionization process involves many final wavefunctions that differ in the state of the conduction band electron. It is natural to assume that the electron–phonon interaction is almost the same for all transitions, as it primarily depends on geometry relaxation, which is governed by localized defect orbitals. Accordingly, we write the photoionization cross-section as:

$$\sigma_{\mathrm{ph}}(\epsilon) = \epsilon \int_{-\infty}^{\infty} \frac{1}{\epsilon'} \tilde{\sigma}_{\mathrm{ph}}(\epsilon') A(\epsilon - \epsilon')\, \mathrm{d}\epsilon', \tag{5.3}$$

where

$$\tilde{\sigma}_{\mathrm{ph}}(\epsilon) = \beta \frac{4\pi^2\alpha}{n_{\mathrm{D}}} \epsilon \sum_j r_{ij}^2 \delta\left(\epsilon - E_{ij}\right), \tag{5.4}$$

is the cross-section in the absence of lattice relaxation (electron–phonon interaction). Here, label i denotes the electronic initial state ψ_i, and the sum runs over all final states ψ_j. $E_{ij} = E_j - E_i$ is the energy difference between the two states, and r_{ij} is the transition's optical matrix element [Eq. (2.109)]. $A(\epsilon)$ is the spectral function of electron–phonon interaction. The refractive index of diamond is $n_{\mathrm{D}} = 2.4$, and $\beta = 1/3$ for an ensemble of randomly oriented diamond NV centers (for discussion about β value, see Sec. 2.6.1).

5.3.2 Electronic structure methods

Electronic structure calculations have been performed within the framework of density functional theory (DFT). We have used the VASP package [77] and PAW method with a plane-wave energy cutoff of 500 eV. Geometry relaxation of the NV center has been performed using $4 \times 4 \times 4$ (512 sites) diamond supercell and a single Γ point for the Brillouin zone sampling. We have used hybrid HSE functional [53] for the ionic relaxation and calculations of excitation energies and thresholds. However, as discussed below, we have to perform integration on a dense k-point grid in the first Brillouin zone to obtain smooth and convergent photoionization cross-sections. Unfortunately, such calculations are computationally too expensive for HSE functional. For this purpose, the transition matrix elements were calculated using the PBE functional [69]. Our estimates for few selected transitions have shown that matrix elements differ by less than 10% for HSE and PBE exchange–correlation functionals.

The energies of excited states ^3E and $^4A_2$ have been calculated using the ΔSCF approach. Electronic structure calculations of the ^3E state have already been discussed in Section 3.2.1. For the total energy calculation of the $^4A_2$ state, we used a single determinant wave function with a spin projection $m_s = +3/2$ (as will be discussed below).

5.3.3 Electronic states and optical matrix elements

Here, we discuss the calculation of optical matrix elements r_{ij} entering equation (5.4). For estimation of r_{ij}, we first need to specify the final states of the transition. As mentioned in Section 5.2, in a single particle picture, once the electron is transferred to the conduction band state, we can identify residual occupied orbitals of NV^0. The lowest energy molecular-orbital configuration of these single-electron states should correspond to the final state of the NV^0 center. However, the whole wave function (NV^0 plus an electron in the conduction) must have the same spin state as the initial one. Otherwise, the transition is forbidden. Such wavefunctions are found by combining different spin states of NV^0 with a single conduction band electron [Eq. (2.45)]:

$$\begin{aligned}\big|(\mathrm{NV}^0 + e_{\mathrm{cb}}); S, m_s\big\rangle \\ = \mathcal{A} \sum_{m_s' + m_s'' = m_s} \big\langle S', m_s'; \tfrac{1}{2}, m_s'' \big| S, m_s \big\rangle \, \big|(\mathrm{NV}^0); S', m_s'\big\rangle \otimes \big|\phi_c, m_s''\big\rangle \,, \quad (5.5)\end{aligned}$$

Here, $\langle S', m_s'; \frac{1}{2}, m_s'' | S, m_s \rangle$ are Clebsch–Gordan coefficients for angular momentum coupling, and $\mathcal{A}$ is an antisymmetrization operator. States, described by

Eq. (5.5), satisfy requirements (i) and (ii) of the molecular orbital wavefunction (see Sec. 2.3.5). However, we relax the requirement for orbital symmetry (iii), as the conduction band electron could be of any irreducible representation. From Eq. (5.5), we can estimate the probability to find the NV^0 center in the spin state $|S', m_s'\rangle$:

$$P(S', m_s') = \left|\left\langle S', m_s'; \tfrac{1}{2}, m_s - m_s' \middle| S, m_s \right\rangle\right|^2 .$$

In general, the matrix element r_{ij} and the energy difference E_{ij} have to be calculated for these many-electron states. However, such calculations are computationally complicated and require some additional approximations described below.

Photoionization from the $^3A_2$ state

Let us first start with the photoionization from the ground state. If NV^- is initially in the $m_s = 1$ spin state, its wavefunction is a single Slater determinant:[1]

$$\left|{}^3A_2; 1\right\rangle = \left|a_1 \bar{a}_1 e_x e_y\right| . \tag{5.6}$$

Here, a number after the semicolon labels the m_s spin quantum number. Once an e electron is excited to the conduction band state, the remaining lowest-energy configuration of NV^0 should be spin-doublet state ^2E. For this transition, the ionized state is given by:

$$\left|({}^2E_{x/y}; \tfrac{1}{2}) \otimes \phi_c\right\rangle = \left|a_1 \bar{a}_1 e_{x/y} \phi_c\right| . \tag{5.7}$$

It is an antisymmetrized product of NV^0 in the ^2E state with spin sublevel $m_s = \frac{1}{2}$, $|{}^2E_{x/y}; \frac{1}{2}\rangle = |a_1 \bar{a}_1 e_{x/y}|$, and a spin-up electron in the conduction band with orbital wavefunction ϕ_c.

We simplify the calculation of optical matrix elements by assuming that all single-electron orbitals are the same in the initial and the final states. Consequently, the excited state differs from the initial one by a single occupied orbital, corresponding to an electron in the e state being excited to the conduction band. This simplification allows the adoption of the Slater–Condon rule to calculate matrix elements. For example, the optical matrix element between states (5.6) and (5.7) reduces to:

$$r_{ij}^2 \equiv \left|\left\langle {}^3A_2; 1 \middle| \mathbf{r} \middle| ({}^2E_{x/y}; \tfrac{1}{2}) \otimes \phi_c; m_s = 1 \right\rangle\right|^2 = \left|\left\langle e_{y/x} \middle| \mathbf{r} \middle| \phi_c \right\rangle\right|^2, \tag{5.8}$$

[1] See Appendix B for MO wavefunctions of the NV center.

where $\langle e_{y/x}|\mathbf{r}|\phi_c\rangle$ is a matrix element of single-particle orbitals. In the context of density functional theory, *we calculate these matrix elements between single-particle Kohn–Sham states*.[2]

In $m_s = 1$ transition, the final state is an orbital doublet. Therefore, we calculate only the excitation to one of the E states and multiply the final result by the degeneracy factor $g = 2$. For $m_s = -1$ transition, we have an analogous picture as for $m_s = 1$, with the only difference that the final spin state of ${}^2E$ is $m_s = -1/2$. Finally, if the initial spin state is $m_s = 0$, the transition is possible to both spin states of ${}^2E$, each with probability $|\langle \frac{1}{2}, \pm\frac{1}{2}; \frac{1}{2}, \mp\frac{1}{2}|0,0\rangle|^2 = 1/2$.

Photoionization from the ${}^3E$ state

For the ionization from the excited state, let us first consider the $m_s = 1$ spin sublevel with a wavefunction:

$$\left|{}^3E_{x/y}; 1\right\rangle = \left|a_1 e_x e_y \bar{e}_{y/x}\right| .$$

For this process, the final state is a mixture of $m_s = 3/2$ and $m_s = 1/2$ states in the NV^0 manifold:

$$\left|({}^4A_2 \otimes \phi_c); S{=}1, m_s{=}1\right\rangle = \frac{\sqrt{3}}{2}\left|({}^4A_2; \tfrac{3}{2}) \otimes \bar{\phi}_c\right\rangle - \frac{1}{2}\left|({}^4A_2; \tfrac{1}{2}) \otimes \phi_c\right\rangle$$

As a result, we have $3/4$ probability of finding NV^0 in the $|{}^4A_2; 3/2\rangle$ state and $1/4$ probability for the $|{}^4A_2; 1/2\rangle$ state. To calculate the matrix element, we first consider the $m_s = 1/2$ component:

$$\left|({}^4A_2; \tfrac{1}{2}) \otimes \phi_c\right\rangle = \frac{1}{\sqrt{3}}\left(|\bar{a}_1 e_x e_y \phi_c| + |a_1 \bar{e}_x e_y \phi_c| + |a_1 e_x \bar{e}_y \phi_c|\right). \qquad (5.9)$$

From this equation, we calculate the matrix element:

$$\left\langle {}^3E_{x/y}; 1\middle|\mathbf{r}\middle|({}^4A_2; \tfrac{1}{2}) \otimes \phi_c\right\rangle = \frac{1}{\sqrt{3}}\left\langle e_{y/x}\middle|\mathbf{r}\middle|\phi_c\right\rangle . \qquad (5.10)$$

This value can be related to the overall matrix element as follows. We expand $|({}^4A_2; \frac{1}{2}) \otimes \phi_c\rangle$ in terms of well defined spin states:

$$\begin{aligned}\left|({}^4A_2; \tfrac{1}{2}){\otimes}\phi_c\right\rangle &= \sum_S \left\langle \tfrac{3}{2}, \tfrac{1}{2}; \tfrac{1}{2}\tfrac{1}{2}\middle|S, 1\right\rangle \left|({}^4A_2 \otimes \phi_c); S, m_s{=}1\right\rangle \\ &= \frac{\sqrt{3}}{2}\left|({}^4A_2{\otimes}\phi_c); S{=}2, m_s{=}1\right\rangle - \frac{1}{2}\left|({}^4A_2{\otimes}\phi_c); S{=}1, m_s{=}1\right\rangle.\end{aligned}$$

[2]This is a standard approximation used in most DFT calculations that deal with optical transitions.

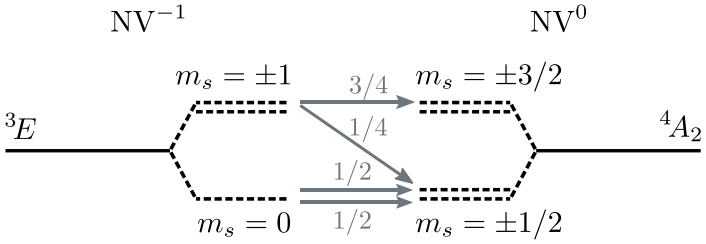

Figure 5.3: Spin physics of the photoionization from the ^3E state. Numbers near arrows show relative probabilities of the transition during photoionization. The $m_s = +1$ (-1) spin sublevel transitions into either the $m_s = +3/2$ $(-3/2)$ or the $m_s = +1/2$ $(-1/2)$ sublevel of the $^4A_2$ manifold with different probabilities. The $m_s = 0$ sublevel transitions to the $m_s = \pm 1/2$ sublevels with equal probability. Spin sublevels are separated by zero-field splittings $D(^3E) = 1.42$ GHz [10] and $D(^4A_2) = 1.69$ GHz [159].

Plugging this expression into Eq. (5.10), we find that

$$r_{ij} = \left\langle {}^3E_{x/y}; 1 \middle| \mathbf{r} \middle| (^4A_2 \otimes \phi_c); S = 1, m_s = 1 \right\rangle = -\frac{2}{\sqrt{3}} \left\langle e_{y/x} \middle| \mathbf{r} \middle| \phi_c \right\rangle ,$$

and

$$r_{ij}^2 = \frac{4}{3} \left| \left\langle e_{y/x} \middle| \mathbf{r} \middle| \phi_c \right\rangle \right|^2 . \tag{5.11}$$

For the $m_s = -1$ transition, we have a similar picture. Except, in this case, the final states of NV^0 are $m_s = -3/2$ and $m_s = -1/2$ with respective probabilities $3/4$ and $1/2$.

Finally, if NV$^-$ is initially in the $m_s = 0$ state, its wavefunction is given by:

$$\left| {}^3E_{x/y}; 0 \right\rangle = \frac{1}{\sqrt{2}} \left(\left| a_1 \bar{e}_x e_{y/x} \bar{e}_{y/x} \right\rangle + \left| \bar{a}_1 e_x e_{y/x} \bar{e}_{y/x} \right\rangle \right) .$$

The corresponding final state is a mixture of $m_s = 1/2$ and $m_s = -1/2$ spin states of $^4A_2$, together with an electron in the conduction band:

$$\left| (^4A_2 \otimes \phi_c); S{=}1, m_s{=}0 \right\rangle = \frac{1}{\sqrt{2}} \left(\left| (^4A_2; \tfrac{1}{2}) \otimes \bar{\phi}_c \right\rangle - \left| (^4A_2; -\tfrac{1}{2}) \otimes \phi_c \right\rangle \right) .$$

This time, there is an equal probability to find NV^0 in the $m_s = \pm 1/2$ spin projections.

Relative transition probabilities between spin sublevels of ^3E and $^4A_2$ manifolds are summarized in Fig. 5.3.

Photoionization from the ^1E state

The orbital components of the spin-singlet ^1E state are multi-determinant wavefunctions given by [160]:

$$\left|{}^1E_x\right\rangle = \frac{1}{\sqrt{2}}\left(|a_1\bar{a}_1 e_x \bar{e}_x| - |a_1\bar{a}_1 e_y \bar{e}_y|\right),$$
$$\left|{}^1E_y\right\rangle = \frac{1}{\sqrt{2}}\left(|a_1\bar{a}_1 \bar{e}_x e_y| - |a_1\bar{a}_1 e_x \bar{e}_y|\right).$$

The final wavefunction of the photoionization from ^1E state is:

$$\begin{aligned}&\left|({}^2E_{x/y}\otimes\phi_c); S{=}0, m_s{=}0\right\rangle \\ &\quad= \frac{1}{\sqrt{2}}\left(\left|({}^2E_{x/y};\tfrac{1}{2})\otimes\bar{\phi}_c\right\rangle - \left|({}^2E_{x/y};-\tfrac{1}{2})\otimes\phi_c\right\rangle\right),\end{aligned}$$

where $|({}^2E_{x/y};-\frac{1}{2})\otimes\phi_c\rangle = |a_1\bar{a}_1\phi_c\bar{e}_{x/y}|$, and $|({}^2E_{x/y};\frac{1}{2})\otimes\bar{\phi}_c\rangle$ is described by Eq. (5.7). Following similar steps as for the ^3E transition, we first calculate the matrix element for single component $\langle{}^1E_x|\mathbf{r}|({}^2E_x;-\frac{1}{2})\otimes\phi_c\rangle = 1/\sqrt{2}\langle e_x|\mathbf{r}|\phi_c\rangle$, and expand the ket in terms of well-defined spin states of NV^0 $|({}^2E_x;-\frac{1}{2})\otimes\phi_c\rangle = \frac{1}{\sqrt{2}}(|({}^2E_x\otimes\phi_c); S{=}1, m_s{=}0\rangle - |({}^2E_x\otimes\phi_c); S{=}0, m_s{=}0\rangle)$. The overall matrix is estimated to be:

$$r_{ij}^2 = \left|\left\langle({}^2E_{x/y}\otimes\phi_c); S{=}0, m_s{=}0\middle|\mathbf{r}\middle|{}^1E_x\right\rangle\right|^2 = \left|\left\langle e_{x/y}\middle|\vec{r}\middle|\phi_c\right\rangle\right|^2.$$

Due to the multi-determinant nature of ^1E, applying the ΔSCF method to calculate its energy is not straightforward. From the theoretical standpoint, there is no consensus regarding the position of this state above the $^3A_2$ ground state [10]. However, the energy difference $\left[E\left({}^1E\right) - E\left({}^3A_2\right)\right] = 0.38$ eV was estimated in Ref. [158] (as discussed in Section 5.2.3).

The main focus of this study is the photoionization from the triplet states. Therefore, for photoionization from the ^1E state, our calculations will be more approximate. First, we assume that optical matrix elements are identical to the photoionization from the $^3A_2$ state. In addition, we will use the same spectral function $A(\epsilon)$ as for the ground state, ignoring the occurrence of the Jahn-Teller effect in the ^1E state. The resulting cross-section is almost identical to ionization from the $^3A_2$ state. The only difference is that the energies that appear in Eqs. (5.3) and (5.4) differ for the two processes.

Calculation of optical matrix elements and transition energies

In the discussion above, we presented how we can evaluate the transition dipole element r_{ij} in terms of single-particle Kohn–Sham states. In the VASP

code, these elements are calculated as $\vec{r}_{ij} = \langle u_i | \vec{\nabla}_{\mathbf{k}} | u_j \rangle$, where u_i and u_j are lattice-periodic parts of single-particle Bloch wavefunctions. Equation (5.4) can also be formulated in terms of momentum matrix elements [120], defined as $\mathbf{p}_{ij} = iE_{ij}\mathbf{r}_{ij}$.

In the formulation based on Kohn-Sham states, E_{ij} in Eq. (5.4) is the difference between single-particle eigenvalues of the defect state and the perturbed bulk state. Due to the bandgap problem of DFT (see Section 2.3.2), the smallest value of E_{ij} does not necessarily correspond to photoionization thresholds obtained from total energy calculations [IP($^3A_2$) or IP(^3E)]. Therefore, we apply a rigid shift to make calculated cross-sections consistent with thresholds. The estimates for the ^1E state are more approximate. In this case, we use Kohn-Sham states of the $^3A_2$ ground state, but the rigid shift of energies corresponds to the "experimental" threshold IP(^1E) = 2.2 eV.

5.3.4 The choice of the charge state

For the computation of matrix elements between single-particle states [Eqs. (5.8) and (5.11)], we use orbitals from a single self-consistent calculation. However, there is an issue regarding the choice of the charge state in which single-particle Kohn–Sham orbitals are calculated. On the one hand, the negatively charged defect is the one that is being ionized. Thus, performing calculations for the NV^- charge state could seem a natural choice. However, while the defect orbitals are represented correctly, conduction band states are not. The final state ϕ_c should be a conduction band state perturbed by a *neutral* defect and not a charged one.

On the other hand, supercell calculations of the neutral NV center should adequately capture perturbations to the conduction bands but might affect the accurate description of localized defect orbitals. We can expect that due to long-range Coulomb interactions, the presence of charge affects localized defect states to a much smaller degree than those of bulk states interacting with the NV center. To test this hypothesis, we use the methodology of Ref. [161] to estimate overlap integrals between defect levels in the case of the neutral and the negatively charged defect. Our calculations show that more than 99.6% of the orbital character of the localized states is preserved when the charge state is changed. Therefore, we conclude that performing calculations in the neutral charge state is a much more accurate approximation. This approximation will be employed in this study.

5.3.5 Brillouin zone integration and supercell effects

For the calculation of cross-sections, we need to evaluate the sum entering equation (5.4). First, let us focus on the matrix element r_{ij} and its calculation in supercell geometry. In a periodic supercell, all single-particle states have the Bloch form:

$$\phi^{\mathrm{sc}}_{\mathbf{k};n} = e^{i\mathbf{kr}} u^{\mathrm{sc}}_{n,\mathbf{k}}(\mathbf{r}),$$

where $\mathbf{k}$ is a vector in the first Brillouin zone of the supercell (label "sc" indicates that the solution is found in the supercell geometry). The Bloch periodic part $u^{\mathrm{sc}}(\mathbf{r})$ is normalized within the volume of supercell Ω_{sc}.

Now consider a single defect embedded in a large supercell of volume $\Omega = N\Omega_{\mathrm{sc}}$. For this system, delocalized conduction band state can be written in terms of $u^{\mathrm{sc}}_{\mathbf{k},n}$:

$$\phi_{\mathbf{k},n} = \frac{1}{\sqrt{N}} e^{i\mathbf{kr}} u^{\mathrm{sc}}_{\mathbf{k},n}(\mathbf{r}).$$

On the other hand, the localized defect state is contained within a single supercell of volume Ω_{sc}, and we don't need a normalization factor $1/\sqrt{N}$:

$$\phi_d = e^{i\mathbf{kr}} u^{\mathrm{sc}}_d(\mathbf{r}).$$

From the equations above, it follows that the optical matrix element of large supercell r_n is related to the matrix element of small supercell r^{sc}_n by:

$$r_n(\mathbf{k}) = \frac{1}{\sqrt{N}} \int_{\Omega_{\mathrm{sc}}} u^{\mathrm{sc}}_d(\mathbf{r}) \mathbf{r} u^{\mathrm{sc}}_{\mathbf{k};n}(\mathbf{r})\, \mathrm{d}\mathbf{r} \equiv \frac{r^{\mathrm{sc}}_n(\mathbf{k})}{\sqrt{N}}.$$

Here, we relabeled matrix element $r_n(\mathbf{k}) \equiv r_{ij}$ by the final state of conduction band electron.

Using this result, we can rewrite the summation over the final states $\psi_j \equiv \psi_n(\mathbf{k})$ in Eq. (5.4) as:

$$\begin{aligned} I(\varepsilon) &= \sum_{\mathbf{k},n} r^2_n(\mathbf{k}) \delta\left(\varepsilon - E_n(\mathbf{k})\right). \\ &= \frac{1}{N} \sum_{\mathbf{k},n} \left(r^{\mathrm{sc}}_n(\mathbf{k})\right)^2 \delta\left(\varepsilon - E_n(\mathbf{k})\right). \end{aligned} \tag{5.12}$$

For a system of volume $\Omega = N\Omega_{\mathrm{sc}}$, the number of $\mathbf{k}$ states in a single band n is N. Therefore, by increasing the size of uniform k-point mesh $N = M \times M \times M$, we effectively increase the size of the system. In practical calculations, we replace δ-functions in Eq. (5.12) with Gaussians of width σ and track the convergence with respect to N.

To converge the cross-section $\sigma_{\rm ph}(\epsilon)$ for a given supercell, a very dense k-point mesh is required. Increasing the mesh in self-consistent supercell calculations becomes computationally very expensive (even at the PBE level). However, the charge density converges much faster as the k-point mesh is increased. Therefore, we first obtain the charge density using self-consistent calculations and the $6\times6\times6$ Monkhorst–Pack k-point mesh. Then, we compute matrix elements using this charge density and non-self-consistent calculations for much denser $14 \times 14 \times 14$ meshes.

The artificial periodicity of the supercell approach causes two undesirable effects: (i) defect–defect interaction in the periodic system and (ii) fictitious perturbation of conduction band states. Effect (i) influences single-particle defect states. To check the convergence of these orbitals with respect to the supercell size, we calculate the optical matrix element r_{ij} for the transition between NV center's a_1 and e levels in $4 \times 4 \times 4$ and $5 \times 5 \times 5$ supercells.[3] Our calculations show that matrix elements calculated in these two supercells differ by less than 3%.

Aspect (ii), however, is more subtle. Periodically distributed NV centers form a superlattice. Simmilar to traditional semiconductor superlattices, one could expect the formation of sub-bands and the opening of "mini-gaps". We illustrate this by applying the band unfolding procedure [162] for the $4 \times 4 \times 4$ supercell. This procedure maps the $\mathbf{k}$ states of the supercell geometry to the first Brillouin zone of the primitive diamond lattice. Fig. 5.4(a) shows such unfolded band structure of conduction band states perturbed by the NV^- cente in the $^4A_2$ state. One can clearly identify discontinuities in the band structure. To explain these discontinuities, we show the band structure of bulk diamond *folded* onto the Brillouin zone of the $4 \times 4 \times 4$ supercell in Fig. 5.4(b). The folding in supercell geometry introduces degeneracies at the band crossing points and Brillouin zone boundaries. Perturbations of periodically repeated defects remove these degeneracies and open up "mini-gaps" [Fig. 5.4(a)]. These mini-gaps affect the density of final states and thus the shape of cross-sections. We also find that the values of optical matrix elements r_{ij} are also affected by artificial periodicity: we observe small jumps of r_{ij}^2 across the "mini gaps". These jumps can be explained using the textbook picture of the behavior of electronic wavefunctions close to the bandgap in pristine solids via the formation of standing electronic waves (see, e.g., Fig. 3 in Chapter 7 of Ref. [78]). The wave function on one edge of the "mini-gap"

[3] In single-particle picture, this matrix element describes intra-defect transition $^3A_2 \leftrightarrow {}^3E$.

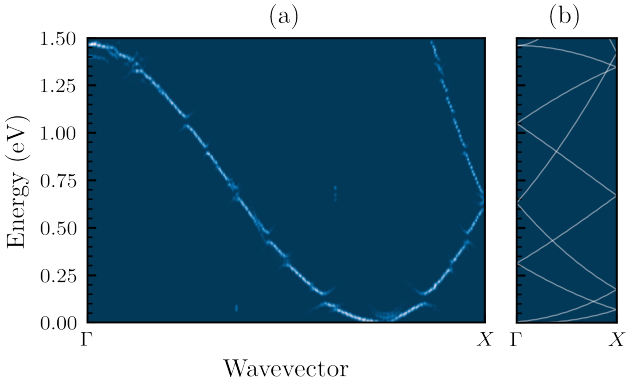

Figure 5.4: (a) Unfolded band structure of conduction band states perturbed by the NV center along the Γ–X path. The color indicates a relative spectral weight (dark blue is zero); see Ref. [162] for more details. (b) The band structure of bulk diamond folded to the first Brillouin zone of the $4 \times 4 \times 4$ supercell along the Γ–X path of the supercell.

has a vanishing weight on the NV center, and r_{ij} of this state tends to zero. The wave function on the other edge has maximum weight on the NV center, and r_{ij} attains a finite value for transition to this state. Therefore, we conclude that *artificial periodicity affects both the energies of conduction band states and the values of optical matrix elements*.

To solve the above issue, we use the following *ad hoc* approach:

(i) Using the methodology of Popescu and Zunger [162], we unfold conduction band states of the defect supercell to the Brillouin zone of the primitive cell. Each k-point of the supercell's Brillouin zone unfolds onto several k-points of the Brillouin zone of the primitive cell.

(ii) We take the k-vector of primitive cell with the highest spectral weight and find the bulk state n with the same k which is closest in energy (typical differences < 0.08 eV). Then, we replace the energy of a single particle conduction band state with the energy of the corresponding bulk state. In such a way, we restore the density of conduction band states to that of pure bulk.

(iii) To eliminate the discontinuities of r_{ij}^2, we replace each optical matrix element r_{ij}^2 with a value averaged in the Brillouin zone of the primitive cell. The averaging is performed for every band n separately, taking the mean of the points situated closer than 0.57 nm^{-1} in the reciprocal space. This procedure "smears" the jumps of the optical matrix elements across "mini gaps". The overall calculation results in smooth values of $\sigma_{\mathrm{ph}}(\epsilon)$ as a function of ϵ.[4]

[4]The effect of such smoothing is illustrated in the Supplemental Material of our paper [T3].

5.4 Spectral functions of electron–phonon interaction

Here, we present *ab initio* calculations of spectral functions of electron–phonon interaction $A(\omega)$ for photoionization from the ground $^3A_2$ and excited ^3E states. Since both excitations are of type $A_2 \leftrightarrow E$, we can apply the same formal theory as for intra-defect transition between triplet levels of NV^-.

For photoionization from the ground $^3A_2$ state, we follow the same steps as for absorption calculations in Chapter 4: we calculate spectral functions pertaining to a_1 and e symmetry modes using equations (2.145) and (2.158). However, for $^3E \rightarrow {}^4A_2$ transition, the Jahn–Teller active system is the initial state and not the final one. Therefore, for ionization from the ^3E state, we calculate the spectral function of e modes using equation:

$$A^e_{\rm abs}(\omega) = \sum_t \left[\left| \left\langle \chi^e_{et} \middle| \chi^{e-}_{g0} \right\rangle \right|^2 + \left| \left\langle \chi^e_{et} \middle| \chi^{e+}_{g0} \right\rangle \right|^2 \right] \delta(\epsilon^e_{et} - \epsilon^e_{e0} - \omega),$$

where $|\chi^{e\pm}_{g0}\rangle$ describe the degenerate ground state of the vibronic manifold.

Spectral functions were calculated using PBE vibrational structures of excited neutral states. Vibrational modes were calculated in $16 \times 16 \times 16$ supercells (32 768 atomic sites) using the embedding methodology discussed in Section 3.3. The calculated densities of electron–phonon coupling for a_1 and e symmetry modes are shown in Fig. 5.5. Fig. 5.5(a) shows spectral densities for the $^3A_2 \rightarrow {}^2E$ transition (photoionization from the ground state $^3A_2$). Fig. 5.5(b) shows the spectrum for the $^3E \rightarrow {}^4A_2$ transition (photoionization from the excited state ^3E). As in the case of $^3A_2 \leftrightarrow {}^3E$ transition, modes of a_2 symmetry do not participate in the electron–phonon interaction. In order to obtain smooth spectral lineshapes, δ-functions in $S(\omega)$ [see Eq. (2.152)] have been replaced by Gaussians with width $\sigma = 5$ meV. This smoothing determines the spectral resolution of final lineshapes.

The contributions of a_1 symmetry modes to the spectral functions, $A_{a_1}(\epsilon)$, were calculated using the generating function approach and are shown in Figs. 5.6. The contributions of Jahn–Teller active e symmetry modes were calculated using the multi-mode Jahn–Teller methodology described in Section 4.3.3. For the current calculations, we chose 20 effective modes that approximate the actual spectral density $S_e(\omega)$. Obtained spectral functions $A_e(\epsilon)$ for the two transitions are shown in Figs. 5.6 (gray lines). The overall spectral function $A(\epsilon)$ is a convolution of the two contributions, A_e and A_{a_1}. These are shown as insets in Fig. 5.6.

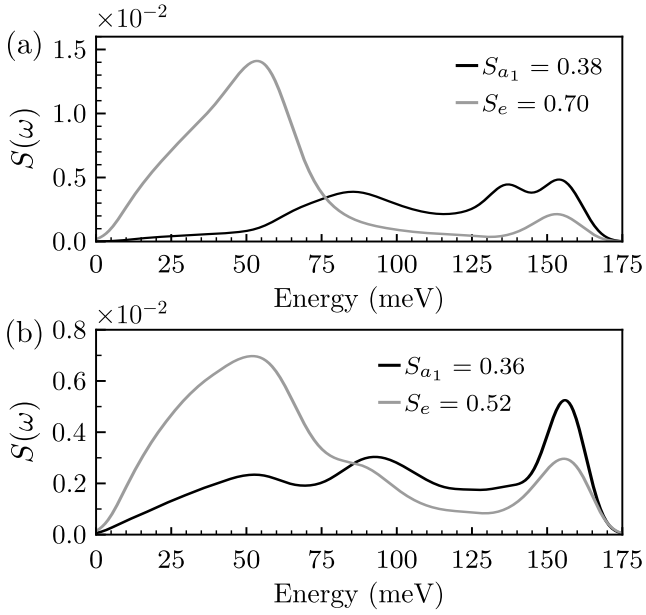

Figure 5.5: Spectral densities of electron–phonon coupling $S(\omega)$ for a_1 (black) and e (gray) vibrations: (a) ${}^3A_2 \rightarrow {}^2E$ transition (photoionization from ${}^3A_2$); (b) ${}^3E \rightarrow {}^4A_2$ transitions (photoionization from ${}^3E$).

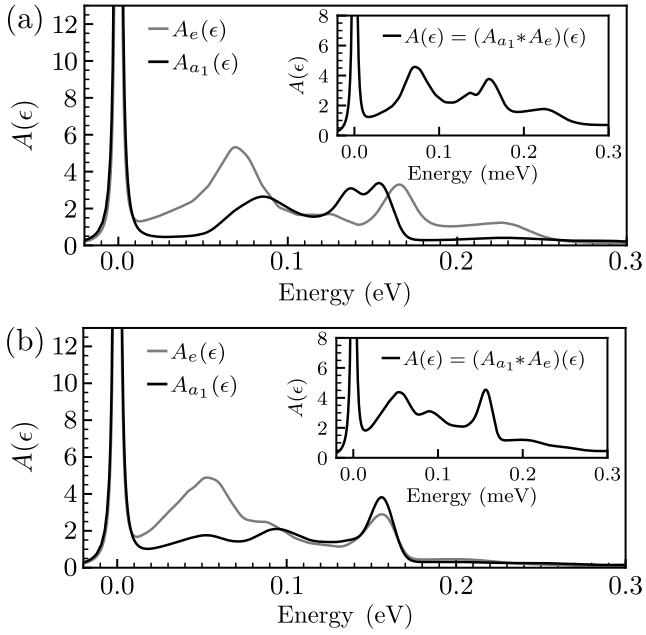

Figure 5.6: Spectral functions $A(\epsilon)$ (in 1/eV) for optical transitions: (a) ${}^3A_2 \rightarrow {}^2E$; (b) ${}^3E \rightarrow {}^4A_2$. Black: the contribution of a_1 modes, $A_{a_1}(\epsilon)$; gray: the contribution of e modes, $A_e(\epsilon)$. The inset shows the total spectral function $A(\epsilon)$.

	IP($^3A_2$)	IP(^3E)	IP(^1E)
theory	2.67	1.15	–
experiment	2.6[a], 2.7[b]	–	*2.2*

[a] Reference [148]
[b] Reference [153]

Table 5.1: Thresholds for photoionization from the $^3A_2$, ^3E, and ^1E states of NV^- (in eV). The experimental results for IP($^3A_2$) are taken from Refs. [148, 153]. The value of IP(^1E) has not been measured directly but deduced from Ref. [158] (shown in italic).

5.5 Results

5.5.1 Photoionization thresholds and excitation energies

Let us first consider calculated values for ionization thresholds and excitation energies. For photoionization from the ground state, we calculate the value of the threshold to be $\mathrm{IP}(^3A_2) = 2.67$ eV. This value is in very good agreement with the experimental energies of 2.6 eV [148] and 2.7 eV [153] (and previous *ab initio* calculations [153, 163]). The calculated ZPL energy of the intra-defect triplet transition is $E(^3E) - E(^3A_2) = 1.996$ eV. Again, this energy agrees well with the experimental value of 1.945 eV and previous theoretical calculations [62]. Furthermore, we calculate the energy difference between quartet $^4A_2$ and doublet ^2E states of NV^0, $E(^4A_2) - E(^2E) = 0.48$ eV. As discussed in Section 5.2.2, this energy is not known experimentally. Finally, from Eq. (5.1), we obtain the value $\mathrm{IP}(^3E) = 1.15$ eV for the photoionization from the excited state ^3E. The calculated and experimental thresholds for photoionization from NV^- states are summarized in Table 5.1.

5.5.2 Cross-sections

Theoretical models

Before presenting calculated cross-sections, let us discuss some available theoretical models of photoionization of deep defects [120]. Most of these models use the formulation based on the momentum matrix element $\vec{p}_{ij} = iE_{ij}\vec{r}_{ij}$ [82]. Therefore, we will use this formulation in the following discussion.

Suppose the conduction band is parabolic close to the CBM. In such case, the photoionization close to the threshold corresponds to the electron excitation to the conduction band with the density of states $D(E) \sim (E - E_{\mathrm{CBM}})^{1/2}$. In this picture of single-particle excitation, there are two limiting cases regarding the dependence of the momentum matrix element $\vec{p}_{ij}$ on the quasi-momentum measured with respect to its value at the CBM, $\Delta\vec{k} = \vec{k} - \vec{k}_{\mathrm{CBM}}$.

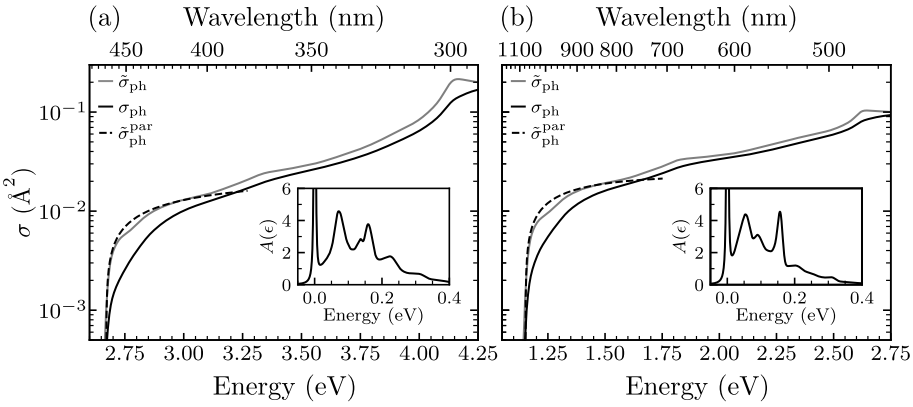

Figure 5.7: Photoionization cross-sections from (a) the $^3A_2$ and (b) the ^3E states of negatively charged NV center. Gray lines: cross-sections $\tilde{\sigma}_{\rm ph}(\epsilon)$ without vibrational broadening [Eq. (5.4)]; solid black lines: actual cross-sections $\sigma_{\rm ph}(\epsilon)$ [Eq. (5.3)]; dashed lines show $\tilde{\sigma}_{\rm ph}$ calculated using a constant momentum matrix element in Eq. (5.4) and DOS corresponding to a parabolic band (see text). Insets show the spectral function of electron–phonon coupling $A(\epsilon)$.

One limit describes a system where the character of the defect wavefunction is principally the same as the character of bulk states near the CBM. For this case, $\vec{p}_{ij} \sim \Delta\vec{k}$ [120], and the cross-section is given by $\tilde{\sigma}_{\rm ph}(\epsilon) \sim (\epsilon - \epsilon_{\rm th})^{3/2}$, where $\epsilon_{\rm th}$ is the threshold for photoionization. The widely-used Lucovsky model describes such a scenario [164].

Another limit occurs when the defect wavefunction has a different character from the bulk states near CBM. This happens, for example, when the defect state has p character, while the conduction band states have s character. In this case, $\vec{p}_{ij}$ is constant for small $\Delta\vec{k}$ [120], and one obtains $\tilde{\sigma}_{\rm ph}(\epsilon) \sim (\epsilon - \epsilon_{\rm th})^{1/2}$ close to the threshold.

Calculated cross-sections

We first calculate photoionization cross-sections without the electron–phonon interaction $\tilde{\sigma}_{\rm ph}$ [see Eq. (5.4)]. The cross-sections $\tilde{\sigma}_{\rm ph}$ for the photoionization from the ground $^3A_2$ and excited ^3E states are shown respectively in Figs. 5.7(a) and (b) (solid gray lines). We have replaced δ functions in Eq. (5.4) with Gaussians of width $\sigma = 30$ meV. Interestingly, for transitions close to the threshold, cross-sections follow $\tilde{\sigma}_{\rm ph}(\epsilon) \sim (\epsilon - \epsilon_{\rm th})^{1/2}$ dependence. This behavior indicates that p_{ij}^2 attains a constant value for the transition close to the band edge (for more details, see Supplemental Material of our paper [T3]). Dashed lines in Fig. 5.7 show $\tilde{\sigma}_{\rm ph}(\epsilon)$ pertaining to this constant value of the

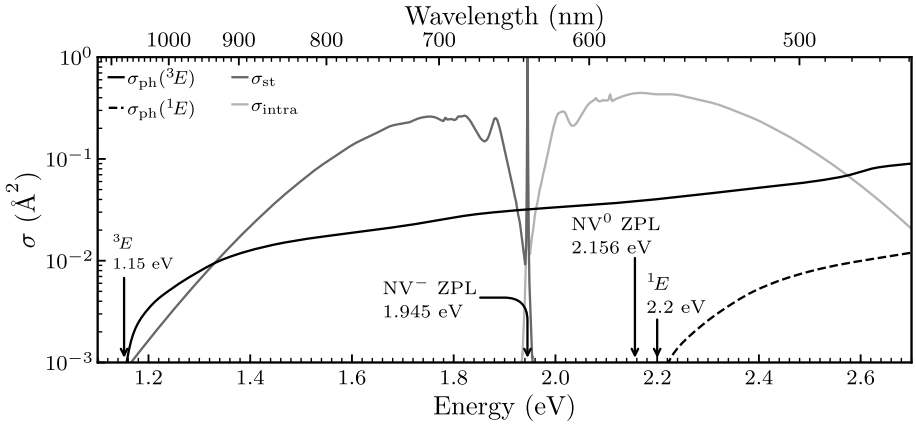

Figure 5.8: Calculated cross-section as a function of photon energy. Solid black line: photoionization from the excited state ^3E, $\sigma_{\rm ph}$; dark gray line: stimulated emission, $\sigma_{\rm st}$; light gray line: intra-defect absorption, $\sigma_{\rm intra}$; dashed black line: photoionization from the singlet state ^1E. Photoionization thresholds from ^3E and ^1E are indicated (estimated error bar 0.1 eV), together with the experimental values of the ZPL energy for NV$^-$ and NV^0.

momentum matrix element and DOS corresponding to a parabolic band. Model parabolic dispersion was described by effective electron masses $m_\parallel = 1.66$ and $m_\perp = 0.32$, obtained by our theoretical calculations (in good agreement with experimental ones [165]). Cross-section $\tilde{\sigma}_{\rm ph}(\epsilon)$ starts to deviate from the $(\epsilon - \epsilon_{\rm th})^{1/2}$ behavior for larger energy. This is because the momentum matrix element begins to differ from the value at the threshold, and the DOS of conduction band states starts to deviate from the parabolic model. For instance, small peaks at 3.35 eV in Fig. 5.7(a) and at 1.85 eV in Fig. 5.7(b) correspond to van Hove singularities at the X-point of the conduction band.

Finally, the convolution of $\tilde{\sigma}_{\rm ph}$ with a spectral function of electron-phonon $A(\omega)$ (shown in insets of Fig. 5.7) yields actual cross-sections $\sigma_{\rm ph}$ shown by solid black lines in Fig. 5.7. The electron–phonon interaction shifts the weight of the cross-section to higher energies, and overall lineshape no longer exhibits the square root behavior close to the threshold.

The most important result of this chapter is shown in Fig. 5.8. We plot the photoionization cross-section $\sigma_{\rm ph}(\epsilon)$ from the excited triplet state ^3E (solid black line) together with the calculated cross sections for stimulated emission from the excited state ^3E ($\sigma_{\rm st}$, dark gray line) and the intra-defect absorption cross-section from the ground state $^3A_2$ ($\sigma_{\rm intra}$, light gray line). Photoionization cross-section from the $^3A_2$ state is not shown. We will discuss the relevance of Fig. 5.8 for the physics of NV centers in the next section.

5.6 Discussions

5.6.1 Ensembles vs. single NV centers

Cross-sections calculated above are for ensembles of randomly oriented NV centers. However, some experiments are performed on single NV centers and depend on the polarization of light and orientation of defects. Therefore, here, we will briefly discuss how cross-sections for ensembles can be used to obtain relevant information about single NVs.

Stimulated emission and intra-defect absorption have non-zero dipole moments only in the plane perpendicular to the N–V axis. They strongly depend on the orientation of the defect. Usually, in the experimental setup, once a single NV center is chosen, polarization is rotated in the plane of the diamond surface to maximize the efficiency of intra-defect triplet excitation. In such a case, from geometric considerations, one can show that $\sigma_{\rm st}$ and $\sigma_{\rm intra}$ are by factor $3/2$ larger than the corresponding cross-section for an ensemble.

In the case of photoionization, an electron is excited close to the conduction band minimum. The CBM of diamond comprises six different conduction band valleys. The presence of NV center lowers the point group symmetry to C_{3v}, and six degenerate single-electron states form linear combinations that result in two a_1 states and two e symmetry doublets.

In a single-particle picture, all photoionization mechanisms (from $^3A_2$, ^3E, and ^1E states) involve the excitation of an electron from an e defect level to a conduction band state. If the final single-electron state is of a_1 symmetry, excitation is polarized perpendicularly to the N–V symmetry axis. On the other hand, excitation to an e state can be polarized in any direction. Our approximate numerical analysis shows that the average cross-section along the symmetry axis is about twice smaller than the average cross-section in the perpendicular directions. Therefore, if polarization is rotated to maximize the efficiency of intra-defect excitation, one can show that the photoionization cross-section $\sigma_{\rm ph}$ is approximately by factor $\sim 6/5$ larger than the value for ensembles.

5.6.2 $^4A_2$ state as a state of NV^0 directly after photoionization

Our finding that after the photoionization from the ^3E state, NV center transitions into the metastable quartet state $^4A_2$ of the neutral defect has important implications for the physics of NV charge dynamics. In particular,

this model might explain the electron spin resonance (ESR) experiments of Felton *et al.* [159]. Felton observed spin polarization of the quartet state $^4A_2$ under the continuous illumination of light. This effect can be understood using Fig. 5.3, where transition probabilities from different spin sublevels of excited NV$^-$ state ^3E to spin sublevels of the $^4A_2$ manifold are shown.

If the NV$^-$ center is initially in the $m_s = \pm 1$ spin sublevel, the probability of the transition to the $m_s = \pm 3/2$ spin state of $^4A_2$ is $3/4$, while that to the $m_s = \pm 1/2$ sublevel is $1/4$. On the other hand, if the initial spin state is $m_s = 0$, $^4A_2$ can be found in one of the $m_s = \pm 1/2$ spin states with equal probabilities. Therefore, one can deduce that if NV$^-$ is initially spin-unpolarized, then there is no spin polarization of the $^4A_2$ state after the ionization of the NV$^-$ center.

In Ref. [159], the spin polarization of the $^4A_2$ state was observed only for laser wavelengths above the ZPL of the neutral NV center, 2.156 eV. For such wavelengths, the NV center is constantly switching between NV$^-$ and NV^0 [146, 148]. Furthermore, under the continuous illumination of light, NV$^-$ polarizes to the $m_s = 0$ level of $^3A_2$ and thus ^3E. Therefore, after some time, the ionization mainly occurs from the $m_s = 0$ sublevel, rendering the final state of NV^0 to be $m_s = \pm 1/2$. The zero-field splitting of $^4A_2$ state separates $m_s = \pm 1/2$ and $m_s = \pm 3/2$ spin sublevels by $D(^4A_2) = 1.69$ GHz [159]. Therefore, the populated $m_s = \pm 1/2$ state of NV^0 gives rise to a strong ESR signal.

5.6.3 Photodynamics: comparison with selected experiments

Here, we focus on a few selected experiments on charge-state dynamics that do not require the knowledge of cross-sections for recombination processes (whereby NV^0 is converted to NV$^-$) [166–168].

Our theoretical calculations can be directly compared to the experiments of Hacquebard and Childress [166], where green (2.33 eV) and infrared (1.62 eV) picosecond laser pulses were used to track the charge-state dynamics of single NV$^-$ centers in [111] diamond. The authors modeled their experimental data to determine the ratio between the cross-section of stimulated emission and the cross-section of the photoionization from the ^3E state. They estimated that for infrared excitation (1.62 eV) $\sigma_{\rm st}/\sigma_{\rm ph} \approx 13$. We can determine this ratio from ensemble data (Fig. 5.8) using our theoretical calculations and prefactors for single centers ($3/2$ for intra-defect absorption and $6/5$ for photoionization).

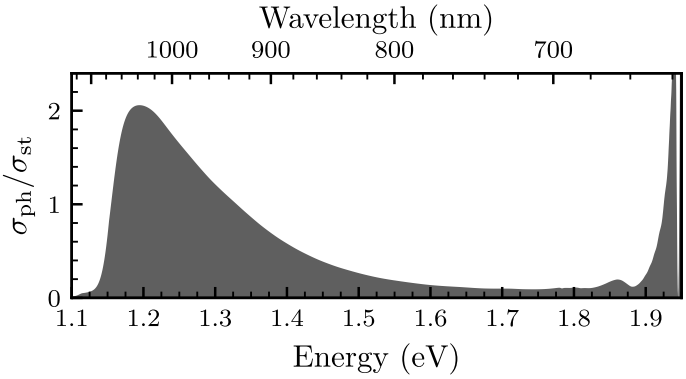

Figure 5.9: The ratio of the photoionization cross-section and the cross-section for stimulated emission, $\sigma_{\rm ph}/\sigma_{\rm st}$, as a function of photon energy.

We obtain a theoretical ratio at the same excitation energy $\sigma_{\rm st}/\sigma_{\rm ph} \approx 10$. The agreement between theory and experiment is rather good, considering the error bars of both approaches.

Another set of experiments that our theoretical calculations can explain is a spin-to-charge conversion with dual-beam excitation in cryogenic temperatures [167, 168]. In such spin-to-charge experiments, one narrow frequency laser is first used to excite the NV^- center into one of the selected spin states. Then, a second laser pulse with the sub-ZPL energy is used to ionize the ^3E state. This specific energy range is chosen to avoid disturbances of other spin states. Irber *et al.* [167], in their experiments, obtained effective photoionization using a sub-ZPL laser of energy 1.93 eV. In another experiment, Zhang *et al.* [168] used a laser emitting at 1.17 eV and also observed effective photoionization.

We can explain the results of Refs. [167, 168] using our theoretical calculations. Since the polarization of the ionizing pulse was unknown in both studies, we use data calculated for an ensemble of randomly oriented NVs. For better comparison, we plot the photoionization cross-section and stimulated emission cross-section ratio ($\sigma_{\rm ph}/\sigma_{\rm st}$) as a function of energy in Fig. 5.9. There are two regions where photoionization of ^3E is most effective in comparison to stimulated emission. The first region is between the photoionization threshold ${\rm IP}(^3E) = 1.15$ eV and 1.3 eV. The second region is between 1.92 eV and the ZPL of triplet transition $E_{\rm ZPL} = 1.945$ eV. These two regions perfectly correspond to energy ranges for which the photoionization was efficient (1.17 eV and 1.93 eV).

5.7 Summary and conclusions

This chapter presented the theory and first-principles calculations of photoionization processes in the negatively charged NV center in diamond. The main achievements and findings of this study can be summarized as follows:

1. We showed that the NV center transitions to the metastable $^4A_2$ state right after the photoionization from the ^3E state. This model explains the ESR experiments of Felton *et al.*[159].
2. We determined the photoionization threshold from the ^3E state to be 1.15 eV. This value was hitherto unknown.
3. We introduced a novel methodology to calculate absolute photoionization cross-sections for deep-level defects and applied it to NV^-. This is the first calculation of absolute photoionization cross-sections for point defects using modern electronic structure theory.
4. Our calculations rationalize recent experiments of spin-to-charge under sub-ZPL illumination [167, 168]. The calculated ratio of cross-sections of stimulated emission and photoionization agrees perfectly with the experimental estimation of Hacquebard and Childress [166].

Thesis statement (IV)

After the photoionization from the ^3E state, NV centers transition to the metastable $^4A_2$ state of NV^0. This explains electron spin resonance experiments and has important consequences for the charge dynamics of the NV center. We determine the threshold for the photoionization to be 1.15 eV.

Thesis statement (V)

Our *ab initio* methodology for the photoionization cross-section calculations explains recent photoionization experiments and elucidates the charge-state dynamics of NV centers.

Appendix A

ELEMENTS OF GROUP THEORY

This appendix briefly reviews some formal ideas of group theory that are used throughout this thesis. Here we will focus on key definitions and general concepts with examples for the C_{3v} group of the diamond NV center.[1] The rigorous theory can be found in many excellent textbooks (see, e.g., Refs. [89, 90, 92]).

A.1 Group and classes

The geometric structure of the point defects often has some symmetries that can be described by a set of coordinate transformations G_i that preserve geometry and keep at least one point fixed. The complete set of such transformations forms algebraic structure $\mathcal{G}$ known as a *point group*. In other words, the multiplicative structure of $\mathcal{G}$ satisfies formal conditions, called *group axioms*.[2] Identification of the group structure has some practical implications for the theoretical analysis, as shown below.

Elements in the group can be partitioned into mutually disjoint sets, which are called "*classes*" [90]. Each class contains equivalent elements $G_a \sim G_b$, which are related by conjugate relation:

$$G_a \sim G_b \;\Leftrightarrow\; G_a = G_i G_b G_i^{-1}, \tag{A.1}$$

for some elements G_i of the group $\mathcal{G}$. From a geometric perspective, each class includes similar transformations, i.e., same angle rotations around different axes [90].

[1] In this review, we assume that groups of interest are *simply reducible groups* [92]. This is the case for most spatial groups in molecular systems.

[2] These are four conditions: (i) multiplication of two element s yield the third element in the same group, $G_a G_b = G_c \in \mathcal{G}$; (ii) group multiplication is associative, $(G_a G_b)G_c = G_a(G_b G_c)$; (iii) there exists identity element e, such that $G_i e = G_i$; (iv) each element has its inverse, $G_i G_i^{-1} = e$.

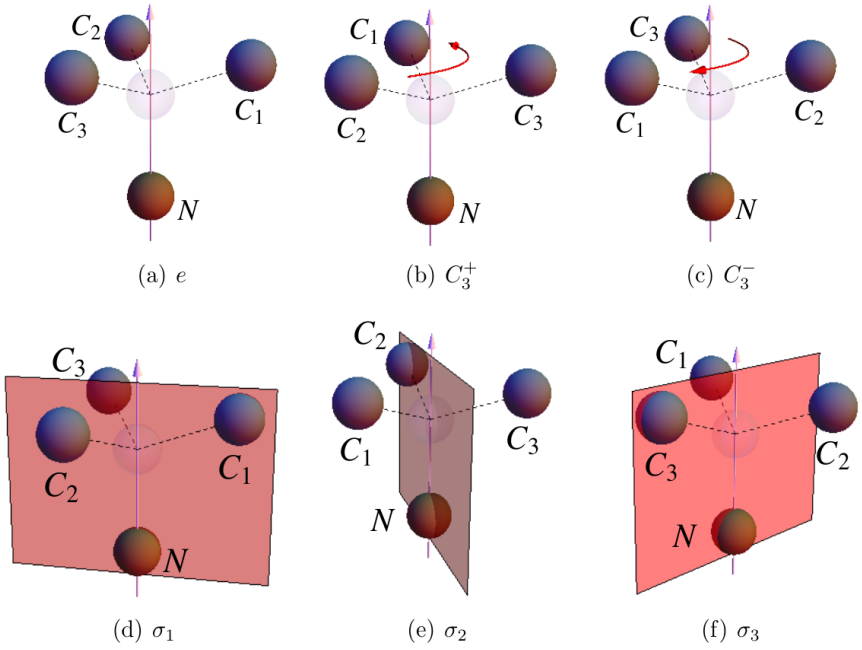

(a) e (b) C_3^+ (c) C_3^-

(d) σ_1 (e) σ_2 (f) σ_3

Figure A.1: The operations of the C_{3v} group elements on the structure of the NV center. The picture is taken from Ref. [116].

	e	C_3^+	C_3^-	σ_1	σ_2	σ_3
e	e	C_3^+	C_3^-	σ_1	σ_2	σ_3
C_3^+	C_3^+	C_3^-	e	σ_3	σ_1	σ_2
C_3^-	C_3^-	e	C_3^+	σ_2	σ_3	σ_1
σ_1	σ_1	σ_2	σ_3	e	C_3^+	C_3^-
σ_2	σ_2	σ_3	σ_1	C_3^-	e	C_3^+
σ_3	σ_3	σ_1	σ_2	C_3^+	C_3^-	e

Table A.1: C_{3v} group multiplication table.

Let us take the NV center as an example (Fig. A.1). Six symmetry operations keep the geometry invariant: identity operation e (which does nothing), two $2\pi/3$ rotations about the symmetry axis (C_3^+, C_3^-), and three vertical reflections through planes containing symmetry axis (σ_1, σ_2, and σ_3). The multiplicative structure of the C_{3v} group is displayed in Table A.1. This table completely encodes the whole structure of a group. The C_{3v} point group has three classes:

$$\begin{aligned} E: &\quad \{e\}, \\ C_3: &\quad \{C_3^+, C_3^-\}, \\ \sigma: &\quad \{\sigma_1, \sigma_2, \sigma_3\}. \end{aligned}$$

The first class, E, contains only identity element e since $G_i e G_i^{-1} = e$ for any $G_i \in \mathcal{G}$. This class is present in all groups. The second class, C_3, comprises two $2\pi/3$ rotations, while the third class σ consists of three vertical reflections.

A.2 Group of the Shrödinger equation

From the practical perspective of this thesis, the group theory becomes important when we have an eigenvalue problem for an operator which is invariant under some symmetry transformations. This is, indeed, the case for the adiabatic description of the point defect. For example, the electronic Shrödinger equation (2.8) is defined in the reference geometrical configuration $\mathbf{R}_0$. The point group $\mathcal{G}$ of this configuration is a set of geometric transformations $G_i \in \mathcal{G}$, for which $G_i \mathbf{R}_0 = \mathbf{R}_0$. One can check that this symmetry also implies invariance of the electronic Hamiltonian $\hat{H}(\mathbf{r})$ with respect to the same spatial transformations. That is, if we define the functional transformation $T(G_i)$ as $T(G_i) f(\mathbf{r}) = f(G_i^{-1}\mathbf{r})$, the invariance is encoded in the following form:

$$T(G_i)\hat{H}(\mathbf{r}) = \hat{H}(G_i^{-1}\mathbf{r}) = \hat{H}(\mathbf{r}). \tag{A.2}$$

From this equation, it follows that it is irrelevant whether $T(G_i)$ appears to the left- or right-hand side of $\hat{H}(\mathbf{r})$, that is, $T(G_i)\hat{H}\psi = \hat{H}T(G_i)\psi$, and both operators commute. The set of all operators which commute with $\hat{H}$ are said to form *the group of Schrödinger equation*. In this case, the group structure is identical to the point group $\mathcal{G}$ of geometric configuration $\mathbf{R}_0$. In a more general case, there could be other symmetries (sets of operators that form a group) that are not related to the spatial configuration.

The harmonic Hamiltonian of the nuclear system (2.50) also is invariant with respect to symmetry transformations of the reference system $\mathbf{R}_0$. Therefore, the implications derived for electronic states also apply to vibrational states of a nuclear subsystem.

A.3 Irreducible representations

Identification of Hamiltonian symmetry has an interesting immediate result for an eigenvalue problem. If we apply one of the commuting transformation operators to the stationary Schrodinger equation ($\hat{H}\psi_n = \varepsilon_n\psi_n$), we get:

$$T(G_i)\left\{\hat{H}(\mathbf{r})\psi_n(\mathbf{r})\right\} = \hat{H}(\mathbf{r})\left\{T(G_i)\psi_n(\mathbf{r})\right\} = \varepsilon_n\left\{T(G_i)\psi_n(\mathbf{r})\right\}.$$

From the above result, we can conclude that any function $T(G_i)\psi_n$ obtained by applying symmetry transformation on eigenfunction ψ_n is also an eigenstate with the same energy as the original one. In principle, if all symmetry transformations are determined correctly, such a procedure should yield all the degenerate states from a single one [89].[3] This result implies that all states of the same degenerate subspace are connected through linear relation:

$$T(G_i)\psi_n = \sum_m \Gamma_{mn}(G_i)\psi_m, \tag{A.3}$$

where scalar coefficients $\Gamma_{mn}(G_i)$ constitute some $M \times M$ matrix (M is the number of mutually degenerate states). The summation is chosen over the first index to ensure that the matrices $\Gamma(G_i)$ form a *matrix representation of a point-group*. By term "representation", we mean that the multiplicative structure of matrices is homomorphic to the multiplicative structure of a group:

$$G_aG_b = G_c \implies \sum_l \Gamma_{nl}(G_a)\Gamma_{lm}(G_b) = \Gamma_{nm}(G_c). \tag{A.4}$$

The functions $\{\psi_i | i = 1, \ldots, s\}$ used to generate representation Γ in Eq. (A.3) are said to form *a set of basis functions for this representation*. Alternatively, we also say that they *transform as a basis of representation* Γ.

For each group, there are infinite possible matrix representations that fulfill Eq. (A.4). For example, if there are two different matrix representations, Γ^α

[3] Exception to this statement could be the degeneracy caused by other hidden mathematical symmetry, which is not reflected in the spatial structure. Such degeneracy is called *accidental-degeneracy*.

	e	C_3^+	C_3^-	σ_1	σ_2	σ_3
A_1	1	1	1	1	1	1
A_2	1	1	1	-1	-1	-1
E	$\begin{pmatrix} 1 & 0 \\ 0 & 1 \end{pmatrix}$	$\begin{pmatrix} -\frac{1}{2} & \frac{\sqrt{3}}{2} \\ -\frac{\sqrt{3}}{2} & -\frac{1}{2} \end{pmatrix}$	$\begin{pmatrix} -\frac{1}{2} & -\frac{\sqrt{3}}{2} \\ \frac{\sqrt{3}}{2} & -\frac{1}{2} \end{pmatrix}$	$\begin{pmatrix} \frac{1}{2} & -\frac{\sqrt{3}}{2} \\ -\frac{\sqrt{3}}{2} & -\frac{1}{2} \end{pmatrix}$	$\begin{pmatrix} \frac{1}{2} & \frac{\sqrt{3}}{2} \\ \frac{\sqrt{3}}{2} & -\frac{1}{2} \end{pmatrix}$	$\begin{pmatrix} -1 & 0 \\ 0 & 1 \end{pmatrix}$

Table A.2: The irreducible matrix representations of the C_{3v} point group. E matrices are represented in the Cartesian (E_x, E_y) form.

and Γ^β, we can always form a third representation with a typical element:

$$\Gamma(G_i) = \begin{pmatrix} \Gamma^\alpha(G_i) & \mathbf{0} \\ \mathbf{0} & \Gamma^\beta(G_i) \end{pmatrix},$$

where $\Gamma^\alpha(G_i)$ and $\Gamma^\alpha(G_i)$ are matrices representing group element G_i. This new set of matrices will also be a representation, as they satisfy a relation of Eq. (A.4). The representation Γ of this enlarged matrix form is said to be *reducible*. This reducibility can be hidden by applying similarity transformation $\Gamma'(G_i) = S\Gamma'(G_i)S^{-1}$ to the set of matrices, breaking the block diagonal form. Note that $\Gamma'(G_i)$ also form a representation since similarity transformation preserves the homomorphic structure of Eq. (A.4). Such two sets of matrices, $\Gamma(G_i)$ and $\Gamma'(G_i)$, are then said to be *equivalent*.

However, there is a special type of representations called *irreducible representation* [89, 90]. The matrices of irreducible representation cannot be reduced to block diagonal form by any similarity transformation. In the group theory, it is proven that there is a finite number of irreducible representations for each discrete group $\mathcal{G}$, and this number *equals the number of classes*. As an example, the C_{3v} group has only three irreducible representations (A_1, A_2, and E) shown in Table A.2.

Irreducible representations are important because of the following theorem [89]: *The set of s degenerate eigenfunctions with the same energy transform as basis functions of a s-dimensional irreducible representation of the group of the Shrödinger equation*. In other words, matrices $\Gamma_{mn}(G_i)$ of Eq. (A.3) that connect eigenstates of the same degenerate subspace must be irreducible representations of the Hamiltonian group $\mathcal{G}$.

From the discussion above it follows, that we can classify eigenstates of the symmetric Hamiltonian according to their transformation properties. The dimension of irreducible representation matrices $\Gamma_{mn}(G_i)$ can vary from one

to an arbitrary number. For example, one-dimensional representations are described by scalars, and objects that transform as such representations cannot be degenerate. The most trivial one-dimensional irreducible representation (that is present in every group) is totally symmetric A_1 (identity) representation (or A_g for geometries with inversion symmetry). In this representation, $\Gamma_{A_1}(G_i) = 1$ for every $G_i \in \mathcal{G}$. Objects of A_1 symmetry are invariant for all symmetry transformations of the group:

$$T(G_i)\psi_{A_1} = 1\psi_{A_1}, \quad \forall G_i \in \mathcal{G}.$$

However, each multi-dimensional irreducible representation is not unique in its numerical form as similarity transformation connects many equivalent forms. In the context of physical applications, the basis of multi-dimensional irreducible representation often corresponds to a degenerate subspace of states. Therefore, similarity transformation just changes the basis of the degenerate subspace. When a certain matrix form of multi-dimensional representation is chosen [e.g., Cartesian (E_x, E_y) representation of Table A.2], we can identify eigenfunction by its row. That is, if we say that wavefunction ψ_n transforms as row n of irreducible representation Γ, we mean that Eq. (A.3) holds for a specific form of $\Gamma_{mn}(G_i)$ matrices. For example, in the C_{3v} group, when we say that functions ψ_{E_x} and ψ_{E_y} transforms as a basis of the irreducible (E_x, E_y) representation, we mean that:

$$T(C_3^+)\psi_{E_x} = -\frac{1}{2}\psi_{E_x} - \frac{\sqrt{3}}{2}\psi_{E_y},$$
$$T(C_3^+)\psi_{E_y} = \frac{\sqrt{3}}{2}\psi_{E_x} - \frac{1}{2}\psi_{E_y},$$

where $-1/2, \pm\sqrt{3}/2$ are the respective coefficients of the C_3^+ matrix.

A.4 Projection operators

In the above section, we showed that eigenstates of the symmetric Hamiltonian could be classified by their symmetry properties. In a general case, any arbitrary function can always be decomposed into parts that transform irreducibly. Formally this is done by using projection operators of group theory [89]:

$$\hat{P}_{\Gamma\gamma} = \frac{s_\Gamma}{g}\sum_i \Gamma^*_{\gamma\gamma}(G_i)T(G_i),$$

where s_Γ is the dimension of representation, and g is the order of the group (number of group elements). Operator $\hat{P}_{\Gamma\gamma}$ projects any function to the part, which transforms as row γ of irreducible representation Γ.

The projection operators are very useful in many different situations. Sometimes *a posteriori*, we want to find the symmetry of an eigenstate. In such a case, we could calculate $\langle\psi|\hat{P}_{\Gamma\gamma}|\psi\rangle$ for all $\hat{P}$'s and check whether it is equal to zero or one. This is how we classified vibrational and electronic states obtained by numerical methods. However, sometimes, we want to solve the eigenvalue problem by utilizing symmetry *a priori*. This time we can use projection operators to symmetrize the zero-order basis into species that transform as irreducible representations of a point group. As shown in Section A.7, such a basis can help reduce the computational complexity of the eigenvalue problem.

A.5 Irreducible sets of operators

Similarly, as for functions (or vectors), we can define an "irreducible set of operators" $\{\hat{S}_{\Gamma\gamma}|\gamma = 1, \ldots, s\}$ by the property:

$$T(G_i)\hat{S}_{\Gamma\gamma}T(G_i)^{-1} = \sum_{\gamma'}^{s} \Gamma_{\gamma'\gamma}(G_i)\hat{S}_{\Gamma\gamma'},$$

where $\Gamma_{\gamma'\gamma}(G_i)$ are matrices of irreducible representation Γ. Such a set of operators $\hat{S}_{\Gamma\gamma}$ is said to transform according to the irreducible representation Γ.

The Hamiltonian always transforms as an identity representation A_1 of the group of Shrödinger equation, since:

$$T(G_i)\hat{H}(\mathbf{r})T(G_i)^{-1} = \hat{H}(\mathbf{r}),$$

for all $G_i \in \mathcal{G}$.

A.6 Clebsh–Gordan coefficients

Let us assume that we have two sets of functions, $\{\psi_{\Gamma^\alpha\gamma^\alpha}|\gamma_\alpha = 1, 2, \ldots, s_\alpha\}$ and $\{\phi_{\Gamma^\beta\gamma^\beta}|\gamma_\beta = 1, 2, \ldots, s_\beta\}$, that transform as irreducible representations Γ^α and Γ^β. If we take a product of any two functions $\psi_{\Gamma^\alpha\gamma^\alpha}\phi_{\Gamma^\beta\gamma^\beta}$, this product generally does not transform as a basis of irreducible representation. However, it is possible to choose linear combinations:

$$\Psi_{\Gamma\gamma} = \sum_{\gamma^\alpha\gamma^\beta} \left\langle \Gamma^\alpha\gamma^\alpha\Gamma^\beta\gamma^\beta \middle| \Gamma\gamma \right\rangle \psi_{\Gamma^\alpha\gamma^\alpha}\phi_{\Gamma^\beta\gamma^\beta} \tag{A.5}$$

which transform irreducibly according to representation Γ_γ. The coefficients $\langle\Gamma^\alpha\gamma^\alpha\Gamma^\beta\gamma^\beta|\Gamma\gamma\rangle$ are usually called *Clebsh–Gordan coefficients for the group*.

These coefficients depend only on the group and form of representation matrices. They can be found from tabulated data [93] or calculated using computer algebra packages (e.g., Ref. [113]). The inverse of Eq. A.5 can be written as:

$$\psi_{\Gamma^\alpha\gamma^\alpha}\phi_{\Gamma^\beta\gamma^\beta} = \sum_\gamma \left\langle \Gamma\gamma \middle| \Gamma^\alpha\gamma^\alpha\Gamma^\beta\gamma^\beta \right\rangle \Psi_{\Gamma\gamma}, \tag{A.6}$$

where $\langle \Gamma\gamma | \Gamma^\alpha\gamma^\alpha\Gamma^\beta\gamma^\beta \rangle$ are inverse Clebsh–Gordan coefficients. These Clebsch–Gordan coefficients are the main parameters for group theory application to physical problems.

A.7 Wigner–Eckart theorem

So far, we have only introduced the language of the group theory and not much of practical implications. The most useful expression of the group theory for physical problems follows from the Wigner–Eckart theorem.

The Wigner–Eckart theorem [92]. *Let $\mathcal{G}$ be a discrete group of coordinate transformations. Let Γ^α, Γ^β, and Γ^δ be unitary irreducible representations of $\mathcal{G}$ of dimensions s_α, s_β, and s_γ, respectively, and suppose that $\phi_{\Gamma^\alpha\gamma^\alpha}(\mathbf{r})$, and $\psi_{\Gamma^\beta\gamma^\beta}(\mathbf{r})$, are sets of basis functions for Γ^α and Γ^β. Finally, let $\hat{X}_{\Gamma^\delta\gamma^\delta}$ be a set of irreducible tensor operators of Γ^δ. Then:*

$$\left\langle \phi_{\Gamma^\alpha\gamma^\alpha} \middle| \hat{X}_{\Gamma^\delta\gamma^\delta} \middle| \psi_{\Gamma^\beta\gamma^\beta} \right\rangle = \langle \Gamma\gamma_\alpha\Gamma_\delta\gamma_\delta | \Gamma\gamma_\beta \rangle \left\langle \phi_{\Gamma^\alpha} \middle\| \hat{X}_{\Gamma^\delta} \middle\| \psi_{\Gamma^\beta} \right\rangle, \tag{A.7}$$

where $\langle \phi_{\Gamma^\alpha} \| \hat{X}_{\Gamma^\delta} \| \psi_{\Gamma^\beta} \rangle$ are "reduced matrix elements" that are independent of γ^α, γ^β, and γ^δ.

The *reduced matrix element* is a scalar that does not depend on rows γ^α, γ^β, and γ^δ of irreducible representation.

From a physical point of view, Eq. A.7 represents the matrix element of some symmetric operator $\hat{X}_{\Gamma^\delta\gamma^\delta}$ (or irreducible set of operators). For example, this operator could be a position operator of the optical matrix element. Actually, if we choose a coordinate system of the NV center, such that the $\hat{e}_z$ axis goes through the symmetry axis of the center, and the $\hat{e}_y$ axis is in the plane σ_2 [Fig. A.1(e)], then position operator z transforms as A_1 representation of C_{3v} group, and x, y operators transform respectively as x and y rows of Cartesian representation (E_x, E_y). From Eq. (A.7), it follows that the symmetry alone allows us to deduce that certain matrix elements are zero and predict connections between the others.

If operator $\hat{X}$ is invariant (transforms as A_1 representation), then it can be shown that Clebsh–Gordan coefficients satisfy $\langle \Gamma^\alpha \gamma^\alpha; A_1 | \Gamma^\beta \gamma^\beta \rangle = \delta_{\Gamma^\alpha \Gamma^\beta} \delta_{\gamma^\alpha \gamma^\beta}$ and:

$$\left\langle \phi_{\Gamma^\alpha \gamma^\alpha} \middle| \hat{X}_{A_1} \middle| \psi_{\Gamma^\beta \gamma^\beta} \right\rangle \sim \delta_{\Gamma^\alpha \Gamma^\beta} \delta_{\gamma^\alpha \gamma^\beta}.$$

For the Shrödinger equation of symmetric Hamiltonian, this says that only the basis of the same symmetry are coupled, and we can decouple the diagonalization problem for each symmetry species.

In the case of degenerate states $\psi_{\Gamma^\alpha \gamma^\alpha}$ and $\phi_{\Gamma^\beta \gamma^\beta}$ (where $s_\alpha > 1$ or/and $s_\beta > 1$), Wigner–Eckart theorem says that single scalar $\langle \phi_{\Gamma^\alpha} \| \hat{X}_{\Gamma^\delta} \| \psi_{\Gamma^\beta} \rangle$ describes all matrix elements for a different choice of degenerate states γ^α and γ^β. The only difference is within the Clebsh–Gordan coefficients. Therefore, we can calculate the matrix element for a single pair of degenerate functions and deduce others from relation (A.7). Also, for some combinations, the Clebsh–Gordan coefficient will be zero.

Appendix B

NV MOLECULAR ORBITAL WAVEFUNCTIONS

In this appendix, using the formal methodology of Section 2.3.5, we derive molecular orbital states of the NV^0 center in diamond. In Section B.1, we obtain orbital parts of multi-electron wavefunctions that have well-defined spatial symmetry properties. In Section B.2, we obtain spin states of the multi-particle spin system. Finally, in Section B.3, we antisymmetrize different products of orbital and spin parts and deduce molecular orbital wavefunctions of NV^0.

B.1 Orbital wavefunctions

The geometric structure of the NV center has C_{3v} point group symmetry. From the electronic structure analysis of NV^- (Sec. 3.2.1), it follows that there are three localized single-particle defect orbitals in the bandgap: fully symmetric a_1 orbital and a doubly-degenerate e orbital (see Fig. 3.2). We use these single-particle states to construct multi-electron orbital wavefunctions that transform as irreducible representations of the C_{3v} point group. The construction is done via Eq. (2.46).

To determine Clebsch–Gordan (CG) coefficients entering Eq. (2.46), we choose the Cartesian form of irreducible representation matrices of the C_{3v} group (Table 2.1). Nonzero CG coefficients for this representation are given by:

$$\begin{aligned}
&\big\langle A_1;\Gamma^i n\big|\Gamma^j m\big\rangle = \delta_{ij}\delta_{nm}, && \langle E_i;E_j|A_2\rangle = \frac{1}{\sqrt{2}}\begin{pmatrix}0&-1\\1&0\end{pmatrix},\\
&\langle A_2;A_2|A_1\rangle = 1, && \langle E_i;E_j|E_x\rangle = \frac{1}{\sqrt{2}}\begin{pmatrix}0&1\\1&0\end{pmatrix},\\
&\langle E_i;E_j|E_y\rangle = \frac{1}{\sqrt{2}}\begin{pmatrix}1&0\\0&-1\end{pmatrix}, && \langle A_2;E_i|E_j\rangle = \begin{pmatrix}0&1\\-1&0\end{pmatrix},\\
&\langle E_i;E_j|A_1\rangle = \frac{1}{\sqrt{2}}\delta_{ij}. &&
\end{aligned} \tag{B.1}$$

$C_{3v} \otimes C_{3v}$	A_1	A_2	E
A_1	A_1	A_2	E
A_2	A_2	A_1	E
E	E	E	$A_1 \oplus A_2 \oplus E$

Table B.1: The C_{3v} point group direct product multiplication table.

These coefficients were determined using the GTPACK software package [113].

The direct product multiplication rules of the C_{3v} point group are given in Table B.1.

B.1.1 Two electrons

Using Eq. (2.46) and CG coefficient values of Eq. (B.1), we obtain the following orbital configurations for two-electron wavefunctions:

$$\begin{aligned}
&\Phi_{A_1}^{\alpha(2)} = a_1 a_1, && \Phi_{A_1}^{\beta(2)} = \frac{1}{\sqrt{2}}\left(e_x e_x + e_y e_y\right), \\
&\Phi_{A_2}^{(2)} = \frac{1}{\sqrt{2}}\left(e_y e_x - e_x e_y\right), && \Phi_{E_{x/y}}^{\alpha(2)} = a_1 e_{x/y}, \\
&\Phi_{E_x}^{\beta(2)} = \frac{1}{\sqrt{2}}\left(e_x e_y + e_y e_x\right), && \Phi_{E_y}^{\beta(2)} = \frac{1}{\sqrt{2}}\left(e_x e_x - e_y e_y\right).
\end{aligned} \tag{B.2}$$

Here, subscript shows the irreducible representation of the resultant wavefunction, greek letters α and β label different wavefunctions of the same symmetry, and the number in the superscript indicates the number of electrons.

B.1.2 Three electrons

Three-electron molecular-orbital states belong to the NV^0 manifold. Those can be found by combing orbitals from Eq. (B.2) with a one-electron orbital of a_1 or e symmetry.[1] The low-lying states (that contain at least one a_1 orbital) are:

$$\begin{aligned}
&\Phi_{A_1}^{(3)} = \frac{1}{\sqrt{2}}\left(a_1 e_x e_x + a_1 e_y e_y\right), && \Phi_{A_2}^{(3)} = \frac{1}{\sqrt{2}}\left(a_1 e_y e_x - a_1 e_x e_y\right), \\
&\Phi_{E_x}^{\alpha(3)} = \frac{1}{\sqrt{2}}\left(a_1 e_x e_y + a_1 e_y e_x\right), && \Phi_{E_y}^{\alpha(3)} = \frac{1}{\sqrt{2}}\left(a_1 e_x e_x - a_1 e_y e_y\right), \\
&\Phi_{E_{x/y}}^{\beta(3)} = a_1 a_1 e_{x/y}.
\end{aligned} \tag{B.3}$$

Note that for orbital wavefunctions, the order of orbitals is not important as long as permutations are simultaneously applied to all terms of the wavefunction.

[1] Note that we normalize the final result.

B.2 Spin eigenstates

To construct spin eigenstates of multi-particle spin operators $\mathbf{S}^2$ and $\mathbf{S}_z$ [see Eq. (2.42)], we use the genealogical construction scheme (see Sec. 2.3.5 for more details) and Eq. (2.45) for angular momentum coupling.

B.2.1 Two electrons

The spin eigenstates of two electrons are constructed by combining two spins. Those are well-known singlet and triplet states:

$$\begin{aligned}
\left|0,0;\tfrac{1}{2}\right\rangle &= \frac{1}{\sqrt{2}}\left(|\uparrow\downarrow\rangle - |\downarrow\uparrow\rangle\right), \\
\left|1,m_s;\tfrac{1}{2}\right\rangle &= \begin{cases} |\uparrow\uparrow\rangle, & \text{if } m_s = 1, \\ \frac{1}{\sqrt{2}}\left(|\uparrow\downarrow\rangle + |\downarrow\uparrow\rangle\right), & \text{if } m_s = 0, \\ |\downarrow\downarrow\rangle, & \text{if } m_s = -1. \end{cases}
\end{aligned} \tag{B.4}$$

Here, we use the notation $|S, S_m; P\rangle$, where P is a list of "parent" states from which N electron wavefunction was constructed. In this case, $1/2$ indicates that the two-electron state was constructed by adding one electron to the spin $1/2$ system.

B.2.2 Three electrons

Adding one electron to a singlet state of Eq. (B.4) could only yield a spin doublet ($S = 1/2$). In this case, non-zero Clebsch–Gordan coefficients are given by $\langle 0,0;\frac{1}{2},\pm\frac{1}{2}|\frac{1}{2},\pm\frac{1}{2}\rangle = 1$, and the following spin states are:

$$\left|\tfrac{1}{2},m_s;0,\tfrac{1}{2}\right\rangle = \begin{cases} |0,0;\frac{1}{2}\rangle\otimes|\uparrow\rangle = \frac{1}{\sqrt{2}}\left(|\uparrow\downarrow\uparrow\rangle - |\downarrow\uparrow\uparrow\rangle\right), & \text{if } m_s = \frac{1}{2}, \\ |0,0;\frac{1}{2}\rangle\otimes|\downarrow\rangle = \frac{1}{\sqrt{2}}\left(|\uparrow\downarrow\downarrow\rangle - |\downarrow\uparrow\downarrow\rangle\right), & \text{if } m_s = -\frac{1}{2}. \end{cases} \tag{B.5}$$

Combining triplet states of Eq. (B.4) with single spin can only yield doublet and quartet states ($S = 1/2$ and $S = 3/2$). Those are:

$$\left|\tfrac{1}{2},m_s;1,\tfrac{1}{2}\right\rangle = \frac{1}{\sqrt{6}}\begin{cases} 2|\uparrow\uparrow\downarrow\rangle - |\downarrow\uparrow\uparrow\rangle - |\uparrow\downarrow\uparrow\rangle, & \text{if } m_s = \frac{1}{2}, \\ 2|\downarrow\downarrow\uparrow\rangle - |\uparrow\downarrow\downarrow\rangle - |\downarrow\uparrow\downarrow\rangle, & \text{if } m_s = -\frac{1}{2}, \end{cases} \tag{B.6}$$

and

$$\left|\tfrac{3}{2}, m_s; 1, \tfrac{1}{2}\right\rangle = \begin{cases} |\uparrow\uparrow\uparrow\rangle, & \text{if } m_s = \frac{3}{2}, \\ \frac{1}{\sqrt{3}}\left(|\downarrow\uparrow\uparrow\rangle + |\uparrow\downarrow\uparrow\rangle + |\uparrow\uparrow\downarrow\rangle\right), & \text{if } m_s = \frac{1}{2}, \\ \frac{1}{\sqrt{3}}\left(|\uparrow\downarrow\downarrow\rangle + |\downarrow\uparrow\downarrow\rangle + |\downarrow\downarrow\uparrow\rangle\right), & \text{if } m_s = -\frac{1}{2}, \\ |\downarrow\downarrow\downarrow\rangle, & \text{if } m_s = -\frac{3}{2}. \end{cases} \tag{B.7}$$

B.3 NV^0 wavefunctions

B.3.1 Ground state

The ground state of NV^0 is a spin-doublet of E symmetry (^2E) [169, 170]. We obtain molecular-orbital wavefunctions of this state by antisymmetrizing the product of $\Phi^{\beta(3)}_{E_{x/y}}$ and $|\frac{1}{2}, m_s; 0, \frac{1}{2}\rangle$ states from Eqs. (B.3) and (B.5).[2]

As an example, let us derive the $m_s = 1/2$ state. First, we multiply orbital and spin counterparts, and then we promote each term to a Slater determinant, as shown below:

$$\begin{aligned} \left|^2E_{x/y}; m_s = \tfrac{1}{2}\right\rangle &= \frac{1}{\sqrt{2}}\mathcal{A}\left[\left(|\uparrow\downarrow\uparrow\rangle - |\downarrow\uparrow\uparrow\rangle\right)\left(a_1 a_1 e_{x/y}\right)\right] \\ &= \frac{1}{\sqrt{2}}\left(\left|a_1\bar{a}_1 e_{x/y}\right| - \left|\bar{a}_1 a_1 e_{x/y}\right|\right) \\ &\overset{\text{norm}}{=} \left|a_1\bar{a}_1 e_{x/y}\right|. \end{aligned}$$

In the last step, we have used the antisymmetric property of Slater determinant $|..b..c..| = -|..c..b...|$ and normalized the final wavefunction (as indicated by "norm" above last equality). We use the same approach for all other states derived below.

The four degenerate wavefunctions of the ground ^2E manifold are given by:

$$\left|^2E_{x/y}; m_s\right\rangle = \begin{cases} |a_1\bar{a}_1 e_{x/y}|, & \text{if } m_s = \frac{1}{2}, \\ |\bar{a}_1 a_1 \bar{e}_{x/y}|, & \text{if } m_s = -\frac{1}{2}. \end{cases}$$

Note that we freely chose the sign of normalized wavefunction to highlight the symmetry between spin states of opposite m_s signs.

[2] Spin states $|\frac{1}{2}, m_s; 1, \frac{1}{2}\rangle$ constructed from triplet wavefunctions are not suitable since they produce wavefunctions where two same-spin electrons occupy one orbital.

B.3.2 Excited spin-doublet states

The lowest optically excited state is the electronic $^2A_2$ state [169, 170]. The molecular orbital wavefunction for this state is obtained combining $\Phi^{\beta(3)}_{A_2}$ and $|\frac{1}{2}, m_s; 0, \frac{1}{2}\rangle$ wavefunctions:

$$\left|^2A_2, m_s\right\rangle = \frac{1}{\sqrt{6}} \begin{cases} \left(|a_1\bar{e}_x e_y| + |a_1 e_x \bar{e}_y| - 2|\bar{a}_1 e_x e_y|\right), & \text{if } m_s = \frac{1}{2} \\ \left(|\bar{a}_1 e_x \bar{e}_y| + |\bar{a}_1 \bar{e}_x e_y| - 2|a_1 \bar{e}_y \bar{e}_x|\right), & \text{if } m_s = -\frac{1}{2}. \end{cases}$$

The second excited doublet state is of the same symmetry as the NV^0 ground state (^2E) [170]. The wavefunction for this state can be obtained by combining $\Phi^{\alpha(3)}_{E_{x/y}}$ orbital wavefunction with doublet spin states. However, $\Phi^{\alpha(3)}_{E_y}$ state [see Eq. (B.3)] contains products where two last orbitals are equal (i.e., $a_1 e_x e_x$). Therefore, spin terms $|\downarrow\uparrow\uparrow\rangle$ and $|\uparrow\downarrow\downarrow\rangle$ combined with such products would yield unphysical states, where two electrons of the same spin occupy one orbital. By taking a linear combination of Eqs. (B.5) and (B.6), we obtain the third form of the spin-doublet wavefunction:

$$\left|\tfrac{1}{2}, m_s; c\right\rangle = \frac{1}{\sqrt{2}} \begin{cases} |\uparrow\uparrow\downarrow\rangle - |\uparrow\downarrow\uparrow\rangle, & \text{if } m_s = \frac{1}{2}, \\ |\downarrow\downarrow\uparrow\rangle - |\downarrow\uparrow\downarrow\rangle & \text{if } m_s = -\frac{1}{2}. \end{cases} \tag{B.8}$$

Antisymmetrizing product of $\Phi^{\alpha(3)}_{E_{x/y}}$ with states of Eq. (B.8) we obtain the following form:

$$\left|^2E'_i; m_s\right\rangle = \frac{1}{\sqrt{2}} \begin{cases} |a_1\bar{e}_x e_y| + |a_1\bar{e}_y e_x|, & \text{if } m_s = \frac{1}{2},\ i = x, \\ |\bar{a}_1 e_x \bar{e}_y| + |\bar{a}_1 e_y \bar{e}_x|, & \text{if } m_s = -\frac{1}{2},\ i = x, \\ |a_1 e_y \bar{e}_y| + |a_1 \bar{e}_x e_x|, & \text{if } m_s = \frac{1}{2},\ i = y, \\ |\bar{a}_1 \bar{e}_y e_y| + |\bar{a}_1 e_x \bar{e}_x|, & \text{if } m_s = -\frac{1}{2},\ i = y. \end{cases}$$

Although in this representation, the wavefunction is not a single Slater determinant, one can show that it attains single-determinant form in the "chiral" representation $E_\pm$ [see Eq. (2.95)]:

$$\left|^2E_\pm, m_s\right\rangle = \begin{cases} |a_1 e_\mp \bar{e}_\mp|, & \text{if } m_s = \frac{1}{2}, \\ |\bar{a}_1 \bar{e}_\mp e_\mp|, & \text{if } m_s = -\frac{1}{2}. \end{cases}$$

The last spin-doublet wavefunction that contains at least one a_1 orbital is the $^2A_1$ state [170]. This state is obtained combining Eq. (B.8) with $\Phi^{\beta(3)}_{A_1}$:

$$\left|^2A_1, m_s\right\rangle = \frac{1}{\sqrt{2}} \begin{cases} |a_1\bar{e}_x e_x| + |a_1\bar{e}_y e_y|, & \text{if } m_s = \frac{1}{2}, \\ |\bar{a}_1 e_x \bar{e}_x| + |\bar{a}_1 e_y \bar{e}_y|, & \text{if } m_s = -\frac{1}{2}. \end{cases}$$

Conf.	Molecular orbital wavefunction

$$a_1^2e^2 \quad |^3A_2; m_s\rangle = \begin{cases} |a_1\bar{a}_1e_xe_y|, & \text{if } m_s = 1, \\ \frac{1}{\sqrt{2}}\left(|a_1\bar{a}_1e_x\bar{e}_y| + |a_1\bar{a}_1\bar{e}_xe_y|\right) & \text{if } m_s = 0, \\ |\bar{a}_1a_1\bar{e}_x\bar{e}_y|, & \text{if } m_s = -1, \end{cases}$$

$$|^1E_i\rangle = \frac{1}{\sqrt{2}} \begin{cases} |a_1\bar{a}_1e_x\bar{e}_x| - |a_1\bar{a}_1e_y\bar{e}_y|, & \text{if } i = x, \\ |a_1\bar{a}_1\bar{e}_xe_y| - |a_1\bar{a}_1e_x\bar{e}_y|, & \text{if } i = y, \end{cases}$$

$$|^1A_1\rangle = \frac{1}{\sqrt{2}}\left(|a_1\bar{a}_1e_x\bar{e}_x| + |a_1\bar{a}_1e_y\bar{e}_y|\right),$$

$$a_1e^3 \quad |^3E_i, m_s\rangle = \begin{cases} |a_1e_xe_y\bar{e}_y|, & \text{if } m_s = 1,\ i = x, \\ \frac{1}{\sqrt{2}}\left(|a_1\bar{e}_xe_y\bar{e}_y| + |\bar{a}_1e_xe_y\bar{e}_y|\right), & \text{if } m_s = 0,\ i = x, \\ |\bar{a}_1\bar{e}_x\bar{e}_ye_y|, & \text{if } m_s = -1,\ i = x, \\ |a_1e_x\bar{e}_xe_y|, & \text{if } m_s = 1,\ i = y, \\ \frac{1}{\sqrt{2}}\left(|a_1e_x\bar{e}_x\bar{e}_y| + |\bar{a}_1e_x\bar{e}_xe_y|\right), & \text{if } m_s = 0,\ i = y, \\ |\bar{a}_1\bar{e}_xe_x\bar{e}_y|, & \text{if } m_s = -1,\ i = y. \end{cases}$$

Table B.2: Molecular orbital states of the NV^- center from Ref. [160].

B.3.3 Metastable quartet state $^4A_2$

Wavefunctions of the $^4A_2$ state are obtained by combining $\Phi^{\alpha(3)}_{E_{x/y}}$ orbitals with quartet spin functions of Eq. (B.7):

$$\left|^4A_2; m_s\right\rangle = \begin{cases} |a_1e_xe_y|, & m_s = \frac{3}{2}, \\ \frac{1}{\sqrt{3}}\left(|\bar{a}_1e_xe_y| + |a_1\bar{e}_xe_y| + |a_1e_x\bar{e}_y|\right), & m_s = \frac{1}{2}, \\ \frac{1}{\sqrt{3}}\left(|a_1\bar{e}_x\bar{e}_y| + |\bar{a}_1e_x\bar{e}_y| + |\bar{a}_1\bar{e}_xe_y|\right), & m_s = -\frac{1}{2}, \\ |\bar{a}_1\bar{e}_x\bar{e}_y|, & m_s = -\frac{3}{2}. \end{cases}$$

B.4 NV^- wavefunctions

Molecular orbital wavefunctions of NV^- manifold were deduced in Ref. [160]. For convenience we present states of Fig. 1.1(c) in the Table. B.2.

Appendix C

DEGENERATE PERTURBATION THEORY FOR $E \otimes (e \otimes e \otimes \cdots)$ PROBLEM

Let us look at how degenerate perturbation theory applies to the Jahn–Teller problem. In general, we want to solve the equation:

$$(\hat{H}^0 + \lambda \hat{H}^{\mathrm{JT}}) \left|\mathbf{nl}; E_\pm\right\rangle = E \left|\mathbf{nl}; E_\pm\right\rangle, \tag{C.1}$$

where λ can take on values ranging from 0 (no perturbation) to 1 (full perturbation). Here $\mathbf{nl} = \{n_1 l_1, \ldots, n_N l_N\}$ stands for vibrational degrees of freedom, and $E_\pm$ represents electronic manifold. As it is usual, we expand the solutions in power series:

$$\begin{aligned} \left|\mathbf{nl}; E_\pm\right\rangle_\lambda &= \left|\mathbf{nl}^{(0)}; E_\pm\right\rangle + \lambda \left|\mathbf{nl}^{(1)}; E_\pm\right\rangle + \lambda^{(2)} \left|\mathbf{nl}^{(2)}; E_\pm\right\rangle + \cdots, \\ E_{\mathbf{n};\pm} &= E^{(0)}_{\mathbf{n}} + \lambda E^{(1)}_{\mathbf{n};\pm} + \lambda^2 E^{(2)}_{\mathbf{n};\pm} + \cdots. \end{aligned} \tag{C.2}$$

Substituting Eq. (C.2) into Eq. (C.1) yields a set of equations for different powers of λ:

$$\begin{aligned} &\lambda^{(0)} : (\hat{H}^0 - E^{(0)}_{\mathbf{n}}) \left|\mathbf{nl}^{(0)}; E_\pm\right\rangle = 0, \\ &\lambda^{(1)} : (\hat{H}^0 - E^{(0)}_{\mathbf{n}}) \left|\mathbf{nl}^{(1)}; E_\pm\right\rangle = (E^{(1)}_{\mathbf{n};\pm} - \hat{H}^{\mathrm{JT}}) \left|\mathbf{nl}^{(0)}; E_\pm\right\rangle, \\ &\lambda^{(2)} : (\hat{H}^0 - E^{(0)}_{\mathbf{n}}) \left|\mathbf{nl}^{(2)}; E_\pm\right\rangle = (E^{(1)}_{\mathbf{n};\pm} - \hat{H}^{\mathrm{JT}}) \left|\mathbf{nl}^{(1)}; E_\pm\right\rangle + E^{(2)}_{\mathbf{n};\pm} \left|\mathbf{nl}^{(0)}; E_\pm\right\rangle, \\ &\cdots. \end{aligned}$$

Diagonal terms of Jahn–Teller Hamiltonian are zero:

$$\left\langle \mathbf{nl}^{(0)}; E_\pm \right| \hat{H}^{\mathrm{JT}} \left|\mathbf{nl}^{(0)}; E_\pm\right\rangle = 0.$$

From the λ^1 equation, it follows that the first-order energy correction is zero:

$$E^{(1)}_{\mathbf{n};\pm} = 0.$$

The first-order equation for wavefunction becomes:

$$\left|\mathbf{nl}^{(1)}; E_\pm\right\rangle = \frac{1}{E^{(0)}_{\mathbf{n}}}\left(\hat{H}^0\left|\mathbf{nl}^{(1)}; E_\pm\right\rangle + \hat{H}^{\mathrm{JT}}\left|\mathbf{nl}^{(0)}; E_\pm\right\rangle\right) \tag{C.3}$$

The simplification for $E\otimes(e\otimes e\otimes\cdots)$ problem comes from the symmetry of Hamiltonian. The eigenstates of vibronic Hamiltonian must be the eigenstates of $\hat{J}_{\mathrm{el}}$ [see Eq (2.94)]. Therefore, the correction term $|\mathbf{nl}^{(1)}; E_\pm\rangle$ cannot have contributions from the degenerate subspace of $|\mathbf{nl}^{(0)}; E_\pm\rangle$ (note that degeneracy is between different values of l and electronic levels $|E_\pm\rangle$). Following this argument, we write the first-order correction term:

$$\left|\mathbf{nl}^{(1)}; E_\pm\right\rangle = \sum_{\tilde{\mathbf{n}}\tilde{\mathbf{l}}\neq\mathbf{nl}} \frac{\langle\tilde{\mathbf{n}}\tilde{\mathbf{l}}^{(0)}; E_\mp|\hat{H}^{\mathrm{JT}}|\mathbf{nl}^{(0)}; E_\pm\rangle}{E^{(0)}_{\tilde{\mathbf{n}}} - E^{(0)}_{\tilde{\mathbf{n}}}}\left|\tilde{\mathbf{n}}\tilde{\mathbf{l}}^{(0)}; E_\mp\right\rangle.$$

This equation applied to the lowest energy eigenstate yields:

$$\left|\mathbf{00}^{(1)}; E_\pm\right\rangle = -\mathcal{A}\sqrt{2}\sum_k K_k\left|E_\mp\right\rangle\left|n_k{=}1, l_k{=}\pm1\right\rangle\prod_{l\neq k}\left|n_l{=}0, l_l{=}0\right\rangle, \tag{C.4}$$

where $\mathcal{A} = 1/\sqrt{1+2\sum_k K^2}$ is the normalization factor. The second-order correction for the ground state can be derived by considering λ^2 order expression:

$$\left(\hat{H}^0 - E^{(0)}_{\mathbf{0}}\right)\left|\mathbf{00}^{(2)}; E_\pm\right\rangle = -\hat{H}^{\mathrm{JT}}\left|\mathbf{00}^{(1)}; E_\pm\right\rangle + E^{(2)}_{\mathbf{0};\pm}\left|\mathbf{00}^{(0)}; E_-\right\rangle. \tag{C.5}$$

Multiplying this equation from the left-hand side by $\langle\mathbf{nl}^{(0)}; E_\pm|$, we get an expression for expansion coefficient:

$$\left\langle\mathbf{nl}^{(0)}; E_\pm\middle|\mathbf{00}^{(2)}; E_\pm\right\rangle = -\frac{\langle\mathbf{nl}^{(0)}; E_\pm|\hat{H}^{\mathrm{JT}}|\mathbf{00}^{(1)}; E_\pm\rangle}{E^{(0)}_{\mathbf{n}} - E^{(0)}_{\mathbf{0}}}.$$

Note that $\langle\mathbf{nl}^{(0)}; E_\mp|\mathbf{00}^{(2)}; E_\pm\rangle = 0$. The second-order correction takes the form:

$$\left|\mathbf{00}^{(2)}; E_\pm\right\rangle = -\sum_{\mathbf{nl}}\frac{\langle\mathbf{nl}^{(0)}; E_\pm|\hat{H}^{\mathrm{JT}}|\mathbf{00}^{(1)}; E_\pm\rangle}{E^{(0)}_{\mathbf{n}} - E^{(0)}_{\mathbf{0}}}\left|\mathbf{nl}^{(0)}; E_\pm\right\rangle.$$

Using Eqs. (C.4) and (2.100) (and after some algebra), we arrive at the expression for the second-order correction:

$$\begin{aligned}&\left|\mathbf{00}^{(2)};E_{\pm}\right\rangle \\ &\quad=\sqrt{2}\sum_{k}K_{k}^{2}\left|\mathbf{00},n_{k}{=}2,l_{k}{=}0,\mathbf{00};E_{\pm}\right\rangle \\ &\quad+\sqrt{8}\sum_{k}\sum_{q\neq k}K_{k}K_{q}\left|\mathbf{00},n_{k}{=}1,l_{k}{=}1,\mathbf{00},n_{q}{=}1,l_{q}{=}{-}1,\mathbf{00};E_{\pm}\right\rangle .\end{aligned} \tag{C.6}$$

Finally, from Eq. (C.5), we can derive the formal expression for the second-order energy correction:

$$E_{\mathbf{n};\pm}^{(2)}=-\sum_{\tilde{\mathbf{n}}\tilde{\mathbf{l}}\neq\mathbf{nl}}\frac{|\langle\tilde{\mathbf{n}}\tilde{\mathbf{l}}^{(0)};E_{\mp}|\hat{H}^{\mathrm{JT}}|\mathbf{nl}^{(0)};E_{\pm}\rangle|^{2}}{E_{\tilde{\mathbf{n}}}^{(0)}-E_{\tilde{\mathbf{n}}}^{(0)}}. \tag{C.7}$$

Substituting Eq. (2.100) and summing over all values of $\mathbf{nl}$, we get a general expression for energy correction:

$$E_{\boldsymbol{nl};\pm}^{(2)}=-\sum_{k}2K_{k}^{2}\omega_{k}(1\pm l_{k}). \tag{C.8}$$

For the ground state, this expression reduces to:

$$E_{\mathbf{n};\pm}^{(2)}=-2\sum_{k}K_{k}^{2}\omega_{k}.$$

BIBLIOGRAPHY

[T1] E. Londero, G. Thiering, L. Razinkovas, A. Gali, and A. Alkauskas, Phys. Rev. B **98**, 035306 (2018).

[T2] L. Razinkovas, M. W. Doherty, N. B. Manson, C. G. Van de Walle, and A. Alkauskas, Phys. Rev. B **104**, 045303 (2021).

[T3] L. Razinkovas, M. Maciaszek, F. Reinhard, M. W. Doherty, and A. Alkauskas, arXiv:2104.09144 [cond-mat.mtrl-sci] (2021), unpublished.

[4] I. Aharonovich, D. Englund, and M. Toth, Nat. Photonics **10**, 631 (2016).

[5] R. Hanson and D. D. Awschalom, Nature **453**, 1043 (2008).

[6] W. F. Koehl, B. B. Buckley, F. J. Heremans, G. Calusine, and D. D. Awschalom, Nature **479**, 84 (2011).

[7] D. D. Awschalom, L. C. Bassett, A. S. Dzurak, E. L. Hu, and J. R. Petta, Science **339**, 1174 (2013).

[8] A. Gottscholl, M. Diez, V. Soltamov, C. Kasper, A. Sperlich, M. Kianinia, C. Bradac, I. Aharonovich, and V. Dyakonov, Sci. Adv. **7**, eabf3630 (2021).

[9] D. D. Awschalom, R. Hanson, J. Wrachtrup, and B. B. Zhou, Nat. Photonics **12**, 516 (2018).

[10] M. W. Doherty, N. B. Manson, P. Delaney, F. Jelezko, J. Wrachtrup, and L. C. Hollenberg, Phys. Rep. **528**, 1 (2013).

[11] R. Schirhagl, K. Chang, M. Loretz, and C. L. Degen, Annu. Rev. Phys. Chem. **65**, 83 (2014).

[12] B. Hensen, H. Bernien, A. E. Dréau, A. Reiserer, N. Kalb, M. S. Blok, J. Ruitenberg, R. F. L. Vermeulen, R. N. Schouten, C. Abellán, W. Amaya, V. Pruneri, M. W. Mitchell, M. Markham, D. J. Twitchen, D. Elkouss, S. Wehner, T. H. Taminiau, and R. Hanson, Nature **526**, 682 (2015).

[13] C. E. Bradley, J. Randall, M. H. Abobeih, R. C. Berrevoets, M. J. Degen, M. A. Bakker, M. Markham, D. J. Twitchen, and T. H. Taminiau, Phys. Rev. X **9**, 031045 (2019).

[14] S. Pezzagna and J. Meijer, Appl. Phys. Rev. **8**, 011308 (2021).

[15] L. Bassett, A. Alkauskas, A. Exarhos, and K.-M. Fu, Nanophotonics **8**, 1867 (2019).

[16] B. Pingault, D.-D. Jarausch, C. Hepp, L. Klintberg, J. N. Becker, M. Markham, C. Becher, and M. Atatüre, Nat. Commun. **8**, 1 (2017).

[17] P. Kehayias, M. W. Doherty, D. English, R. Fischer, A. Jarmola, K. Jensen, N. Leefer, P. Hemmer, N. B. Manson, and D. Budker, Phys. Rev. B **88**, 165202 (2013).
[18] L. du Preez, *Electron paramagnetic resonance and optical investigations of defect centres in diamond*, Ph.D. thesis, University of the Witwatersrand, Johannesburg (1965).
[19] M. Doherty, F. Dolde, H. Fedder, F. Jelezko, J. Wrachtrup, N. Manson, and L. Hollenberg, Phys. Rev. B **85**, 205203 (2012).
[20] A. Gruber, A. Dräbenstedt, C. Tietz, L. Fleury, J. Wrachtrup, and C. Von Borczyskowski, Science **276**, 2012 (1997).
[21] F. Jelezko, T. Gaebel, I. Popa, A. Gruber, and J. Wrachtrup, Phys. Rev. Lett. **92**, 076401 (2004).
[22] G. Balasubramanian, P. Neumann, D. Twitchen, M. Markham, R. Kolesov, N. Mizuochi, J. Isoya, J. Achard, J. Beck, J. Tissler, *et al.*, Nat. Mater. **8**, 383 (2009).
[23] N. Bar-Gill, L. M. Pham, A. Jarmola, D. Budker, and R. L. Walsworth, Nat. Commun. **4**, 1 (2013).
[24] S.-Y. Lee, M. Widmann, T. Rendler, M. W. Doherty, T. M. Babinec, S. Yang, M. Eyer, P. Siyushev, B. J. Hausmann, M. Loncar, *et al.*, Nat. Nanotechnol. **8**, 487 (2013).
[25] E. Neu, D. Steinmetz, J. Riedrich-Möller, S. Gsell, M. Fischer, M. Schreck, and C. Becher, New J. Phys. **13**, 025012 (2011).
[26] T. Azumi and K. Matsuzaki, Photochem. Photobiol. **25**, 315 (1977).
[27] I. B. Bersuker and V. Z. Polinger, *Vibronic interactions in molecules and crystals* (Springer, 1989).
[28] I. Bersuker, *The Jahn-Teller Effect* (Cambridge University Press, 2006).
[29] P. Hohenberg and W. Kohn, Phys. Rev. **136**, B864 (1964).
[30] W. Kohn and L. J. Sham, Phys. Rev. **140**, A1133 (1965).
[31] M. Levy, Proc. Natl. Acad. Sci. **76**, 6062 (1979).
[32] E. H. Lieb, Int. J. Quantum Chem. **24**, 243 (1983).
[33] C. R. Jacob and M. Reiher, Int. J. Quantum Chem. **112**, 3661 (2012).
[34] U. von Barth and L. Hedin, J. Phys. C: Solid State Phys. **5**, 1629 (1972).
[35] O. Gunnarsson and B. I. Lundqvist, Phys. Rev. B **13**, 4274 (1976).
[36] J. F. Janak, Phys. Rev. B **18**, 7165 (1978).
[37] R. G. Parr and Y. Weitao, *Density functional theory of atoms and molecules* (Oxford University Press, Inc, 1989).
[38] J. P. Perdew, R. G. Parr, M. Levy, and J. L. Balduz, Phys. Rev. Lett. **49**, 1691 (1982).
[39] A. R. Williams and U. von Barth, Applications of density functional theory to atoms, molecules, and solids, in *Theory of the Inhomogeneous Electron Gas*, edited by S. Lundqvist and N. H. March (Springer US, Boston, MA, 1983) pp. 189–308.
[40] J. P. Perdew and M. Levy, Phys. Rev. Lett. **51**, 1884 (1983).
[41] L. J. Sham and M. Schlüter, Phys. Rev. Lett. **51**, 1888 (1983).
[42] J. P. Perdew, Int. J. Quantum Chem. **28**, 497 (1985).

[43] E. Runge and E. K. U. Gross, Phys. Rev. Lett. **52**, 997 (1984).
[44] R. W. Godby, M. Schlüter, and L. J. Sham, Phys. Rev. B **37**, 10159 (1988).
[45] M. S. Hybertsen and S. G. Louie, Phys. Rev. B **34**, 5390 (1986).
[46] G. Onida, L. Reining, and A. Rubio, Rev. Mod. Phys. **74**, 601 (2002).
[47] T. Klüner, N. Govind, Y. A. Wang, and E. A. Carter, J. Chem. Phys. **116**, 42 (2002).
[48] L. Hedin, J. Phys.: Condens. Matter **11**, R489 (1999).
[49] A. Seidl, A. Görling, P. Vogl, J. A. Majewski, and M. Levy, Phys. Rev. B **53**, 3764 (1996).
[50] Z.-h. Yang, H. Peng, J. Sun, and J. P. Perdew, Phys. Rev. B **93**, 205205 (2016).
[51] J. P. Perdew, W. Yang, K. Burke, Z. Yang, E. K. U. Gross, M. Scheffler, G. E. Scuseria, T. M. Henderson, I. Y. Zhang, A. Ruzsinszky, H. Peng, J. Sun, E. Trushin, and A. Görling, Proc. Natl. Acad. Sci. U.S.A. **114**, 2801 (2017).
[52] A. D. Becke, J. Chem. Phys. **98**, 1372 (1993).
[53] J. Heyd, G. E. Scuseria, and M. Ernzerhof, J. Chem. Phys. **118**, 8207 (2003).
[54] C. Lee, W. Yang, and R. G. Parr, Phys. Rev. B **37**, 785 (1988).
[55] J. Sun, A. Ruzsinszky, and J. P. Perdew, Phys. Rev. Lett. **115**, 036402 (2015).
[56] A. J. Garza and G. E. Scuseria, J. Phys. Chem. Lett. **7**, 4165 (2016).
[57] E. J. Baerends and O. V. Gritsenko, J. Phys. Chem. A **101**, 5383 (1997).
[58] A. Hellman, B. Razaznejad, and B. I. Lundqvist, J. Chem. Phys. **120**, 4593 (2004).
[59] R. O. Jones and O. Gunnarsson, Rev. Mod. Phys. **61**, 689 (1989).
[60] J. P. Goss, R. Jones, S. J. Breuer, P. R. Briddon, and S. Öberg, Phys. Rev. Lett. **77**, 3041 (1996).
[61] A. Gali, M. Fyta, and E. Kaxiras, Phys. Rev. B **77**, 155206 (2008).
[62] A. Gali, E. Janzén, P. Deák, G. Kresse, and E. Kaxiras, Phys. Rev. Lett. **103**, 186404 (2009).
[63] A. Görling, Phys. Rev. A **59**, 3359 (1999).
[64] J. P. Perdew and K. Schmidt, AIP Conf. Proc. **577**, 1 (2001).
[65] P. A. M. Dirac, Math. Proc. Camb. Philos. Soc. **26**, 376–385 (1930).
[66] D. M. Ceperley and B. J. Alder, Phys. Rev. Lett. **45**, 566 (1980).
[67] D. C. Langreth and M. J. Mehl, Phys. Rev. B **28**, 1809 (1983).
[68] A. D. Becke, Phys. Rev. A **38**, 3098 (1988).
[69] J. P. Perdew, K. Burke, and M. Ernzerhof, Phys. Rev. Lett. **77**, 3865 (1996).
[70] R. Van Noorden, B. Maher, and R. Nuzzo, Nature News **514**, 550 (2014).
[71] J. P. Perdew, S. Kurth, A. c. v. Zupan, and P. Blaha, Phys. Rev. Lett. **82**, 2544 (1999).
[72] J. Tao, J. P. Perdew, V. N. Staroverov, and G. E. Scuseria, Phys. Rev. Lett. **91**, 146401 (2003).

[73] A. D. Becke, J. Chem. Phys. **88**, 1053 (1988).
[74] A. D. Becke, J. Chem. Phys. **98**, 5648 (1993).
[75] B. G. Janesko, T. M. Henderson, and G. E. Scuseria, Phys. Chem. Chem. Phys. **11**, 443 (2009).
[76] A. J. Cohen, P. Mori-Sánchez, and W. Yang, Phys. Rev. B **77**, 115123 (2008).
[77] G. Kresse and J. Furthmüller, Phys. Rev. B **54**, 11169 (1996).
[78] C. Kittel, *Introduction to Solid State Physics* (Wiley, 2004).
[79] H. J. Monkhorst and J. D. Pack, Phys. Rev. B **13**, 5188 (1976).
[80] C. Freysoldt, J. Neugebauer, and C. G. Van de Walle, Phys. Rev. Lett. **102**, 1 (2009).
[81] P. E. Blöchl, Phys. Rev. B **50**, 17953 (1994).
[82] A. M. Stoneham, *Theory of defects in solids* (Oxford University Press, 2001).
[83] C. A. Coulson and M. J. Kearsley, Proc. R. Soc. A **241**, 433 (1957).
[84] J. H. N. Loubser and J. A. van Wyk, Rep. Prog. Phys. **41**, 1201 (1978).
[85] A. Gali and J. R. Maze, Phys. Rev. B **88**, 235205 (2013).
[86] A. Gali, P. Soc. Photo-opt. Ins. **8**, 1907 (2019).
[87] M. Mackoit-Sinkevičienė, M. Maciaszek, C. G. Van de Walle, and A. Alkauskas, Appl. Phys. Lett. **115**, 212101 (2019).
[88] C. E. Dreyer, A. Alkauskas, J. L. Lyons, A. Janotti, and C. G. Van de Walle, Annu. Rev. Mater. Res. **48**, 1 (2018).
[89] M. Tinkham, *Group theory and quantum mechanics* (Dover, 2003).
[90] J. Elliott and P. Dawber, *Symmetry in Physics, Volume 1 and 2* (Macmillan, 1979).
[91] R. Pauncz, *Spin eigenfunctions: construction and use* (Springer Science & Business Media, 2012).
[92] J. F. Cornwell, *Group theory in physics: An introduction* (Academic press, 1997).
[93] J. S. Griffith, *The irreducible tensor method for molecular symmetry groups* (Courier Dover Publications, 2006).
[94] R. S. Mulliken, J. Chem. Phys. **23**, 1997 (1955).
[95] R. M. Martin, *Electronic structure. Basic theory and practical methods* (Cambridge University Press, 2004).
[96] M. Born and K. Huang, *Dynamical theory of crystal lattices* (Oxford University Press, 1954).
[97] I. Lifshitz, Nuovo Cim. Suppl. **3**, 716 (1956).
[98] A. A. Maradudin, Rep. Prog. Phys. **28**, 331 (1965).
[99] R. J. Elliott, *Vibrations of Defects in Lattices*, Vol. 7237 (Argonne National Laboratory, 1966).
[100] A. Maradudin, in *Solid state physics*, Vol. 18 (Elsevier, 1966) pp. 273–420.
[101] A. Maradudin, in *Phonons and Phonon Interactions*, edited by T. A. Bak (W. A. Benjamin Inc., 1964) pp. "424–504".
[102] P. H. Dederichs and R. Zeller, Phys. Rev. B **14**, 2314 (1976).

[103] R. Brout and W. Visscher, Phys. Rev. Lett. **9**, 54 (1962).
[104] A. Gali, T. Simon, and J. Lowther, New J. Phys. **13**, 025016 (2011).
[105] J. Zhang, C.-Z. Wang, Z. Zhu, and V. Dobrovitski, Phys. Rev. B **84**, 035211 (2011).
[106] G. Thiering and A. Gali, Phys. Rev. B **96**, 081115 (2017).
[107] A. Hashemi, C. Linderälv, A. V. Krasheninnikov, T. Ala-Nissila, P. Erhart, and H.-P. Komsa, Phys. Rev. B **103**, 125203 (2021).
[108] J. Bouquiaux, S. Poncé, Y. Jia, A. Miglio, M. Mikami, and X. Gonze, Adv. Opt. Mater. **9**, 2100649 (2021).
[109] A. Alkauskas, B. B. Buckley, D. D. Awschalom, and C. G. Van de Walle, New J. Phys. **16**, 073026 (2014).
[110] G. Davies, Rep. Prog. Phys. **44**, 787 (1981).
[111] T. A. Abtew, Y. Sun, B.-C. Shih, P. Dev, S. Zhang, and P. Zhang, Phys. Rev. Lett. **107**, 146403 (2011).
[112] M. C. M. O'Brien, J. Phys. C: Solid State Phys. **5**, 2045 (1972).
[113] R. M. Geilhufe and W. Hergert, Front. Phys. **6**, 86 (2018).
[114] C. Cohen-Tannoudji, B. Diu, and F. Laloë, *Quantum Mechanics, Vols I and II* (Hermann and John Wiley & Sons, 1977).
[115] F. S. Ham, Phys. Rev. **166**, 307 (1968).
[116] M. W. Doherty, *The Theory of the Nitrogen-Vacancy Colour Centre in Diamond*, Ph.D. thesis, The University of Melbourne (2012).
[117] H. C. Longuet-Higgins, U. Öpik, M. H. L. Pryce, and R. Sack, Proc. R. Soc. Lond., Ser. A. **244**, 1 (1958).
[118] B. Halperin and R. Englman, Phys. Rev. Lett. **31**, 1052 (1973).
[119] M. C. M. O'Brien and S. N. Evangelou, J. Phys. C: Solid State Phys. **13**, 611 (1980).
[120] B. K. Ridley, *Quantum processes in semiconductors* (Oxford University Press, 2013).
[121] J. J. Sakurai and E. D. Commins, Modern quantum mechanics, revised edition (1995).
[122] M. Fox, *Quantum optics: an introduction*, Vol. 15 (OUP Oxford, 2006).
[123] F. Duschinsky, Acta Physicochimica URSS **7**, 551 (1937).
[124] J. J. Markham, Rev. Mod. Phys. **31**, 956 (1959).
[125] H. Kun and R. Avril, Proc. R. Soc. Lond., Ser. A. **204**, 406 (1950).
[126] M. Lax, J. Chem. Phys. **20**, 1752 (1952).
[127] G. Kresse, J. Furthmüller, and J. Hafner, Europhys. Lett. **32**, 729 (1995).
[128] O. Madelung, *Semiconductors: group IV elements and III-V compounds* (Springer, 2012).
[129] E. S. Zouboulis, M. Grimsditch, A. K. Ramdas, and S. Rodriguez, Phys. Rev. B **57**, 2889 (1998).
[130] J. Warren, J. Yarnell, G. Dolling, and R. Cowley, Phys. Rev. **158**, 805 (1967).
[131] A. Togo and I. Tanaka, Scr. Mater. **108**, 1 (2015).
[132] S. A. Solin and A. K. Ramdas, Phys. Rev. B **1**, 1687 (1970).
[133] B. Kramer and A. MacKinnon, Rep. Prog. Phys. **56**, 1469 (1993).

[134] A. Lenef and S. C. Rand, Phys. Rev. B **53**, 13441 (1996).
[135] N. B. Manson, M. Hedges, M. S. J. Barson, R. Ahlefeldt, M. W. Doherty, H. Abe, T. Ohshima, and M. J. Sellars, New J. Phys. **20**, 113037 (2018).
[136] G. Davies and M. Hamer, Proc. R. Soc. Lond., Ser. A. **348**, 285 (1976).
[137] C. Campos and J. E. Roman, Numer. Algorithms **60**, 279 (2012).
[138] V. Hernandez, J. E. Roman, and V. Vidal, ACM Trans. Math. Softw. **31**, 351 (2005).
[139] P. R. Amestoy, I. S. Duff, and J.-Y. L'Excellent, Comput. Methods Appl. Mech. Eng. **184**, 501 (2000).
[140] J. P. Goss, P. R. Briddon, and M. J. Shaw, Phys. Rev. B **76**, 075204 (2007).
[141] A. Dietrich, K. D. Jahnke, J. M. Binder, T. Teraji, J. Isoya, L. J. Rogers, and F. Jelezko, New J. Phys. **16**, 113019 (2014).
[142] H. Sternschulte, K. Thonke, R. Sauer, P. C. Münzinger, and P. Michler, Phys. Rev. B **50**, 14554 (1994).
[143] L. J. Rogers, K. D. Jahnke, M. W. Doherty, A. Dietrich, L. P. McGuinness, C. Müller, T. Teraji, H. Sumiya, J. Isoya, N. B. Manson, and F. Jelezko, Phys. Rev. B **89**, 235101 (2014).
[144] I. Osad'ko, Sov. Phys.-Uspekhi. **22**, 311 (1979).
[145] K.-M. C. Fu, C. Santori, P. E. Barclay, L. J. Rogers, N. B. Manson, and R. G. Beausoleil, Phys. Rev. Lett. **103**, 256404 (2009).
[146] K. Beha, A. Batalov, N. B. Manson, R. Bratschitsch, and A. Leitenstorfer, Phys. Rev. Lett. **109**, 097404 (2012).
[147] P. Siyushev, H. Pinto, M. Vörös, A. Gali, F. Jelezko, and J. Wrachtrup, Phys. Rev. Lett. **110**, 167402 (2013).
[148] N. Aslam, G. Waldherr, P. Neumann, F. Jelezko, and J. Wrachtrup, New J. Phys. **15**, 013064 (2013).
[149] E. Bourgeois, A. Jarmola, P. Siyushev, M. Gulka, J. Hruby, F. Jelezko, D. Budker, and M. Nesladek, Nat. Commun. **6**, 8577 (2015).
[150] G. Waldherr, J. Beck, M. Steiner, P. Neumann, A. Gali, T. Frauenheim, F. Jelezko, and J. Wrachtrup, Phys. Rev. Lett. **106**, 157601 (2011).
[151] B. J. Shields, Q. P. Unterreithmeier, N. P. de Leon, H. Park, and M. D. Lukin, Phys. Rev. Lett. **114**, 136402 (2015).
[152] D. A. Hopper, H. J. Shulevitz, and L. C. Bassett, Micromachines **9**, 437 (2018).
[153] E. Bourgeois, E. Londero, K. Buczak, J. Hruby, M. Gulka, Y. Balasubramaniam, G. Wachter, J. Stursa, K. Dobes, F. Aumayr, M. Trupke, A. Gali, and M. Nesladek, Phys. Rev. B **95**, 041402 (2017).
[154] J. Jeske, D. W. M. Lau, X. Vidal, L. P. McGuinness, P. Reineck, B. C. Johnson, M. W. Doherty, J. C. McCallum, S. Onoda, F. Jelezko, T. Ohshima, T. Volz, J. H. Cole, B. C. Gibson, and A. D. Greentree, Nat. Commun. **8**, 14000 (2017).
[155] R. Ulbricht and Z.-H. Loh, Phys. Rev. B **98**, 094309 (2018).
[156] V. M. Acosta, A. Jarmola, E. Bauch, and D. Budker, Phys. Rev. B **82**, 201202 (2010).

[157] S. R. Nair, L. J. Rogers, X. Vidal, R. P. Roberts, H. Abe, T. Ohshima, T. Yatsui, A. D. Greentree, J. Jeske, and T. Volz, P. Soc. Photo-opt. Ins. **9**, 4505 (2020).
[158] M. L. Goldman, M. W. Doherty, A. Sipahigil, N. Y. Yao, S. D. Bennett, N. B. Manson, A. Kubanek, and M. D. Lukin, Phys. Rev. B **91**, 165201 (2015).
[159] S. Felton, A. M. Edmonds, M. E. Newton, P. M. Martineau, D. Fisher, and D. J. Twitchen, Phys. Rev. B **77**, 081201 (2008).
[160] M. W. Doherty, N. B. Manson, P. Delaney, and L. C. L. Hollenberg, New J. Phys. **13**, 025019 (2011).
[161] M. E. Turiansky, A. Alkauskas, M. Engel, G. Kresse, D. Wickramaratne, J.-X. Shen, C. E. Dreyer, and C. G. Van de Walle, Comput. Phys. Commun. **267**, 108056 (2021).
[162] V. Popescu and A. Zunger, Phys. Rev. B **85**, 085201 (2012).
[163] P. Deák, B. Aradi, M. Kaviani, T. Frauenheim, and A. Gali, Phys. Rev. B **89**, 075203 (2014).
[164] G. Lucovsky, Solid State Commun. **3**, 299 (1965).
[165] F. Nava, C. Canali, C. Jacoboni, L. Reggiani, and S. Kozlov, Solid State Commun. **33**, 475 (1980).
[166] L. Hacquebard and L. Childress, Phys. Rev. A **97**, 063408 (2018).
[167] D. M. Irber, F. Poggiali, F. Kong, M. Kieschnick, T. Lühmann, D. Kwiatkowski, J. Meijer, J. Du, F. Shi, and F. Reinhard, Nat. Commun. **12**, 532 (2021).
[168] Y. Zhang, Qiand Guo, W. Ji, M. Wang, F. Yin, Junand Kong, Y. Lin, F. Yin, Chunmingand Shi, Y. Wang, and J. Du, Nat. Commun. **12**, 1529 (2021).
[169] A. Gali, Phys. Rev. B **79**, 235210 (2009).
[170] A. Ranjbar, M. Babamoradi, M. Heidari Saani, M. A. Vesaghi, K. Esfarjani, and Y. Kawazoe, Phys. Rev. B **84**, 165212 (2011).
[171] C. Hepp, T. Müller, V. Waselowski, J. N. Becker, B. Pingault, H. Sternschulte, D. Steinmüller-Nethl, A. Gali, J. R. Maze, M. Atatüre, and C. Becher, Phys. Rev. Lett. **112**, 036405 (2014).

SANTRAUKA

1 Įžanga

Jei pažiūrėtume į kristalą geru mikroskopu, pamatytume, kad jis turi labai tvarkingą periodinę atominę struktūrą. Tačiau kristale visada galime rasti defektų, kurie pažeidžia periodinę simetriją ir pakeičia kristalo fizikines savybes. Defektų yra įvairių rūšių, o pati paprasčiausia yra taškiniai defektai. Tokie defektai sutrikdo artimąją tvarką vieno arba kelių atomų aplinkoje. Pavyzdžiui, kai kurių atomų gali trūkti (vakansija) arba tam tikri atomai gali būti pakeisti svetimais (pakaitinis defektas). Puslaidininkiuose taškiniai defektai yra skirstomi į dvi grupes: seklieji (angl. *shalow*) ir gilieji (angl. *deep*) defektai. Seklieji defektai lengvai atiduoda elektronus kristalo laidumo juostai arba juos pasiima iš valentinės juostos, taip nulemdami puslaidininkio laidumą ir jo tipą. Tuo tarpu, giliesiems defektams energija, reikalinga išlaisvinti arba pagauti elektroną, yra daug didesnė nei charakteringa šiluminė energija. Šių defektų elektroninės būsenos yra stipriai lokalizuotos ir primena atomų arba molekulių sistemas. Ši disertacija ir yra apie tokius giliuosius kristalo defektus bei jų teorinį aprašymą.

Žiūrint iš istorinės pusės, gilieji defektai buvo laikomi žalingais, nes jie dažnai neigiamai veikia medžiagos savybes, pageidautinas technologiniams taikymams. Tačiau paskutinių dvidešimties metų bėgyje atsirado naujas susidomėjimas optiškai aktyviais giliaisiais kristalo defektais (spalviniais centrais). Visų pirma, tam tikri defektai pasižymi stabilia optine spinduliuote. Ši savybė leidžia aptikti pavienius centrus ir juos naudoti kaip pavienių fotonų šaltinius kvantinės optikos taikymuose [4]. Be to, kai kurių giliųjų defektų lokalizuotos elektroninės būsenos gali būti kontroliuojamos bei nuskaitomos, naudojant optinius ir/ar elektrinius metodus. Šiuo metu didžiausias technologinis progresas yra pasiektas giliųjų defektų sukininių būsenų valdyme [5–8]. Dėl silpnos sąveikos su aplinka puslaidininkio defektų sukiniai turi ilgus koherentiškumo laikus (kartais net kambario temperatūroje). Šių savybių dėka galime valdyti kvant-mechanines koherentines būsenas laiko skalėse, tinkamose modernioms kvantinėms technologijoms [9]. Tokie defektai dažnai vadinami tiesiog „kvantiniais defektais“.

Šioje disertacijoje tiriamas neigiamai įkrautas azoto ir vakansijos kompleksas deimanto kristale, kitaip vadinamas NV^- centru [10]. Šis gilusis defektas yra optiškai aktyvus ir pasižymi stabilia optine spinduliuote. NV^- centro sukininės būsenos gali būti paruoštos (inicializuotos) ir nuskaitytos naudojant lazerio spinduliuotę, o vėliau ir koherentiškai valdomos mikrobangomis [21]. Sukinių koherentiškumo laikai siekia milisekundes kambario temperatūroje [22] ir net sekundes kriogeninėse temperatūrose [23]. Šių savybių dėka deimanto NV^- centras tapo viena iš pagrindinių sistemų, taikomų tirti ir realizuoti įvairias kvantines technologijas [9]. Daug sėkmingų eksperimentų yra pademonstruota kvantinės metrologijos [11], kvantinės komunikacijos [12] ir kvantinės kompiuterijos [13, 14] srityse. Šie pasiekimai įkvėpė ieškoti kitų defektų, tinkančių kvantinių reiškinių tyrimui bei technologijų kūrimui [15]. Šiuo metu yra aptiktos ir kitos sistemos, turinčios panašias kvant-mechanines savybes į NV centrą [6, 8, 16]. Viena iš jų yra neigiamai įkrautas silicio–vakansijos (SiV^-) centras deimante [16, 171], kuris taip pat yra teoriškai nagrinėjamas disertacijoje.

Giliųjų defektų tyrimai reikalauja daug eksperimentinių ir teorinių pastangų. Visų pirma, defektas kompleksiškai sąveikauja su jį supančia kristalo aplinka, kurioje apstu kitų struktūrinių ir izotopinių defektų. Todėl eksperimente kartais yra sunku atskirti tik defektui būdingas savybes nuo jį supančios aplinkos. Net defekto cheminės struktūros nustatymas yra gana sudėtinga užduotis. Dėl šių priežasčių defekto teorinis aprašymas yra ir svarbus, ir naudingas.

Ši disertacija yra apie giliųjų defektų elektroninės, virpesinės ir vibroninės[1] struktūros teorinį nagrinėjimą. Šios struktūros yra pamatinės ir patikimas jų nustatymas yra svarbus žingsnis, siekiant suprasti sudėtingą giliųjų defektų fiziką. Tikslus šių struktūrų aprašymas leidžia modeliuoti defekto sąveiką su šviesa ir nustatyti spinduliuotės bei sugerties spektrus. Dėl sąveikos su gardele spalvinio centro liuminescencijos ir sugerties spektrų linijos dažnai turi unikalią formą, kuri yra savotiškas „defekto parašas“. Taigi, lygindami modelinį spektrą su eksperimentu, galime įvertinti teorinių metodų patikimumą, o tikslus spektrų nustatymas pasitarnautų defektų identifikavimui. Šioje disertacijoje tobulinamos ir vystomos *ab initio* teorinės metodologijos, skirtos: (i) virpesinės ir vibroninės struktūros, (ii) elektron–fononinės sąveikos, (iii) optinių linijų ir (iv) fotojonizacijos skerspjūvių aprašymui. Šios metodologijos pritaikomos deimanto giliųjų defektų teoriniam nagrinėjimui. Darbe pateiktos kelios svarbios fizikinės išvados apie SiV^- ir NV^- centrų virpesinę struktūrą bei NV^- centro sąveiką su šviesa.

[1] Šioje disertacijoje sąvoka „vibroninis“ reikšia būseną, kurioje negalime adiabatiškai atskirti elektroninių ir virpesinių laisvės laipsnių.

1.1 Tyrimo tikslai ir uždaviniai

Pirmasis šios disertacijos tikslas yra išvystyti teorines metodologijas, skirtas virpesinių struktūrų, optinių linijų ir fotojonizacijos procesų aprašymams. Antrasis tikslas yra šių metodų taikymas paaiškinti SiV^- ir NV^- centrų virpesinę struktūrą bei NV^- centro fotojonizacijos mechanizmus. Šiems tikslams pasiekti buvo suformuluoti keli uždaviniai:

(1) Tobulinti teorinę skaitinę metodologiją pavienių defektų virpesinės struktūros nagrinėjimui.

(2) Sukurti praktinę teorinę metodologiją neadiabatinių Jahn–Teller sąveikų analizei daugelio virpesinių modų sistemoje.

(3) Sukurti teorinę metodologiją giliųjų defektų fotojonizacijos skerspjūvių kiekybiniam skaičiavimui.

(4) Teoriškai ištirti neigiamai įkrauto silicio–vakansijos (SiV^-) centro virpesinę struktūrą bei paaiškinti liuminescencijos spektre stebimą izotopinį fononų piko poslinkį.

(5) Sumodeliuoti neigiamai įkrauto azoto–vakansijos (NV^-) centro liuminescencijos ir sugerties spektrus bei paaiškinti eksperimente stebimą asimetriją tarp šių dviejų spektrų.

(6) Ištirti galimus NV^- centro fotojonizacijos mechanizmus ir suskaičiuoti šių jonizacijos procesų slenksčius bei skerspjūvius.

1.2 Ginamieji teiginiai

(I) Deimanto SiV^- centro fotoliuminescencijos spektro aštri fononų smailė atsiranda dėl e_u simetrijos virpesinio rezonanso. Šios smailės egzistavimas spektre nepaaiškinamas Frank–Condon artinio ribose ir reikalauja tikslesnės elektron–fononinės sąveikos teorijos. Galima šios smailės egzistavimo spektre priežastis yra Herzberg–Teller efektas.

(II) Darbe išvystyta nauja *ab initio* teorinė metodologija, skirta daugelio modų Jahn–Teller sąveikų analizei. Ši metodologija patobulina esamus teorinius metodus, kurie remiasi vienos modos artiniu.

(III) Mūsų *ab initio* liuminescencijos ir sugerties linijų skaičiavimo metodologija dideliu tikslumu atkartoja NV^- centro eksperimentinius spektrus.

(IV) Jonizavus NV^- centrą iš sužadintos ^3E būsenos, neutralus NV centras atsiduria kvartetinėje $^4A_2$ būsenoje. Šio jonizacijos proceso slenksčio energija yra 1.15 eV. Kvartetinės būsenos modelis paaiškina elektronų sukinių rezonanso eksperimentus, kuriuose stebima $^4A_2$ būsenos sukinių poliarizacija.

(V) Mūsų *ab initio* fotojonizacijos skerspjūvių skaičiavimai puikiai paaiškina naujus NV^- centro fotojonizacijos eksperimentus ir suteikia naujų svarbių žinių apie NV krūvio dinamiką.

1.3 Darbo aktualumas ir naujumas

Disertacijoje nagrinėjami optiškai aktyvūs gilieji kristalo defektai ir jų *ab initio* teorinio aprašymo galimybės. Darbe pristatomi nauji teoriniai metodai, skirti nagrinėti defekto virpesinę ir vibroninę struktūras. Didelė disertacijos dalis yra apie optinių spektrų modeliavimą, kurių nustatymas turėtų pasitarnauti naujų defektų analizei ir atpažinimui. Toliau trumpai aptariamos darbe išvystytos metodologijos bei jų praktinis taikymas tiriamoms sistemoms.

Virpesių ir virpesinių rezonansų analizės metodologija. Doktorantūros metu tobulinta defekto virpesių skaičiavimo metodologija bei parašytas virpesių skaičiavimo programinis paketas, kuris tinka aukšo našumo kompiuteriams. Ši programa skaičiuoja defekto virpesius labai didelėse supergardelėse, kurios efektyviai aprašo izoliuoto defekto sistemą. Taip pat darbe pristatomas naujas metodas analizuoti defekto virpesinius rezonansus bei jų izotopinius poslinkius.

Ši virpesių skaičiavimo metodologija buvo praktiškai pritaikyta deimanto kristalo silicio–vakansijos (SiV) ir azoto–vakansijos (NV) defektų nagrinėjimui. Tyrimo metu gautos naujos fizikinės išvados apie šių centrų virpesinę struktūrą.

Daugelio modų Jahn–Teller sistemų analizės metodologija. Elektroninės būsenos išsigimimas lemia Jahn–Teller efektą, dėl kurio negalime efektyviai atskirti jonų ir elektronų dinamikos, kaip tai daroma adiabatiniame artinyje. Tokios sistemos analizė yra labai sudėtinga ir iki šiol defektuose Jahn–Teller efektai nagrinėti naudojant vienos sąveikaujančios modos modelį. Šioje disertacijoje pristatome naują praktinį metodą, pagrįstą tankio funkcionalo teorijos skaičiavimais, kurio dėka galima aprašyti daugelio virpesinių modų Jahn–Teller sistemą. Ši metodologija atveria naujas galimybes teoriniam išsigimusių defekto būsenų aprašymui.

Disertacijoje Jahn–Teller sistemos analizė pritaikyta modeliuojant NV^- centro emisijos ir sugerties spektrus. Gautos linijos puikiai atitinka eksperimentą ir demonstruoja metodologijos bei tankio funckionalo teorijos skaičiavimų patikimumą.

Fotojonizacijos skerspjūvių skaičiavimo metodologija. Kiekybiniai *ab initio* fotojonizacijos skerspjūvių skaičiavimai defektams iki šiol nebuvo pademonstruoti. Šiame darbe pristatoma nauja metodologija, skirta jonizacijos skerspjūvių skaičiavimui, naudojant tankio funkcionalo teoriją.

Ši metodologija buvo praktiškai pritaikyta nagrinėjant NV^- centro fotojonizacijos mechanizmus. Tyrime suskaičiuoti jonizacijos, sugerties ir stimuliuotos emisijos skerspjūviai. Šių duomenų pagalba parodyta, kuriose energijos ruožuose fotojonizacija dominuoja prieš stimuliuotą emisiją bei sugertį. Gauti rezultatai suteikia naujų žinių apie NV krūvio dinamiką bei puikiai sutampa su naujausiais fotojonizacijos eksperimentais.

1.4 Autoriaus indėlis ir rezultatų pristatymas mokslinei visuomenei

Disertacijos darbo rezultatai buvo pristatyti penkiose mokslinėse publikacijose:

(I) E. Londero, G. Thiering, L. Razinkovas, A. Gali, and A. Alkauskas, *Vibrational modes of negatively charged silicon-vacancy centers in diamond from ab initio calculations*, Phys. Rev. B **98**, 035306 (2018).

(II) L. Razinkovas, M. W. Doherty, N. B. Manson, C. G. Van de Walle, and A. Alkauskas, *Vibrational and vibronic structure of isolated point defects*: *The nitrogen-vacancy center in diamond*, Phys. Rev. B **104**, 045303 (2021).

(III) L. Razinkovas, M. Maciaszek, F. Reinhard, M. W. Doherty, and A. Alkauskas, *Photoionization of negatively charged NV centers in diamond*: *theory and ab initio calculations*, Phys. Rev. B, *priduotas* (2021).

(IV) L. Skuja, K. Smits, A. Trukhin, F. Gahbauer, R. Ferber, M. Auzinsh, L. Busaite, L. Razinkovas, M. Mackoit-Sinkeviciene, and A. Alkauskas, *Dynamics of Singlet Oxygen Molecule Trapped in Silica Glass Studied by Luminescence Polarization Anisotropy and Density Functional Theory*, J. Phys. Chem. C **124**, 7244 (2020).

(V) M. Maciaszek, L. Razinkovas and A. Alkauskas, *Thermodynamics of carbon defects in hexagonal boron nitride*, Phys. Rev. Mater., *priduotas* (2021).

Šios disertacijos autorius yra pagrindinis publikacijų (II) ir (III) autorius. Autoriaus darbo rezultatai buvo pristatyti keliose mokslinėse konferencijose:

(1) L. Razinkovas (pranešėjas), A. Alkauskas, *Virpesinės izoliuotų taškinių defektų savybės*, 42-oji Lietuvos Nacionalinė Fizikos konferencija, 2017-10-04, Vilnius, Lietuva.

(2) L. Razinkovas (pranešėjas), A. Alkauskas, *Defektų liuminescencijos linijos modeliavimas ab initio metodais*, FizTech, 2018-10-17, Vilnius, Lietuva.

(3) L. Razinkovas (pranešėjas), G. Thiering, A. Gali, A. Alkauskas, *Vibrational modes of negatively charged silicon-vacancy centers in diamond from ab initio calculations*, Diamond Workshop SBDD XXIV, 2019-03-13, Haseltas, Belgija.

(4) L. Razinkovas (pranešėjas), E. Londero, G. Thiering, A. Gali, A. Alkauskas, *Vibrational modes of negatively charged silicon-vacancy centers in diamond from ab initio calculations*, FizTech, 2019-10-23, Vilnius, Lietuva.

(5) L. Razinkovas (pranešėjas), M. Maciaszek, F. Reinhard, M.W. Doherty, A. Alkauskas, *Photoionization of negatively charged NV centers in diamond: theory and ab initio calculations*, ICDS 31, 2021-07-25, Oslas, Norvegija.

2 Disertacijos sandara

Šią disertaciją sudaro penki pagrindiniai skyriai. Įvadiniame skyriuje trumpai aptariami gilieji kristalo defektai ir jų svarba, kuriant kvantines technologijas. Čia suformuluojamas tiriamojo darbo tikslas ir pagrindiniai uždaviniai. Formali defekto elektroninės, virpesinės ir vibroninės struktūros teorija pristatoma antrame skyriuje. Šio skyriaus turinys daugiausia remiasi kitais moksliniais šaltiniais. Autoriaus originalus indėlis yra pateiktas skyreliuose 2.5.3, 2.6.3 ir 2.6.4, kuriuose nagrinėjama NV centro Jahn–Teller sistema. Šiuose skyreliuose pristatomos ir išvedamos lygtys, taikomos nagrinėjant NV centro vibroninę struktūrą. Trečias disertacijos skyrius pristato defekto virpesinės struktūros tyrimo metodologiją. Ši metodologija pritaikyta dviems neigiamai įkrautiems deimanto defektams: azoto–vakansijos (NV) ir silicio–vakansijos (SiV) centrams. Silicio-vakansijos virpesinės struktūros tyrimo medžiaga publikuota disertacijos straipsnyje [T1]. Ketvirtame skyriuje pristatomi NV^- centro liuminescencijos ir sugerties spektrų skaičiavimai. Gauti spektrai lyginami su eksperimentu ir aptariamas teorijos patikimumas ir trūkumai. Šio tyrimo medžiaga publikuota disertacijos straipsnyje [T2]. Penktame skyriuje nagrinėjama NV centro fotojonizacija, kurios metu defektas pakeičia krūvio būseną iš neigiamai įkrautos (NV^-) į neutralią (NV^0). Čia pristatomi fotojonizacijos slenksčių ir skerspjūvių skaičiavimai, kurie publikuoti disertacijos straipsnyje [T3]. Toliau trumpai apžvelgsime disertacijos turinį ir pagrindines išvadas.

2.1 Teorijos ir metodologijos apžvalga: elektroninė, virpesinė ir vibroninė defekto struktūra

Kalbėdami apie virpesių molekulėse ar kietuosiuose kūnuose aprašymą naudojant kvantinę mechaniką, visada turime omenyje adiabatinę aproksimaciją, kuri efektyviai atskiria branduolių sistemą nuo elektronų. Iš tikrųjų, adiabatinių aproksimacijų yra keletas rūšių, o pati paprasčiausia yra statinė adiabatinė aproksimacija (žr. 2.2 skyrelį). Ji naudojama šiame darbe. Nors šis adiabatinis artinys yra grubiausias iš visų, jis yra labai patogus nagrinėjant sudėtingesnius neadiabatinius reiškinius (Jahn–Teller efektą). Statinėje aproksimacijoje elektroninės sistemos Schrödinger lygtis yra sprendžiama laikant, kad branduoliai yra klasikinės nejudančios dalelės. Suradę elektroninės lygties sprendinius, galime suskaičiuoti adiabatinės potencinės energijos paviršius branduoliams, o šie paviršiai pilnai apibrėžia kvant-mechaninį uždavinį gardelės dinamikai. Formaliai, adiabatinis bendrosios sistemos sprendinys užsirašo taip:

$$\Psi_{i,n}(\mathbf{r},\mathbf{R}) = \psi_i(\mathbf{r})\chi_{i,n}(\mathbf{R}),$$

čia $\psi_i(\mathbf{r})$ yra elektroninė banginė funkcija, o $\chi_{i,n}(\mathbf{R})$ yra branduolių banginė funkcija, elektronams esant būsenoje i. Taigi, kai kalbame apie elektroninę ir virpesinę struktūrą, visada turime omenyje šias dvi dedamąsias.

Elektroninės sistemos sprendimas: tankio funkcionalo teorija

Adiabatiniame artinyje pirmoji užduotis yra elektroninių būsenų $\psi_i(\mathbf{r})$ radimas. Daugelio dalelių sistemoms tikslus elektroninės Schrödinger lygties sprendimas yra neįmanomas, todėl naudojami artutiniai metodai. Šiame darbe mes pasirinkome tankio funkcionalo teoriją (angl. *density functional theory*, DFT), kuri leidžia apytiksliai spręsti elektroninį uždavinį skaitiniais metodais (žr. 2.3 skyrelį). Defekto elektroninių būsenų skaičiavimams naudojamas geometrinis supergardelės modelis (žr. 2.3.4 skyrelį), kuriame defektas yra patalpinamas į didelį, periodiškai atsikartojantį kristalo gardelės fragmentą.

Tankio funkcionalo teorija yra griežtai apibrėžta pagrindinės elektroninės būsenos radimui, o teorijos netobulumai atsiranda dėl apytisklių pakaitos–koreliacijos funcionalo formų (angl. *exchange–correlation functional*). Naudodami modernius funkcionalus, dideles supergardeles ir šiuolaikinius superkompiuterius galime gana tiksliai surasti pagrindinę elektroninę būseną ir suskaičiuoti jos adiabatinius potencinės energijos paviršius. Tačiau sužadintų būsenų skaičiavimas yra labiau apytikslis ir sudėtingesnis. Šių būsenų modeliavimui naudojame taip vadinamą ΔSCF metodologiją (2.3.2 skyrelis) ir molekulinių defekto orbitalių modelį (2.3.5 skyrelis).

Defekto virpesiai: įterpimo metodologija

Suradus elektroninės sistemos būsenas, defekto gardelės virpesiai skaičiuojami taikant harmoninę aproksimaciją, kurioje virpesiai atitinka mažos amplitudės judėjimą apie pusiausvyrąsias padėtis (žr. 2.4 skyrelį). Tokie sprendiniai įprastai vadinami „fononais“ arba „modomis“. Defektas pakeičia idealios gardelės virpesinę struktūrą. Įterpus defektą, gali atsirasti *lokalios* arba *rezonansinės* modos, kurių amplitudė defekto aplinkoje yra didesnė, lyginant su erdviškai išplitusiais kristalo virpesiais. Dėl šios priežasties, tokio tipo virpesiai stipriau sąveikauja su elektronine sistema ir yra svarbūs, aprašant elektron fononinius defekto reiškinius. Lokalios modos atsiranda energijos srityje, kurioje idealus kristalas neturi virpesių. Šios modos yra stipriai lokalizuotos. Tuo tarpu rezonansinės modos yra perturbuoti kristalo virpesiai. Jos susigrupuoja tam tikros energijos diapazone. Taigi, kalbėdami apie virpesinį rezonansą, visada turime omenyje ne vieną modą, o lokalizuotų modų rinkinį.

Deja, praktiniai virpesinės struktūros skaičiavimai supergardelės geometrijoje nėra labai tikslūs. Supergardelėje modeliuojamas tankiai periodiškai atsikartojantis defektas. Tačiau realiame kristale defektų koncentracija yra labai maža ir tikslesnis modelis būtų „izoliuotas defektas begaliniame kristale“. Dėl skaičiavimų sudėtingumo ir laiko, tankio funkcionalo teorijos skaičiavimuose supergardelės dydis negali viršyti šimtų ar tūkstančių atomų. Disertacijos tyrime parodome, kad tokiose gardelėse virpesinė struktūra netiksliai atspindi izoliuoto defekto modelį. Šios problemos sprendimui naudojame įterpimo metodologiją (angl. *embedding methodology*), kurioje iš skaičiavimų mažose supergardelėse sukonstruojamas virpesinės struktūros modelis labai didelėms supergardelės geometrijoms (3.3 skyrelis). Šiose sistemose atomų skaičius gali siekti dešimtis tūkstančių atomų.

Jahn–Teller sistema ir vibroninės būsenos

Adiabatinė aproksimacija yra gana tiksli, kada energijos skirtumai tarp elektroninių lygmenų yra daug didesni nei charakteringa virpesinės sistemos sužadinimo energija. Tačiau aukšta defekto taškinė simetrija dažnai lemia išsigimusias elektronines būsenas. Šiuo atveju adiabatinė aproksimacija tampa nekorektiška ir nebegalime atskirai nagrinėti elektronų ir branduolių dinamikos. Paprastai kalbant, išsigimusios sistemos branduolių dinamika stipriai veikia elektroninę posistemę ir atvirkščiai. Tokios būsenos literatūroje vadinamos Jahn–Teller (JT) sistemomis (žr. 2.5 skyrelį), o jų bendra banginė funkcija turi pavidalą:

$$\Psi(\mathbf{r}, \mathbf{R}) = \sum_i \psi_i(\mathbf{r})\chi_i(\mathbf{R}),$$

čia i sumuojamas per išsigimusius elektroninius lygmenis $\psi_i(\mathbf{r})$. Jahn–Teller sistemos sprendimas yra sudėtingas, todėl dažniausiai defektų fizikoje yra naudojamas efektyvus vienos modos modelis [106, 111]. Nors šis modelis paaiškina kokybinę sistemos elgseną, kiekybiniam aprašymui jis tinka tik labai stiprios Jahn–Teller sąveikos atveju [112]. Dėl šios priežasties disertacijoje detaliai nagrinėjamas teorinis Jahn–Teller sistemų aprašymas. Čia pirmą kartą pristatoma *ab initio* metodologija, skirta teoriniam daugelio modų JT sistemos nagrinėjimui.

2.2 Virpesinė defekto struktūra

Šios disertacijos trečiame skyriuje nagrinėjama deimanto NV^- ir SiV^- centrų virpesinė struktūra. Šiame skyriuje pristatoma įterpimo metodologija (angl. *embedding methodology*), skirta nagrinėti virpesius efektyviai izoliuotoje defekto sistemoje. Taikant šią metodologiją, suskaičiuoti centrų virpesiniai spektrai ir atlikta virpesių lokalizacijos bei simetrijos analizė. NV^- defekto virpesinis spektras vėliau naudojamas optinių linijų modeliavimui, kuris pristatomas ketvirtame disertacijos skyriuje. SiV^- centro virpesinių rezonancų bei jų izotopinių poslinkių tyrimas buvo publikuotas disertacijos straipsnyje [T1]. Toliau trumpai pristatysime SiV^- centro tyrimą ir pagrindines išvadas.

SiV^- centro virpesinė struktūra

Per pastarąjį dešimtmetį neigiamai įkrautas silicio–vakansijos (SiV) centras deimante tapo perspektyviu konkurentu NV centrui [171]. Šis centras turi geras spektrines charakteristikas: jo liuminescencijos fononinė pajuostė yra labai silpna ir maždaug apie 70% spinduliuotės intensyvumo tenka befononei linijai [142] (žr. 3.11(b) pav.). Toks befononės linijos ryškumas yra labai svarbus koherentinių fotonų emisijai, kuri reikalinga kvantinės optikos ir kvantinių technologijų taikymams.

Neseniai atliktame SiV centro eksperimentiniame tyrime buvo stebėtas liuminescencijos piko, nutolusio nuo befononės linijos per 64 meV, poslinkis žemesnių energijų kryptimi [141], atsirandantis keičiant silicio izotopą. Ankstesni tankio funkcionalo teorijos skaičiavimai aptiko lokalizuotą modą su panašia energija (56.5 meV) [140], tačiau teoriškai suskaičiuoti izotopiniai poslinkiai yra daug mažesni nei stebima eksperimente. Eksperimente ^{29}Si ir ^{30}Si izotopams piko energija sumažėjo atitinkamai 1.02 meV ir 2.21 meV. Tuo tarpu teoriniai poslinkiai yra 0.62 meV ir 1.24 meV.

1 lentelė: Teorinių skaičiavimų palyginimas su ekperimentiniais duomenimis. Teorija: a_{2u} ir e_u simetrijos virpesinių rezonansų dažniai Ω ir izotopiniai poslinkiai. Eksperimentas: liuminescencsijos fononų pikų dažniai Ω ir izotopiniai poslinkiai. Eksperimentiniai duomenys iš šaltinio [141]. ND = „neužfiksuotas“.

Teorija: virpesiniai rezonansai

simetrija	Ω_{28} (meV)	Ω_{28}/Ω_{29}	Ω_{28}/Ω_{30}
a_{2u}	43.4	1.018	1.035
e_u	60.1	1.021	1.039

Eksperimentas: fotoliuminescencijos fononų pikai

	Ω_{28} (meV)	Ω_{28}/Ω_{29}	Ω_{28}/Ω_{30}
	64	1.016	1.036
	42	ND	ND

Disertacijoje, taikant tankio funkcionalo teoriją ir įterpimo metodologiją, nagrinėta neigiamai įkrauto SiV centro virpesinė struktūra. Įterpimo metodologijos pagalba tirti defekto virpesiniai spektrai gardelėse, talpinančiose iki 5832 atomų. Tyrime nustatyta, kad defekto perturbacija lemia dviejų a_{2u} ir e_u simetrijos virpesinių rezonansų atsiradimą. Savo skaičiavimuose parodome, kad izotopinio poslinkio nustatymas, nagrinėjant vieną rezonanso virpesį, nėra korektiškas. Būtent ši priežastis ir lėmė izotopinių poslinkių neatitikimą tarp eksperimento ir ankstesnių teorinių skaičiavimų [140]. Tuo tikslu darbe pristatyta nauja metodologija virpesinių rezonansų nagrinėjimui ir jų izotopinių poslinkių nustatymui. Naudojant šią metodologiją suskaičiuotos virpesinių rezonansų energijos ir izotopiniai poslinkiai. Šie rezultatai, kartu su eksperimentiniais fononų piko matavimais, pateikti 1 lentelėje. Matome, kad teorinė e_u rezonanso energija ir izotopinis poslinkis puikiai sutampa su 64 meV eksperimentiniu piku ir jo poslinkiu. Šis sutapimas leidžia spėti, kad liuminescencijos pikas ties 64 meV atsiranda dėl e_u virpesinio rezonanso. Tačiau mūsų tyrimas rodo, kad e_u simetrijos modų atsiradimas liuminescencijos spektre yra nepaaiškinamas Franck–Condon artinio ribose. Dėl šios priežasties, darbe iškelta hipotezė: e_u *fononai dalyvauja optiniame šuolyje dėl Herzberg–Teller efekto*, kurio metu branduolių virpesys moduliuoja optinio šuolio matricinį elementą. Šis tyrimas publikuotas pirmame disertacijos straipsnyje [T1].

2.3 Deimanto NV^- centro liuminescencijos ir sugerties linijos

Ketvirtas disertacijos skyrius yra skirtas giliųjų defektų optinio spektro linijų modeliavimui. Šios linijos turi defektams specifišką formą, kuri yra nulemta elektroninės ir virpesinės defekto struktūros. Todėl tikslūs tokių linijų skaičiavimai turi keleriopą svarbą. Visų pirma, gebėjimas tiksliai atkartoti eksperimentinį spektrą pasitarnautų identifikuojant giliuosius kristalo defektus. Tačiau ne mažiau svarbus yra ir teorinis aspektas. Tokių spektrinių linijų modeliavimas remiasi į elektroninės ir virpesinės struktūros teorinį aprašymą. Lygindami teoriją su eksperimentu mes galime įvertinti teorinių metodų bei artinių patikimumą. Defektų optinių linijų skaičiavimas yra sena teorinės fizikos problema, nagrinėta jau daugiau nei prieš pusę šimtmečio [124, 125]. Deja, tikslūs šių linijų skaičiavimai, naudojant pirminius kvantinės mechanikos principus, yra gana sudėtingi ir iki šiol nėra gerai išvystyti.

Disertacijoje nagrinėjamos neigiamai įkrauto deimanto NV centro optinio spektro linijos. Šis defektas turi gerai ištirtas spektrines charakteristikas, kurių fizikinė prigimtis dar nėra iki galo paaiškinta. NV^- centras yra įdomus ir tuo, kad optiškai sužadinta elektroninė būsena yra dvigubai išsigimusi. Šis išsigimimas lemia dinaminį Jahn–Teller efektą. Todėl, darbe daug dėmesio skirta Jahn–Teller efekto teoriniam nagrinėjimui. Vienas iš pagrindinių disertacijos pasiekimų yra naujos praktinės metodologijos, skirtos daugelio modų $E \otimes (e \oplus e \oplus \cdots)$ Jahn–Teller sistemos analizei, sukūrimas.

Disertacijoje pristatomas NV^- centro elektroninės, virpesinės ir vibroninės sistemos tyrimas naudojant tankio funckionalo teorijos skaičiavimus. Siekiant didelės optinių linijų spektrinės raiškos, defekto virpesinė struktūra skaičiuota labai didelėse supergardelėse (iki 64 000 atomų). Skaičiavimai atlikti naudojant PBE ir HSE pakaitos–koreliacijos funkcionalus. Šie funkcionalai yra dažniausiai naudojami defektų elektroninės struktūros skaičiavimams. Mūsų tyrimas rodo, kad abu tankio funkcionalai gerai aprašo virpesinę NV centro struktūrą: teorinės PBE optinio spektro pikų vertės beveik idealiai sutampa su eksperimentinėmis, tuo tarpu, HSE funkcionalui šios energijos yra šiek tiek didesnės (žr. 4.9 ir 4.10 pav.). Nors bendra teorinė liuminescencijos ir sugerties spektrų forma gerai sutampa su eksperimentu, matomas nedidelis neatitikimas šių spektrų svorių pasiskirstyme. Šis nesutapimas atsiranda dėl netiksliai įvertintos gardelės relaksacijos po optinio šuolio, o jo priežastis yra netikslus sužadintos būsenos modeliavimas. Tyrimo metu pastebėta, kad neatitikimas, aprašant elektroninės sistemos sąveiką su virpesiais, yra sistemingas ir maždaug vienodas visoje spektrinėje srityje. Tuo tikslu įvestas fenomenologi-

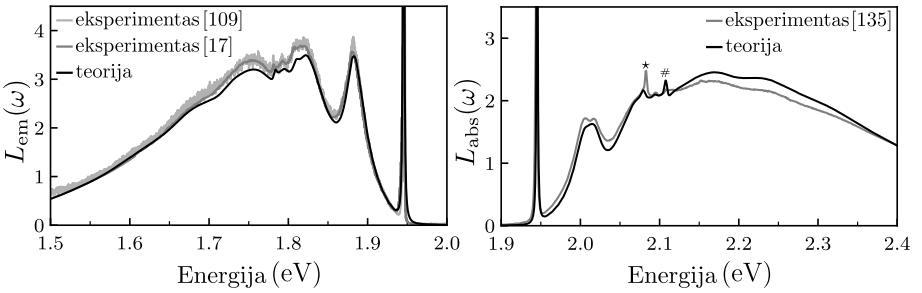

1 pav.: Teorinės ir eksperimentinės (a) liuminescencijos ir (b) sugerties linijos. Teoriniuose skaičiavimuose PBE Huang–Rhys spektrai padauginti iš fenomenologinės konstantos $\zeta = 1.2$: $S'_{a_1} = \zeta S_{a_1}(\omega)$ ir $S'_e = \zeta S_e(\omega)$. Eksperimentiniai spektrai iš [17], [109] ir [135].

nis daugiklis ζ, iš kurio dauginamos elektron–fononinės sąveikos konstantos (Huang–Rhys parametrai). Parinkus vertę $\zeta = 1.2$, gautos teorinės kreivės puikiai sutampa su eksperimentu. 1 paveiksle pavaizduotos galutinės teorinės (a) liuminescencijos ir (b) sugerties linijos kartu su eksperimentiniais spektrais. Iš šių palyginimų matome, kad teorija puikiai atkartoja bendrą asimetriją tarp emisijos ir absorbcijos bei paaiškina skirtingą pirmojo fononų piko struktūrą. Mūsų skaičiavimai rodo, kad šio piko išplitimas sugerties spektre yra virpesinės struktūros pokyčio sužadintoje būsenoje pasekmė. Šį piką lemia visiškai simetrinės a_1 modos, o ne Jahn–Teller aktyvios modos (kaip buvo manoma anksčiau [111]).

Šio tyrimo rezultatai parodo, kad naudojant modernius tankio funckionalo teorijos skaičiavimus galime dideliu tikslumu nustatyti giliųjų defektų optines linijas. Tačiau iki idealaus tikslumo trūksta geresnių funkcionalų ir metodų, skirtų sužadintų būsenų skaičiavimams. Neskaitant to, pristatytas tyrimas patobulina pirminių principų skaičiavimo metodologiją elektron–fononinės sąveikos aprašymams. Šis tyrimas publikuotas antrame disertacijos straipsnyje [T2].

2.4 Deimanto NV^- centro fotojonizacija

Dauguma praktinių NV centro taikymų reikalauja optinio sužadinimo. Tačiau stipriai šviesdami lazeriu, galime sukelti spindulinio centro fotojonizaciją, kurios metu defekto sistema pakeičia krūvio būseną iš neigiamai įkrautos (NV^-) į neutralią (NV^0). Daugumai taikymų šis procesas yra nepageidautinas, tačiau egzistuoja ir atvejų, kada fotojonizacija yra naudinga. Pavyzdžiui, neseniai pristatyti du nauji sukinio nuskaitymo protokolai, kurie pagrįsti neigiamo centro fotojonizacijos mechanizmais [149, 150].

2 lentelė: Neigiamai įkratuto NV centro fotojonizacijos slenksčiai. Eksperimentiniai duomenys paimti iš šaltinių [148, 153]. Fotojonizacijos iš singletinės būsenos IP(^1E) vertė nebuvo tiesiogiai suskaičiuota, bet nustatyta naudojant eksperimentinius duomenis iš šaltinio [158].

	IP($^3A_2$)	IP(^3E)	IP(^1E)
teorija	2.67	1.15	*2.2*
eksperimentas	2.6[a], 2.7[b]	–	–

[a] Šaltinis [148]
[b] Šaltinis [153]

Eksperimentinis NV centro fotojonizacijos slenksčių ir skerspjūvių matavimas yra sudėtingas. Visų pirma, šviečiant lazeriu pastoviai vyksta jonizacijos ir rekombinacijos procesai, kurių metu defektas keičia krūvio būsenas. Todėl, matavimuose yra sunku atskirti šiuos du procesus. Neskaitant to, NV^- centro fotojonizacija iš sužadintos būsenos konkuruoja su stimuliuotos emisijos procesu, kas padaro eksperimentinį tyrimą dar sudėtingesniu. Iš visų galimų NV^- centro fotojonizacijos mechanizmų yra žinomas tik jonizacijos iš pagrindinės būsenos eksperimentinis energijos slenkstis (energija virš kurios prasideda fotojonizacijos procesas). Tačiau praktiniams taikymams (kai jonizacija žalinga ir naudinga) svarbiausias mechanizmas yra jonizavimas iš sužadintos ^3E būsenos, kuris iki šiol nėra gerai ištirtas.

Šios disertacijos penktame skyriuje tiriama neigiamai įkrauto NV centro fotojonizacija iš trijų elektroninių būsenų: $^3A_2$, ^3E ir ^1E. Pirmoje tyrimo dalyje nagrinėjama defekto elektroninė struktūra prieš ir po jonizacijos. Darbe nustatyti procesų mechanizmai ir galutinės neutralaus centro būsenos, pavaizduotos 2 paveikslėlyje. Matome, kad po jonizacijos iš pagrindinės tripletinės ($^3A_2$) ir metastabilios singletinės (^1E) būsenų, defektas atsiduria ^2E būsenoje, kuri yra pagrindinė neutralaus centro būsena. Tačiau, jonizavus defektą iš sužadintos ^3E būsenos, NV^0 centras atsiduria metastabilioje kvartetinėje būsenoje $^4A_2$. Šis rezultatas prieštarauja nusistovėjusiai nuomonei, kad šio proceso galutinė būsena irgi yra pagrindinė neutralaus centro būsena ^2E. Darbe parodome, kaip NV^- sukinio poliarizacija lemia kvartetinės būsenos sukinio poliarizaciją. Šis modelis paaiškina iki šiol nesuprastus elektronų paramagnetinio rezonanso eksperimentus [159].

Antroje tyrimo dalyje skaitmeniškai nagrinėjami fotojonizacijos slenksčiai ir skerspjūviai. Suskaičiuotos slenksčių vertės pateiktos 2 lentelėje (IP(^3E) ir IP(^1E) vertės iki šiol nebuvo žinomos). Fotojonizacijos skerspjūvių nustatymui

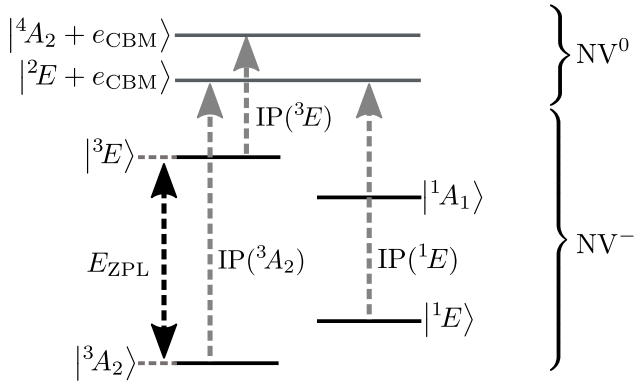

2 pav.: NV$^-$ centro fotojonizacijos mechanizmai iš $^3A_2$, ^3E ir ^1E būsenų. Horizontalios juodos linijos žymi NV$^-$ energetinius lygmenis, o pilkos – NV^0 būsenas po jonizacijos. Brūkšniuotos rodyklės žymi galimus fotojonizacijos perėjimus. E_{ZPL} yra befononė tripletinio šuolio energija.

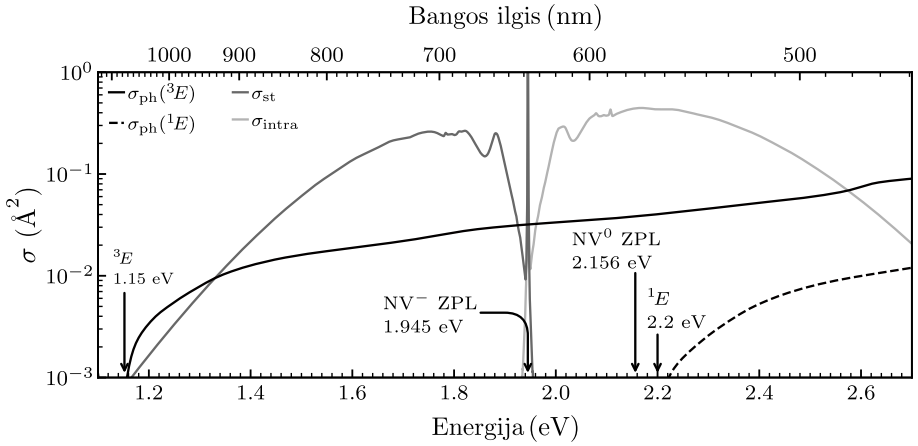

3 pav.: Teoriniai pagavos skerspjūviai. Ištisinė juoda linija (σ_{ph}): fotojonizacija iš sužadintos ^3E būsenos; tamsiai pilka ištisinė linija (σ_{st}): NV$^-$ stimuliuota emisija; šviesiai pilka ištisinė linija (σ_{intra}): NV$^-$ sugertis; brūkšniuota juoda linija: fotojonizacija iš singletinės ^1E būsenos.

sukurta nauja metodologija, kuri remiasi tankio funkcionalo teorijos skaičiavimais, defekto molekulinių orbitalių modeliu ir elektron–fononinės sąveikos aprašymu. Šios metodologijos pagalba suskaičiuoti visų trijų mechanizmų skerspjūviai. Svarbiausias tyrimo rezultatas yra pateiktas 3 paveikslėlyje, kuriame atvaizduoti jonizacijos skerspjūviai iš ^3E ir ^1E būsenų, kartu su tripletinio šuolio ($^3A_2 \leftrightarrow {}^3E$) stimuliuotos emisijos ir sugerties skerspjūviais. Nagrinėjant santykį tarp ^3E jonizacijos ir stimuliuotos emisijos, nustatytos dvi energijos sritys ($\sim 1.25 \pm 1$ eV ir $\sim 1.92 \pm 0.25$ eV), kuriose fotojonizacija dominuoja prieš stimuliuotą emisiją. Šios teorinės sritys puikiai sutampa su naujais eksperimentiniais tyrimais, kuriuose efektyvi fotojonizacija buvo užfiksuota, naudojant 1.93 eV ir 1.17 eV lazerius [167, 168]. Taip pat gautas geras atitikimas su Hacquebard ir Childress eksperimentiniu tyrimu [166], kuriame įvertintas pavienio centro fotojonizacijos ir stimuliuotos emisijos skerspjūvių santykis, žadinant infraraudonos spinduliuotės lazeriu (1.62 eV) $\sigma_{\rm st}/\sigma_{\rm ph} \approx 13$. Mūsų teorinė vertė, suskaičiuota šiai energijai yra $\sigma_{\rm st}/\sigma_{\rm ph} = 12$. Šis atitikimas pagrindžia teorinės metodologijos patikimumą.

Šio tyrimo turinys buvo publikuotas trečiame disertacijos straipsnyje [T3].

PUBLICATIONS OF DOCTORAL DISSERTATION

(I) E. Londero, G. Thiering, L. Razinkovas, A. Gali, and A. Alkauskas, *Vibrational modes of negatively charged silicon-vacancy centers in diamond from ab initio calculations*, Phys. Rev. B **98**, 035306 (2018); doi: 10.1103/PhysRevB.98.035306.

(II) L. Razinkovas, M. W. Doherty, N. B. Manson, C. G. Van de Walle, and A. Alkauskas, *Vibrational and vibronic structure of isolated point defects: The nitrogen-vacancy center in diamond*, Phys. Rev. B **104**, 045303 (2021); doi: 10.1103/PhysRevB.104.045303.

(III) L. Razinkovas, M. Maciaszek, F. Reinhard, M. W. Doherty, and A. Alkauskas, *Photoionization of negatively charged NV centers in diamond: Theory and ab initio calculations*, Phys. Rev. B, *under review* (2021); arXiv:2104.09144.

(IV) L. Skuja, K. Smits, A. Trukhin, F. Gahbauer, R. Ferber, M. Auzinsh, L. Busaite, L. Razinkovas, M. Mackoit-Sinkevičienė, and A. Alkauskas, *Dynamics of singlet oxygen molecule trapped in silica glass studied by luminescence polarization anisotropy and density functional theory*, J. Phys. Chem. C **124**, 7244 (2020); doi: 10.1021/acs.jpcc.9b11581.

(V) M. Maciaszek, L. Razinkovas, and A. Alkauskas, *Thermodynamics of carbon defects in hexagonal boron nitride*, *submitted to Phys. Rev. Mater.* (2021); arXiv:2110.12167.

CURRICULUM VITAE

About the author

Lukas Razinkovas was born in 1987 in Vilnius, Lithuania. In 2012 he received his bachelor degree in Physics at the Faculty of Physics, Vilnius University. In 2016 he received his master degree in Theoretical Physics at Faculty of Physics, Vilnius University. In 2016 he started doctoral studies in the Center for Physical Sciences and Technology.

Apie autorių

Lukas Razinkovas gimė Vilniuje 1987 metais. 2012 metais baigė Fizikos bakalauro studijas Vilniaus universiteto Fizikos fakultete. 2016 metais baigė Teorinės fizikos magistro studijų programą Vilniaus universiteto Fizikos fakultete. 2016 metais pradėjo doktorantūros studijas Fizinių ir technologijos mokslų centre.

NOTES

NOTES

Vilnius University Press
9 Saulėtekio Ave., Building III, LT-10222 Vilnius
Email: info@leidykla.vu.lt, www.leidykla.vu.lt
Print run copies 15